

**COMBUSTION PERFORMANCE AND
MATERIAL CHARACTERISTICS OF AN
AMMONIUM PERCHLORATE COMPOSITE PROPELLANT
(APCP) WITH VARYING ALUMINUM PARTICLE SIZE**

by

David A. Avalos Violante

Submitted in Partial Fulfillment
of the Requirements for the Degree of
Master of Science in Mechanical Engineering
with Specialization in Explosives Engineering



New Mexico Institute of Mining and Technology
Socorro, New Mexico
January, 2025

This thesis is accepted on behalf of the faculty of the Institute by the following committee:

Michael J. Hargather

Academic and Research Advisor

Chelsey Hargather

Jamie Kimberley

I release this document to the New Mexico Institute of Mining and Technology.

David A. Avalos Violante

July 21st, 2024

This thesis is dedicated to...

My mom and dad, Blanca and Jose Luis Avalos, for their guidance and support, which made me into the man I am today. I would not have the opportunities I have in this life if it wasn't for their sacrifice. Last but not least, my friend and loyal companion, Kuma.

David A. Avalos Violante
New Mexico Institute of Mining and Technology
January, 2025

ACKNOWLEDGMENTS

I would first like to thank my research advisor, Dr. Michael Hargather, for his unwavering support and guidance over the past several years. I would not be the engineer I am today without his patience, encouragement, and invaluable contributions. I would also like to thank Mark Grubelich and Michael McPherson for their support in this research; their significant guidance has greatly contributed to my knowledge and experience. I'd like to thank Dr. Chelsey Hargather for allowing me to use her facilities to conduct research. Without her support, accomplishing my work elsewhere would have been challenging. I want to thank Dr. Jamie Kimberley for his detailed explanations of difficult concepts, which provided valuable insight into key aspects of my research.

Thank you to everyone in the mechanical engineering department who has helped me, especially Kimberly A. As I neared the end of my work, you were there to take some of the load off my shoulders. Thank you also to Patrick Madigan. Your support helped me to target my goals and develop my design-for-manufacturing skills.

To everyone in SGDL, thank you for your support and for being there for me when I needed it. I will always cherish the friendships and memories made. I would also like to thank my best friend, Levi, for his continuous support and friendship.

To my family, thank you for your invaluable support. My achievements would mean little without you. Thank you for pushing me towards my full potential.

This research was supported by the DOE MSIPP award DE-NA0004108 – The Rio Grand Consortium for Advanced Research on Exascale Simulation (Rio Grande CARES) and the New Mexico Space Grant Consortium (NMSGC).

This thesis was typeset with \LaTeX ¹ by the author.

¹The \LaTeX document preparation system was developed by Leslie Lamport as a special version of Donald Knuth's \TeX program for computer typesetting. \TeX is a trademark of the American Mathematical Society. The \LaTeX macro package for the New Mexico Institute of Mining and Technology thesis format was written by John W. Shipman.

ABSTRACT

The combustion performance and material response characterization of solid propellants are important for multiple applications, including space exploration, satellite payload delivery, and military applications. Two formulations of an ammonium perchlorate composite propellant (APCP) with $3\text{ }\mu\text{m}$ and $10\text{ }\mu\text{m}$ aluminum particle sizes were developed and analyzed here. Theoretical performance parameters were first acquired through modeling using NASA CEA to predict the chemical equilibrium of various mixture ratios for the final selection of the final propellant composition. A pressurized strand burner was designed and manufactured for small-scale burn rate analysis and bulk flame temperature measurements using non-intrusive optical diagnostic systems. Small-scale burn rate analysis was performed to determine the burn rate coefficient and exponent, a and n , respectively. Emitted light from the propellant flame was collected and analyzed using both a 4-color pyrometer and spectrometer, and Wein's law was used to calculate bulk flame temperatures. Several static tests were conducted to study the variance in burn rate as a function of pressure from 3.45 to 6.89 MPa (500 to 1000 psi). Young's modulus (E) and Poisson's ratio (ν) were experimentally measured using tensile testing with an in situ 3D digital image correlation (DIC) system, which measured the full-field strain response of conventional tensile geometries, such as JANNAF Type-C and micro tensile samples. These geometries were used to compare to an ASTM standard and a scaled-down version of the more common JANNAF tensile sample. The strain response was found to be invariant across strain rates of 0.5 , 5 , and 20 mm/s for these composite materials. For a given formulation, all geometries tested exhibited similar E and ν . As anticipated, both E and ν of the $3\text{ }\mu\text{m}$ aluminum particle size composition increased compared to the $10\text{ }\mu\text{m}$. This study emphasizes the significance of both material composition and geometric considerations in the development of advanced rocket propellants, which are demanded by the growing interest in space exploration and military applications.

Keywords: APCP; Combustion performance; aluminum particle size; DIC; Young's modulus; Poisson's ratio

CONTENTS

	Page
LIST OF TABLES	x
LIST OF FIGURES	xii
NOMENCLATURE	xxii
CHAPTER 1. INTRODUCTION	1
1.1 Research Motivation	1
1.2 Literature Review	2
1.3 Objectives for Present Research	8
CHAPTER 2. COMPUTATIONAL MODELING OF CHEMICAL EQUILIBRIUM AND BALLISTIC PROFILES	9
2.1 Chemical Equilibrium Modeling with NASA CEA	9
2.1.1 Introduction to NASA CEA	9
2.1.2 Initial parameters for NASA CEA simulations	10
2.1.3 NASA CEA Results	10
2.2 Propellant Composition	14
2.3 Ballistic Profile Modeling	15
2.4 Solid Rocket Motor Design	17
2.4.1 MATLAB simulations of 76 mm BATES grains	17
2.4.2 SolidWorks design of motor components	20
2.5 Casting Techniques and Facilities	22
CHAPTER 3. EXPERIMENTAL METHODS FOR STRAND BURNING AND STATIC FIRE TESTING	24
3.1 Propellant Strand Burning	24
3.1.1 Strand burner design	24
3.2 Strand Burning Experimental Methods	28
3.2.1 Temperature measurement principles	30
3.2.2 Pyrometer diagnostic methods	32
3.2.3 Spectrometer diagnostic methods	33
3.3 Static Fire Experimental Methods	33

CHAPTER 4. RESULTS AND DISCUSSION OF TEMPERATURE AND BURN RATE ANALYSIS	36
4.1 Strand Burning Results and Discussion	36
4.1.1 Burn rate analysis	36
4.1.2 Bulk flame temperature measurements	40
4.2 Combustion Performance Analysis of 76 mm SRMs	46
4.2.1 76 mm burn rate analysis	46
4.2.2 Burn rate analysis comparison	49
4.2.3 Nozzle correction factor	51
4.2.4 Experimental performance parameters	56
4.2.5 Bulk flame temperature measurements	57
4.3 Discussion	64
CHAPTER 5. EXPERIMENTAL METHODS FOR DETERMINING MECHANICAL PROPERTIES OF APCP USING 3D-DIC	65
5.1 Uniaxial Testing for Studying Mechanical Properties	65
5.2 Test Specimen Dimensions and Preparations	66
5.3 Experimental Methods	68
5.3.1 Digital Image Correlation	68
5.3.2 Calibration of the stereo camera system	70
5.3.3 Application of speckle pattern	71
5.3.4 Uniaxial loading of propellant samples	71
5.3.5 VIC 3D data processing	73
CHAPTER 6. RESULTS AND DISCUSSION OF THE MECHANICAL PROPERTIES OF APCP COMPOSITIONS	74
6.1 DIC Results	74
6.2 Uncertainty of DIC Measurements	82
6.3 Material Analysis Results for H-10 Composition	83
6.4 Material Analysis Results for H-3 Composition	86
6.5 Discussion	88
CHAPTER 7. CONCLUSIONS AND RECOMMENDATIONS FOR FUTURE RESEARCH	92
7.1 Conclusions	92
7.2 Recommendations for Future Research	93
REFERENCES	94

APPENDIX A. BATES GRAIN SURFACE REGRESSION MODELING	98
A.1 Ballistic Test and Evaluation System (BATES)	99
APPENDIX B. MATLAB CODE	102
B.0.1 BATES Grain Ballistic Modeling	103
B.0.2 Strand Burner Burn Rate Analysis	107
B.0.3 SRM Burn Rate Analysis	110
B.0.4 Bulk Flame Temperature Analysis	116
B.0.5 DIC Analysis	124
APPENDIX C. ENGINEERING DRAWINGS	130
C.0.1 76 mm Motor Engineering Drawings	131
C.0.2 Strand Burner	137
APPENDIX D. TEST PLANS	143
D.0.1 Propellant Mixing and Casting Test Plan	144
D.0.2 Strand Burner Test Plan	158
D.0.3 Static Fire Test Plan	170
D.0.4 Tensile Testing Test Plan	183

LIST OF TABLES

Table	Page
2.1 Simulations parameters to determine the equilibrium state using NASA CEA	10
2.2 Simulations results showing <i>O/F</i> ratio, T_c , M_w , A_e/A_t , and the I_{sp} from NASA CEA for 3.45 MPa (500 psi) chamber pressure for all simulations.	13
2.3 Simulations results showing <i>O/F</i> ratio, T_c , M_w , A_e/A_t , and the I_{sp} from NASA CEA for 5.17 MPa (750 psi) chamber pressure for all simulations.	13
2.4 Simulations results showing <i>O/F</i> ratio, T_c , M_w , A_e/A_t , and the I_{sp} from NASA CEA for 6.89 MPa (1000 psi) chamber pressure for all simulations.	14
2.5 APCP composition with the weight percent <i>wt%</i> for each constituent.	14
2.6 Results show the maximum pressure, average steady-state pressure, throat diameter, and total burn time from the in-house MATLAB code for modeling the ballistic profiles for nominally 3.45, 5.17, 6.89 MPa (500, 750, and 1000 psi) chamber pressures.	18
3.1 Weight percent (<i>wt%</i>) of chemical ingredients for inhibiting propellant samples.	29
4.1 Tabulated results of a and n adapted from [1–3].	37
4.2 Measured burn rates and pressures of the APCP with H-10 composition.	38
4.3 Measured burn rates and pressures of the APCP with H-3 composition.	38
4.4 Summary of results of burn rate r and four-color pyrometer and spectrometer data, top and bottom measurements, respectively, with the standard deviation from the average bulk flame temperatures for both compositions.	46
4.5 Percent difference of the average chamber pressure between predicted and experimental data.	47
4.6 Results for r_{MB} and r_{TOT} for H-10 composition.	51
4.7 Results for r_{MB} and r_{TOT} for H-3 composition.	51
4.8 Measure slag thickness (δ) and throat diameter (D_t) with their calculated effective diameter (D^*) for H-10 and H-3 compositions with their respective uncertainties determined from the tolerances of the measuring devices used.	52
4.9 Percent difference of the average chamber pressure between predicted and experimental data with correction factor due to slag buildup and using a and n values determined though the r_{MB} method.	55

4.10	Theoretical rocket parameters for 3.45, 5.17, and 6.89 MPa from NASA CEA	56
4.11	Experimental rocket performance parameters of the APCP SRM with H-10 aluminum composition.	56
4.12	Experimental rocket performance parameters of an APCP SRM with H-3 aluminum composition.	57
4.13	Experimental results with the standard deviation from the average temperature (T_{avg}) measured from a four-color pyrometer at the nozzle exit for an APCP composition with H-10 aluminum powder.	62
4.14	Experimental results with the standard deviation from the average temperature (T_{avg}) measured from a four-color pyrometer at the nozzle exit for an APCP composition with H-3 aluminum powder.	63
4.15	Experimental results with the standard deviation from the average temperature (T_{avg}) measured from a spectrometer at the nozzle exit for the APCP composition with H-10 aluminum powder.	63
5.1	Theoretical masses with the corresponding average mass and % error of all tensile geometries with H-10 Aluminum powder.	68
5.2	Theoretical masses with the corresponding average mass and % error of all tensile geometries with H-3 Aluminum powder.	68
6.1	Average mass of samples between geometries for H-10 and H-3 composition. At least 5 samples per geometry were averaged.	75
6.2	Average gauge thickness, width, cross-sectional area, initial longitudinal gauge length, and initial lateral gauge length of all geometries and both APCP compositions.	75
6.3	Parameters used to conduct strain analysis using VIC-3D for all geometries for both H-10 and H-3 compositions.	76
6.4	Young's modulus (E), average Poisson's ratio (ν_{avg}), and dewetting stress (σ_d) of all experimental tests for all tensile geometries of the H-10 composition.	83
6.5	Young's modulus (E), average Poisson's ratio (ν_{avg}), and dewetting stress (σ_d) of all experimental tests for all tensile geometries of the H-3 composition.	86

LIST OF FIGURES

Figure	
Figure 1.1 Various burn rate versus pressure models for solid propellant, adapted from Greatrix [4].	4
Figure 1.2 Burning time definitions adapted by the Miller & Barrington model [3].	5
Figure 1.3 Mass flow rate versus chamber pressure: Stability criterion derived from mass balance relationships, as adapted by [5].	6
Figure 1.4 A schematic of an APCP showing different AP particle sizes with Al fuel and HTPB serving as the binder system.	7
Figure 2.1 Specific impulse and exhaust velocity of an ideal rocket propulsion system as a function of the chamber temperature (T_c) and molecular weight (M_w) at various pressure ratios.	11
Figure 2.2 Molecular composition at the exit of an ideal rocket propulsion system with an aluminized APCP as a function of the mixture oxidizer-to-fuel ratio.	12
Figure 2.3 Solid rocket motor schematic with single BATES grain showing chamber volume (V_c) highlighted in yellow at pressure and temperature P and T_c respectively.	16
Figure 2.4 A sectional view of a BATES grain and the critical parameters used to develop a surface regression model.	16
Figure 2.5 Predicted ballistic profile of a 76 mm BATES grain at 3.45 MPa (500 psi) chamber pressure determined through by the predicted NASA performance parameters.	18
Figure 2.6 Predicted ballistic profile of a 76 mm BATES grain at 5.17 MPa (750 psi) chamber pressure determined through by the predicted NASA performance parameters.	19
Figure 2.7 Predicted ballistic profile of a 76 mm BATES grain at 6.89 MPa (1000 psi) chamber pressure determined through by the predicted NASA performance parameters.	19
Figure 2.8 Schematic of 76 mm SRM case with internal components listed . .	20
Figure 2.9 Factor of safety of aluminum-6061 motor case	21
Figure 2.10 Schematic of a straight-wall contoured nozzle with converging and diverging sections	21
Figure 2.11 Hobart mixer and a PolyScience water heater for propellant mixing	22

Figure 2.12 Vac-cast pot with a large stainless steel funnel and pot. Propellant flows through several 6 mm diameter slits and is poured into molds	23
Figure 3.1 Half sectional view of strand burner with all working systems.	25
Figure 3.2 Strand burning platform showing ignition wire, six-embedded wires, strand sample holder, and ignition start-up and shutdown distances.	26
Figure 3.3 Front, isometric, and side views of the wire pass-throughs manufactured.	26
Figure 3.4 Sapphire window port assembly: a) Fixed window mounting point for the window port. b) Window port for sapphire window with two Viton gaskets and several Viton washers.	27
Figure 3.5 Internal view of strand burner with the platform for holding propellant samples in place. Six embedded wires for measuring burn rate and ignition wire placement are shown.	27
Figure 3.6 a) Side of the strand burner with collimating lens for optical measurements of light emission and ball valve for purging ambient air. b) Opposite side of strand burner with pressure transducer	28
Figure 3.7 From top left to bottom right: Inlet/Outlet solenoid control box for operating solenoids remotely, C-DAQ modules and driver for DAQ system, ignition box with redundant systems to safely ignite propellant strands, ignition wire leads connection point, and embedded wire controller.	30
Figure 3.8 Linear relation of Wien's approximation showing individual quantities corresponding to a specific wavelength λ where the slope of the line equals the measured temperature.	32
Figure 3.9 An image of the four-color pyrometer and b) A schematic that shows the light path from the emitted light from the propellant flame entering the pyrometer and to the individual photodetectors at specific wavelengths.	33
Figure 3.10 Components of the solid rocket motor assembly.	34
Figure 3.11 Experimental setup implemented for static fires of the 76 mm BATES grain solid rocket motor.	35
Figure 3.12 Image of the TD1000 pressure transducer mounted into the forward closure attached to the force transducer mount by a 3/8-16 all thread. The image also shows the WMC2000 force transducer mounted.	35
Figure 4.1 Raw data set of the pressure history and trigger times for a strand burning test at a nominal pressure of 6.89 MPa for an H-10 composition.	37
Figure 4.2 Power law relation determined from strand burn analysis for the burn rate and pressure for H-10 composition. Note that the pressure range is less than one decade, so the log-log-axis is not very pronounced here.	39
Figure 4.3 Power law relation determined from strand burn analysis for the burn rate and pressure for H-3 composition. Note that the pressure range is less than one decade, so the log-log-axis is not very pronounced here.	39
Figure 4.4 Bulk temperature and pyrometer history at 6.89 MPa of H-10 composition showing a range when measurements were taken.	40

Figure 4.5 Bulk flame temperature history measured with the pyrometer at 6.89MPa of H-10 composition with $\varepsilon_\lambda = \text{const.}$ with the standard deviation of all the measurements being considered.	41
Figure 4.6 Bulk flame temperature history measured with the pyrometer at 6.89MPa of H-10 composition with $\varepsilon_\lambda = 1/\lambda^{-1}$ with the standard deviation of all the measurements being considered.	41
Figure 4.7 Bulk flame temperature history measured with the pyrometer at 6.89MPa of H-10 composition with $\varepsilon_\lambda = 1/\lambda^{-2}$ with the standard deviation of all the measurements being considered.	42
Figure 4.8 Bulk flame temperature history measured with the spectrometer at 6.89MPa (1000 psi) of H-10 composition with $\varepsilon_\lambda = \text{const.}$ with the standard deviation of all the measurements being considered.	43
Figure 4.9 Bulk flame temperature history measured with the spectrometer at 6.89MPa (1000 psi) of H-10 composition with $\varepsilon_\lambda = 1/\lambda^{-1}$ with the standard deviation of all the measurements being considered.	44
Figure 4.10 Bulk flame temperature history measured with the spectrometer at 6.89MPa (1000 psi) of H-10 composition with $\varepsilon_\lambda = 1/\lambda^{-2}$ with the standard deviation of all the measurements being considered.	44
Figure 4.11 Sequential images in time of a strand burn test show variations in light intensities from $t = 0$ to $t = 22$ s.	45
Figure 4.12 Experimental and theoretical pressure and thrust curves as a function of time for the BATES SRM with H-10 aluminum powder a nominal 3.45 MPa chamber pressure.	47
Figure 4.13 Experimental and theoretical pressure and thrust curves as a function of time for the BATES SRM with H-10 aluminum powder a nominal 5.17 MPa chamber pressure.	48
Figure 4.14 Experimental and theoretical pressure and thrust curves as a function of time for the BATES SRM with H-10 aluminum powder a nominal 6.89 MPa chamber pressure.	48
Figure 4.15 Experimental and theoretical pressure and thrust curves as a function of time for the BATES SRM with H-3 aluminum powder a nominal 6.89 MPa chamber pressure.	49
Figure 4.16 Power law relation between burn rate and pressure determined from the strand burner, mass balance, and thickness/time applied to the BATES grain and the strand burner testing of the H-10 composition. . . .	50
Figure 4.17 Power law relation between burn rate and pressure determined from the strand burner, mass balance, and thickness/time applied to the BATES grain and the strand burner testing of the H-3 composition. . . .	50
Figure 4.18 Experimental pressure and thrust histories with a model that uses a correction factor for slag buildup and the coefficient measured from the r_{MB} method for the H-10 composition intended for 3.45 MPa.	52
Figure 4.19 Experimental pressure and thrust histories with a model that uses a correction factor for slag buildup and the coefficient measured from the r_{MB} method for the H-10 composition intended for 5.17 MPa.	53

Figure 4.20 Experimental pressure and thrust histories with a model that uses a correction factor for slag buildup and the coefficient measured from the r_{MB} method for the H-10 composition intended for 6.89 MPa.	53
Figure 4.21 Experimental pressure and thrust histories with a model that uses a correction factor for slag buildup and the coefficient measured from the r_{TOT} method for the H-10 composition intended for 3.45 MPa.	54
Figure 4.22 Experimental pressure and thrust histories with a model that uses a correction factor for slag buildup and the coefficient measured from the r_{TOT} method for the H-10 composition intended for 5.17 MPa.	54
Figure 4.23 Experimental pressure and thrust histories with a model that uses a correction factor for slag buildup and the coefficient measured from the r_{TOT} method for the H-10 composition intended for 6.89 MPa.	55
Figure 4.24 Bulk flame temperature history plotted with pyrometer data at 6.89 MPa (1000psi) of an H-10 composition.	58
Figure 4.25 Bulk flame temperature history measured with pyrometer at 6.89MPa (1000 psi) of H-10 composition $\varepsilon_\lambda = \text{const.}$	58
Figure 4.26 Bulk flame temperature history measured with pyrometer at 6.89MPa (1000 psi) of H-10 composition $\varepsilon_\lambda = 1/\lambda^{-1}$	59
Figure 4.27 Bulk flame temperature history measured with pyrometer at 6.89MPa (1000 psi) of H-10 composition $\varepsilon_\lambda = 1/\lambda^{-2}$	59
Figure 4.28 Bulk flame temperature history plotted with spectrometer data at 6.89 MPa (1000psi) of an H-10 composition.	60
Figure 4.29 Bulk flame temperature history measured with spectrometer at 6.89MPa (1000 psi) of H-10 composition $\varepsilon_\lambda = \text{const.}$	61
Figure 4.30 Bulk flame temperature history measured with spectrometer at 6.89MPa (1000 psi) of H-10 composition $\varepsilon_\lambda = 1/\lambda^{-1}$	61
Figure 4.31 Bulk flame temperature history measured with spectrometer at 6.89MPa (1000 psi) of H-10 composition $\varepsilon_\lambda = 1/\lambda^{-2}$	62
Figure 5.1 Schematic representation of the stress-strain response of composite materials adapted from [2].	66
Figure 5.2 Tensile samples with dimensions in mm: a) ASTM D638 Type-III (9 mm thick) as per the ASTM D638-10 b) JANNAF sample (12.7 mm thick) as adapted by [6].	67
Figure 5.3 Tensile samples with dimensions in mm: a) Scaled-JANNAF (6.7 mm thick) b) MICRO tensile sample (5 mm thick) as adapted by [6].	67
Figure 5.4 Experimental test setup of the stereo camera system and Mark-10 test stand with a JANNAF propellant sample in slotted tensile heads	69
Figure 5.5 a) Isometric view of a typical stereo system b) Top-view of a stereo system showing the stereo angle θ_s and the stand-off distance L_{SOD}	70
Figure 5.6 Speckled tensile samples for ASTM, JANNAF, scaled-JANNAF, and MICRO from a to d, respectively.	71

Figure 5.7 JANNAF tensile sample positioned within the tensile heads printed using a Markforged 3D printed using Onyx with fiberglass reinforcement.	72
Figure 5.8 Lateral and longitudinal virtual strain gauge (VSG) placements for ASTM, JANNAF, scaled-JANNAF, and MICRO annotated from a to d, respectively, through VIC 3D.	73
Figure 6.1 Reference image of a JANNAF tensile sample showing the longitudinal and lateral virtual strain gauges in addition to the region of interest for calculating strain.	75
Figure 6.2 Raw data from VIC-3D of a JANNAF tensile test showing the static region, including the start and end of the test at frame 164 and 345, respectively.	76
Figure 6.3 Engineering stress and strain of a JANNAF tensile sample showing the toe region originating from point O to C, and the linear part of the curve from C to D.	77
Figure 6.4 Engineering stress-strain curve of ASTM geometry with H-10 aluminum powder at 0.5 mm/s.	78
Figure 6.5 Engineering stress-strain curve of JANNAF geometry with H-10 aluminum powder at 0.5 mm/s, 5mm/s and 20 mm/s.	79
Figure 6.6 Stress-Strain curve of MICRO geometry with H-10 aluminum powder at 0.5 mm/s.n	79
Figure 6.7 Engineering stress-Strain curve of SJF geometry with H-10 aluminum powder at 0.5 mm/s.	80
Figure 6.8 Engineering stress-strain curve of ASTM geometry with H-3 aluminum powder at 0.5 mm/s	80
Figure 6.9 Engineering stress-strain curve of JANNAF geometry with H-3 aluminum powder at 0.5 mm/s	81
Figure 6.10 Engineering stress-strain curve of MICRO geometry with H-3 aluminum powder at 0.5 mm/s	81
Figure 6.11 Engineering stress-strain curve of SJF geometry with H-3 aluminum powder at 0.5 mm/s	82
Figure 6.12 Engineering stress-strain response for all geometry types for H-10 composition.	84
Figure 6.13 Calculated Young's modulus (E) with the averages and errors for all geometry types of H-10 composition.	84
Figure 6.14 Calculated average Poisson's ratio (ν_{avg}) with the averages and errors for all geometry types of H-10 composition.	85
Figure 6.15 Engineering stress-strain response of ASTM, JANNAF Type-C, MICRO, and scaled-JANNAF tensile samples for H-3 composition.	87
Figure 6.16 Calculated Young's modulus (E) with the averages and errors for all geometry types of H-3 composition.	87
Figure 6.17 Calculated average Poisson's ratio (ν_{avg}) with the averages and errors for all geometry types of H-3 composition.	88

Figure 6.18 Engineering stress-strain response curves for H-10 (black) and H-3 (red) with all geometries plotted.	89
Figure 6.19 Average Young's modulus (E_{avg}) for H-10 and H-3 ammonium perchlorate compositions for ASTM, JANNAF, MICRO, and SJF tensile geometries with the standard deviation from the average value.	90
Figure 6.20 Average Poisson's ratio (ν_{avg}) for H-10 and H-3 ammonium perchlorate compositions for ASTM, JANNAF, MICRO, and SJF tensile geometries with the standard deviation from the average value.	90
Figure 6.21 Average dewetting stress ($\sigma_{d,avg}$) for H-10 and H-3 composition with the standard deviation from the average value.	91
Figure A.1 Grain geometry of BATES grains with grain length L_o , inner length L_i , taper angle θ_t , and both inner and outer diameters D_i and D_o respectively.	100
Figure A.2 a) Schematic of a conical frustum showing the inner and outer radius r_i and r_o respectively and the slant height L_s . b) A sectional view of a BATES grain highlighting the surface regression directions, s_1 and s_2 , in addition to the taper angle θ_t , the angle between the outer surface and grain ends θ , and the angle, γ , that the regression direction s_2 makes at a given time step dt	100
Figure A.3 A 2D contour of the burning surface is shown in red at t_{i+1} shows the inner length L_i is reduced to $L_i - 2s_{2,i+1}$. The new slant height, $L_{s_{i+1}}$ is shown to reduce in length which can be described by the change in the inner radius, r_i	101

NOMENCLATURE

δ	thickness of slag buildup (mm)
A^*	effective throat area (mm^2)
r^*	effective throat radius (mm)
s_b	propellant burning surface area (mm^2)
V_c	chamber volume (mm^3)
W_{avg}	average web thickness (mm)
c	speed of light in vacuum: 299,792,458 (m/s)
g_o	standard acceleration due to gravity: 9.80665 (m/s^2)
h	planck constant: $6.62607015 \times 10^{-34} (\text{m}^2/\text{kgs})$
k_B	boltzmann constant: $1.380649 \times 10^{-23} \text{ m}^2 \text{ kg} / \text{K}^2$
R_u	universal gas constant: 8314.3 (J/kg mol-K)
δ_{blur}	pixel blur (px)
δ_{res}	image resolution error (px)
δ_{strain}	lateral strain uncertainty
ε	strain rate (mm/s)
ε_{lat}	lateral strain (mm/mm)
ε_{long}	longitudinal strain (mm/mm)
$\varepsilon_{d,avg}$	average dewetting strain (mm/mm)
ε_d	dewetting strain (mm/mm)
ε_{eng}	engineering strain (mm/mm)
ν	poisson's ratio
σ_θ	hoop stress (MPa)
$\sigma_{d,avg}$	average dewetting stress (MPa)

σ_d	dewetting stress (MPa)
σ_{eng}	engineering stress (MPa)
θ_s	camera stereo angle
A_o	gauge section initial area (mm^2)
E	young's modulus (MPa)
F_s	uniaxial load (N)
f_{lens}	camera focal length (mm)
FOV	camera field of view (mm)
L	instantaneous length (mm)
L_o	initial gauge length (mm)
L_{CS}	horizontal distance of camera sensor (mm)
L_{SOD}	length of stand-off distance (mm)
t_s	camera exposure time (μs)
w_g	gauge width (mm)
w_t	gauge thickness (mm)
Δ	standard deviation
\dot{m}_d	rate of mass ejection (kg/s)
\dot{m}_g	rate of gas generation (kg/s)
\dot{m}_t	rate of mass flow at nozzle throat (kg/s)
ε	expansion ratio (A_e/A_t)
ρ_g	gas density (g/m^3)
ρ_p	propellant density (g/m^3)
A_e	nozzle exit area (mm^2)
A_t	nozzle throat area (mm^2)
c^*	characteristic exhaust velocity (m/s)
C_D	nozzle discharge coefficient
C_F	thrust coefficient
D_e	nozzle exit diameter (mm)

D_i	grain inner diameter (mm)
D_o	grain outer diameter (mm)
D_t	nozzle throat diameter (mm)
dA	change in area (mm^2)
dP	change in pressure (MPa)
F_{avg}	average thrust (N)
I_{sp}	specific impulse (s)
L_g	Length of BATES grain (mm)
M	mach number (m/s)
M_w	molecular weight (g/mol)
O/F	oxidizer-to-fuel ratio
P_1	nozzle inlet pressure (MPa)
P_3	atmospheric pressure (MPa)
P_c	chamber pressure (MPa)
P_e	nozzle exit pressure (MPa)
P_t	nozzle throat pressure (MPa)
$P_{avg,SB}$	average pressure in strand burner (MPa)
P_{avg}	average chamber pressure (MPa)
T_c	chamber temperature (K)
v_1	nozzle inlet velocity (m/s)
v_e	nozzle exit velocity (m/s)
k	specific heat ratio
t_b	total burn time (s)
a	burn rate coefficient $\left(\frac{\text{mm/s}}{\text{MPa}^n} \right)$
n	burn rate exponent
r	burn rate (mm/s)
r_{MB}	burn rate mass balance (mm/s)

r_{TOT}	burn rate thickness/time (mm/s)
ϵ_λ	emissivity
λ	wavelength (nm)
c_λ	light correction factor
I_{cal}	calibration light intensity (arb. units)
I_{ref}	published light intensity for calibration lamps (arb. units)
$T_{avg,bulk}$	average bulk flame temperature (K)

CHAPTER 1

INTRODUCTION

1.1 Research Motivation

The optimization of propellant characterization has undergone significant advancements over the past several decades. Higher-performing solid propulsion systems for military and space applications are the driving force for such innovations. Of particular interest are Ammonium Perchlorate Composite Propellants (APCPs) due to their high compatibility with other propellant materials, such as aluminum powder, and their high energy-release rates [2, 7]. Propulsion systems undergo exothermic chemical reactions within a combustion chamber. These reactions result in the production of a significant number of gas species that are ejected at high velocities through a nozzle, converting the momentum of the gases into thrust. The complexity of such systems requires knowledge of the expected combustion behavior of the solid rocket motor (SRM), the geometrical parameters controlling its pressure and thrust profiles, and the material response to ensure survival under the variety of mechanical stresses it will be subjected to throughout its lifespan.

In the past several decades, much work has been conducted to understand the complexity of the combustion and material properties of aluminized APCPs. Propellant studies require large-scale testing for proper propellant characterization; however, conventional studies often use small-scale analysis methods for rapid testing. Theoretical chemical equilibrium calculations often lead to an overestimation of composition performance due to differences in residence times and the higher temperatures experienced at the larger scale motors [8]. Inadequate combustion efficiency caused by the ejection of agglomerated aluminum particles from the burning surface has also been observed [7]. These ejected particles produce several losses, such as two-phase flow and limiting the heat feedback to the burning surface [7].

The particle size distribution of metal powders has been shown to affect combustion efficiency [9]. Smaller particles have a larger surface area relative to their volume. This increase in surface area results in an increase in burn rate due to the high combustion temperatures that are experienced. Methods such as pyrometry and spectroscopy are non-intrusive optical techniques that have been used in the past for dynamic temperature measurements of APCP compositions [10]. Understanding the details of initial particle size on metal combustion is an area that presents research opportunities.

The addition of smaller aluminum powder also produces tighter particle packing within the propellant. This leads to a more uniform distribution of combustion and material properties since smaller particle sizes increase the surface area of the aluminum fuel available to react with the oxidizer. As a result, improvements in the vibrational and shock response can be modified by using smaller aluminum particles that can tailor a

composition for mission-specific objectives [2]. Methods such as static tensile tests using standard JANNAF (Joint Army Navy NASA Air Force) uniaxial tensile specimens are the most common for studying stress-strain response; however, work performed by Peihao et al. has shown this method to be insufficient for determining force-displacement measurements and demonstrates more applicable methods such as Digital Image Correlation (DIC) [11].

1.2 Literature Review

Intensive research performed in the 1960s by Newman and Spickernell showed that the addition of aluminum fuel in solid propellant resulted in an improvement in performance with measured specific impulses as high as 245 s at 6.89 MPa compared to the common 170 - 230 s for compositions consisting of AP alone [12, 13]. Newman and Spickernell concluded that the aluminum particle size did not have any effect on the specific impulse I_{sp} of the propellants [12], where the I_{sp} is the thrust per unit weight of propellant which serves as a metric for measuring the performance of any propulsion system [2]. However, work performed by E. W. Price showed how varied the combustion behavior is for metal powders when varying their particle size [7]. Work conducted by Dokhan et al. [14] showed that the agglomeration of aluminum occurs at the burning surface and is ejected out into the fully combusted products. The ejected particle's participation in the radiative and conductive heat transfer to the burning surface varies due to factors such as the thickness of the aluminum oxide layer, particle size, and the oxidizer-to-fuel ratio, which either increases or decreases the specific impulse. Varunkumar and Mukunda defined ultra-fine aluminum (UFAl) as the particle size where changes in burn rate (r) behavior begin to occur. For aluminized APCPs, this was determined to be when the nominal size of the aluminum particles was 15 μm [15].

A heterogeneous quasi-one-dimensional model was extended to aluminized propellant that accounted for aluminum particle ejection from the binder system into the gas phase products, leading to changes in the heat feedback process [15]. It proposed that the increase in r of UFAl propellants occurred by the rupturing of the oxide layer through the expansion of the aluminum core, which is highly dependent on the surface-to-volume of the aluminum particles [15]. Smaller aluminum particles have thinner aluminum oxide layers and high surface-to-volume; however, there comes a point when the aluminum particle becomes too small that the expansion of the internal volume can no longer rupture the oxide layer. Due to these real-world effects, theoretical chemical equilibrium calculations often lead to an overestimation of composition performance due to the inadequate combustion efficiency caused by the ejection of agglomerated aluminum particles from the burning surface.

In recent studies by Yi Chin et al. [16], novel diagnostics methods using digital imaging holography and pyrometry were used for determining particle size and agglomeration effects of aluminum combustion. They implemented high-speed imaging techniques to quantify the three-dimensional position, size, and velocity of condensed phase products. Emission spectroscopy methods have been used to monitor the emitted light from propellant samples for average flame temperatures [17]. Flame temperatures from 2600 to 3000 K have been estimated with pyrometry methods [16]. These non-intrusive diagnostic techniques are commonly used for thermal analysis and provide temperature measurements comparable to predicted temperatures [18–20]. Combustion temperature

predictions are paramount for the ballistic modeling of SRMs. Any excursions in the predicted temperature can lead to variations in the burn rate of the propellant surface, which has been shown to correlate to 1.2 - 2% variations in the thrust with only a 1% variation in burn rate [3, 8].

Conventional methods used for quantifying the burn rate of APCPs include strand burning, small-scale motor firings with 76 mm Ballistic and Test Evaluations System (BATES), followed by full-scale static fire testing to characterize a propellant formulation [3]. Strand burners are small pressure vessels designed for operating pressures that range as high as 35 MPa [21]. Smaller samples are conventionally used for strand burners and are commonly used to characterize the burn rate r in novel propellant formulations. Sub-scale motors are typically used for the further analysis required due to temperature variation expected from transitioning from sub-to full-scale motors [8]. The mass rate balance and the thickness/time are two forms of empirical burn rate definitions that are standard methods used for burn rate analysis [3].

The burn rate of a solid propellant is largely dependent on the combustion front structure. The combustion front structure in APCP is a function of the propellant composition, initial temperature, chamber pressure, and various other parameters related to the operating conditions of a SRM [7]. One of the fundamental parameters that influence the ballistic model for solid propellants is the burn rate r [8]. The burn rate of a solid propellant is determined experimentally by measuring the power law relation:

$$r = aP^n \quad (1.1)$$

between pressure P and burn rate r [3, 22]. The burn rate coefficient a and exponent n are used to develop surface regression models and design mission-specific ballistic profiles. They vary in value since the coefficient and exponent are dependent on the chemical composition and the initial temperature of the propellant, respectively [7]. For aluminized APCPs, the burn rate is in the range of 6-8 mm/s at 6.89 MPa [2, 23, 24] where the a and n range from 1.0 - 3.0 and 0.25 - 0.6, respectively [1-3]. Note that Equation 1.1 is a dimensional equation. The burn rate r has units of either mm/s or in/s, the pressure P is either MPa or psi, the exponent n is dimensionless, and the coefficient a can either have units of $\frac{\text{mm/s}}{\text{MPa}^n}$ or $\frac{\text{in/s}}{\text{psi}^n}$. This work used SI units to report these values.

Several methods for burn rate analysis have been developed by the US and other NATO countries, which outline specific criteria for ballistic evaluation systems [3, 8]. Propellants can show various r behaviors with variations in pressure. Figure 1.1 shows three relationships that have been shown to exist. When the pressure exponent n is reduced or becomes zero at a given pressure range, these propellants are known as plateau propellants. This is typically the situation for double-base propellants with specific additives such as lead [3]. For propellants that experience small negative values of n for a given pressure range, these propellants are known as mesa propellants and have a range of pressures where r decreases. Lastly, when r shows a power law relationship represented by a constant power law exponent with pressure, these propellants behave as explained by Vielle's law, seen in Equation 1.1.

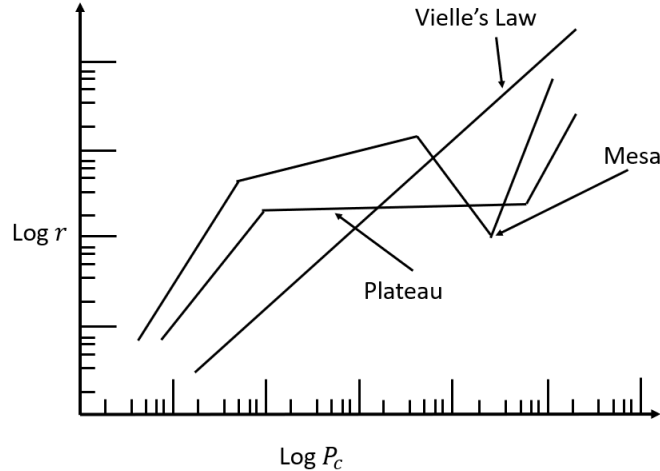


Figure 1.1: Various burn rate versus pressure models for solid propellant, adapted from Greatrix [4].

There are many parameters affecting the structure of the combustion wave within solid propellant. Theoretical models have yet to explain the complexity surrounding r , which is why experimental analysis at the sub-scale size is first performed to study r variation at various pressures. Currently, there are no theories or models that are capable of predicting r within 1% [3]. There has been work performed by Morrow that attempted to correlate the effects of AP particle size on r [23]. His model was able to predict r of an APCP with an average error of 7.3% for AP particle sizes of 4 μm - 200 μm . Regardless of theoretical modeling, experimental testing can also have large variations due to different ingredients used from other vendors and the unavoidable batch-to-batch variations experienced due to conventional casting techniques.

The APCP composition studied in this work follows that of Vielle's law (Equation 1.1). This work will focus on the average mass balance rate and thickness/time empirical methods for sub-scale burn rate analysis developed by NATO [3]. Mass balance methods apply the conservation of mass around the rocket motor case and nozzle to determine the propellant burn rate. The methods generally account for gas storage in the combustion chamber as a change in gas density, the mass flow input from the burning propellant surface, and the mass flow out through the nozzle. The mass balance method used for this work evaluates the steady regime of r by taking into account real-world effects such as non-uniform surface regression and non-instantaneous ignition and burnout effects, all while neglecting the gas storage within the combustion chamber. This results in an average mass balance method burn rate (r_{MB}) given by [3]:

$$r_{MB} = \frac{W_A - W_G}{t_E - t_B} \frac{\int_B^E P_c dt}{\int_A^G P_c dt} = \frac{W_{avg}}{t_b} \frac{\int_B^E P_c dt}{\int_A^G P_c dt} \quad (1.2)$$

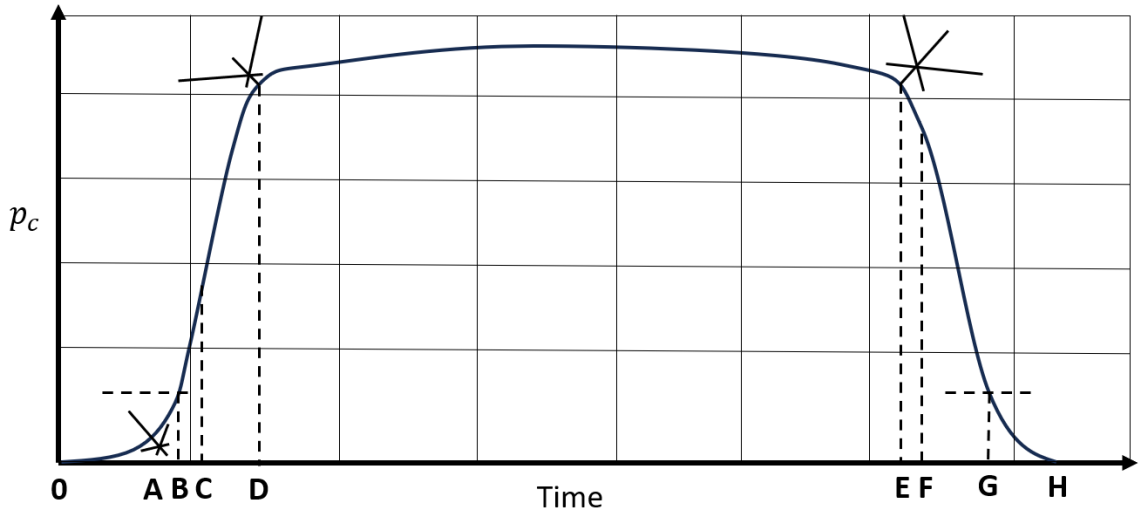


Figure 1.2: Burning time definitions adapted by the Miller & Barrington model [3].

All terms are defined as follows. Points **A** - **D**, shown in Figure 1.2, constitute the ignition transient of the pressure profile. The instant of the first pressure rise t_o is extracted directly from the pressure profile. The bisecting point **A** represents the initial point in time t_A where local ignition of the front portion of the propellant grain begins while W_A represents the web thickness at t_A . The web thickness is the thickness of the propellant grain from the case to the burn surface and varies with time as the motor burns. Any time before t_A , the pressure rise is from the igniter alone. Points **A** to **C** represent the time it takes for the flame to spread to the remaining surface of the propellant. Point **D** is the time t_D it takes for the pressurization of the chamber to reach steady-state pressure. The time at which all of the propellant has been consumed is t_E . The point **F** is the moment in time when the maximum rate of change of depressurization occurs. Points **B** and **G** are defined as a fixed percentage of the average steady-state pressure chosen here as 7.5%. Note that points **C**, **D**, **F**, and **H** are not used for equation 1.2. The web thickness W_G is assumed to be zero since all of the propellant has been consumed; therefore, $W_A - W_G = W_{avg}$ which is defined as $W_{avg} = 0.5(D_o - D_i)$ where D_o and D_i are the outer and inner diameter of the grain before ignition, respectively. The quantity $(t_E - t_B)$ is the difference in time when burnout occurs to the beginning stages of when the flame spreads within the motor. The term P_c is the chamber pressure measurement from the pressure transducer, and integration is performed as noted in Equation 1.2 with respect to time.

The ignition process is critical for a SRM to perform nominally. Design requirements for initiation systems of SRMs vary based on the specific envelope for thrust, pressure, or impulse [8]. Common examples specified by Harrett [25] are to attain a performance level of 10% of the maximum pressure or 75% of the average thrust from the ignition system.

The mass balance method r_{MB} yields errors in r that are consistently low compared to other burn rate analysis methods, such as the thickness/time, by accounting for non-instantaneous ignition and burnout transients that cannot be avoided [3].

The conventional definition for the thickness/time burn rate (r_{TOT}) is given by [3]:

$$r_{TOT} = \frac{W_E - W_B}{t_E - t_B} = \frac{w_b}{t_b} \quad (1.3)$$

The terms W_E and W_B are the web thickness at time **E** and **B**, respectively. All other quantities are the same as previously described. The term w_b is analogous to W_{avg} and was directly measured before conducting the static fire tests; however, t_b requires the determination of the parameters given by [3]:

$$t_b = (t_E - t_D) \frac{\int_O^H p_c dt}{\int_D^E p_c dt} \quad (1.4)$$

Unlike r_{MB} , r_{TOT} does not account for non-instantaneous burnout, accounting more for real-world effects, which are observed through transient effects; therefore, this method has been shown to differ from r_{MB} but can be made to partially avoid large errors from burnout effects if the end-point is correctly identified, [3].

The determination of a and n provide insight into the combustion process of the APCP [7]. Stable combustion can be determined by plotting the rate at which mass is ejected from the nozzle \dot{m}_d and the rate of gas generation \dot{m}_g as a function of pressure, shown in Figure 1.3. The mass generated is a function of propellant density ρ_p , burning surface area s_b , and the r . The rate at which the mass within the combustion chamber exits is a function of the nozzle discharge coefficient C_D , the area of the nozzle throat A_t , and the chamber pressure P . Unstable combustion occurs for $n > 1$ in the instance that $\dot{m}_g < \dot{m}_d$. In this case, the chamber pressure tends towards zero, and the motor extinguishes. For $n > 1$ and $\dot{m}_g > \dot{m}_d$, the motor may over-pressurize, which will lead to a rapid disassembly. When $n < 1$, the rate at which mass is generated tends to an equilibrium point, $\dot{m}_g = \dot{m}_d$.

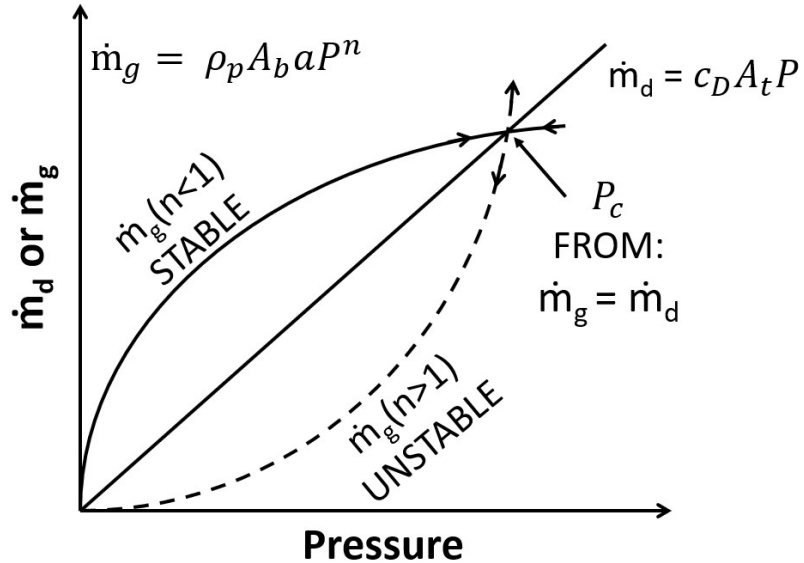


Figure 1.3: Mass flow rate versus chamber pressure: Stability criterion derived from mass balance relationships, as adapted by [5].

In addition to the various effects that particle sizes have on the combustion performance of APCPs, the material response to external disturbances changes as a result of the particle packing within the binder matrix. With the development of high-performance propellants, the material strength required to survive storage and handling, thermal cycling, ignition events, and tactical maneuvers is paramount. Ammonium perchlorate composite propellants are made up of an oxidizer, fuel, and a polymer that binds the solid particles into a place, as shown in Figure 1.4.

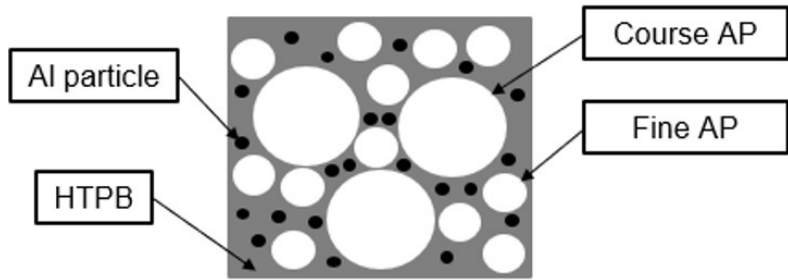


Figure 1.4: A schematic of an APCP showing different AP particle sizes with Al fuel and HTPB serving as the binder system.

The particle size of AP is often considered for tailoring both the mechanical response of the cured propellant and the viscosity of the propellant slurry, which influences the casting process. Finer particles improve the homogeneity of the cured propellant and have also been shown to increase the mechanical strength [6]. The viscosity is a large proponent of the manufacturing process of propellant, often improved by decreasing the particle size, thus improving the quality of the final product [26].

Previous research has also shown that the material properties of APCPs are strongly affected by temperature, composition, and aging. Several studies have been conducted on the material strength of APCPs, showing high sensitivity to the material properties by varying the temperature and large ranges of strain rates [6, 27]. Low temperatures around -30 to -60 °C have been shown to decrease the material strength of APCP due to the reduction of the mobility of the binder system, resulting in a more rigid material. In contrast, the material strength increases for higher temperatures due to the softening of the binder system, increasing the ductility of the APCP [6, 28]. Jarocki's works measured various APCP formulations while varying several aspects of the baseline formulation and focusing on the changes in Young's modulus E . The range of values measured for Young's modulus E are 6.89 to 41 MPa [6].

Work performed by Liang et al. [27] showed that at strain rates from 25×10^{-4} to 7.5 mm/s, the material response varied in the final stress at fracture but exhibited similar values for Young's modulus measured at 10 MPa for strain rates between 2.5 - 7.5 mm/s. The study focused experimental and computational analysis on the damaged zones between the particles and the binder system, showing that at higher strain rates, the damage zones are significantly more pronounced than under lower strain rates. These local areas between the AP and binder interface quantify the dewetting stress of APCP by the quantity of the damage zones and their extent after the interfacial damage has occurred.

The Poisson's ratio (ν) for composite propellant is a critical parameter for analyzing structural integrity, with measured values for ν ranging from 0.45 to 0.5 [29, 30]. It helps predict the material's response to external stresses and potential degradation from aging due to storage. Composite propellants are often considered incompressible, largely due to the dominant influence of the polymer matrix on the material's overall behavior. This incompressibility assumption is based on the observation that the polymer matrix tends to dominate the mechanical response of the composite propellants [30].

Research by Oberth et al. [31] demonstrated that stress concentrations in filler particles, or solid inclusions, relieve stress within the binder matrix, causing the matrix to deform less than it would in the absence of these particles. This stress-relief mechanism is crucial in maintaining the structural integrity of composite propellants. Furthermore, the use of bonding agents, as discussed by Jarocki et al. [6], can enhance the adhesion between particles and the binder. This strengthened bond delays the onset of dewetting between the binder and particle interfaces, thereby prolonging the material's mechanical stability.

Conventional diagnostic techniques measure the strain response using bonded strain gauge measurements. While these methods provide valuable data, difficulties in the installation process of bonded gauge sections tend to reduce the measurement accuracy [32]. Digital Image Correlation is a non-intrusive diagnostics technique that was first applied in 1975 by Yamaguchi and Ranson et al. [33, 34]. This method provides a full-field strain response through a correlation process that involves tracking a subset of pixels in a set of images and correlating these translations into specific quantities of interest. DIC has been used extensively and offers non-intrusive measurements, eliminating the bias experienced in conventional methods [6, 11, 35]. Modern diagnostic techniques, such as DIC, provide robust methods that can be optimized for low-stiffness materials such as composite propellants [30].

1.3 Objectives for Present Research

The present work will focus on two APCP compositions with 3 and 10 μm aluminum particle sizes to study the differences in combustion performance and material properties. Chemical equilibrium simulations will be conducted through NASA CEA to optimize the propellant composition. Burn rate measurements at controlled pressure conditions of 3.45, 5.17, and 6.89 MPa will be performed in a strand burner. The burn rates will be directly measured at each pressure, along with bulk flame temperature measurements using spectroscopy and pyrometry. Theoretical rocket parameters will be acquired using NASA CEA for ballistic profile modeling of 76 mm BATES grain SRMs and ground tested for comparison between experimental and the predictions made by NASA CEA. Uniaxial tensile testing with a Mark-10 tensile machine and an in situ 3D DIC system will be used to measure the full-field stress-strain response and to extract experimental measurements of Young's Modulus (E) and Poisson's ratio (ν). Tensile test geometries will include the JANNAF Type-C, MICRO, ASTM D638 Type III, and a scaled-down version of the JANNAF Type C tensile sample. The variability in material response and propellant composition will be compared to measure the extent of any geometrical or compositional effects on the material response.

CHAPTER 2

COMPUTATIONAL MODELING OF CHEMICAL EQUILIBRIUM AND BALLISTIC PROFILES

The thermodynamic mixture properties of APCP formulations were acquired through NASA CEA. Various oxidizer-to-fuel (O/F) ratios were studied to determine the final chemical composition. The final composition consists of 74% ammonium perchlorate (AP), 10% aluminum (Al), and 16% of a polymer matrix using hydroxyl-terminated polybutadiene (HTPB). The rocket performance parameters found through NASA CEA were used to design ballistic profiles for 76 mm BATES at operating pressures of 3.45, 5.17, and 6.89 MPa (500, 750, and 1000 psi).

2.1 Chemical Equilibrium Modeling with NASA CEA

2.1.1 Introduction to NASA CEA

NASA CEA is an open-source code for modeling the minimization of free energy in equilibrium combustion reactions. The analysis methods used in this work follow those outlined by Gordon and McBride [36]. The procedures for rocket performance modeling within NASA CEA require the use of either a finite-area combustion chamber (FAC) or an infinite-area combustion chamber (IAC). In this work, the IAC was used with the assumption that the thermodynamic derivatives of the composition are frozen. This reduction in complexity of the theoretical model permits the use of ideal rocket assumptions [36].

The assumptions made for an ideal rocket are that the mixture is homogeneous in composition, gases are assumed ideal, interactions among phases are neglected, there is no heat transfer, inviscid flow, no shocks or discontinuities within the nozzle, combustion products have zero velocity at the chamber inlet, the propellant flow rate is constant, and transient effects are negligible [2, 7, 36]. These ideal rocket assumptions allow for basic thermodynamic principles to be used to express, in simple mathematical relationships, the complex gas dynamics and thermodynamic processes occurring in SRMs [2].

The initial chamber pressure P_c , initial combustion temperature, initial temperature of ingredients, and pressure ratio P_c/P_e , where P_e is the pressure at the exit of the nozzle, must also be defined. The chemical constituents for the propellant compositions are assigned through pre-defined molecular formulas within the software or are manually inputted. The weight percent $wt\%$ of each constituent is assigned along with their heat of formation. NASA CEA outputs the predicted performance parameters, propellant density, equilibrium composition, and several other mixture properties.

2.1.2 Initial parameters for NASA CEA simulations

The procedures for obtaining frozen rocket performance parameters in NASA CEA require an assumed combustion temperature conventionally set to 3800 K [36] with a defined pressure ratio P_c/P_e . Several chemical equilibrium simulations of APCP compositions with varying O/F ratios were developed using NASA CEA and served as a preliminary step before arriving at the final composition. Conditions for modeling equilibrium states with varying wt% of Al, AP, and HTPB with an initial temperature of 298 K are shown in Table 2.1. Various pressure ratios P_c/P_e of 40, 60, and 80 were studied. Lastly, the exit pressure was set to match the atmospheric conditions for Socorro NM, which is 8,618.45 Pa or 12.5 psi.

Table 2.1: Simulations parameters to determine the equilibrium state using NASA CEA

Initial Temperature K	Al wt%	AP wt%	HTPB wt%	O/F -	P_c MPa (psi)
298	25	59	16	1.44	3.45 (500)
					5.17 (750)
					6.89 (1000)
298	20	64	16	1.8	3.45 (500)
					5.17 (750)
					6.89 (1000)
298	15	69	16	2.23	3.45 (500)
					5.17 (750)
					6.89 (1000)
298	10	74	16	2.85	3.45 (500)
					5.17 (750)
					6.89 (1000)
298	5	79	16	3.76	3.45 (500)
					5.17 (750)
					6.89 (1000)

2.1.3 NASA CEA Results

Results for the calculated I_{sp} as a function of the ratio of the chamber temperature T_c over the molecular mass of the exhaust products M_w are shown in Figure 2.1. Figure 2.1 shows that for larger ratios of T_c/M_w , the higher the I_{sp} attained for each pressure ratio. It also shows that the higher the pressure ratio, the higher the performance is for any given formulation with the same T_c/M_w ratio.

Figure 2.2 shows that low percentages of AP result in large amounts of aluminum slag (Al_2O_3). In other words, as the O/F ratio decreases, more production of Al_2O_3 is observed. The more Al_2O_3 is present in the combustion products, the more thermal energy is carried away from the burning surface, resulting in a decrease in the degree of participation in the combustion process from the metal fuel additive. Additionally,

for small values of the O/F ratio, species such as carbon monoxide (CO) and hydrogen gas (H_2) make up the majority of the mole percent of the combustion products. Carbon monoxide and H_2 represent incomplete combustion, and while they are light in molecular weight, they result in low energy release, reducing the efficiency of the combustion process [7]. For larger values of the O/F ratio, the combustion is more complete, as seen by the presence of carbon dioxide (CO_2) and water vapor (H_2O). Carbon dioxide and H_2O have relatively higher molecular weight than H_2 and CO, but they have higher energy release rates leading to more efficient combustion [7].

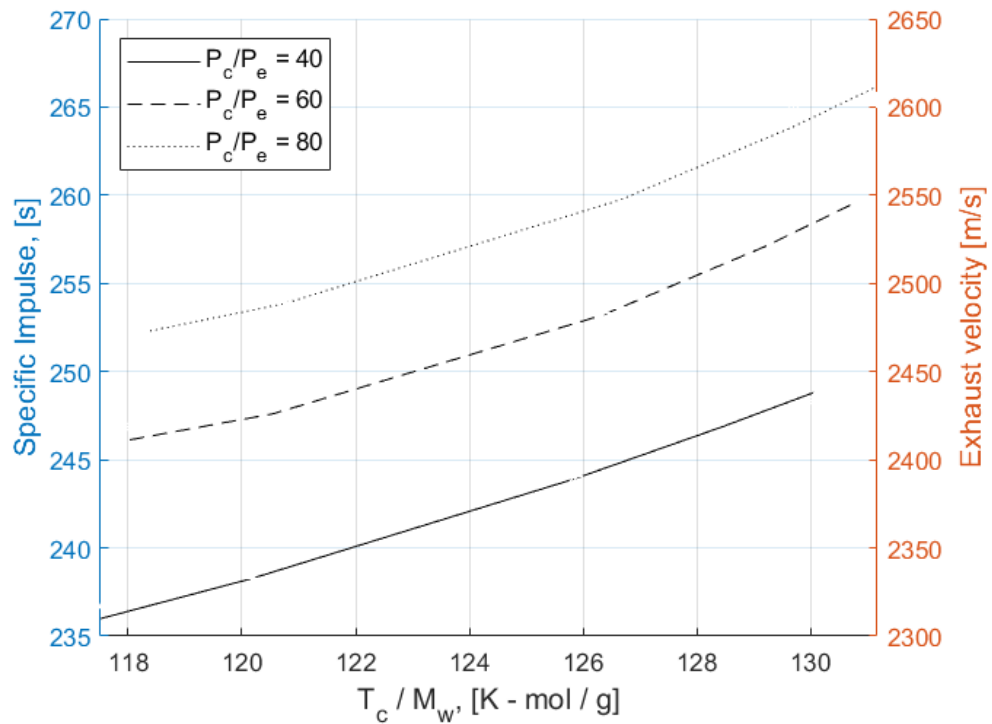


Figure 2.1: Specific impulse and exhaust velocity of an ideal rocket propulsion system as a function of the chamber temperature (T_c) and molecular weight (M_w) at various pressure ratios.

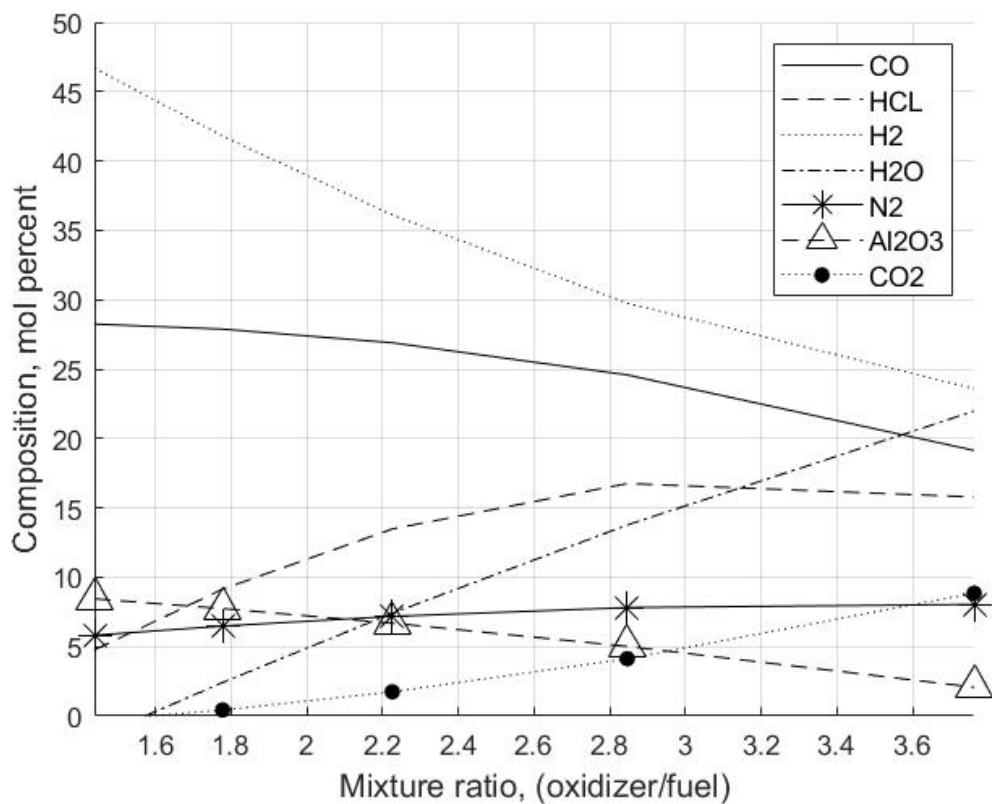


Figure 2.2: Molecular composition at the exit of an ideal rocket propulsion system with an aluminized APCP as a function of the mixture oxidizer-to-fuel ratio.

Tables 2.2, 2.3, and 2.4 show the results for the chamber temperature, molecular weight of the exhaust products at the exit, the expansion ratio A_e/A_t , and the theoretical specific impulse for chamber pressures of 3.45, 5.17, and 6.89 MPa, respectively. From observation, all three tables consistently show that the maximum I_{sp} occurs near an O/F ratio of 1.8 - 2.23. Higher oxidizer loading results in complete combustion, and excess oxidizer can lead to higher temperatures that often result in smaller amounts of Al_2O_3 production. This reduction of aluminum slag correlates to higher nozzle efficiencies that minimize deposition of slag in the nozzle, preventing a further reduction in specific impulse and thrust [2, 7]. Since NASA CEA does not account for the scale of the SRM, in discussions with Mark Grubelich, the decision was made to have lower concentrations of Al content in the final propellant composition. To reduce the error between experimental and theoretical predictions due to anticipated small-scale effects, the final composition was chosen to have an O/F ratio of 2.85.

Table 2.2: Simulations results showing O/F ratio, T_c , M_w , A_e/A_t , and the I_{sp} from NASA CEA for 3.45 MPa (500 psi) chamber pressure for all simulations.

O/F Ratio	T_c	M_w	A_e/A_t	I_{sp}
-	K	g/mol	-	s
3.76	2873	24.08	5.87	237
2.85	3022	24.28	6.14	244
2.23	3140	24.48	6.78	248
1.8	3134	24.76	6.82	248
1.44	2914	25.21	6.74	236

Table 2.3: Simulations results showing O/F ratio, T_c , M_w , A_e/A_t , and the I_{sp} from NASA CEA for 5.17 MPa (750 psi) chamber pressure for all simulations.

O/F Ratio	T_c	M_w	A_e/A_t	I_{sp}
-	K	g/mol	-	s
3.76	2885	24.08	7.85	247
2.85	3040	24.28	8.22	253
2.23	3163	24.49	8.67	258
1.8	3160	24.85	9.22	258
1.44	2933	25.28	9.39	246

Table 2.4: Simulations results showing O/F ratio, T_c , M_w , A_e/A_t , and the I_{sp} from NASA CEA for 6.89 MPa (1000 psi) chamber pressure for all simulations.

O/F Ratio	T_c	M_w	A_e/A_t	I_{sp}
-	K	g/mol	-	s
3.76	2893	24.08	9.68	255
2.85	3052	24.28	10.14	259
2.23	3179	24.49	10.70	265
1.8	3179	24.92	11.45	265
1.44	2947	25.30	11.96	254

2.2 Propellant Composition

The final propellant composition is shown in Table 2.5 with an O/F ratio of 2.85. A bimodal AP particle size of 50-50 ratio using 400 μm and 90 μm was used. Two formulations using H-3 and H-10 spherical aluminum powders from Valimet with nominally 4.5 μm and 12 μm particle size distribution, respectively, were used. The binder between the oxidizer and fuel ingredients used for the composition was HTPB which is one of the most common binding agents due to its mechanical strength compared to other polymers [2].

The HTPB is cured using the curative dimethyl diisocyanate (DDI) and the curing catalyst triphenyl bismuth (TPB), which reduces the curing time while not affecting the performance or mechanical properties of the propellant. The addition of isodecyl pelargonate (IDP) reduces the viscosity of the propellant slurry aiding in the mixing and degassing processes. 10-centistokes (CST) silicone oil is added to lower the surface tension of voids/bubbles within the propellant slurry allowing for more efficient void removal. Other propellant ingredients such as carbon black powder and COA-5 provide protection from radiation from the combustion flame at the propellant surface with negligible effects on the burn rate [23], with low concentrations, and increase the shelf-life [37] respectively. The propellant ingredient CAO-5 is an anti-oxidant, stabilizing the oxidizer particles from oxidation over time. It helps maintain the structural integrity, preventing propellant degradation and extending the shelf-life of propellants [2].

Table 2.5: APCP composition with the weight percent wt% for each constituent.

Chemical ingredient	Purpose	wt%
Ammonium perchlorate ^a	Oxidizer	74
Aluminum ^b	Metal fuel	10
Carbon black	Stabilizer	0.50
CAO-5	Anti-oxidant	0.05
Hydroxyl-terminated polybutadiene	Binder	9.6
Dimethyl diisocyanate	Curative	2.4
Isodecyl pelargonate	Plasticizer	3.9
Triphenylbismuth	Catalyst	0.05
10 CST silicone oil	Lubricant	0.50

^a AP particle size was 400 μm and 90 μm at a ratio of 50-50

^b H-3 and H-10 spherical aluminum from Valimet

2.3 Ballistic Profile Modeling

Ballistic Test and Evaluation System (BATES) grain motors were designed using MATLAB code for the operating conditions of interest. Using theoretical parameters from NASA CEA, including the predicted T_c , M_w , k , and characteristic velocity (c^*), preliminary designs of motor grains were developed. Generally, BATES grains are radial burners with uninhibited ends that produce neutral pressure profiles. Regressive and progressive motors are typically avoided since they provide less accurate results of the pressure exponent [3]. Regressive motors exhibit a decrease in the pressure and thrust profiles over time due to a decrease in the burning surface area. Progressive motors, on the other hand, exhibit an increase in the pressure and thrust profiles due to an increase in the burning surface area over time.

A schematic of a BATES SRM and of the burning surfaces are shown in Figure 2.3 and 2.4. The equilibrium pressure P_{eq} , analogous to P_c excluding transient events, generated within a chamber volume V_c , can be determined by solving the mass balance equation:

$$\dot{m}_g - \dot{m}_t = \frac{dm}{dt} \quad (2.1)$$

The rate of gas generated from the burning propellant surface area (s_b) is denoted by \dot{m}_g while \dot{m}_t is the mass flow rate at the nozzle throat and $\frac{dm}{dt}$ is the rate of accumulation of the gas in V_c . Here, $\dot{m}_g = s_b r \rho_p$ and $\dot{m}_t = P A_t / c^*$ [3].

The Ideal Gas Law was used to solve for mass m in the combustion chamber and substituted into the right-hand side of Equation 2.1 resulting in:

$$\frac{d}{dt} \left(\frac{PV_c}{RT_c} \right) = \left[\frac{V_c}{RT_c} \frac{dP}{dt} + \frac{P}{RT_c} \frac{dV_c}{dt} \right] \quad (2.2)$$

Here we can note that $\frac{P}{RT_c} = \rho_g$ where ρ_g is the density of the gas in the combustion chamber. The term:

$$\frac{dV_c}{dt} = s_b r = s_b a P^n \quad (2.3)$$

is substituted into Equation 2.2 which results in:

$$\frac{d}{dt} \left(\frac{PV_c}{RT_c} \right) = \left[\frac{V_c}{RT_c} \frac{dP}{dt} + \rho_g s_b a P^n \right] \quad (2.4)$$

The left-hand side of equation 2.1 is substituted by the previously mentioned equations resulting in the final equation:

$$P_{eq} = \left[\frac{s_b a (\rho_p - \rho_g) c^*}{A_t} \right]^{\left(\frac{1}{1-n}\right)} \quad (2.5)$$

In the final result, the relationship between P_c and n holds to what was discussed and shown in Section 1.2 and shown in Figure 1.3. Values of the pressure exponent n closer to one result in high chamber pressures, which can be catastrophic; therefore, the value for n must be much less than unity such that small perturbations do not cause large pressure excursions from the desired pressure profile. For composite propellants, n ranges from 0.25-0.6 [1–3].

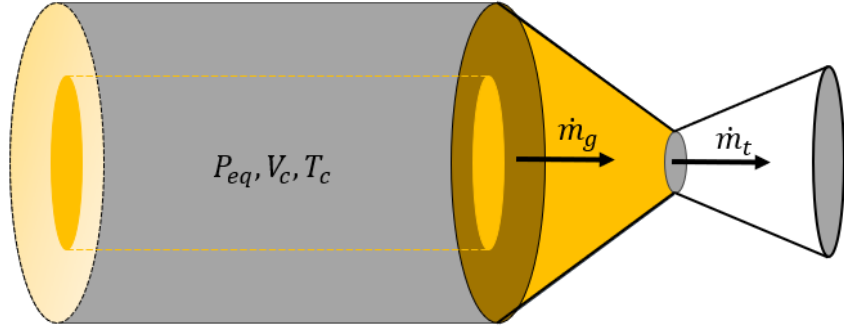


Figure 2.3: Solid rocket motor schematic with single BATES grain showing chamber volume (V_c) highlighted in yellow at pressure and temperature P and T_c respectively.

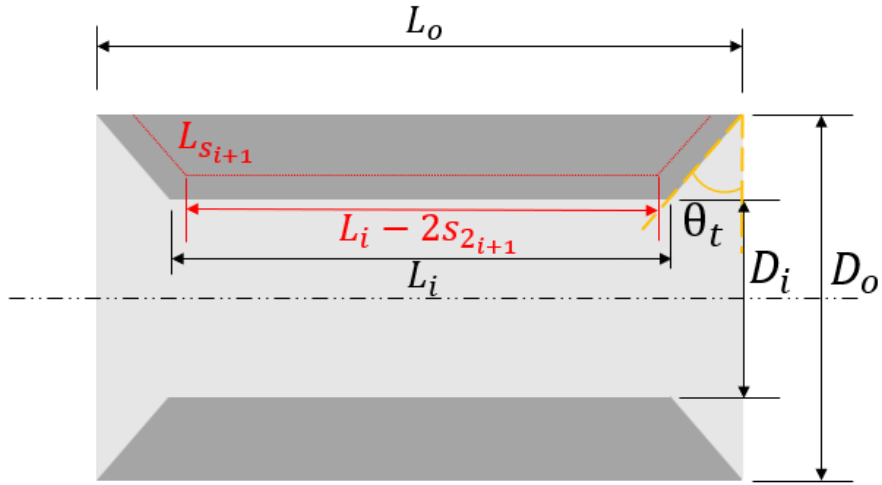


Figure 2.4: A sectional view of a BATES grain and the critical parameters used to develop a surface regression model.

Due to time constraints, the preliminary modeling of the ballistic profiles for the H-10 and H-3 compositions was designed using a value of 2.86 and 0.45 for a and n , respectively. Conventionally, a and n for new propellant formulations are determined from small-scale strand burning, as discussed in future sections. Equation 2.5 highlights how important the burning surface area s_b is for tailoring the ballistic profile. Initial thrust, critical maneuvers, trajectory characteristics, warhead separation, and aerodynamic considerations are some examples of mission requirements where s_b plays a critical role[2][7].

The design and operation of a SRM are mostly influenced by the evolution of the r , s_b , and the grain geometry with respect to time. The expansion ratio ($\epsilon_{exp} = A_e/A_t$) is generally greater than 6 and the grain length-to-diameter ratio, L/D, is ≤ 1 to minimize erosive burning [2, 3]. The final result, derived in Appendix A, of the evolution of the burning surface in time is shown by:

$$s_b = \pi \left[(D_i + 2s_1)(L_i - 2s_2) + (D_o + (D_i + 2s_1)) \frac{r_o - (r_i + s_1)}{\sin(\theta)} \right] \quad (2.6)$$

With this, P_c can be solved for. Once the steady-state pressure is known, the predicted thrust (F) can be solved for [2]:

$$F = A_t P_c \sqrt{\frac{2k^2}{k-1} \left(\frac{2}{k+1} \right)^{\frac{k+1}{k-1}} \left[1 - \frac{P_e}{P_c} \right]^{\frac{k-1}{k}}} + (P_e - P_3) A_t \quad (2.7)$$

The expansion ratio found through NASA CEA was used to solve for the exit area (A_e). In addition, P_e is determined using the pressure ratio P_e/P_c using compressible flow equations. For perfectly expanded nozzles, the exit pressure at the nozzle is equal to the ambient pressure (P_3). Underexpanded nozzles have an exit pressure greater than P_3 ; the discharged high-velocity gas expansion is incomplete, so further expansion must occur external to the nozzle. Overexpanded nozzle flow occurs when the pressure at the exit of the nozzle is lower than P_3 . This is primarily due to having too large of an exit area, causing overexpansion within the nozzle that may lead to flow separation within the nozzle [2]. To maximize thrust with the planned static testing, all nozzles were designed to be perfectly expanded at local Socorro atmospheric pressure. With these considerations, the surface regression model was developed. A complete derivation for modeling the surface regression of BATES grains with tapered edges is shown in Appendix A.

2.4 Solid Rocket Motor Design

2.4.1 MATLAB simulations of 76 mm BATES grains

Several simulations were performed using a MATLAB code for designing the ballistic profile for the 76 mm BATES grains; refer to Appendix B.0.1. The results for chamber pressures of 3.45, 5.17, and 6.89 MPa are shown in Figures 2.5, 2.6, and 2.7. The blue curve represents the predicted pressure P_c , while the red curve is the predicted thrust F .

Table 2.6 shows the results for the nozzle throat diameter (D_t), maximum chamber pressure (P_{max}), average chamber pressure (P_{avg}), and the total burn time (t_b). From

the simulations, the nozzle throat size to achieve the desired chamber pressures was determined iteratively in addition to the nozzle exit diameter (D_e). These results for each operating pressure were used to design the BATES grain geometry and the nozzle dimensions required to achieve the operating pressures of interest for burn rate analysis and comparison of the predicted and experimental performance parameters for each pressure range.

Table 2.6: Results show the maximum pressure, average steady-state pressure, throat diameter, and total burn time from the in-house MATLAB code for modeling the ballistic profiles for nominally 3.45, 5.17, 6.89 MPa (500, 750, and 1000 psi) chamber pressures.

P_{max} MPa	P_{avg} MPa	D_t mm	t_b s
3.63	3.47	8.89	3.22
5.34	5.10	8.00	2.71
7.21	6.89	7.34	2.36

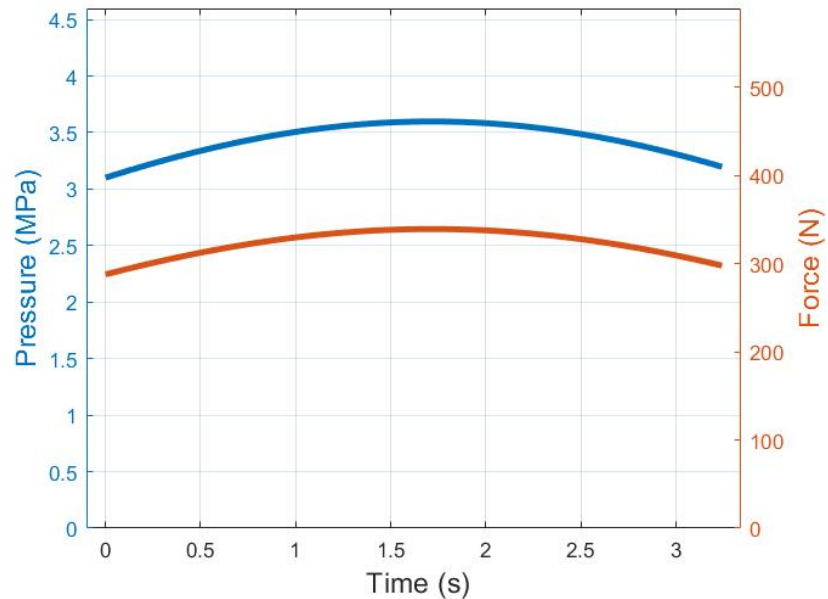


Figure 2.5: Predicted ballistic profile of a 76 mm BATES grain at 3.45 MPa (500 psi) chamber pressure determined through by the predicted NASA performance parameters.

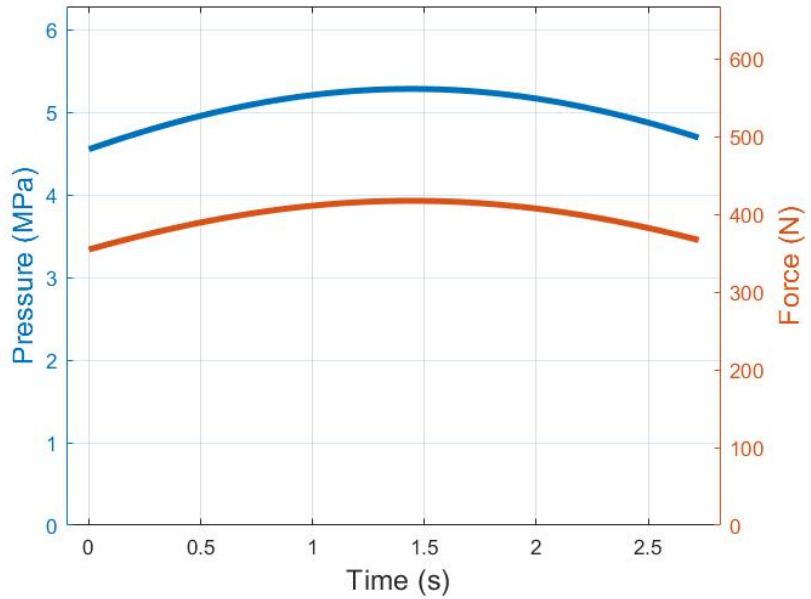


Figure 2.6: Predicted ballistic profile of a 76 mm BATES grain at 5.17 MPa (750 psi) chamber pressure determined through by the predicted NASA performance parameters.

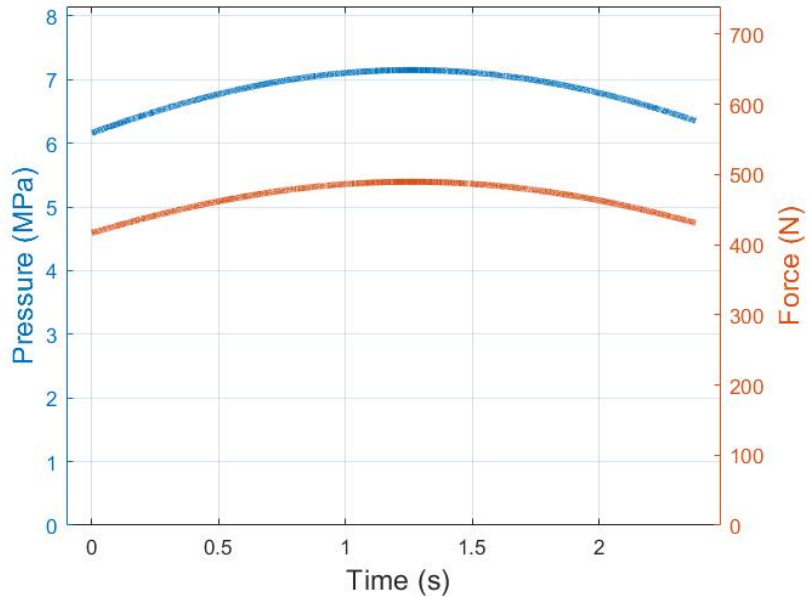


Figure 2.7: Predicted ballistic profile of a 76 mm BATES grain at 6.89 MPa (1000 psi) chamber pressure determined through by the predicted NASA performance parameters.

2.4.2 SolidWorks design of motor components

A schematic of the overall internal components of the designed SRM is shown in Figure 2.8. The SRM case consisted of a diagnostics mount for both pressure and force transducers named the P&F mount. The P&F mount is secured into the case by the forward retaining ring. An inert grain was cast to fill the internal volume of the motor case, which was longer than necessary for the BATES grains tested. An insulator plug, made from G-10 fiberglass, was machined to provide insulation between the motor case and the high-temperature gases. Graphite nozzles were designed in-house and machined by Fisher Design. The 76 mm SRM case was manufactured using Aluminum 6061. The cylindrical stress in the case was calculated using the thin-walled equations for hoop stress ($\sigma_\theta = Pr/t$), where P is pressure, r is the internal radius of the cylinder, and t is the wall thickness. The results are shown in Figure 2.9. For the operating pressures expected, the factor of safety does not drop below 2.07. Case rupture is predicted to occur if the internal pressure reaches 2000 psi, ignoring temperature effects. This assumption was justified using a thermocouple attached to the external part of the motor case by recorded temperature histories that showed a maximum temperature of 99 °C, which is not high enough for aluminum 6061 to lose its strength [38].

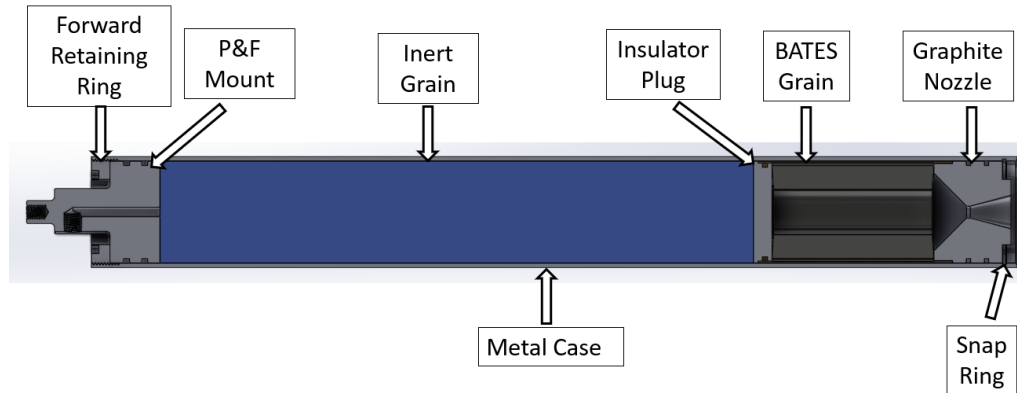


Figure 2.8: Schematic of 76 mm SRM case with internal components listed

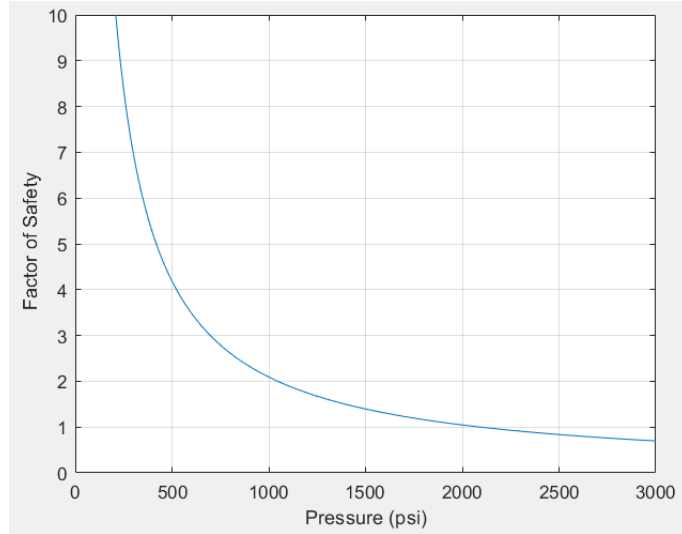


Figure 2.9: Factor of safety of aluminum-6061 motor case

The graphite nozzles were designed with a straight-walled contour. The logistics of using bell-shaped nozzles, which have only been shown to improve the specific impulse by 1 - 2 % compared to conical nozzles [2], was unnecessary. Figure 2.10 shows a schematic of the straight-wall contour with a 15° and 45° divergence and convergence angles, respectively. Static seals were designed into the nozzle for sealing the internal pressure using the Parker O-Ring Handbook [39]. All engineering drawings for all motor components are provided in Appendix C.0.1

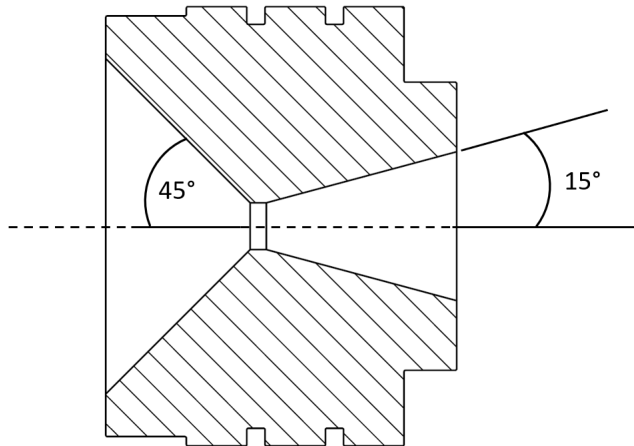


Figure 2.10: Schematic of a straight-wall contoured nozzle with converging and diverging sections

2.5 Casting Techniques and Facilities

The propellant mixing facility used for all casting operations is capable of mixing approximately 6.8 Kg of propellant. A Hobart mixer is operated remotely from a control bunker and is monitored via a live camera feed. Propellant ingredients were weighed and poured into a temperature-controlled mixing bowl set to 115 °C using a PolyScience circulating water heater, which is shown in Figure 2.11. This aided in lowering the viscosity of the binder matrix, predominantly the HTPB, which facilitated ease of mixing and degassing, which reduced the amount of voids present before pouring the propellant slurry into molds.

Mixing was divided into two stages. The first stage consisted of mixing all inert ingredients such as Al, carbon black, CAO-5, HTPB, IDP, and silicone oil. To prevent dry powder from aerosolizing when the mixer was turned on, the liquids were poured on top of the dry powders. Once all the ingredients were wetted, the successive small portions of AP were added to the mixer. The Hobart mixed under vacuum at 25 in Hg. This aided in the reduction of voids present and also prevented voids from being introduced due to the mixing process. A data acquisition unit monitors live measurements of internal pressure, bowl temperature, and consumed voltage from the mixture for health monitoring of the propellant slurry and to ensure the propellant isn't curing in the bowl. This ensured control over the quality and consistency of the propellant slurry from batch to batch.

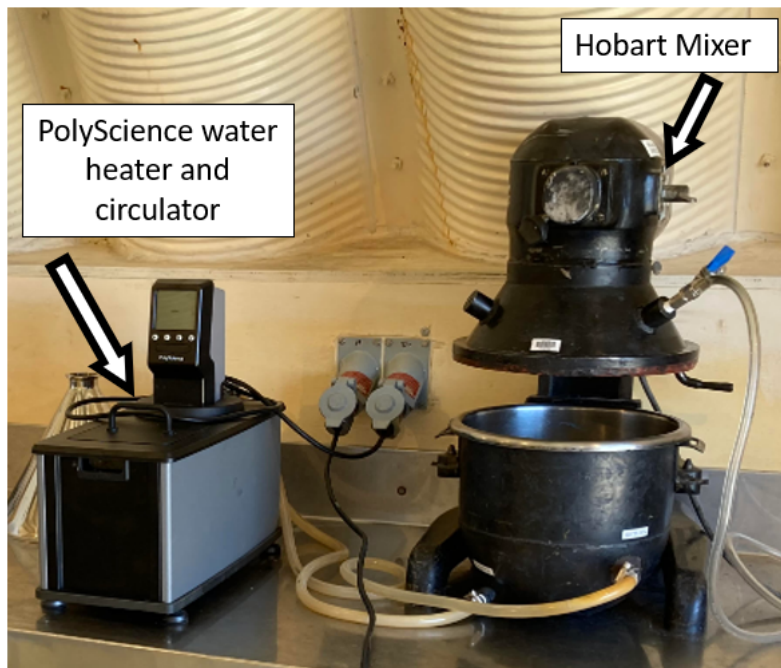


Figure 2.11: Hobart mixer and a PolyScience water heater for propellant mixing

Casting into the molds was conducted once the propellant slurry was thoroughly mixed. All molds were cleaned with 70 % isopropyl alcohol and coated with a thin layer of Molykote 111 compound that served as the mold release agent. The propellant slurry

was then slowly poured into a large stainless steel funnel that sits on top of a vacuum-cast pot (vac-cast pot), which is shown in Figure 2.12. The vac-cast pot consists of a slit plate with several 6 mm holes. This increased the propellant surface areas, which further increased the rate at which voids were reduced when the propellant slurry fell into the mold. The vac-cast pot sat on top of a pneumatic vibrating table, which vigorously shook the propellant slurry, further assisting in the reduction of voids. The entire process was manually controlled using a plunger to adjust the mass flow rate of propellant into the vacuum pot, as seen in Figure 2.12. Refer to Appendix D.0.1 for the detailed casting operations.

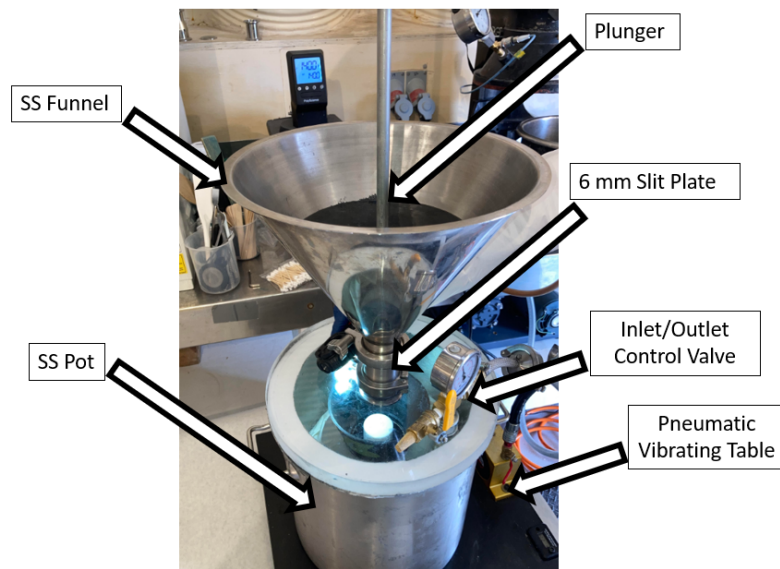


Figure 2.12: Vac-cast pot with a large stainless steel funnel and pot. Propellant flows through several 6 mm diameter slits and is poured into molds

CHAPTER 3

EXPERIMENTAL METHODS FOR STRAND BURNING AND STATIC FIRE TESTING

Experimental methods for strand burning and the ballistic evaluation of the ammonium perchlorate composite propellant (APCP) and solid rocket motors (SRMs) are discussed. Small-scale strand burning allows for determining the burn rate coefficient (a) and exponent (n) for the propellant, which can then be used for ballistic profile modeling. Bulk flame temperature measurements using non-intrusive optical pyrometry and spectroscopy are applied for both strand burning and static firing of 76 mm grains. Lastly, multiple burn rate analysis methods are presented to determine a and n using experimental data from the 76 mm motor firings.

3.1 Propellant Strand Burning

Small-scale burn rate characterization of the APCP was conducted. Strand propellant samples were burned within a pressure vessel, hereafter referred to as a strand burner, to record burn rate r and bulk flame temperature histories, refer to Figure 3.1. The dimensions of the samples were 6.35 x 6.35 x 101.6 mm (0.25 x 0.25 x 4 in). The length of the strands was chosen to be 101.6 mm (4 in) to prevent errors from ignition and burnout effects near the edges of the strand samples and to allow enough space for several embedded nichrome wires, refer to Figure 3.2. All propellant strand samples were secured onto a platform, which fixed the sample at the center of the strand burner. Burn rate histories were recorded versus time using six embedded 30-gauge nichrome wires spaced 12.7 mm (0.5 in) apart. A 30-gauge nichrome wire served as a hot-wire initiator with a constant 3.5 A supplied from a DC power supply. A spectrometer and pyrometer measured emitted light through a sapphire window. The pressurization of the strain burner was performed remotely by controlling a solenoid ball valve located at the bottom of the strand burner. After testing, the strand burner was depressurized from the top of the strand burner into an exhaust fan. Figure 3.1 shows a schematic of the strand burner in addition to the strand burning platform showing the 25.4 mm (1 in) and 12.7 mm (0.5 in) ignition and shutdown distances.

3.1.1 Strand burner design

The strand burner was designed to measure the burn rate dependence on pressure, allowing optical diagnostics for bulk flame temperature measurements. Hydrostatic testing

was performed at 3.45, 6.89, and 12 MPa, which validated the strand burner's integrity across the primary operating range.

The strand burner consists of a platform constructed with mild steel and aluminum to secure the samples during testing. The platform has two vertical columns that provide structural support for the embedded wire connections, along with a 3D-printed cover that protects wiring from the high temperatures experienced during testing. The platform can accommodate 7 conductive paths for 6 embedded wires and 1 ignition wire. A wiring harness connects to two wire pass-throughs, which consist of 7 conductive paths for all 14 wires. The wire pass-throughs were manufactured using straight ejector pins and high-strength epoxy. Figure 3.3 shows an assembled wire pass-through developed for internal-to-external electrical signal acquisition. These wires all connect to the data acquisition system (DAQ).

Two 1/4-NPT mounting points for a pressure transducer to measure internal pressure and a manual ball valve for purging ambient air before testing were machined into the side flanges of the strand burner. Two windows ports for 50 mm diameter sapphire windows (WHS5099) with light transmission between UV and IR at 150 nm to 5500 nm for spectral analysis were machined and mounted to each of the side flanges as shown in Figure 3.4. A reflective collimating lens (RC08SMA-P01) from THORLABS was center-mounted on the sapphire window for light emission measurements. An internal view with a mounted propellant strand and images of the strand burner assembly are shown in Figures 3.5 and 3.6, respectively. The secondary window port was used for direct imaging and troubleshooting ignition/misfires at the initial stages of testing.

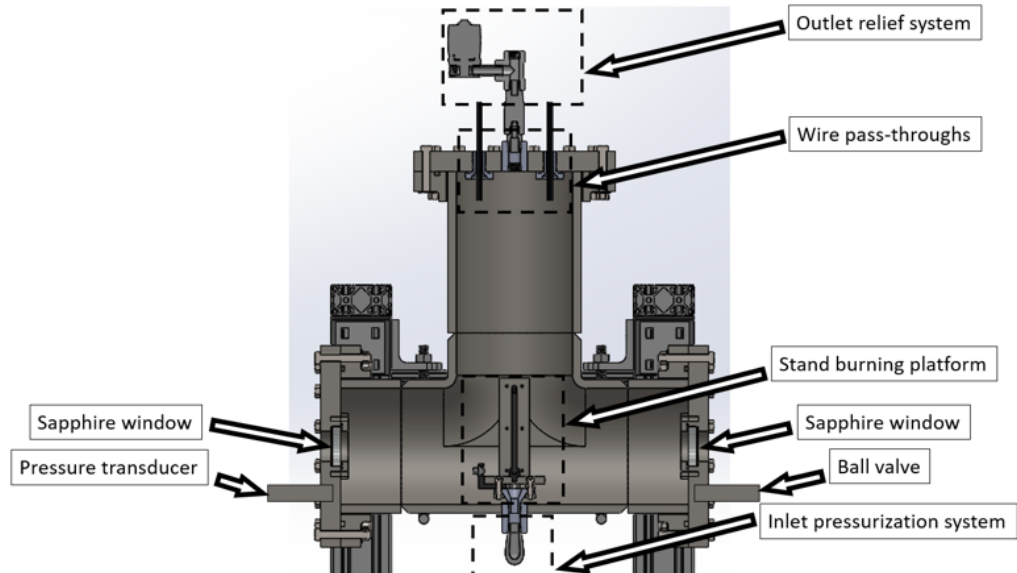


Figure 3.1: Half sectional view of strand burner with all working systems.

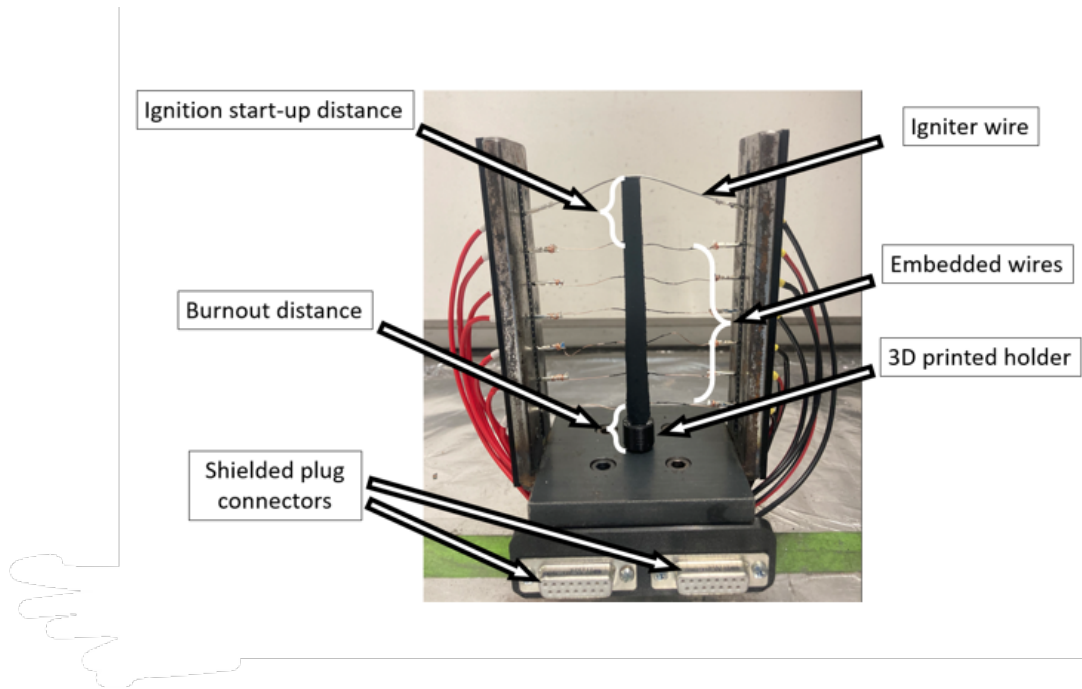


Figure 3.2: Strand burning platform showing ignition wire, six-embedded wires, strand sample holder, and ignition start-up and shutdown distances.



Figure 3.3: Front, isometric, and side views of the wire pass-throughs manufactured.

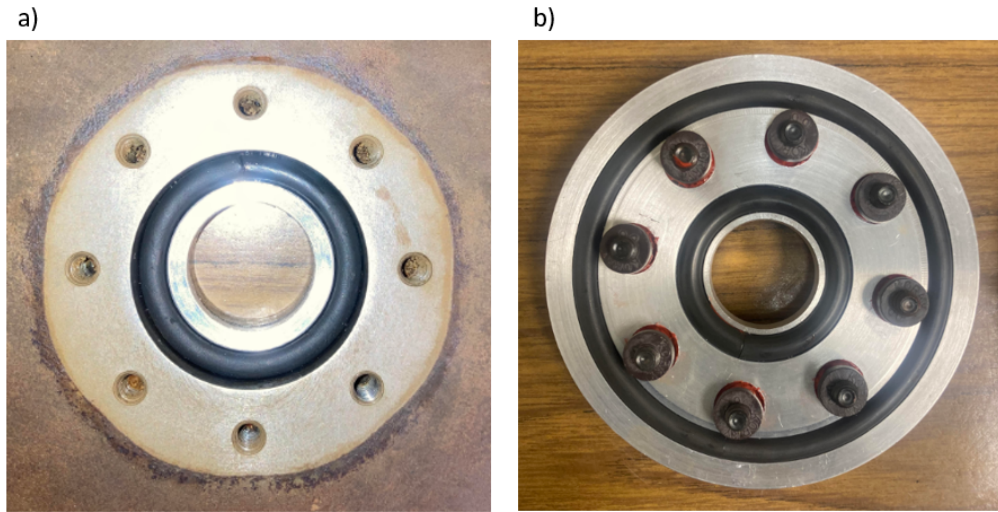


Figure 3.4: Sapphire window port assembly: a) Fixed window mounting point for the window port. b) Window port for sapphire window with two Viton gaskets and several Viton washers.



Figure 3.5: Internal view of strand burner with the platform for holding propellant samples in place. Six embedded wires for measuring burn rate and ignition wire placement are shown.

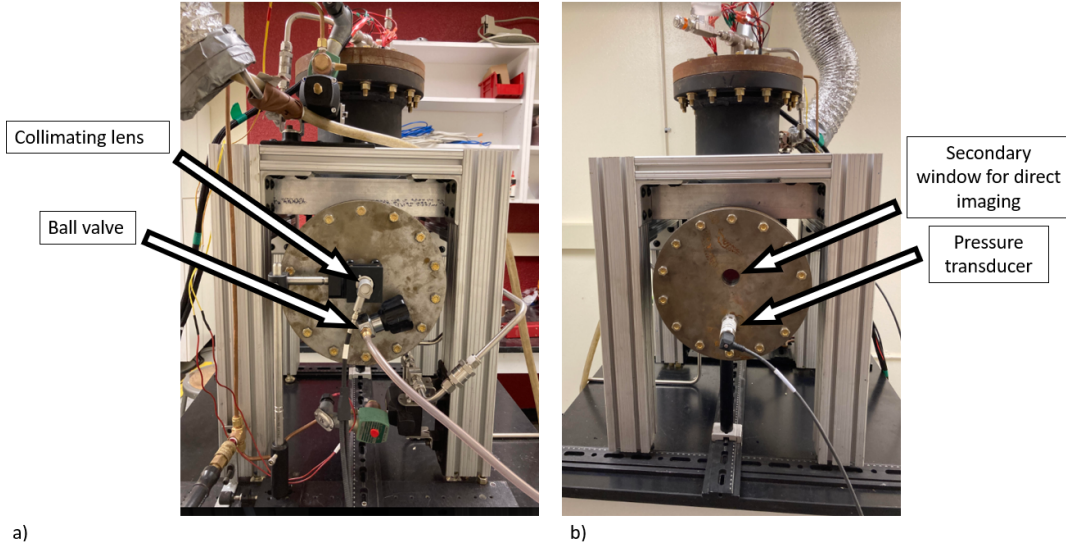


Figure 3.6: a) Side of the strand burner with collimating lens for optical measurements of light emission and ball valve for purging ambient air. b) Opposite side of strand burner with pressure transducer

3.2 Strand Burning Experimental Methods

All operations involving pressurization of the strand burner, burning of propellant samples within the strand burner, or ventilation of the exhaust products were conducted remotely. Before testing, all propellant samples were inhibited using the constituents shown in Table 3.1. The percentages of HTPB, DDI, and TPB were derived from the weight percentage (wt%) shown in Table 2.5. The addition of dibutyltin dilaurate (DBTDL) served as an additional curing catalyst to allow the inhibitor to cure within 24 hours at room temperature. The inhibitor prevented the side walls of the propellant from ignition, allowing the 6.35 mm x 6.35 mm (0.25 x 0.25 in) cross-section to be the only burn surface as the burning surface propagated through the samples. Six 30-gauge nichrome wires were inserted through the samples at 25.4 mm (0.5 in) spacing with 25.4 mm (1 in) and 12.7 mm (0.5 in) ignition and burnout distances, respectively.

The ignition start-up distance ensures the combustion wave has reached a steady state due to heat transfer from the burning surface into the propellant samples. As mentioned in Section 1.2, the rate of decomposition is a function of how much heat is transferred into the propellant, specifically at the initial stages of burning. The shutdown distance is required as a result of the change in thermal conductivity from the propellant to the burning platform. Less distance was required for the shutdown distance, but to prevent any changes in the rate of decomposition due to heat loss or boundary effects at the end of the burn, 12.7 mm (0.5 in) was used. Further discussion as to why this distance is sufficient is presented in Chapter 4.

Table 3.1: Weight percent (*wt%*) of chemical ingredients for inhibiting propellant samples.

Chemical ingredient	<i>wt%</i>
Hydroxyl-terminated polybutadiene	66.4
Dimethyl diisocyanate	16.6
Triphenylbismuth	0.26
Carbon black	16.7
Dibutyltin dilaurate	0.04

A 30-gauge nichrome wire was secured to the top of the strand to ignite the sample. A continuity check was performed to ensure all lines were connected properly, followed by securing the side flanges. After sealing the strand burner, ambient air was removed from the interior volume using a vacuum pump. The strand burner was then supplied with nitrogen (N_2) gas using a 24 MPa compressed N_2 gas tank. A Swagelok pressure regulator sets the desired pressure for the strand burner. The pressure history in the strand burner was recorded using a TD1000 pressure transducer from Transducers Direct. An NI-9203 c-DAQ provided a constant 24 V excitation voltage while recording the variance in current output using LabVIEW VI. A NI-9205 c-DAQ was used to provide a constant 20 mA current through the six embedded nichrome wires. After the strand burner was pressurized, another continuity check was conducted to ensure all wires remained connected. After ignition, an NI-9263 c-DAQ was used to record the instance in time at which the break wires were severed by the flame, allowing for the determination of the burn rate r . Figure 3.7 shows the control systems used to operate the strand burner. Once the propellant sample was consumed, the exhaust products were vented through an exhaust fan, and additional N_2 gas was introduced into the system to assist in the ventilation process.

A bifurcated fiber cable (BFY105HS02) from THORLABS was used to collect output light from the burning propellant event and direct it into the pyrometer and spectrometer. The four-color pyrometer was calibrated by using a 2700 K halogen lamp (SLS201 L) from THORALBS. The compact spectrometer was previously calibrated by THOR-LABS with the corresponding bifurcated cable.

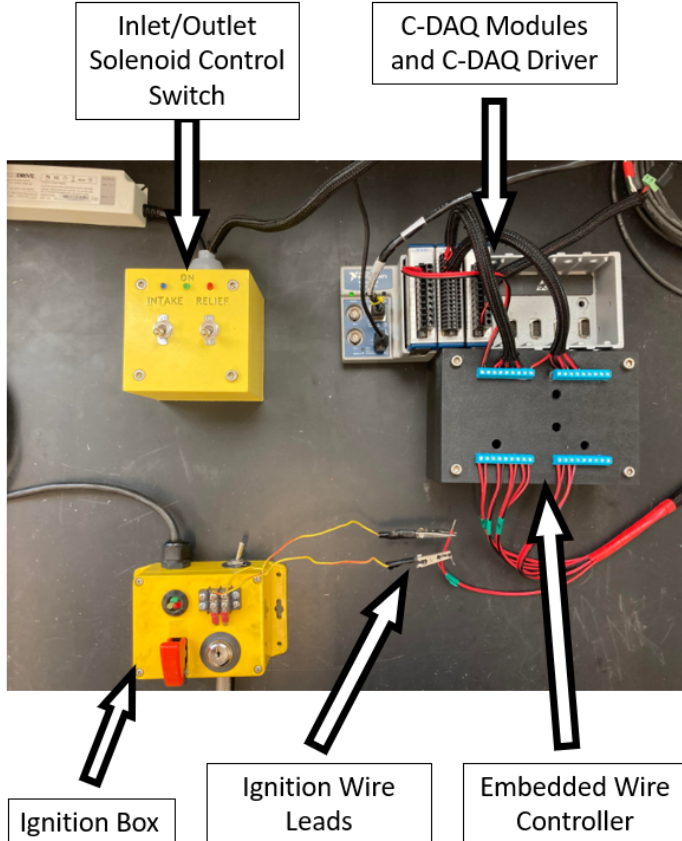


Figure 3.7: From top left to bottom right: Inlet/Outlet solenoid control box for operating solenoids remotely, C-DAQ modules and driver for DAQ system, ignition box with redundant systems to safely ignite propellant strands, ignition wire leads connection point, and embedded wire controller.

3.2.1 Temperature measurement principles

Temperature analysis using non-intrusive optical pyrometry and spectroscopy diagnostics was performed. The four-color pyrometer was calibrated using a 2700 K calibration lamp prior to testing. A pre-ignition data set from a pressurized strand burner with N₂ gas was used to subtract ambient noise from the measured values of light intensity during the combustion process of the propellant samples. The following relation was used to calibrate the measured values from the photodetectors:

$$c_{\lambda} = \frac{I_{exp,cal}}{I_{ref}} \quad (3.1)$$

The average intensity values of the experimental measurement ($I_{exp,cal}$) were scaled by the factor of the reference intensity values (I_{ref}) at a particular wavelength (λ) as published by the manufacturer of the 2700 K lamp. Once the correction factors for each

wavelength were determined, the light intensity measurements recorded during the combustion process were scaled by a factor of $1/c_\lambda$.

Under the gray body assumption, the intensity of light ($I(\lambda, T)$) is proportional to the intensity of a blackbody ($I_b(\lambda, T)$) and the emissivity of the light is assumed to be invariant with respect to wavelength, ($\varepsilon_\lambda = \text{const}$). Additional assumptions explored in this work were $\varepsilon_\lambda = 1/\lambda^{-1}$ and $\varepsilon_\lambda = 1/\lambda^{-2}$ which account for emissivity variations in wavelength. These variations are also used by Woodruff et al. [40], which is similar work to that done here.

In summary, the intensity of an object is related to the intensity of a blackbody by:

$$I(\lambda, T) = \varepsilon_\lambda I_b(\lambda, T) \quad (3.2)$$

A simplified variation of Planck's equation, known as Wein's approximation, is given by:

$$I(\lambda, T) = \frac{C_1}{\lambda^5 e^{\left(\frac{C_2}{\lambda T}\right)}} \quad (3.3)$$

Solving for temperature using Equations 3.2 and 3.3 results in:

$$T = \frac{C_2 / \lambda}{\ln(C_1) - \ln(\lambda^5 I \varepsilon_\lambda)} \quad (3.4)$$

The radiation constants C_1 and C_2 are $2hc^2$ and hc/k , respectively. The constants h , c , and k represent Plank's constant, the speed of light in vacuum, and Boltzmann's constant, respectively.

With the system calibrated, the temperature was directly determined through Equation 3.4 by substituting the measured light intensity (I) and its respective wavelength λ . A linear relation was extrapolated to give bulk flame temperature measurements as a function of time. Figure 3.8 shows the linear relation of Wien's approximation, showing individual quantities corresponding to a specific wavelength λ where the slope of the line equals the measured temperature. Spectral calculations were also performed using the same method.

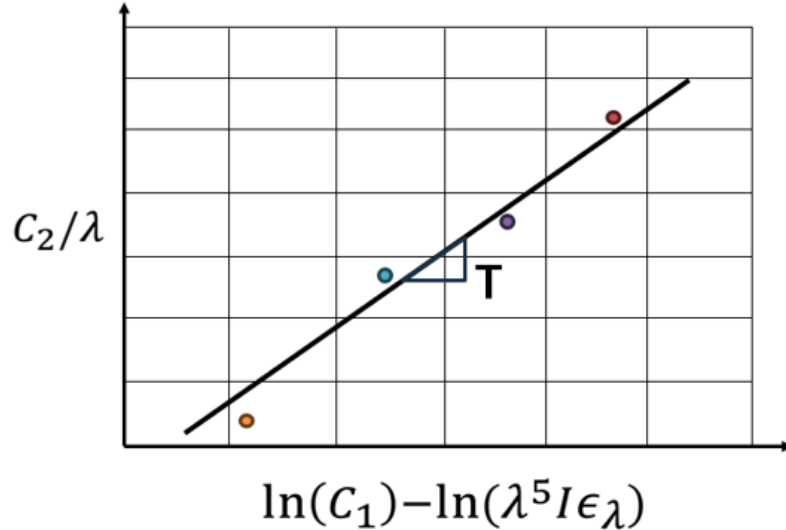


Figure 3.8: Linear relation of Wien’s approximation showing individual quantities corresponding to a specific wavelength λ where the slope of the line equals the measured temperature.

3.2.2 Pyrometer diagnostic methods

The pyrometer used for this work is a four-color pyrometer that collected emitted light from the burning propellant samples. The pyrometer was modeled after that described by [40]. A collimating lens was placed 279.4 mm (11 in) from the sample on the outside of the strand burner to capture the light from the event before entering the breakout junction of the two fiber optic cables. One of the two high-grade optical fiber cables was threaded into a secondary collimating lens that collimated the light into the first kinematic cube containing a short-pass dichroic mirror. The mirror has 400 nm - 788 nm and 823 nm - 1300 nm transmission and reflection bands, respectively. The reflected light enters through a 1000 nm bandpass filter (FB1000-10) with ± 10 nm full-width half maximum (FWHM) of the filter response curve. The light then proceeds through one of the four amplified photodetectors (PDA100A2) from THORLABS set to a gain of 60. The transmitted light then propagates through two additional short-pass dichroic mirrors with 410 nm - 633 nm and 685 nm - 1600 nm, 390 nm - 550 nm and 584 nm - 800 nm transmission and reflection bands, respectively. The remaining amplified photodetectors had 700 nm (FB700-10), 600 nm (FB600-10), and 550 nm (FB550-10) bandpass filters, all with 10 nm FWHM. The pyrometer is shown in the image and schematic in Figure 3.9.

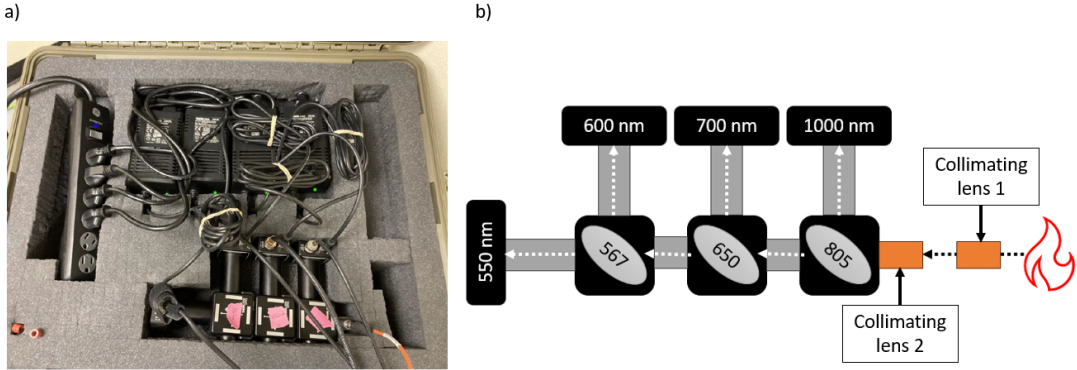


Figure 3.9: An image of the four-color pyrometer and b) A schematic that shows the light path from the emitted light from the propellant flame entering the pyrometer and to the individual photodetectors at specific wavelengths.

3.2.3 Spectrometer diagnostic methods

A compact spectrometer (CS200) from THORLABS operating on a Czerny-Turner design [41] was used to record the emission spectrum from the propellant burning surface. The spectrometer offers a 200 nm - 1100 nm spectral range with 2 nm FWHM. It operates using a 600 groove/mm grating blazed at 800 nm and offers 10 μ s - 60 s integration time. It was experimentally determined that the integration time should be set to 1 ms for all experiments to ensure enough saturation occurred within the spectrometer and to prevent oversaturation from the event. A 5 V TTL was used to synchronize the spectrometer and pyrometer using a Standford box timing unit.

3.3 Static Fire Experimental Methods

Single BATES grain 76 mm motors are inserted into a 76 mm aluminum motor case. Figure 3.10 shows the 76 mm SRM assembly of all internal components. Engineering drawings of the aluminum 6061 motor case, the forward grain insulating plug, and all nozzles for attaining 3.45 MPa, 5.17 MPa, and 6.89 MPa (500 psi, 750 psi, and 1000 psi) are presented in Appendix C.0.1. The forward closure has a 1/4-NPT internal thread that serves as the port for measuring chamber pressure using a TD1000 pressure transducer. Before each test, the cavity of the pressure transducer was filled with vacuum grease for thermal protection against the high-temperature combustion products.

Several measurements were taken before static firing that served as parameters used for post-processing, such as initial throat diameter D_t , propellant weight m_p , initial port diameter D_i , and the length of the grain L_g . The assembly procedure consisted of first inserting the required nozzle with its corresponding viton o-rings after applying a copious amount of high-temperature grease to the o-rings and to the nozzle/motor case interface. The rear snap ring was then secured and put in place. Next, the propellant grain was inserted into the phenolic tube. The insulating plug, along with an o-ring and applied high-temperature grease, was inserted into the forward end of the phenolic tube. The

phenolic/grain assembly was inserted into the motor case after more grease was applied to the outside of the phenolic. Following this step, the inert grain was inserted into the case, followed by the forward closure and its corresponding retaining ring. The fully assembled motor case, shown in Figure 3.11, was then secured onto a rail system which ensured the motor case remained concentric with a WMC2000 compression load cell from Interface rated for 8896 N (2000 lbf) during firing directing the thrust into the force transducer, which is shown Figure 3.12. Once the SRM was secured, a single commercial pyrogen igniter was inserted through the nozzle and positioned toward the front end of the BATES grain.

The bifurcated fiber optic cable used for temperature measurements was placed 610 mm (24 in) from the center line of the motor tube and in line with the front of the nozzle exit as shown in Figure 3.11. Both pyrometer and spectrometer diagnostic equipment systems, in addition to the data analysis as described in section 3.2.1, were the same in all respects as the system developed for strand. Note that a difference of 1000 K, compared to the combustion temperature, was expected as a consequence of the thermal energy conversion to velocity through the nozzle. All static fire testing was performed in a rocket test facility (REF) at EMRTC [42]

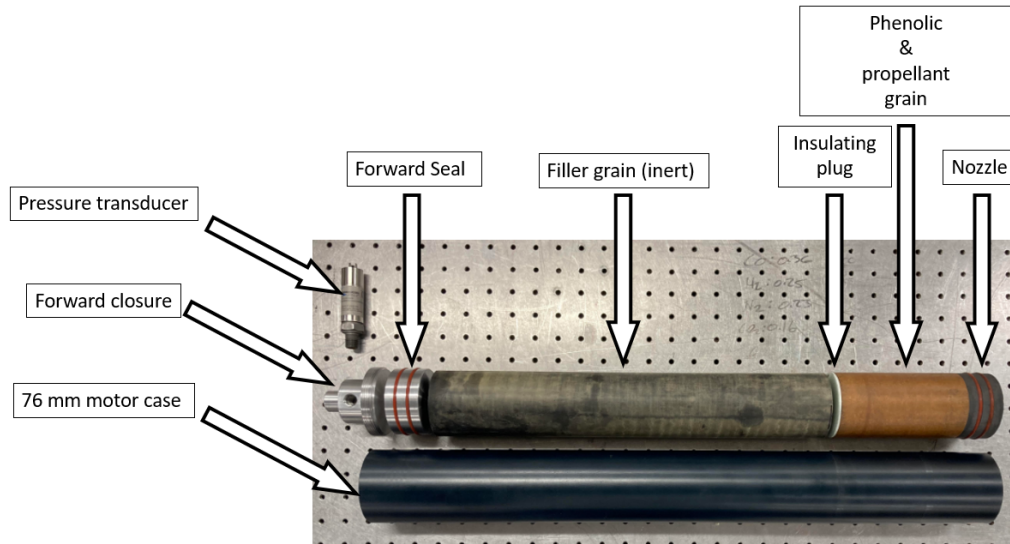


Figure 3.10: Components of the solid rocket motor assembly.

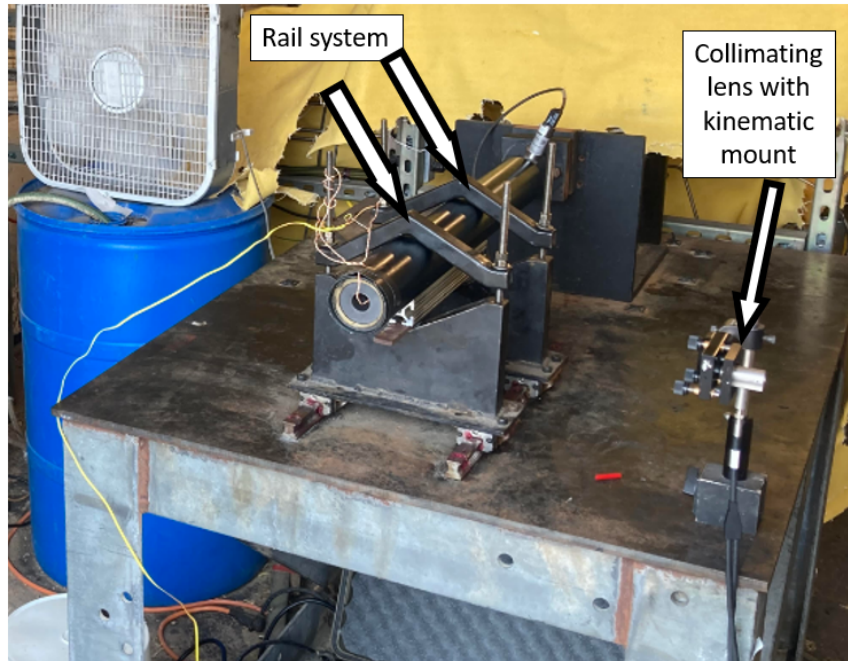


Figure 3.11: Experimental setup implemented for static fires of the 76 mm BATES grain solid rocket motor.

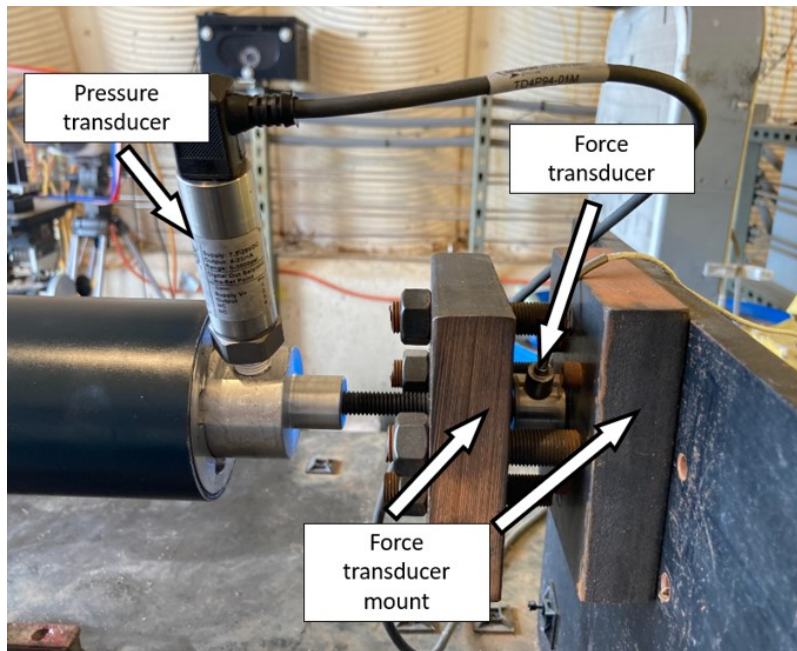


Figure 3.12: Image of the TD1000 pressure transducer mounted into the forward closure attached to the force transducer mount by a 3/8-16 all thread. The image also shows the WMC2000 force transducer mounted.

CHAPTER 4

RESULTS AND DISCUSSION OF TEMPERATURE AND BURN RATE ANALYSIS

The power law relation for the burn rate pressure dependence of the two APCP compositions was explored. Experimental testing was conducted using strand burning and static motor test fires of 76 mm SRMs at 3.45, 5.17, and 6.89 MPa. Bulk flame temperature measurements were recorded using a four-color pyrometer and spectrometer to measure the bulk combustion temperature of propellant strand samples, as well as the temperature at the exit of the SRM. Experimental performance parameters were compared to the parameters predicted by NASA CEA. In addition, a correction factor was incorporated into the model to account for slag buildup, which further improved the correlation of the model to the experimental pressure and thrust histories.

4.1 Strand Burning Results and Discussion

4.1.1 Burn rate analysis

Burn rate analysis was conducted to determine the burn rate parameters a and n of the two APCPs with the H-10 and H-3 Al powders. Several tests were performed in varied pressure environments from 3.45 to 6.89 MPa (500 to 1000 psi). A raw data set is for a 6.89 MPa test presented in Figure 4.1. The LabView VI was triggered before all other instrumentation, which sets the time $t = 0$ on the horizontal axis. For the test shown, the sample began burning at about $t = 37$ s as indicated in Figure 4.1. It was observed that nominally a roughly 0.4 MPa (60 psi) pressure rise was observed as a result of the closed volume design of the strand burner and thermal effects from the hot gases. The first break wire is severed by the flame front at $t = 42$ s, which is identified by the drop in voltage on that individual channel. In the graph of Figure 4.1 an orange vertical line is observed, indicating the drop in voltage. Each sequential wire was severed by the flame front moving through the sample, indicated by a drop in voltage on the given wire's channel. After the sample finished burning, cool-down effects resulted in a pressure drop following extinction. Since the pressure was not constant, a moving average between break wires was calculated for the respective burn rates. The burn rate r was calculated between each set of wires as a finite difference, providing a total of 5 data points per burn sample.

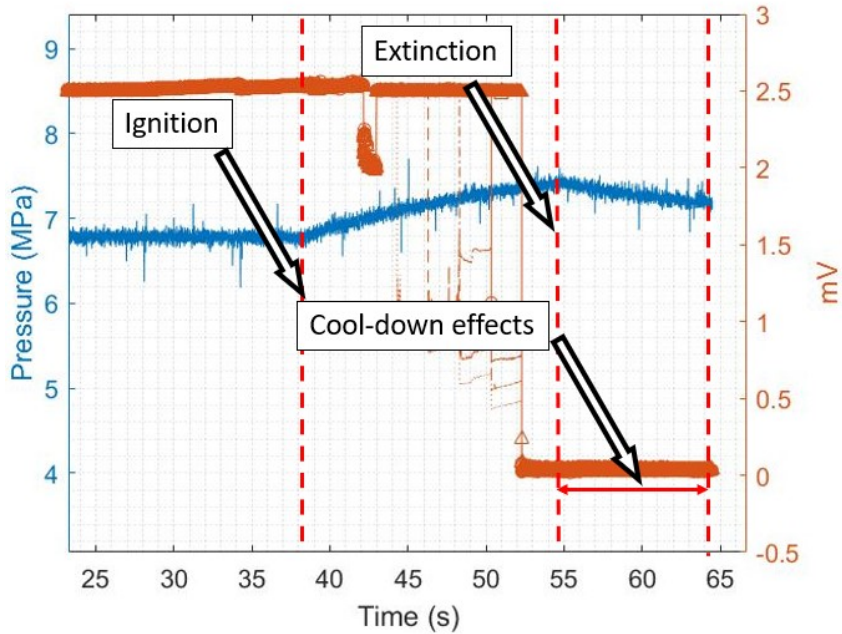


Figure 4.1: Raw data set of the pressure history and trigger times for a strand burning test at a nominal pressure of 6.89 MPa for an H-10 composition.

The burn rate was calculated by taking the natural logarithm of both sides of Equation 1.1 resulting in:

$$\ln(r) = n \cdot \ln(P_{avg,SB}) + \ln(a) \quad (4.1)$$

This is the equation of a line on a log-log scale where n is the slope and $\ln(a)$ is the y-intercept. Once acquiring the burn rate pressure dependence, a linear line was fitted to the data to extract the y-intercept $\ln(a)$. From there, the coefficient a was determined by:

$$a = e^{\ln(a)} \quad (4.2)$$

The values of a and n found are similar to those found in the literature and are shown in Table 4.1. The values of a and n were experimentally determined for composite propellants that also use AP, Al, and HTPB. The similarities between the formulations show that propellant compositions that use the aforementioned ingredients have values of a and n that allow for variations in burn rate that could range from 2 to 9 mm/s.

Table 4.1: Tabulated results of a and n adapted from [1–3].

a	n
1.0 - 3.0	0.25 - 0.6

Tables 4.2 and 4.3 show the individual data points for r and average pressure between wires ($P_{avg,SB}$). Figure 4.2 and 4.3 show the power law relation determined for the H-10

and H-3 compositions, respectively. The H-3 composition was found to have a faster burn rate than the H-10 composition, which was expected with the smaller particle size of the aluminum. The H-3 has a larger exponent, 0.4012, compared to the H-10 composition, 0.3747, which would suggest the composition is slightly more sensitive to pressure excursions and is prone to combustion instability [7]. The pressure ranges shown are higher than the operating pressures as a result of the increase in pressure due to the close volume design.

Table 4.2: Measured burn rates and pressures of the APCP with H-10 composition.

3.45 MPa (500 psi)		5.17 MPa (750 psi)		6.89 MPa (1000 psi)	
$P_{avg,SB}$	r	$P_{avg,SB}$	r	$P_{avg,SB}$	r
MPa	mm/s	MPa	mm/s	MPa	mm/s
3.45	3.69	5.17	4.19	6.89	6.21
3.49	3.88	5.35	4.69	7.14	5.26
3.55	3.60	5.44	4.69	7.31	4.92
3.57	4.10	5.52	4.58	7.38	5.02
3.65	3.60	5.58	4.57	7.40	4.92
3.75	4.06	5.26	4.69	6.57	5.18
3.71	4.10	5.45	4.47	6.68	4.76
3.60	3.79	5.44	4.28	6.73	4.76
3.56	4.10	5.53	4.54	7.05	5.00
3.52	4.37	5.61	4.16	6.76	5.18
3.61	3.86	5.52	4.22	7.08	5.00

Table 4.3: Measured burn rates and pressures of the APCP with H-3 composition.

3.45 MPa (500 psi)		5.17 MPa (750 psi)		6.89 MPa (1000 psi)	
$P_{avg,SB}$	r	$P_{avg,SB}$	r	$P_{avg,SB}$	r
MPa	mm/s	MPa	mm/s	MPa	mm/s
3.60	4.77	5.30	5.25	7.12	6.05
3.66	4.95	5.39	5.83	7.20	6.07
3.72	4.95	5.45	5.26	7.28	5.77
3.76	4.78	5.50	5.82	7.34	6.37
3.81	4.63	5.55	5.25	7.39	6.57
3.63	4.32	5.32	5.31	7.05	6.49
3.68	4.69	5.39	5.79	7.13	6.26
3.72	4.82	5.46	5.47	7.20	6.36
3.74	4.69	5.51	5.97	7.28	6.24
3.78	4.68	5.54	5.61	7.33	6.50

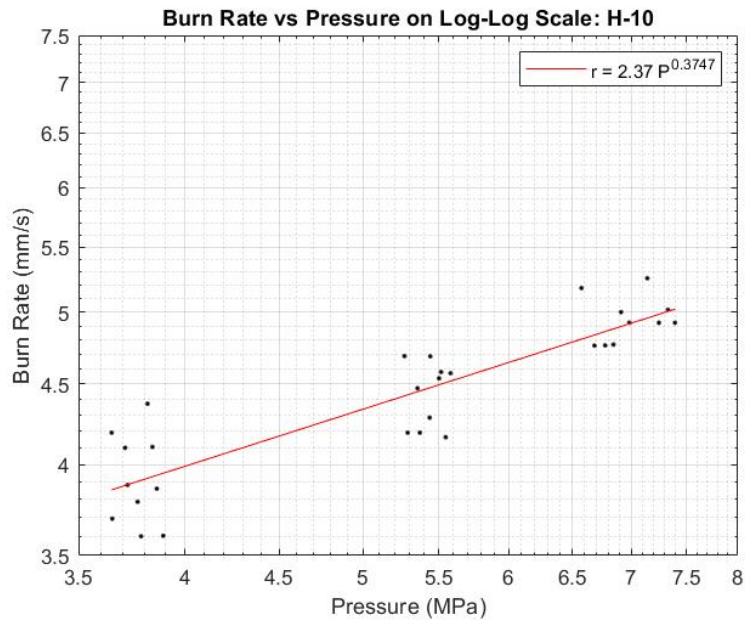


Figure 4.2: Power law relation determined from strand burn analysis for the burn rate and pressure for H-10 composition. Note that the pressure range is less than one decade, so the log-log-axis is not very pronounced here.

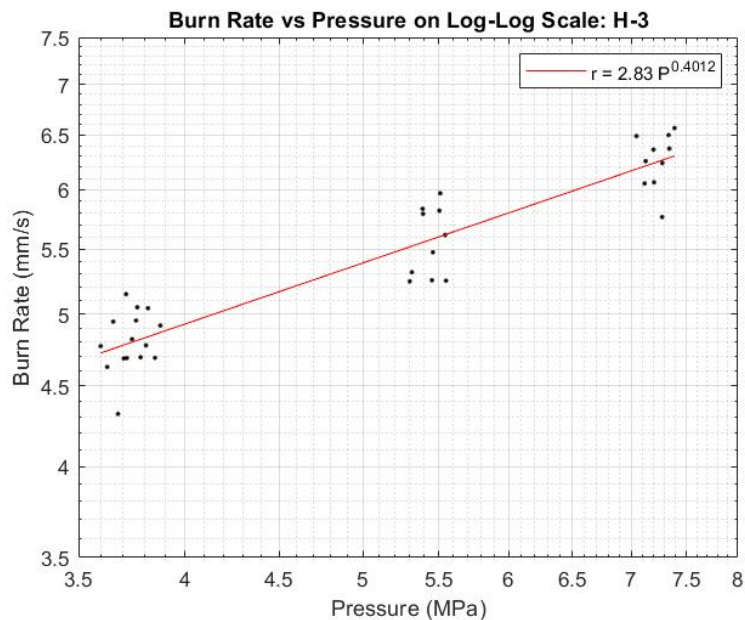


Figure 4.3: Power law relation determined from strand burn analysis for the burn rate and pressure for H-3 composition. Note that the pressure range is less than one decade, so the log-log-axis is not very pronounced here.

4.1.2 Bulk flame temperature measurements

Figure 4.4 shows the pyrometer and temperature histories at 6.89 MPa. The figure shows the flame front entering the field of view, followed by variation occurring due to the reduction of light that was observed due to the closed-volume design of the strand burner. This caused an accumulation of gas products, reducing the light intensity that can be seen by the pyrometer. An optimal range was specified to include the initial stages of the flame front entering the field of view indicated in Figure 4.4. Similar methods were used for spectrometer measurements. Figure 4.5 to 4.7 show the measured $T_{avg,bulk}$ with various values of ε_λ . Note that the measured values for when $\varepsilon_\lambda = const.$ has the highest measured value of $T_{avg,bulk} = 2271 \pm 79$ K, where ± 79 K is the standard deviation of all the measurements being considered.

This measurement is slightly lower than the expected values in the range of 2600 to 3000 K; however, the large difference between experimental and predicted values is due to the anticipated loss of heat to the environment [3], in addition to the measuring bulk temperatures of the entire plume rather than the actual combustion temperature that NASA CEA is predicting.

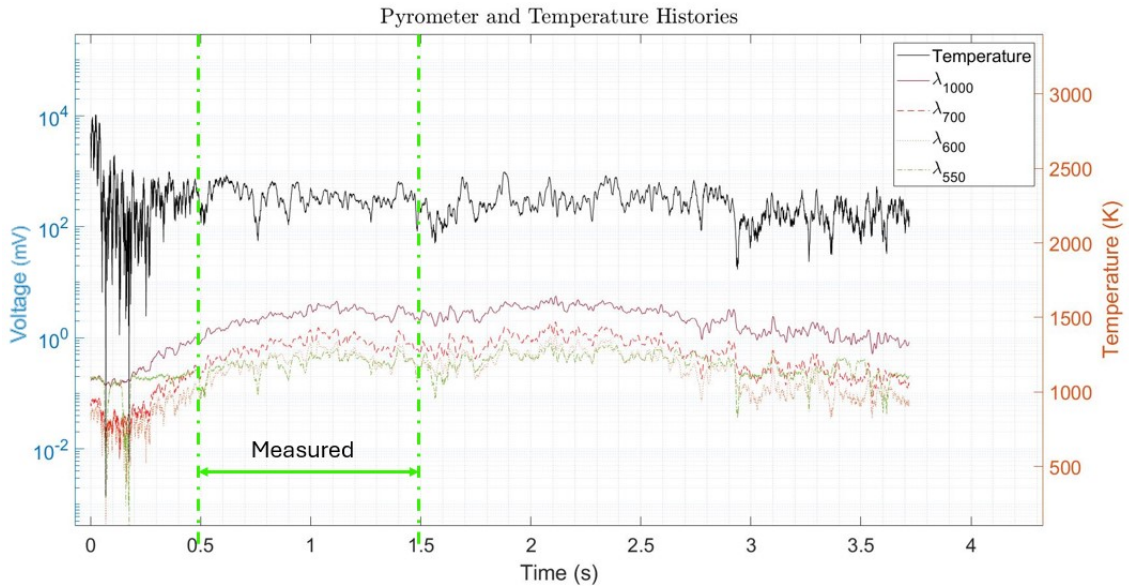


Figure 4.4: Bulk temperature and pyrometer history at 6.89 MPa of H-10 composition showing a range when measurements were taken.

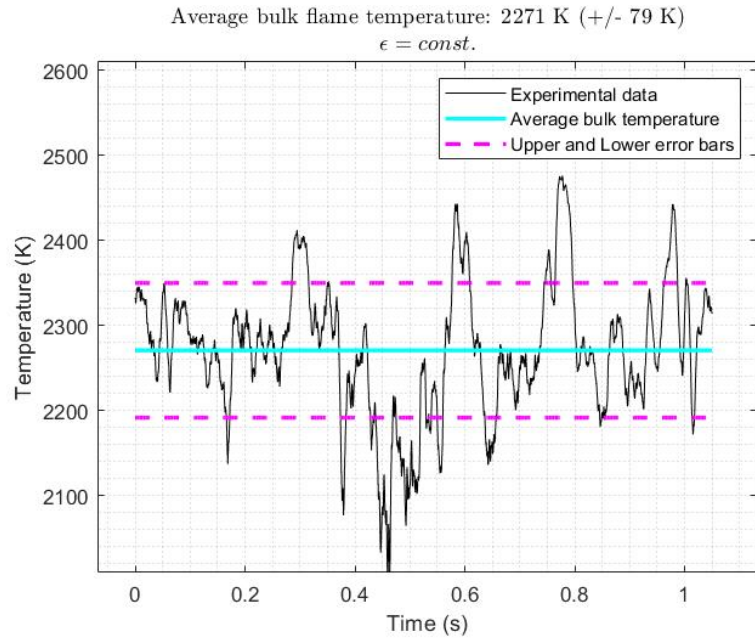


Figure 4.5: Bulk flame temperature history measured with the pyrometer at 6.89MPa of H-10 composition with $\epsilon_\lambda = \text{const.}$ with the standard deviation of all the measurements being considered.

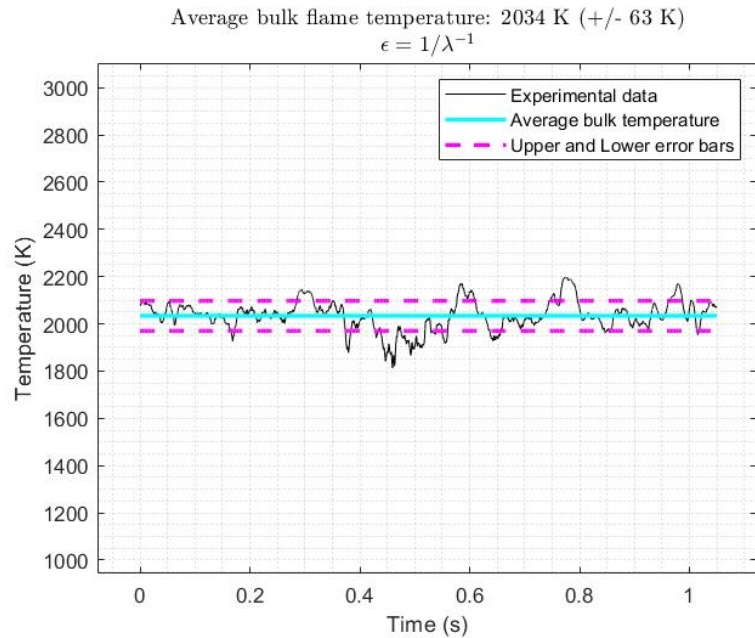


Figure 4.6: Bulk flame temperature history measured with the pyrometer at 6.89MPa of H-10 composition with $\epsilon_\lambda = 1/\lambda^{-1}$ with the standard deviation of all the measurements being considered.

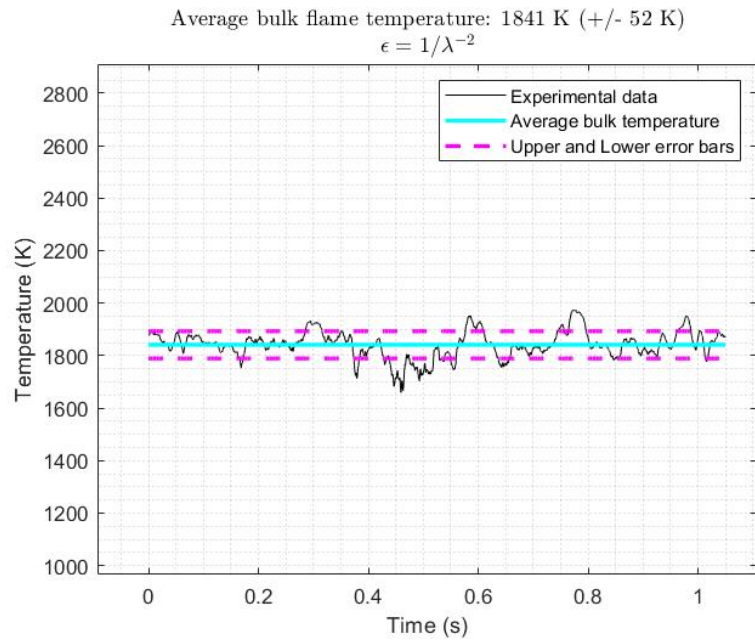


Figure 4.7: Bulk flame temperature history measured with the pyrometer at 6.89MPa of H-10 composition with $\epsilon_\lambda = 1/\lambda^{-2}$ with the standard deviation of all the measurements being considered.

Figure 4.8 to 4.10 show the bulk flame temperature histories measured with the spectrometer at 6.89 MPa for the same H-10 composition strand burner test. Although the temperatures are closer to the expected range, it was observed that the spectrometer was reading higher light intensity values for the 700 nm λ compared to the 1000 nm λ . During experimental testing, it was observed that the misalignment of the collimator had a larger effect on the measurements from the spectrometer than the pyrometer. This is believed to have caused the higher temperature measurements observed by the spectrometer.

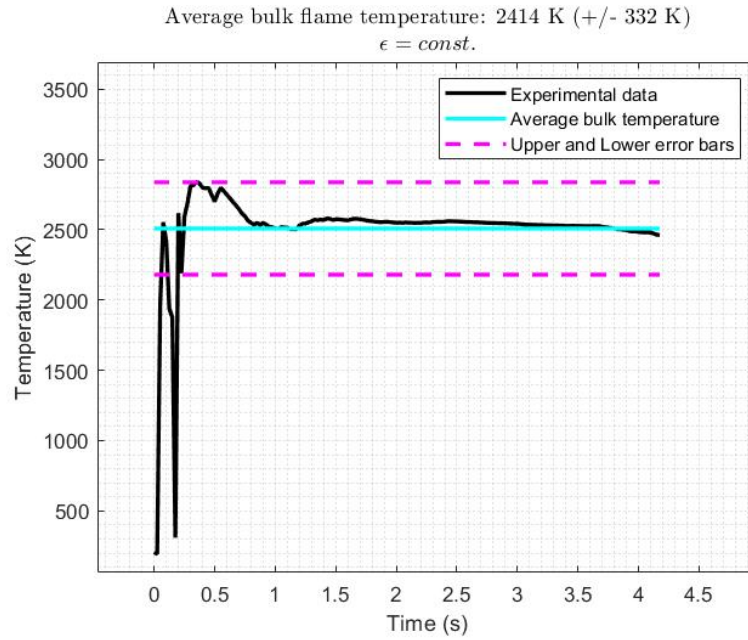


Figure 4.8: Bulk flame temperature history measured with the spectrometer at 6.89MPa (1000 psi) of H-10 composition with $\epsilon_\lambda = \text{const.}$ with the standard deviation of all the measurements being considered.

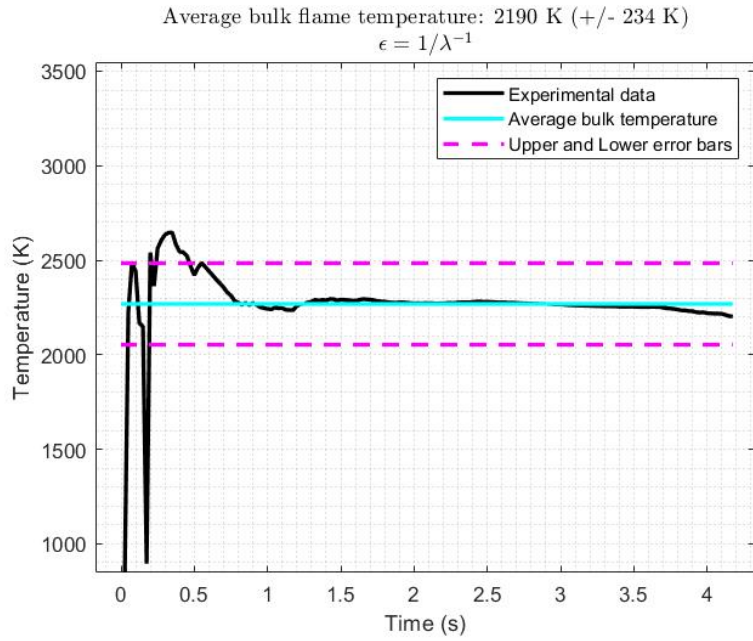


Figure 4.9: Bulk flame temperature history measured with the spectrometer at 6.89MPa (1000 psi) of H-10 composition with $\epsilon_\lambda = 1/\lambda^{-1}$ with the standard deviation of all the measurements being considered.

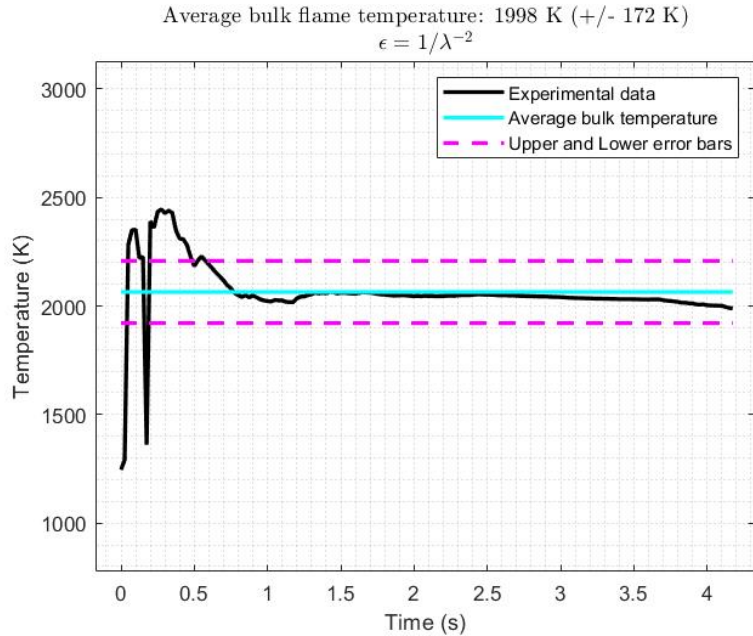


Figure 4.10: Bulk flame temperature history measured with the spectrometer at 6.89MPa (1000 psi) of H-10 composition with $\epsilon_\lambda = 1/\lambda^{-2}$ with the standard deviation of all the measurements being considered.



Figure 4.11: Sequential images in time of a strand burn test show variations in light intensities from $t = 0$ to $t = 22$ s.

Table 4.4 provides a summary of burn rate measurements at their respective operating pressures and the variance between the four-color pyrometer and spectrometer bulk flame temperature measurement measured in the burn rate analysis, respectively. The burn rate r is shown with the average standard deviation calculated for each individual pressure range for each individual. The assumption for when $\varepsilon_\lambda = \text{const.}$ consistently measured the highest bulk flame temperature compared to the $\varepsilon_\lambda = 1/\lambda^{-1}$ and $\varepsilon_\lambda = 1/\lambda^{-2}$. This trend is expected, as shown by others [18], and is due to the additional term in Equation 3.4 that reduces the temperatures since the emissivity is dropping with increasing wavelength. In other words, at larger wavelengths, the emissivity becomes significantly smaller when it follows the λ^{-2} dependence compared to the λ^{-1} . Overall, the pyrometer measured bulk flame temperatures that were nominally 39% different than the predicted, while the spectrometer ranged from 8-39% for both compositions.

The standard deviations in the bulk flame temperature measurements for the spectrometer and pyrometer are large. The error in the measurements can be attributed to the closed-volume design of the strand burner, which does not continuously vent the combustion products. Figure 4.11 provides sequential images in time of a strand burning test that shows the internal environment from ignition to extinction. The pyrometer and spectrometer were triggered around $t = 12$ s. Visible combustion products are seen condensing and filling the internal volume of the strand burner, absorbing some of the radiated light. This is assumed to be causing the light intensity to decrease as the burn progresses, causing the pyrometer to measure lower bulk flame temperatures when compared to the spectrometer. This could potentially have affected the measured light intensities from the spectrometer, in addition to the error caused by misalignment in the collimator.

Table 4.4: Summary of results of burn rate r and four-color pyrometer and spectrometer data, top and bottom measurements, respectively, with the standard deviation from the average bulk flame temperatures for both compositions.

	P_{avg} MPa	r mm/s	$\varepsilon_\lambda = const.$	$\varepsilon_\lambda = 1/\lambda^{-1}$	$\varepsilon_\lambda = 1/\lambda^{-2}$
H-10	3.78 ± 0.09	3.78 ± 0.24	1838 ± 220 K	1679 ± 182 K	1546 ± 154 K
			1846 ± 568 K	1723 ± 460 K	1608 ± 381 K
	5.44 ± 0.13	4.44 ± 0.21	1862 ± 91 K	1670 ± 75 K	1563 ± 63 K
H-3	7.23 ± 0.26	5.27 ± 0.38	2288 ± 633 K	2049 ± 523 K	1855 ± 273 K
			2271 ± 79 K	2034 ± 63 K	1841 ± 52 K
	3.71 ± 0.07	4.81 ± 0.17	2414 ± 332 K	2190 ± 234 K	1998 ± 172 K
	5.43 ± 0.08	5.48 ± 0.25	1863 ± 342 K	1704 ± 281 K	1571 ± 234 K
			2758 ± 562 K	2414 ± 451 K	2137 ± 361 K
	7.26 ± 0.11	6.16 ± 0.30	1856 ± 529 K	1718 ± 441 K	1594 ± 370 K
	2565 ± 827 K	2253 ± 632 K	2253 ± 632 K	2009 ± 493 K	
			1931 ± 95 K	1758 ± 80 K	1613 ± 69 K
	2820 ± 1024 K	2480 ± 786 K	2480 ± 786 K	2205 ± 651 K	

4.2 Combustion Performance Analysis of 76 mm SRMs

4.2.1 76 mm burn rate analysis

Burn rate analysis was conducted on several 76 mm BATES grain geometry SRMs using the mass balance method and thickness/time methods described in Section 1.2. There were three tests conducted across a range of pressures for both H-10 and H-3 compositions to assess the repeatability of the burns. An additional two tests were conducted at 6.89 MPa for the H-10 composition.

Figures 4.12 to 4.14 show pressure versus time of experimental and theoretical curves at 3.45, 5.17, and 6.89 MPa of the APCP SRMs with H-10 aluminum power, respectively. Figure 4.15 shows a graph of the APCP SRM using H-3 aluminum power at 6.89 MPa. All tests took longer than expected to reach their operating pressure and thrust. Direct image footage observed that the time between the first instance of smoke exiting the nozzle and the instant at which a flame ejected from the nozzle was nominally 1 s. At 3.45 MPa, the predicted conditions are lower than the experimental, which was initially assumed to be signs of slag deposition within the nozzle.

The combustion process is said to be neutral if the average pressure P_{avg} remains within 15% of the expected pressure within the steady-state [3, 8]. Table 4.5 shows the percent difference between the predicted and experimental pressure profiles. Only a single motor fire surpasses the criteria, which is the first shown for the predicted pressure of 6.89 MPa, whose average is 18% different from the predicted. All other static firing falls within the corridor specified for a neutral burning profile.

Table 4.5: Percent difference of the average chamber pressure between predicted and experimental data.

	Predicted	Experimental	Percent Difference
	P_{avg} MPa	P_{avg} MPa	- % diff.
H-10	3.47	3.86	11
	5.10	4.33	15
	6.89	5.64	18
	6.89	6.23	10
	6.89	5.89	15
	3.47	3.88	12
H-3	5.10	5.22	2
	6.89	6.01	13

A better agreement with the predicted could be achieved through an improved ignition system that provides 10% of the maximum pressure for optimal ignition. It was also observed that the experimental burn times were nominally 400, 600, and 800 ms longer than predicted for the 3.45, 5.17, and 6.89 MPa motor firing, respectively. Nozzle deposition of Al slag is also assumed to have caused the progressive behavior in all motor firings. Since the 3.45 MPa had a cooler chamber temperature, it experienced a higher deposition of slag within the nozzle throat, causing the experimental pressure and thrust to be higher than predicted. In Figures 4.13 to 4.14, the chamber temperatures are assumed to have increased, which caused less deposition with the nozzle, hence the decrease observed in the experimental data.

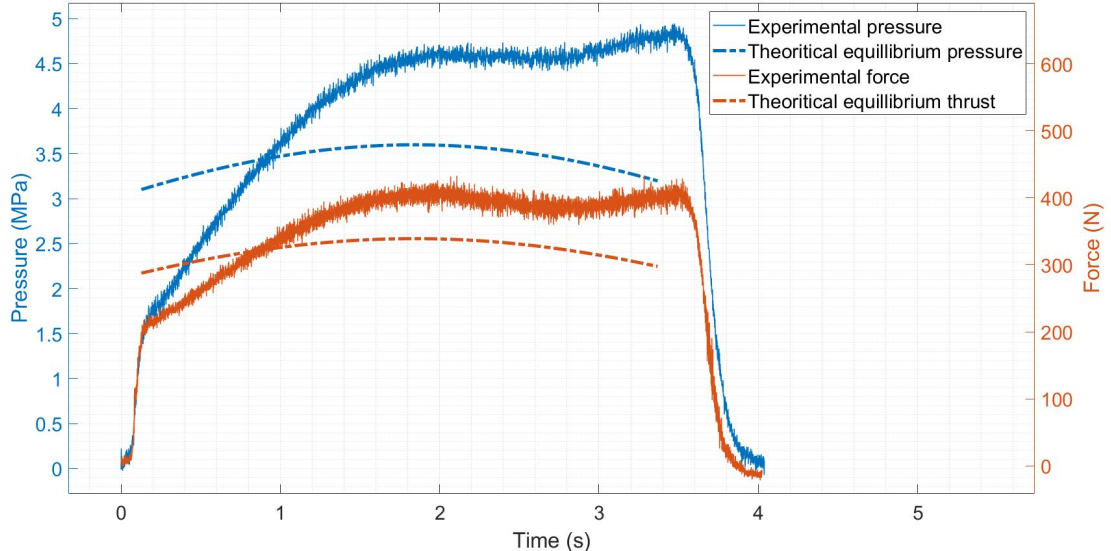


Figure 4.12: Experimental and theoretical pressure and thrust curves as a function of time for the BATES SRM with H-10 aluminum powder a nominal 3.45 MPa chamber pressure.

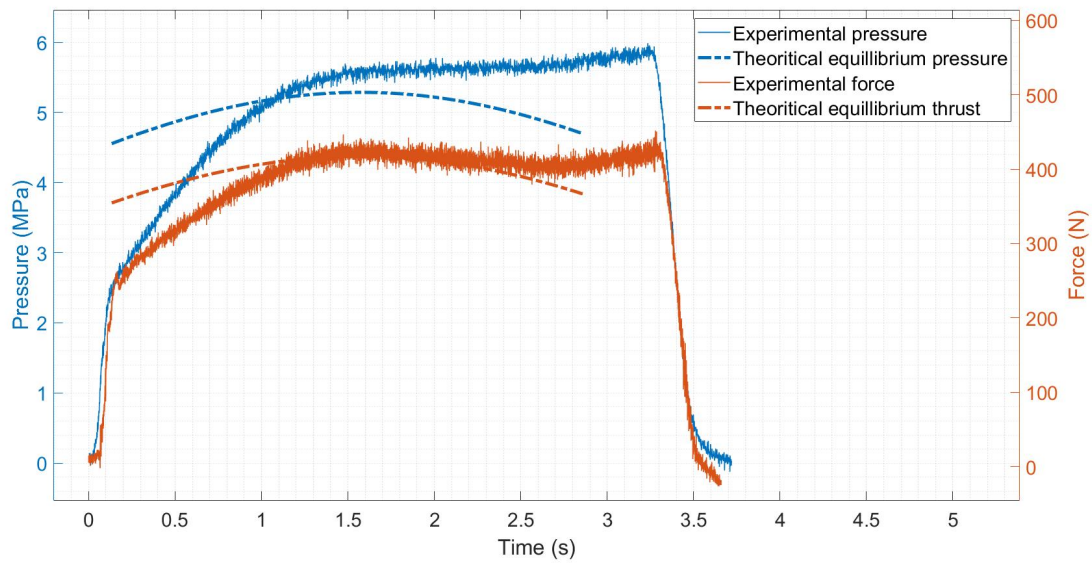


Figure 4.13: Experimental and theoretical pressure and thrust curves as a function of time for the BATES SRM with H-10 aluminum powder a nominal 5.17 MPa chamber pressure.

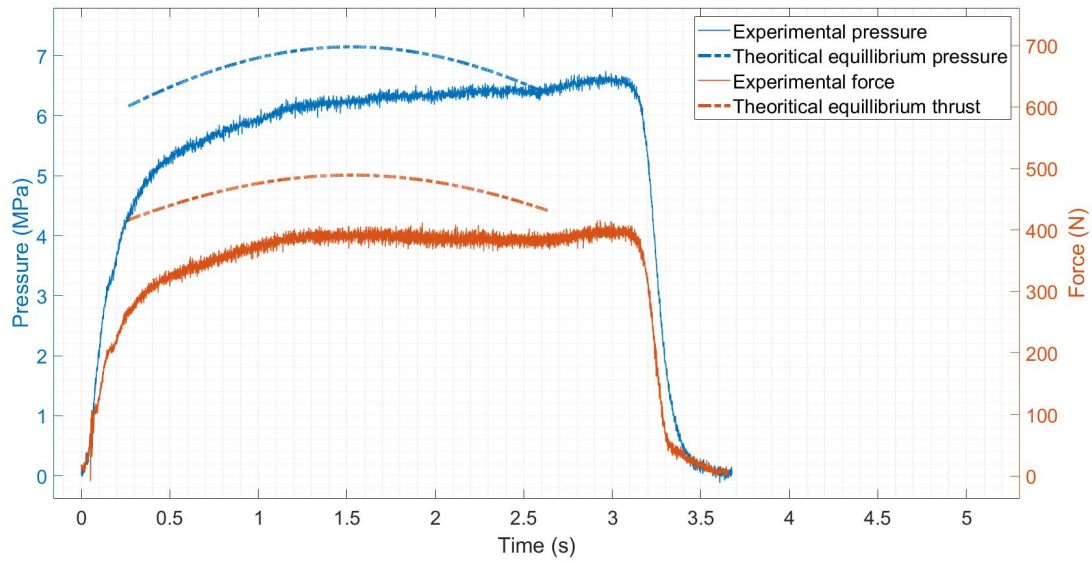


Figure 4.14: Experimental and theoretical pressure and thrust curves as a function of time for the BATES SRM with H-10 aluminum powder a nominal 6.89 MPa chamber pressure.

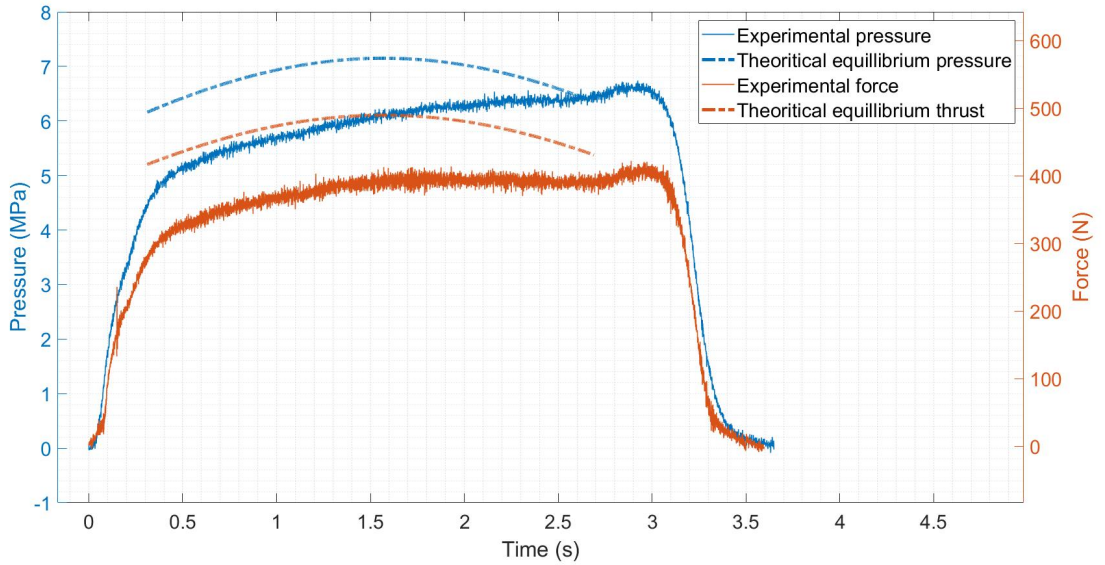


Figure 4.15: Experimental and theoretical pressure and thrust curves as a function of time for the BATES SRM with H-3 aluminum powder a nominal 6.89 MPa chamber pressure..

4.2.2 Burn rate analysis comparison

The a and n values used to model all SRMs were 2.862 and 0.45, respectively. Figures 4.16 to 4.17 show the expected power law relation of burn rate and pressure determined from the strand burner (r_{SB}), mass balance (r_{MB}), and thickness/time (r_{TOT}) burn rate analysis methods with their corresponding a and n shown.

In Figure 4.16, the measured burn rate r_{SB} lies between r_{MB} and r_{TOT} . These results were not expected given that large-scale SRMs always have higher burn rates than small-scale testing [3, 8]. However, the commercial pyrogen igniters used in this work appear to be causing large ignition delay times preventing nominal ignition. As discussed in Section 1.2, an assumed 7.5% of the average pressure was chosen for points **B** and **G**, refer to Figure 1.2. However, this percentage was only assumed because a fixed percentage must be chosen to use Equation 1.2 and Equation 1.3. That being said, during ground testing, no pressure rise was ever observed purely due to the igniters. Conventional designs ensure the igniter provides at least 10% of the operating pressure to ensure the ignition process occurs rapidly [3]. The ignition times (t_{ig}) observed during static testing ranged from 500 – 1000 ms. These ignition times, although long in duration, provided no such pressure rise, causing the non-nominal flame to spread within the motor. This non-nominal flame spread is believed to have caused the pressure lag seen in all motor firings resulting in the lower chamber temperatures and Al slag deposition in the nozzles.

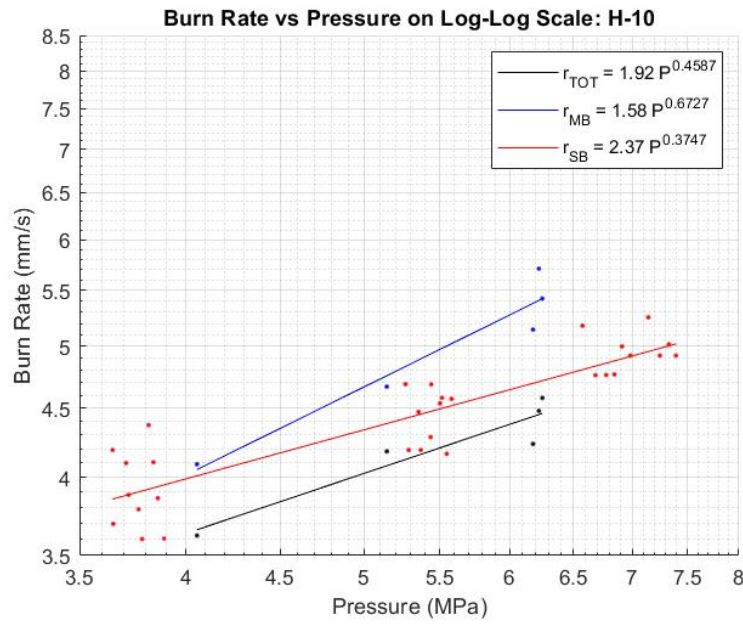


Figure 4.16: Power law relation between burn rate and pressure determined from the strand burner, mass balance, and thickness/time applied to the BATES grain and the strand burner testing of the H-10 composition.

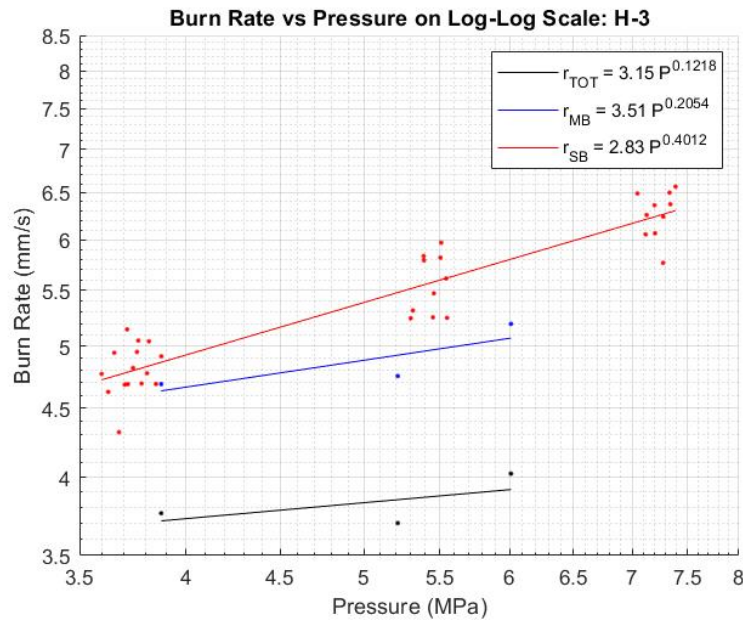


Figure 4.17: Power law relation between burn rate and pressure determined from the strand burner, mass balance, and thickness/time applied to the BATES grain and the strand burner testing of the H-3 composition.

Comparing the burn rate r_{MB} and r_{TOT} methods, the r_{MB} always had higher measured values compared to r_{TOT} . As mentioned in Section 1.2, this was expected given that the r_{TOT} method does not account for non-instantaneous burnout [3]. As shown in Table 4.6 and Table 4.7, the r_{MB} method measured higher values than the r_{TOT} method from 10.5 to 21.5 % for the H-10 composition and 19.8 to 22.7 % for the H-3 composition. For future work, the optimization of these endpoints would be interesting to validate just how close the burn rate r_{MB} and r_{TOT} methods can be made to agree.

Table 4.6: Results for r_{MB} and r_{TOT} for H-10 composition.

Test	P_{avg} MPa	r_{MB} mm/s	r_{TOT} mm/s	$(r_{MB}-r_{TOT})/r_{MB} \times 100$ % diff.
Test 1	3.86	4.09	3.62	11.5
Test 2	4.33	4.67	4.18	10.5
Test 3	5.64	5.43	4.58	15.7
Test 4	6.23	5.71	4.48	21.5
Test 5	5.89	5.15	4.23	17.9

Table 4.7: Results for r_{MB} and r_{TOT} for H-3 composition.

Test	P_{avg} MPa	r_{MB} mm/s	r_{TOT} mm/s	$(r_{MB}-r_{TOT})/r_{MB} \times 100$ % diff.
Test 1	3.88	4.69	3.76	19.8
Test 2	5.22	4.75	3.70	22.1
Test 3	6.01	5.20	4.02	22.7

4.2.3 Nozzle correction factor

Slag build-up at the nozzle throat was observed during the static SRM tests. This buildup results in a reduced nozzle throat diameter throughout the test. This was accounted for by introducing a correction factor to the theoretical model. Given the radius of the throat (r_t) and the thickness of the slag (δ), the new effective radius is then:

$$r^* = r_t - \delta \quad (4.3)$$

The new effect throat area is then given by:

$$A^* = \pi \cdot r^{*2} \quad (4.4)$$

Results for the 3.45 - 6.89 MPa for the H-10 composition are shown in Figure 4.18 - 4.23 that introduce the correction factor. Table 4.8 lists the slag thickness δ , nozzle throat diameter D_t , and the effective diameter D^* .

Table 4.8: Measure slag thickness (δ) and throat diameter (D_t) with their calculated effective diameter (D^*) for H-10 and H-3 compositions with their respective uncertainties determined from the tolerances of the measuring devices used.

Aluminum Series	Pressure MPa	δ mm	D_t mm	D^* mm
H-10	3.45	0.6985 ± 0.0005	8.86 ± 0.03	7.46 ± 0.03
	5.17	0.6640 ± 0.0005	8.05 ± 0.03	6.722 ± 0.03
	6.89	0.5080 ± 0.0005	7.44 ± 0.03	6.42 ± 0.03
	6.89	0.4699 ± 0.0005	7.44 ± 0.03	6.50 ± 0.03
		0.4826 ± 0.0005	7.44 ± 0.03	6.47 ± 0.03
H-3	3.45	0.6477 ± 0.0005	8.86 ± 0.03	7.56 ± 0.03
	5.17	0.4572 ± 0.0005	8.05 ± 0.03	7.14 ± 0.03
	6.89	0.4826 ± 0.0005	7.44 ± 0.03	6.47 ± 0.03

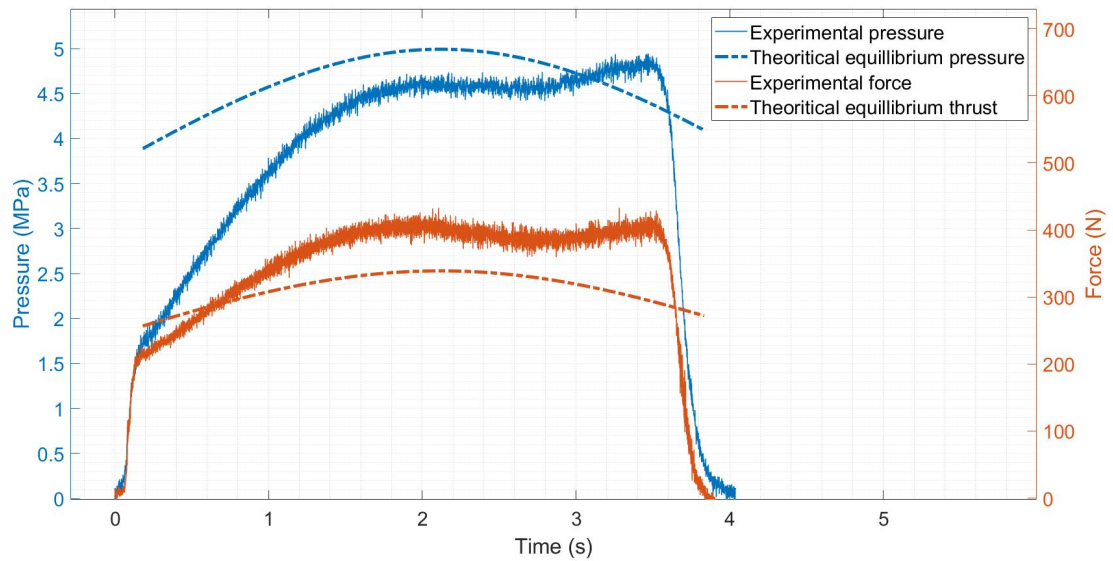


Figure 4.18: Experimental pressure and thrust histories with a model that uses a correction factor for slag buildup and the coefficient measured from the r_{MB} method for the H-10 composition intended for 3.45 MPa.

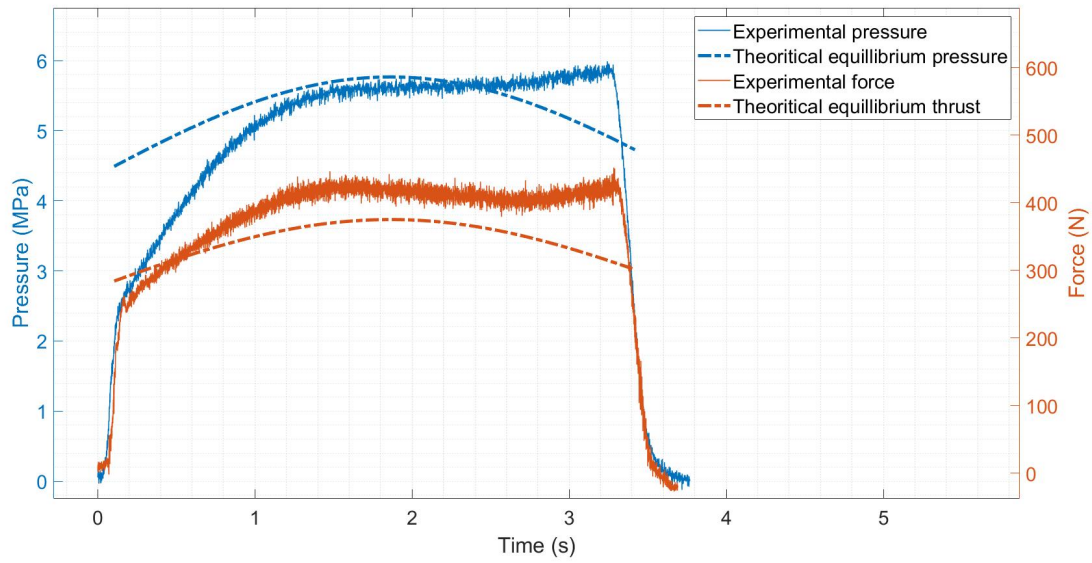


Figure 4.19: Experimental pressure and thrust histories with a model that uses a correction factor for slag buildup and the coefficient measured from the r_{MB} method for the H-10 composition intended for 5.17 MPa.

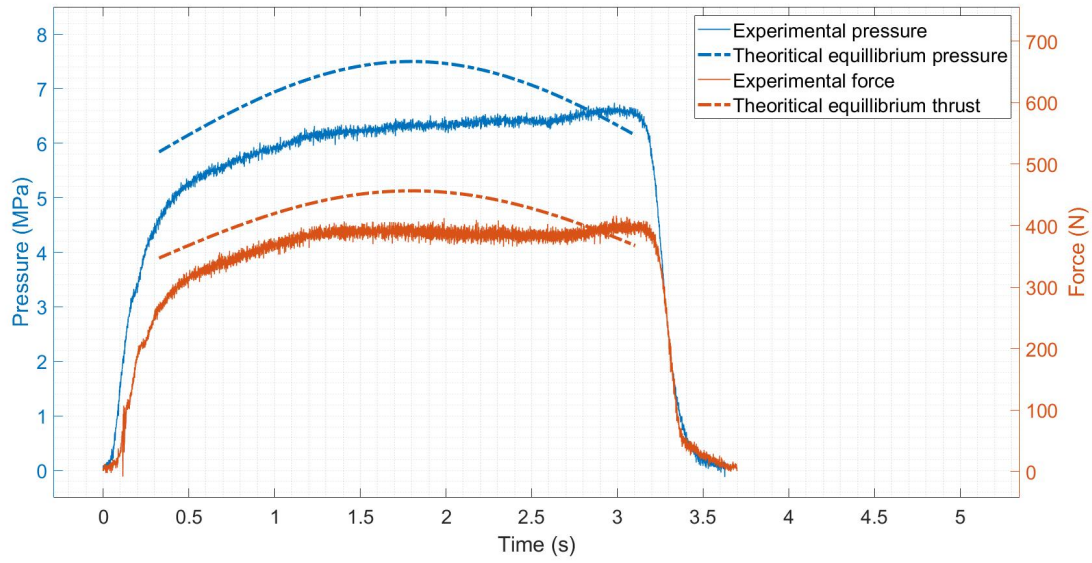


Figure 4.20: Experimental pressure and thrust histories with a model that uses a correction factor for slag buildup and the coefficient measured from the r_{MB} method for the H-10 composition intended for 6.89 MPa.

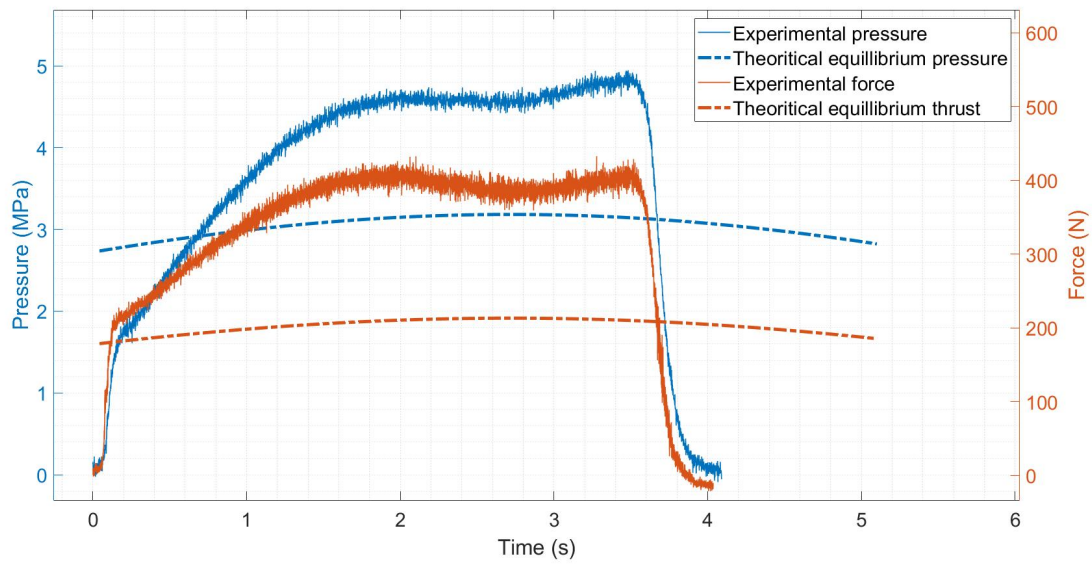


Figure 4.21: Experimental pressure and thrust histories with a model that uses a correction factor for slag buildup and the coefficient measured from the r_{TOT} method for the H-10 composition intended for 3.45 MPa.

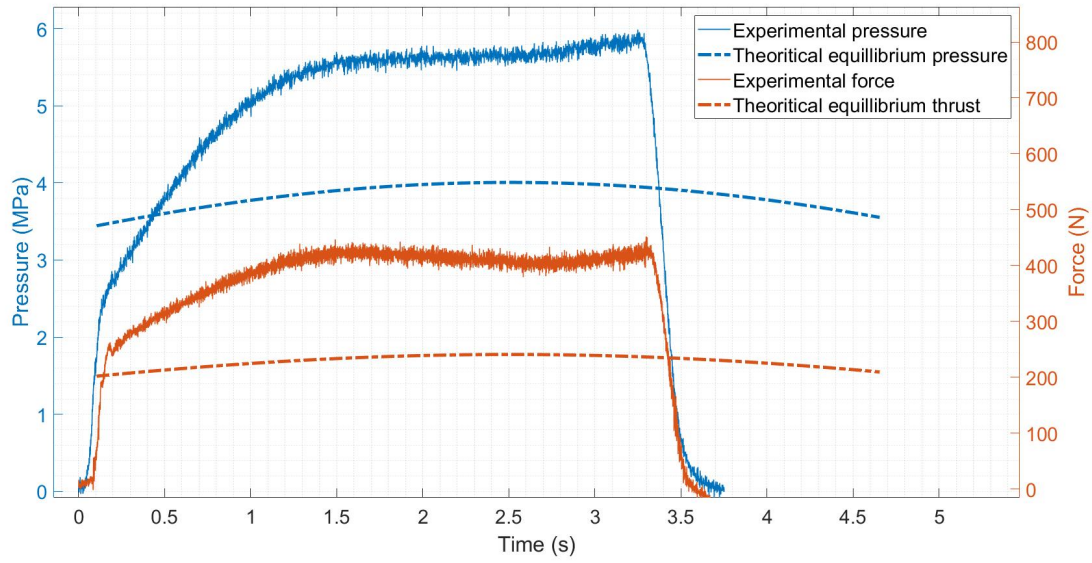


Figure 4.22: Experimental pressure and thrust histories with a model that uses a correction factor for slag buildup and the coefficient measured from the r_{TOT} method for the H-10 composition intended for 5.17 MPa.

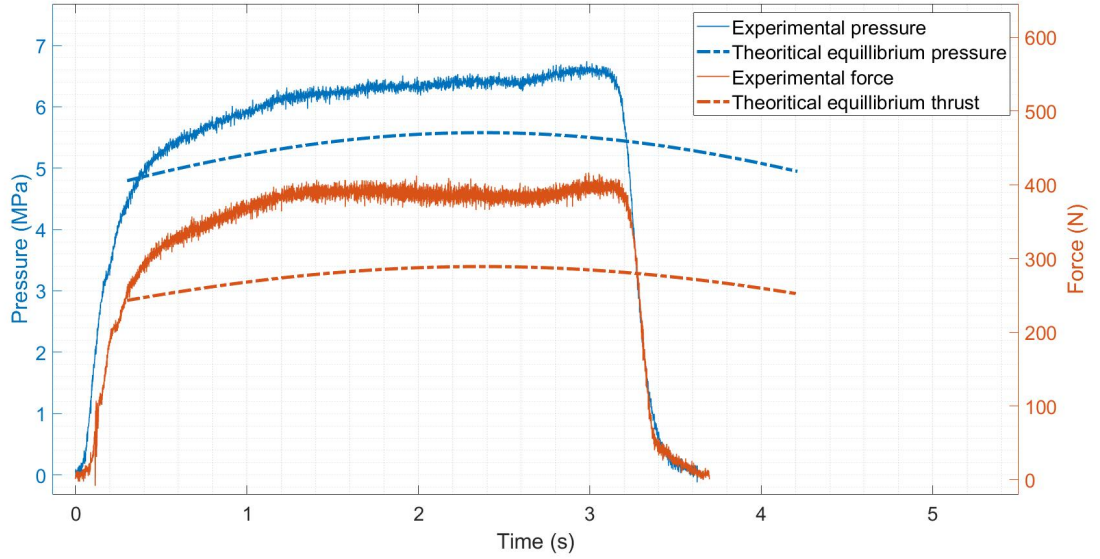


Figure 4.23: Experimental pressure and thrust histories with a model that uses a correction factor for slag buildup and the coefficient measured from the r_{TOT} method for the H-10 composition intended for 6.89 MPa.

Table 4.9: Percent difference of the average chamber pressure between predicted and experimental data with correction factor due to slag buildup and using a and n values determined through the r_{MB} method.

	Predicted	Experimental	Percent Difference
	P_{avg} MPa	P_{avg} MPa	- % diff.
H-10	4.5	3.86	14
	5.0	4.33	13
	6.70	5.64	16
	6.70	6.23	7
	6.70	5.89	12
	4.5	3.88	14
H-3	5.0	5.22	4
	6.70	6.01	9

One can immediately note that the r_{MB} is producing predicted pressure and thrust curves that closely match the experimental data compared to the r_{TOT} method if referencing the original date from Figures 4.12 - 4.14. After using the mass balance method and the correction factor, the percent difference was calculated to determine the error between the predicted and experimental pressure profiles. Table 4.9 shows in general, the

error between all tests was reduced. For both H-10 and H-3, the previously anticipated pressure for the 3.47 MPa was increased to 4.5 MPa. Although the percent error in the average pressure increased, burn times which varied from 400, 600, and 800 ms longer than predicted for the 3.45, 5.17, and 6.89 MPa motor firing, respectively, are shown to have decreased to nominally 100 ms for all pressure ranges.

The average pressure for some of the predicted operating pressures was found to decrease, specifically for the higher pressure ratio, excluding the H-3 test for nominally 5.22 MPa, which was shown to increase by 2%. The H-10 test with an average pressure of 5.64 MPa decreased in error by 2.2%, but the final difference was still above the allowed 15%.

4.2.4 Experimental performance parameters

Theoretical performance parameters acquired through NASA CEA are listed in Table 4.10 for the operating conditions of interest. The chamber pressure (P_c) and exit temperature (T_e) were measured using a pressure transducer and non-intrusive diagnostic techniques. The total impulse I_t was determined by the integration of the force measurements with respect to time within the steady-state region. The relation for specific impulse (I_{sp}) with I_t was then used to determine the I_{sp} for all motor firings.

Table 4.10: Theoretical rocket parameters for 3.45, 5.17, and 6.89 MPa from NASA CEA

Operating Pressure MPa	T_e K	I_{sp} s
3.45	1746	243
5.17	1621	253
6.89	1536	259

Table 4.11: Experimental rocket performance parameters of the APCP SRM with H-10 aluminum composition.

Operating Pressure MPa	P_{avg} MPa	F_{avg} N	I_{sp} s
3.45	3.58	307	236
5.17	4.33	295	204
6.89	5.64	385	239
6.89	6.23	364	224
6.89	5.89	311	221

Table 4.12: Experimental rocket performance parameters of an APCP SRM with H-3 aluminum composition.

Operating Pressure MPa	P_{avg} MPa	F_{avg} N	I_{sp} s
3.45	3.4	285	199
5.17	4.85	349	220
6.89	5.99	361	226

All measured values of the experimental data for each composition are presented in Tables 4.11 and 4.12 for H-10 and H-3 compositions, respectively. Many of the theoretical parameters are expected to decrease relative to the theoretical due to the variance of the residence times of aluminum fuel within the chamber, as well as the limitations of the energy release encountered from the formation and ejection of agglomerates of aluminum.

Previous work conducted by Newman et al. [12] experimentally determined the specific impulse of an aluminized APCP at 6.89 MPa (1000 psi) to be 238 s in a 127 mm (5 in) diameter motor. The average I_{sp} for the three repeated tests at 6.89 MPa found in this work was 228 s. The experimental values are within 4% of that found by Newman. Other reported values for I_{sp} of aluminized APCPs range from 260 - 265 s for operational solid propellants used in large boosters [2]. These values found in Sutton are measured from much larger SRMs, such as the solid rocket boosters on the ATLAS V, which have a 3.8 m (12 ft) diameter and 32.5 m (107 ft) length. The small-scale effects seen in this work result in about a 14% difference between the theoretical and those measured in SRMs such as the ATLAS V.

4.2.5 Bulk flame temperature measurements

Temperature measurements were experimentally determined as described in Section 3.3, and the analysis was performed as discussed in Section 4.1.2 for all static fire tests. The results at 6.89 MPa are presented and shown in Figures 4.24 - 4.27 for the H-10 composition. The black line is the calculated bulk flame temperature which nominally remains within its error bars. The wavelength corresponding to each pyrometer channel is graphed. Note that the pyrometer has the highest light intensity values for the 1000 nm λ . The theoretical value for T_e was determined by CEA to be 1536 K. The measured value at 6.89 MPa using the four-color pyrometer was determined to be 1447 ± 98 K, falling within 6% of the predicted value determined by NASA CEA.

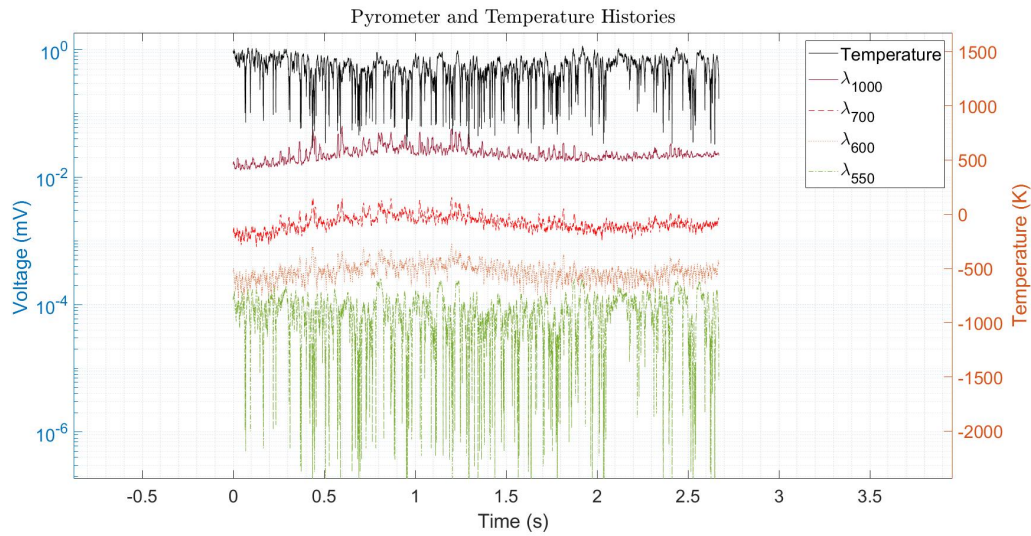


Figure 4.24: Bulk flame temperature history plotted with pyrometer data at 6.89 MPa (1000psi) of an H-10 composition.

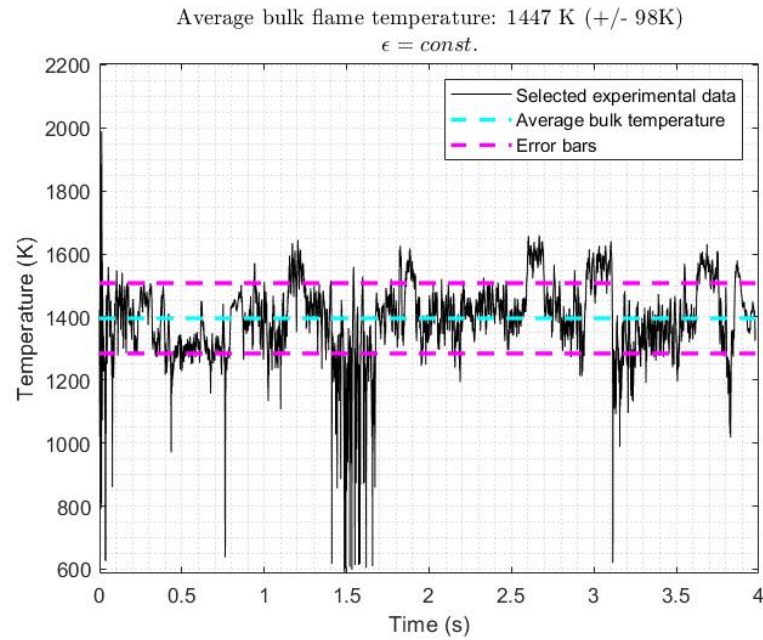


Figure 4.25: Bulk flame temperature history measured with pyrometer at 6.89MPa (1000 psi) of H-10 composition $\epsilon_\lambda = \text{const.}$

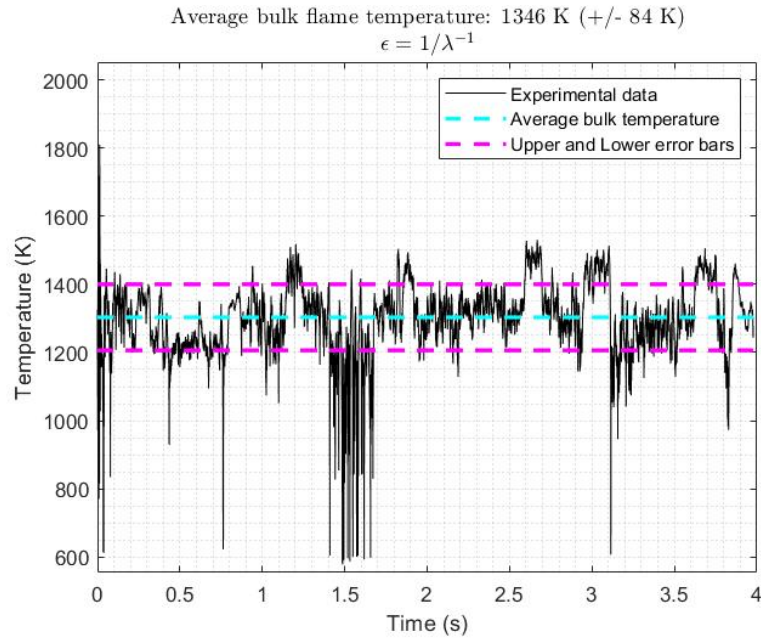


Figure 4.26: Bulk flame temperature history measured with pyrometer at 6.89MPa (1000 psi) of H-10 composition $\epsilon_\lambda = 1/\lambda^{-1}$.

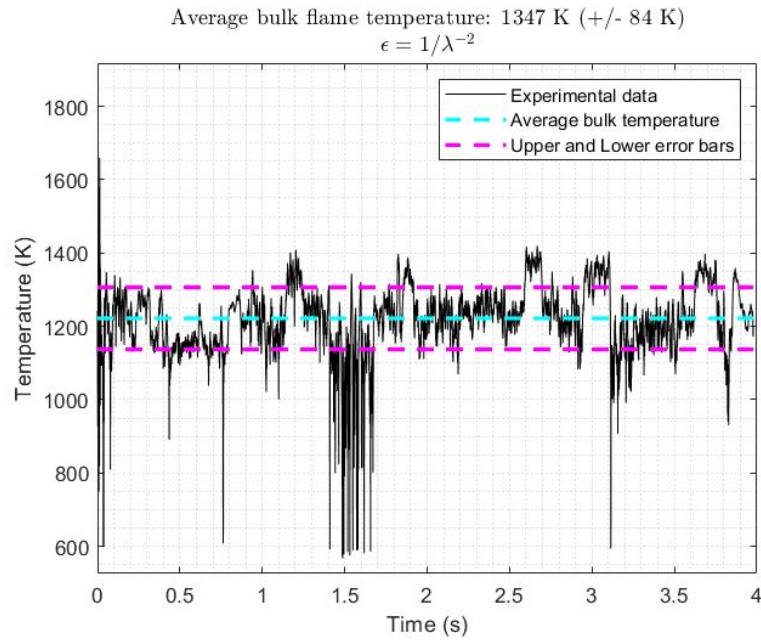


Figure 4.27: Bulk flame temperature history measured with pyrometer at 6.89MPa (1000 psi) of H-10 composition $\epsilon_\lambda = 1/\lambda^{-2}$.

The bulk flame temperature found using the spectrometer was found to vary from approximately 2500 to 2600 K. The spectrometer was consistently getting much higher

temperatures that were not expected at the exit for any of the operating pressures. By varying the emissivity in Equation 3.4, the temperatures were observed to approach the theoretical values. Note that the 700 nm and 650 nm wavelengths have higher values of light intensities, which correspond to the higher measured temperatures. The thermal radiation emitted by aluminum slag exiting the nozzle could also affect the true measurements of the exhaust plume.

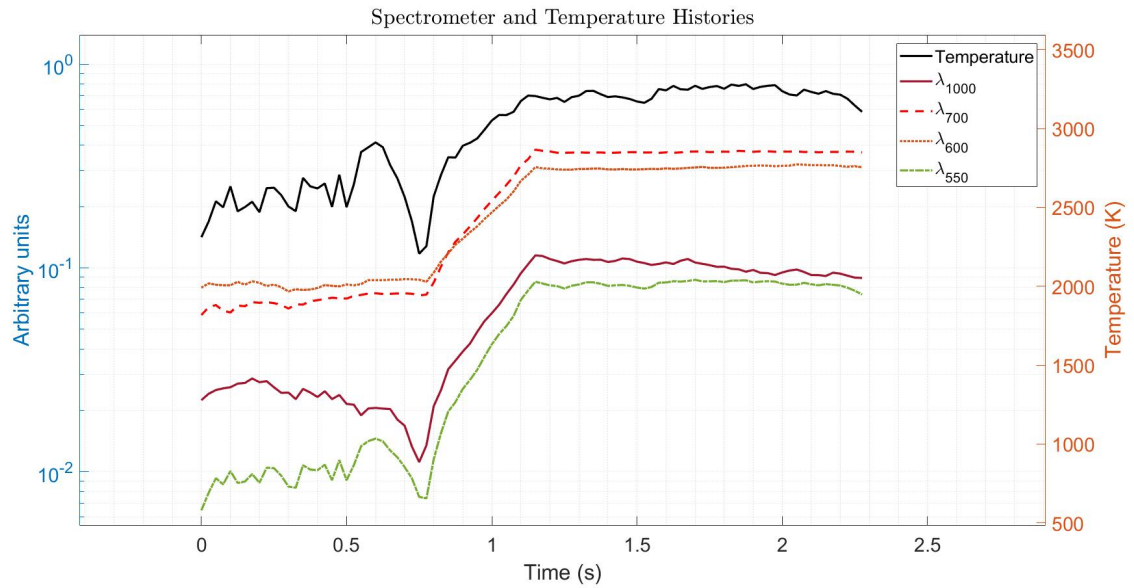


Figure 4.28: Bulk flame temperature history plotted with spectrometer data at 6.89 MPa (1000psi) of an H-10 composition.

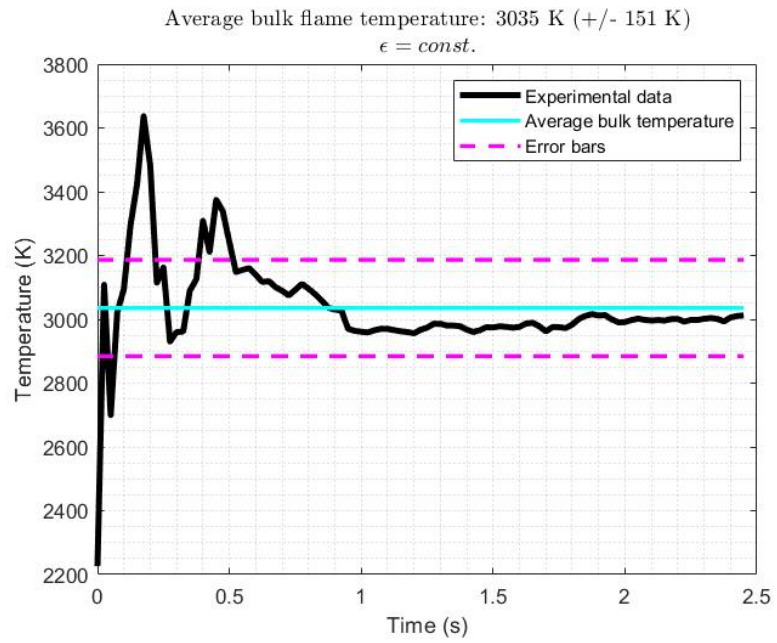


Figure 4.29: Bulk flame temperature history measured with spectrometer at 6.89MPa (1000 psi) of H-10 composition $\varepsilon_\lambda = \text{const.}$

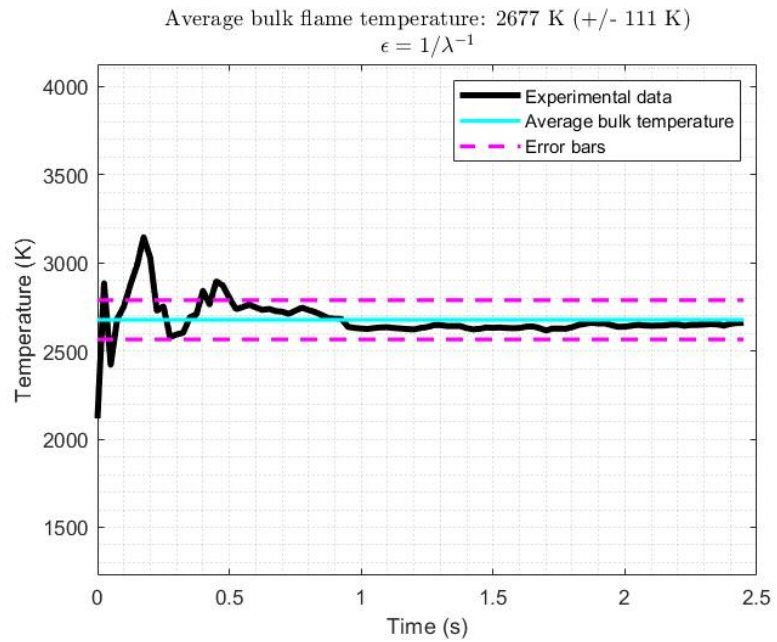


Figure 4.30: Bulk flame temperature history measured with spectrometer at 6.89MPa (1000 psi) of H-10 composition $\varepsilon_\lambda = 1/\lambda^{-1}$.

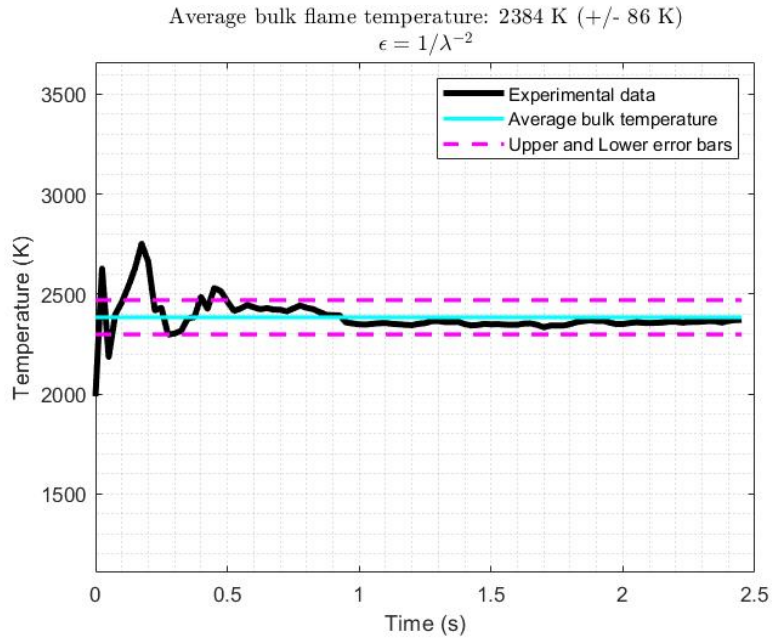


Figure 4.31: Bulk flame temperature history measured with spectrometer at 6.89MPa (1000 psi) of H-10 composition $\epsilon_\lambda = 1/\lambda^{-2}$.

Table 4.13: Experimental results with the standard deviation from the average temperature (T_{avg}) measured from a four-color pyrometer at the nozzle exit for an APCP composition with H-10 aluminum powder.

		3.45 MPa	5.17 MPa	6.89 MPa	6.89 MPa	6.89 MPa
$\epsilon_\lambda = const.$	T_{avg} (K)	1267	1263	1324	1447	1336.46
	$\Delta (\pm K)$	89	96	120	98	153
$\epsilon_\lambda = 1/\lambda^{-1}$	T_{avg} (K)	1192	1187	1241	1346	1251
	$\Delta (\pm K)$	78	84	105	84	117
$\epsilon_\lambda = 1/\lambda^{-2}$	T_{avg} (K)	1124	1120	1167	1347	1176
	$\Delta (\pm K)$	69	74	93	84	117

Table 4.14: Experimental results with the standard deviation from the average temperature (T_{avg}) measured from a four-color pyrometer at the nozzle exit for an APCP composition with H-3 aluminum powder.

		3.45 MPa	5.17 MPa	6.89 MPa
$\epsilon_\lambda = const.$	T_{avg} (K)	1193	1249	1393
	$\bar{\Delta}$ (\pm K)	133	188	110
$\epsilon_\lambda = 1/\lambda^{-1}$	T_{avg} (K)	1126	1174	1300
	$\bar{\Delta}$ (\pm K)	117	165	956
$\epsilon_\lambda = 1/\lambda^{-2}$	T_{avg} (K)	1066	1108	1209
	$\bar{\Delta}$ (\pm K)	103	145	83

Table 4.15: Experimental results with the standard deviation from the average temperature (T_{avg}) measured from a spectrometer at the nozzle exit for the APCP composition with H-10 aluminum powder.

		3.45 MPa	5.17 MPa	6.89 MPa	6.89 MPa	6.89 MPa
$\epsilon_\lambda = const.$	T_{avg} (K)	2683	2716	3035	2615	2552
	$\bar{\Delta}$ (\pm K)	140	81	151	67	83
$\epsilon_\lambda = 1/\lambda^{-1}$	T_{avg} (K)	2356	2383	2677	2305	2256
	$\bar{\Delta}$ (\pm K)	111	66	54	111	62
$\epsilon_\lambda = 1/\lambda^{-2}$	T_{avg} (K)	2101	2123	2384	2061	2022
	$\bar{\Delta}$ (\pm K)	90	54	43	86	48

4.3 Discussion

Burn rate analysis for determining a and n of the APCP compositions with varying aluminum particle size with in-situ flame temperature measurements nominally found the H-3 composition to have higher burn rates (Table 4.4), for the small scale analysis performed using a strand burner. The burn rate was calculated from experimental static fire tests of 76 mm BATES grains at 3.45, 5.17, and 6.89 MPa (500, 750, and 1000psi) operating pressures using the average mass balance and thickness/time methods. All three burn rate analysis methods found similar values to those found in the literature, which range from 1.0 to 3.0 and 0.4 to 0.6, respectively, for aluminized APCP [1].

The deviation in the experimental and predicted profile curves for both compositions was observed. The experimental burn times were longer by about 400, 600, and 800 ms for the 3.45, 5.17, and 6.89 MPa pressures, respectively. Comparison between the power law relation for the burn rate pressure dependence of all three methods, shown in Figure 4.16 and 4.17, would suggest the r measured in the strand burner is higher; however, further analysis suggests the ignition system that was incorporated into the design for this work was inadequate causing ignition delays on average of $t_{ig} = 300\text{ms}$. This ignition delay consumed propellant, causing non-nominal surface regression, as can be observed by the pressure and thrust profiles.

Future work would suggest an igniter capable of providing the required heat flux to ensure the ignition system aids propellant ignition. Hump effects are also attributed to slag build-up at the nozzle throat. The correction factor that was introduced, along with the a and n measured with the r_{MB} method, lowered the percent difference between the average pressure between predicted and experimental while also decreasing the error in the burn times to within 4 %. The variation in experimental rocket performance parameters (Table 4.11) fell with 4% from an experimental test conducted by Newman et al. [12], for an aluminized solid propellant which also used 10% aluminum. Small-scale effects, such as a reduction in residence times of the aluminum and lower chamber temperatures, are assumed to have caused these differences.

Bulk flame temperature measurements observed varied between the two diagnostic methods. During strand burning, the pyrometer suffered losses due to the reduction of light caused by the condensing species within the stand burner. The spectrometer measured values within the expected range of 2600 - 3000 K; however, the discrepancy in the peak wavelength is expected to have been caused by experimental error during setup. The experimental results of the SRM nozzle exit temperatures for both diagnostic systems did not agree with each other (Tables 4.15 to 4.14); however, the pyrometer did provide measured bulk flame temperatures that were nominally within 39% and ranged from 9 to 32% for the strand burner and static tests respectively.

CHAPTER 5

EXPERIMENTAL METHODS FOR DETERMINING MECHANICAL PROPERTIES OF APCP USING 3D-DIC

The mechanical response of two ammonium perchlorate composite propellants (APCPs) with varying aluminum particle sizes of 3 μm and 10 μm were measured using a Mark-10 test stand and a 3D digital image correlation (DIC) system under uniaxial loading. Preliminary testing was conducted at 0.5, 5, and 20 mm/s to determine whether the material would respond consistently regardless of the strain rate. After concluding the strain response was independent of strain rate, all samples were uniformly tested at 0.5 mm/s. Several tensile sample geometries were cast into shape and tested under uniaxial loading. Conventional geometries used for consistency and reproducibility tested in this work were the Joint-Army-Navy-NASA-Air Force (JANNAF) Type-C, MICRO, and ASTM D-338 Type III tensile geometries. In addition, a scaled-down version of the JANNAF geometry was developed to assess its performance in parallel, suggesting an alternative geometry for decreasing batch sizes or increasing total samples per batch.

5.1 Uniaxial Testing for Studying Mechanical Properties

The mechanical strength of APCP is limited in part by the strength of the polymer matrix due to its 3D structure and covalent bonds. Furthermore, the adhesion between the solid particles and the binder matrix plays a significant role in the mechanical strength [43]. The onset of failure of the particle-matrix interface, or dewetting, is the dominating factor in controlling the mechanical properties of APCP. Bonding agents such as amine and aziridine can be used to increase the adhesion between the solid particles and the polymer matrix [44]. In this work, no bonding agents were investigated. The main focus here is to determine the effects of tensile specimen size and if smaller specimens can provide as consistent data as that provided by the standard JANNAF sample size. Since particle-to-matrix failure plays such a significant role in the material properties of APCP, identifying when dewetting occurs in these smaller geometries could provide insight into how small the cross-section of propellant samples could be while providing accurate results.

Three-dimensional DIC and a Mark-10 test stand are used to experimentally determine the stress-strain response of APCP during uniaxial loading. The engineering stress (σ_{eng}) and strain (ε_{eng}) are determined by $\sigma_{eng} = F/A_o$ and $\varepsilon_{eng} = (L - L_o)/L_o$ respectively. The force F is applied to the cross-sectional area A_o for a sample with gauge length L_o deforming to length L . The mechanical properties of interest are Young's modulus (E) and Poisson's ratio (ν). Young's modulus is the slope of the linear portion of the stress-strain curve defined by $E = \sigma_d/\varepsilon_d$ where σ_d and ε_d are the dewetting stress and

strain, respectively. Poisson's ratio is the ratio of the transverse strains to the axial strain, $\nu = -d\epsilon_{trans}/d\epsilon_{axial}$, determined directly from DIC.

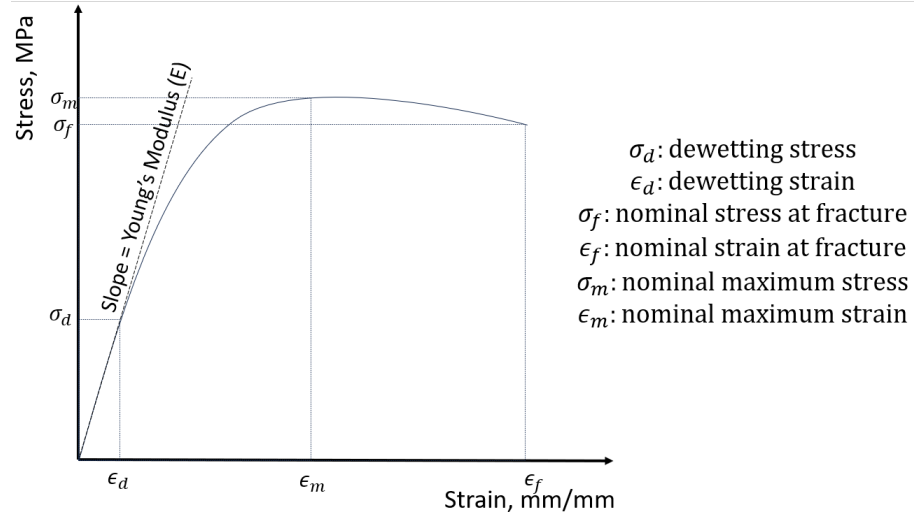


Figure 5.1: Schematic representation of the stress-strain response of composite materials adapted from [2].

5.2 Test Specimen Dimensions and Preparations

Tensile specimens of each composition were prepared in a single batch to limit any batch-to-batch variants. The only batch-to-batch variation was due to casting two separate batches for the H-10 and H-3 aluminum powders. The uncured propellant, or propellant slurry, was poured directly into a chem-cast acrylic mold. The molds were machined using a CNC for the larger JANNAF and ASTM geometries, while the smaller and thinner SJF and MICRO were manufactured using an LS-1630 CO₂ laser cutter. The dimension tolerances for the ASTM D638-10 standard are ± 0.5 mm for the gauge width w_g and gauge thickness w_t , +6.4 mm for grips, ± 0.25 mm for the gauge length L_o , ± 5 mm for the distance between grips, and ± 1 mm for the grip radius as stated in the ASTM D638-10.

The SJF specimen was created by scaling all dimensions of the JANNAF so the gauge width (w_g) measured 5 mm. This minimum thickness was desired to be at least 10 times the diameter of the largest particle size to have a sufficient number of large particles represented across the sample to approximate a homogeneous sample. Here, the largest particle is the 400 μm AP; therefore, the desired minimum thickness was 4 mm. Given that the MICRO tensile sample had $w_g = w_t = 5$ mm, the choice was made to have the w_g of the SJF to be the same 5 mm. This allowed both gauge widths between the MICRO and SJF to be equal and decreased the variability in the gauge section between both geometries. To ensure the propellant would not adhere to the acrylic, a thin layer of molykote 111 was applied to the mold surface. Then, the propellant slurry was carefully poured into the molds, which were set on top of a vibrating table to remove any voids that may have been introduced during the pour.

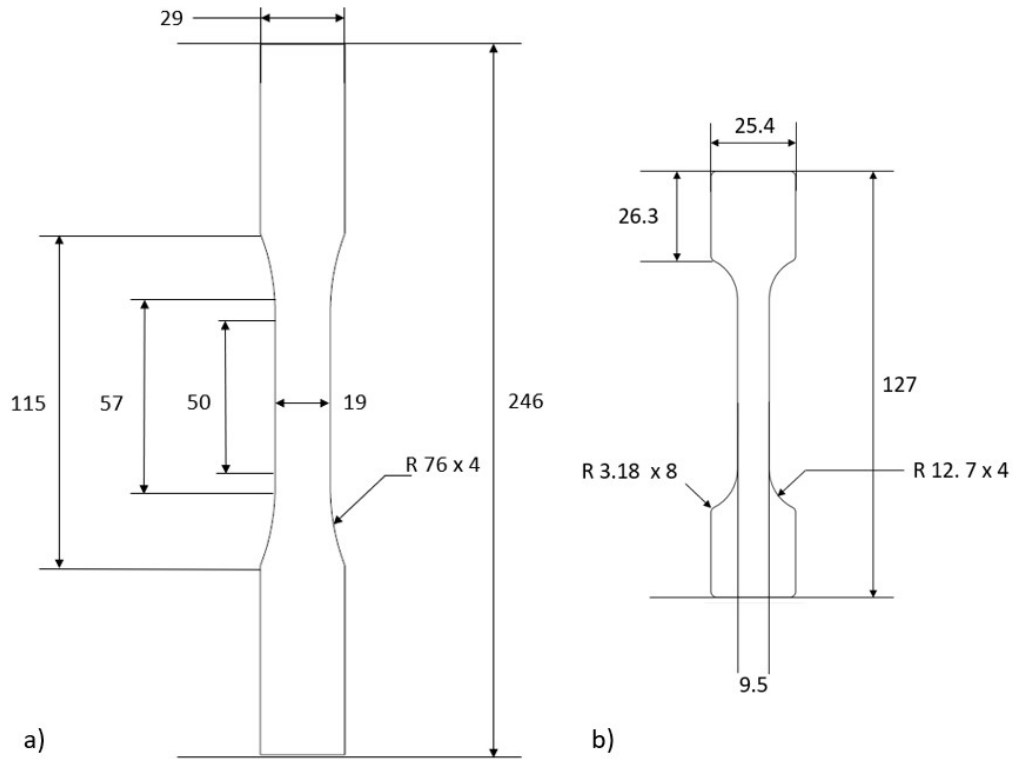


Figure 5.2: Tensile samples with dimensions in mm: a) ASTM D638 Type-III (9 mm thick) as per the ASTM D638-10 b) JANNAF sample (12.7 mm thick) as adapted by [6].

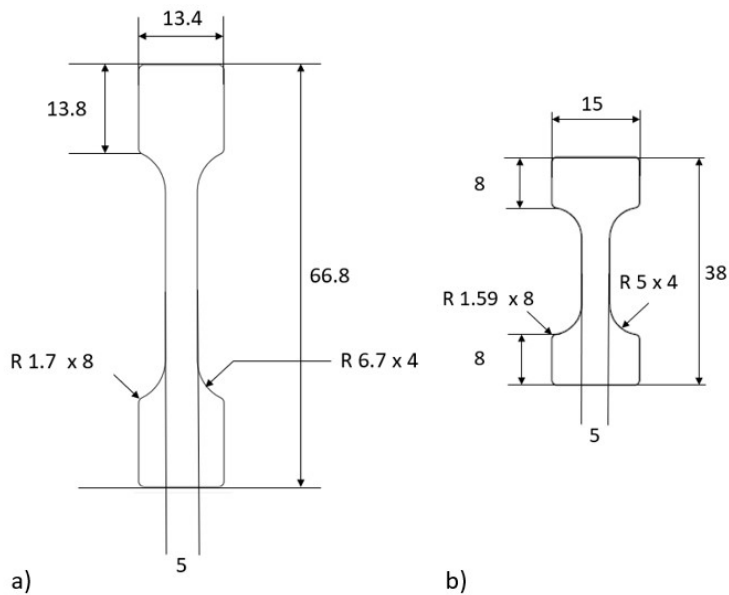


Figure 5.3: Tensile samples with dimensions in mm: a) Scaled-JANNAF (6.7 mm thick) b) MICRO tensile sample (5 mm thick) as adapted by [6].

	JANNAF	MICRO	SJF	ASTM
Theoretical Mass (g)	45.44	3.12	6.73	87.15
Average Weight (g)	46.84	2.98	6.51	85.46
% Error	3.00	4.52	3.24	1.93

Table 5.1: Theoretical masses with the corresponding average mass and % error of all tensile geometries with H-10 Aluminum powder.

	JANNAF	MICRO	SJF	ASTM
Theoretical Mass (g)	46.84	3.12	6.73	87.15
Average Weight (g)	45.86	3.00	6.62	85.50
% Error	2.09	3.75	1.74	1.89

Table 5.2: Theoretical masses with the corresponding average mass and % error of all tensile geometries with H-3 Aluminum powder.

Once the molds were vibrated for about 5 minutes, the molds were placed in an oven at 60 °C for 4 - 5 days to cure. After this, the samples were allowed to cool to room temperature on their own to prevent thermal stresses from developing within the samples from rapid cooling. This was done by turning off the ovens while the samples remained in them, allowing the heat to dissipate naturally. Each sample was weighed after curing and before testing. Tables 5.1 and 5.2 show the masses of the tensile samples with average masses and their respective error from the theoretical max density of the APCP. Due to the variation in the tolerance of each mold for all geometries, a correlation to the masses alone is insufficient to compare the densities between the H-3 and H-10 aluminum.

5.3 Experimental Methods

5.3.1 Digital Image Correlation

DIC is an optically based, non-intrusive diagnostic technique used to measure dynamic full-field 2D or 3D responses of materials under deformation. Two-dimensional DIC is commonly used when out-of-plane motion can be ignored to determine a given quantity of interest (QOI). Three-dimensional DIC is used when in- and out-of-plane motion is present and cannot be ignored. However, even when out-of-plane motion can be ignored, some QOIs may still require 3D DIC.

This research used 3D DIC, hereinafter referred to as stereo DIC, for conducting mechanical testing of composite propellant. The stereo DIC system developed for tensile testing includes a stereo mounting system and two cameras. The frame of the mounting system uses a double-slotted 80/20 framing rail with several flanged sleeve bearings that allow for adaptable configurations of the stereo system. Mounted to two of the sleeve bearings are two Oben BE-117 ball head camera mounts with leveling indicators and a 360° panning angle adjustment knob. Two HUSKY (Model K40068) LED lights are mounted to the 80/20 frame. Lastly, the entire frame is mounted to a tripod that provides additional levelers for further adjustment versatility.

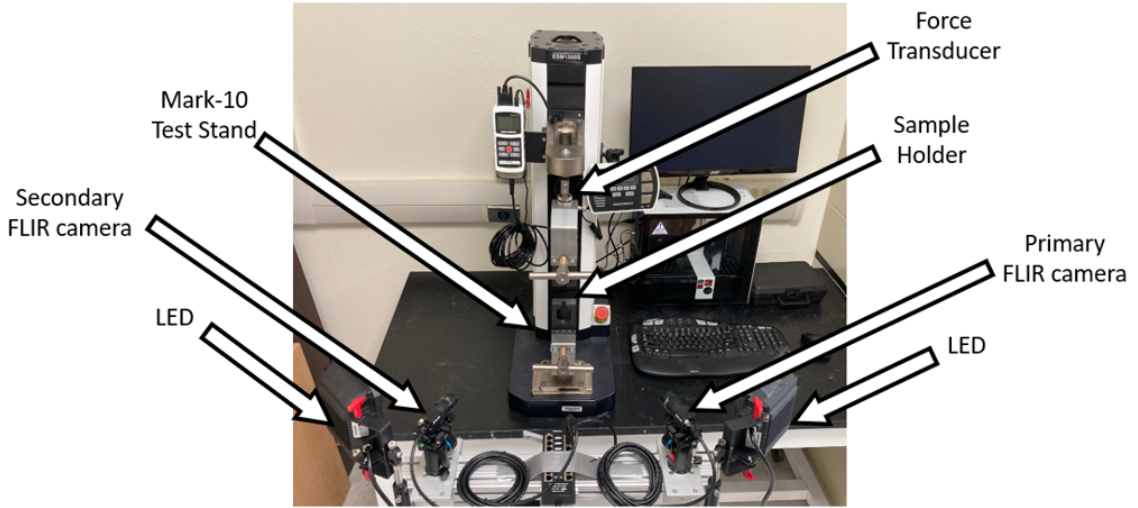


Figure 5.4: Experimental test setup of the stereo camera system and Mark-10 test stand with a JANNAF propellant sample in slotted tensile heads

The cameras used are two monochrome Blackfly S cameras. A set of 25 mm and 12 mm lenses were used throughout this study. The 25 mm lenses were used for both the JANNAF and ASTM specimens due to the larger field of view (FOV) required, whereas the 12 mm lenses were used for the much smaller SJF and MICRO tensile samples. The cameras have a resolution of 5 megapixels (MP), a frame rate of 22 frames per second (fps), and exposure times in the range of $11\mu\text{s}$ - 3 s. To determine the camera and lens settings, first, the appropriate FOV of the lens required to image the samples during deformation was found. A region of interest (ROI) was required to determine the FOV. This ROI was initially set to ensure the entire specimen remained within the FOV of the camera for initial tests. Later, optimization for the resolution of the speckle pattern in the ROI was conducted by decreasing the ROI to only the gauge section of the specimen, allowing for 5 - 20 mm of vertical displacement, which in turn resulted in a decrease of the FOV. This was done to optimize the measurements of the strain and displacement within the gauge section of the tensile specimens.

The FOV of the camera can be determined by: $\text{FOV} = L_{CS} \left(\frac{L_{SOD} - f_{lens}}{f_{lens}} \right)$ where L_{CS} and L_{SOD} are the horizontal length of the camera sensor and the stand-off distance from the cameras lens to the specimen, respectively. In this case, the FOV was chosen to be 5-20 mm larger than the length of all specimens leaving the only unknown to be the L_{SOD} ; therefore, the above equation can be rearranged as: $L_{SOD} = f_{lens} \left(\frac{\text{FOV}}{L_{CS}} + 1 \right)$.

To reduce the uncertainty of the 3D correlation process, the angle between both cameras or the stereo angle (θ_s) shown in Figure 5.5, was required to be between 15° to 35° [45]. To reduce the uncertainty in both the in-plane and out-of-plane measurements corresponding with the 12 mm and 25 mm lenses, the stereo angle was required to be slightly larger for the 12 mm lens while a smaller θ_s was used for the 25 mm. Smaller stereo angles increase the accuracy of in-plane measurements while sacrificing out-of-plane measurement accuracy and vice versa. Large stereo angles can lead to image-to-image differences between both cameras. Taking into account L_{SOD} between the cameras

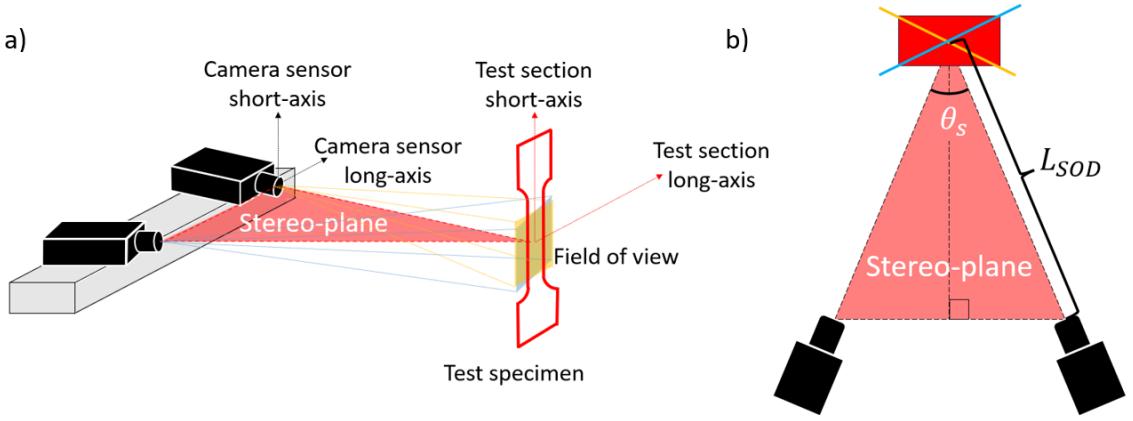


Figure 5.5: a) Isometric view of a typical stereo system b) Top-view of a stereo system showing the stereo angle θ_s and the stand-off distance L_{SOD} .

and the tensile specimen for the required FOV, optimizing the in-plane and out-of-plane accuracy resulted in a θ_s of 35° and 25° for the 12 mm and 25 mm lenses respectively.

Calibration is performed by placing inert samples with geometries similar to that of the propellant specimens in the test section to set the lens aperture, exposure, and gain levels. The lens aperture setting, or *f*-number, sets the depth of field (DOF). The *f*-number and gain level were set to *f*/8 and zero for all experiments, respectively. The motion blur (δ_{blur}), which is a function of the strain rate ($\dot{\epsilon}$), the image scale (C_{px}) in pixels/mm, and the exposure time (t_{exp}) of the camera. The maximum t_{exp} to limit pixel blur can be quantified by:

$$t_{exp} = \frac{\delta_{blur}}{\dot{\epsilon}C_{px}} \quad (5.1)$$

5.3.2 Calibration of the stereo camera system

The calibration process determines parameters such as the distance between cameras and the stereo angle. Any adjustments to the physical setup were conducted prior to performing the calibration. Several calibration images of precision-marked targets were taken to calibrate the stereo system. The calibration images were then processed with the Correlated Solutions VIC-3D software to obtain the imaging parameters to perform the correlation. After tests were completed, an end-of-day calibration was performed similar to that outlined in section 5.3.2. This was conducted to ensure that the stereo system was not accidentally bumped during the process of testing.

5.3.3 Application of speckle pattern

Prior to the application of the speckle pattern, the dimensions of the gauge thickness and width were measured for each sample using digital calipers. All samples were also weighed prior to the application of paint. The propellant samples were prepared by cleaning the surfaces with isopropyl alcohol. A base coat of white matte spray paint was applied to the surface. Several light coats were applied to prevent any paint from running. Once the natural black surface of the propellant was no longer visible, matte black paint was carefully sprayed onto the surface from about 20 cm away to ensure small droplets of spray paint were exhausted from the nozzle. The final results are shown in Figure 5.6.

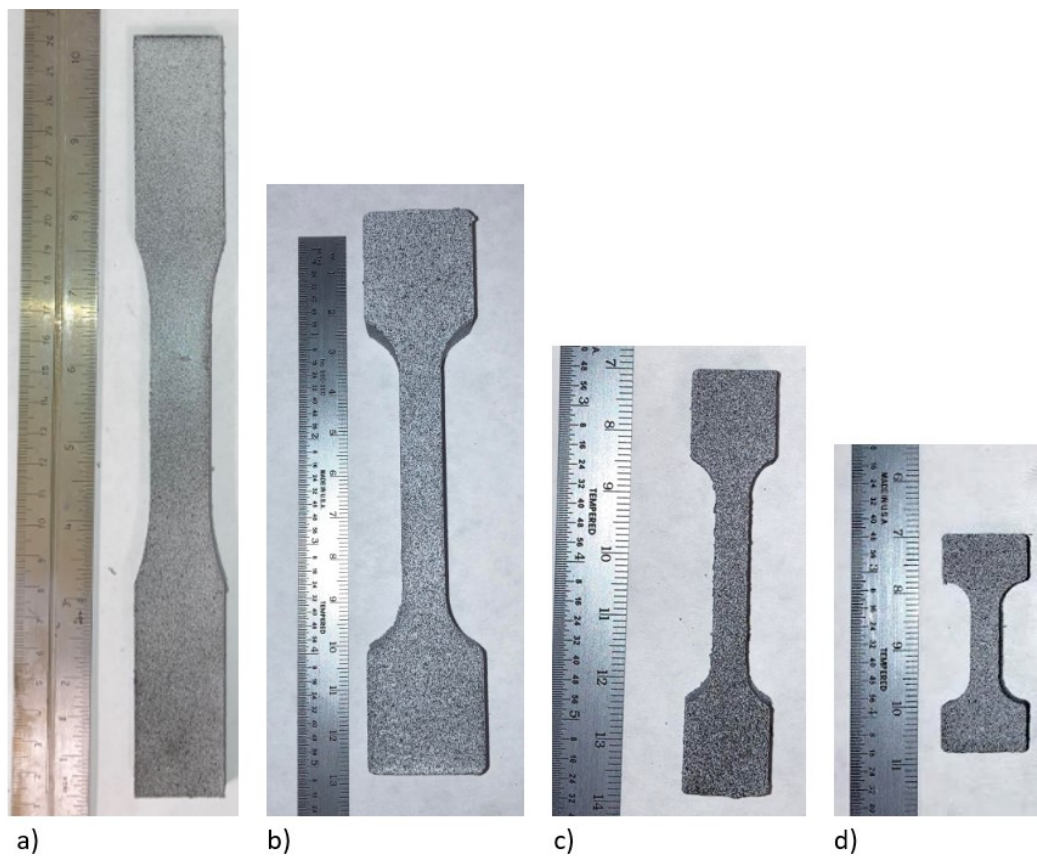


Figure 5.6: Speckled tensile samples for ASTM, JANNAF, scaled-JANNAF, and MICRO from a to d, respectively.

5.3.4 Uniaxial loading of propellant samples

An ESM1500S Mark-10 test stand with an R01-100 load cell with $\pm 0.15\%$ of full-scale accuracy (± 0.2 N) was used for performing uniaxial testing. The strain rates investigated were 0.5, 5, and 20 mm/s. Two G1100 parallel jaw grips were used, and a

set of slotted tensile heads 3D printed using Markforged onyx material were used for the JANNAF, SJF, and MICRO tensile samples, as shown in Figure 5.7.



Figure 5.7: JANNAF tensile sample positioned within the tensile heads printed using a Markforged 3D printed using Onyx with fiberglass reinforcement.

The JANNAF, SJF, and MICRO tensile samples were mounted such that the edge of the tensile heads terminated right at the start of the gauge section. The ASTM sample was directly mounted into the G1100 jaw grips so that they were secured 115 mm apart per the ASTM standard. This was performed by zeroing the displacement on the Mark-10 while the grips were in contact and then manually adjusted using the precision stepper motor until the digital readout read 115 mm. All other samples were also mounted by zeroing the tensile heads installed onto the Mark-10 and adjusting until the digital read-out read the required gauge length for each specimen. Samples were then tested by initiating the stereo system, allowing a short time to pass to ensure no moving was present, followed by initiating the Mark-10.

After the acquisition of the Mark-10 and stereo system was complete, the displacement measurements were determined using VIC 3D. The ASTM standard has specific diagnostic tools, such as extensometers or displacements from a test stand, to measure the stress, strain, and Young's modulus E ; however, since the focus of this work was to perform the measurements using a 3D stereo system, the diagnostic tools deviated slightly from the ASTM standard. Note that the methods for calculating Young's modulus remained the same as per the ASTM for all geometries. The methods for calculating the stress-strain deviated from the standard in terms of reporting engineering stress and strain compared to the percent strain noted in the standard. Additionally, the calculation of Poisson's ratio differed. Poisson's ratio was determined by finding the value of ν for each data point extracted through VIC 3D and averaged for the entire linear region. The largest difference preventing this work from performing the calculation for ν per the ASTM standard is that the standard requires a Type I geometry.

5.3.5 VIC 3D data processing

The correlation process for determining the experimental strain for the tensile samples was performed using VIC 3D. This software was used to manually select the ROI. The ROI for the JANNAF, SJF, and MICRO samples were selected to encompass the entire gauge section with additional space near the top and bottom of the sample to ensure the full gauge length was selected. The ROI of the ASTM was made to also encompass its ROI, which was slightly larger than the gauge area required.

Once the ROIs were selected and the correlation process was complete, a virtual strain gauge (VSG) was then manually selected to measure the longitudinal strain that matched the required gauge length of each tensile sample, which was 50, 50.8, 26.7, and 10 mm for the ASTM, JANNAF, SJF, and MICRO tensile samples, respectively. A VSG was also manually placed at the center of each sample to measure the lateral strain of each specimen. Refer to Figure 5.8 for referencing the ROIs used and the placement of the lateral and longitudinal strain gauges. The placement of all lateral strain gauges was limited by how well the correlation process was performed, which set the maximum width within the ROI. In other words, the selected ROI was nominally selected to be at the edge of the vertical sides of the samples, but the ROI would generally become smaller after the correlation process, which set the lateral strain gauges to be slightly smaller than the actual gauge width of the samples.

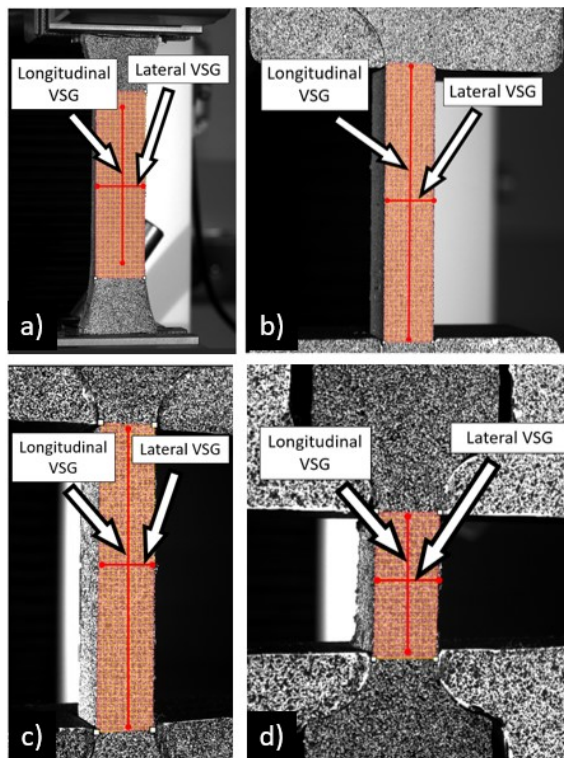


Figure 5.8: Lateral and longitudinal virtual strain gauge (VSG) placements for ASTM, JANNAF, scaled-JANNAF, and MICRO annotated from a to d, respectively, through VIC 3D.

CHAPTER 6

RESULTS AND DISCUSSION OF THE MECHANICAL PROPERTIES OF APCP COMPOSITIONS

The mass, gauge width (w_g), and gauge thickness (w_t) were measured for each tensile sample before applying the speckle pattern. Table 6.1 and Table 6.2 show the average mass and dimensions, respectively, of each sample geometry for both the H-10 and H-3 compositions. These measurements were used to record sample-to-sample variations due to casting and for measuring the initial cross-sectional area (A_o) to determine the engineering stress and strain, σ_{eng} and ε_{eng} , respectively. Results from the 3D-DIC stereo camera system for material characterization of the two APCP formulations with both H-10 and H-3 aluminum powders were compared. Several tensile geometries were tested to study geometrical effects on material parameters such as the dewetting stress (σ_d), dewetting strain (ε_d), Young's Modulus (E), and Poisson's ratio (ν).

6.1 DIC Results

Using VIC-3D, a region of interest was manually selected to encompass the entire gauge section. The subset and step sizes for each geometry were chosen based on the recommendations from Bigger [45] and are shown in Table 6.3. Two virtual strain gauges (VSGs) were manually selected to measure the longitudinal strain (ε_{long}) and lateral strain (ε_{lat}) of the tensile sample as shown in Figure 6.1. All parameters remained the same for a given geometry for both propellant compositions.

The VSG tracked a local region of the reference image to determine the displacement of the pixel locations that were selected as the endpoints of the VSGs. It must be noted that the location at which the VSG selected to measure ε_{lat} did not always capture the maximum lateral strain due to the variation of the location of the fracture; therefore, an average Poisson's ratio (ν_{avg}) is presented in this work. The initial length of the gauge section (L_o) and the instantaneous length (L) were provided from the extracted data from VIC-3D and were used to calculate the ε_{eng} given by:

$$\varepsilon_{eng} = \frac{L - L_o}{L_o} \quad (6.1)$$

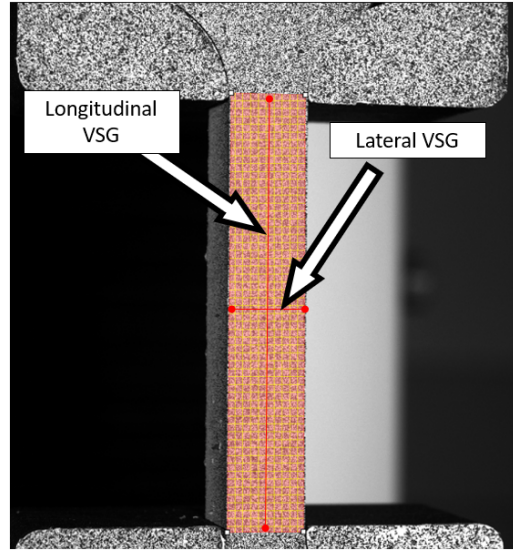


Figure 6.1: Reference image of a JANNAF tensile sample showing the longitudinal and lateral virtual strain gauges in addition to the region of interest for calculating strain.

Table 6.1: Average mass of samples between geometries for H-10 and H-3 composition. At least 5 samples per geometry were averaged.

Geometry:	ASTM	JANNAF	SJF	MICRO
H-10	85.46 ± 1.08 g	45.83 ± 0.20 g	6.65 ± 0.04 g	2.98 ± 0.03 g
H-3	85.50 ± 1.03 g	45.21 ± 0.13 g	6.61 ± 0.07 g	2.99 ± 0.02 g

Table 6.2: Average gauge thickness, width, cross-sectional area, initial longitudinal gauge length, and initial lateral gauge length of all geometries and both APCP compositions.

	Geometry	$w_{t,avg}$ (mm)	$w_{g,avg}$ (mm)	$L_{o,long}$ (mm)	$L_{o,lat}$ (mm)
H-10	ASTM	8.28 ± 0.2	18.28 ± 1.4	50.10 ± 0.1	14.47 ± 0.4
	JANNAF	12.77 ± 0.2	9.45 ± 0.1	50.65 ± 0.3	7.45 ± 0.1
	SJF	6.65 ± 0.1	5.14 ± 0.1	25.97 ± 0.4	4.20 ± 0.1
	MICRO	4.98 ± 0.2	4.91 ± 0.1	10.60 ± 0.3	4.11 ± 0.1
H-3	ASTM	8.66 ± 0.02	18.92 ± 0.2	50.17 ± 0.3	14.56 ± 0.4
	JANNAF	12.74 ± 0.04	9.48 ± 0.02	50.78 ± 0.2	6.42 ± 0.6
	SJF	6.68 ± 0.1	5.12 ± 0.05	25.89 ± 0.3	4.12 ± 0.3
	MICRO	5.01 ± 0.1	4.97 ± 0.1	10.43 ± 0.23	3.77 ± 0.1

Table 6.3: Parameters used to conduct strain analysis using VIC-3D for all geometries for both H-10 and H-3 compositions.

Geometry	Subset Size (pixels)	Step Size
ASTM	21×21	7
JANNAF	21×21	7
SJF	29×29	9
MICRO	29×29	9

After extracting the measurements from VIC-3D, the force measurements from the Mark-10 test stand and the VIC-3D data were synchronized to determine E and v_{avg} . The force measurements were synchronized using the frame index of a given test and the frames per second of the cameras to convert the frame index to time. Once the time was known, linear interpolation was used to determine the uniaxial load (F_s) at each time. The engineering stress (σ_{eng}) was then calculated by:

$$\sigma_{eng} = \frac{F_s}{A_o} \quad (6.2)$$

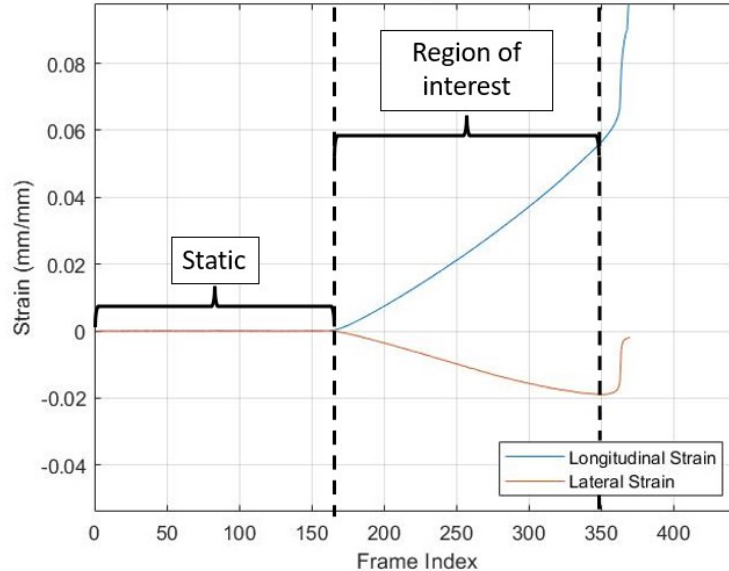


Figure 6.2: Raw data from VIC-3D of a JANNAF tensile test showing the static region, including the start and end of the test at frame 164 and 345, respectively.

A raw data set is presented in Figure 6.2 for a JANNAF tensile sample showing both ε_{long} and ε_{lat} as a function of the frame index. At the lower frame numbers of the graph in Figure 6.2, ε_{long} and ε_{lat} steadily vary until the point the samples fractured. The frame index at which the fracture occurred served as the point at which the data was no longer useful for determining strain, [45]. Note that the first frame used is not frame 1, and that

is because the camera is initiated for several seconds before the tensile test begins; these static frames where strain is zero are omitted here. It was noted that the point of fracture always occurred at or near the maximum ϵ_{lat} . given that the cross-section of the tensile samples relaxed back to their original shape upon fracture.

Figure 6.3 shows the engineering stress and strain curve from the strain data from Figure 6.2, where the linear portion of the curve was manually selected. The dewetting stress and strain, σ_d and ϵ_d , respectively, were then acquired to determine E . These points are chosen manually as the points when the slope departs from a constant value. These methods were conducted for all test geometries. Figure 6.4 - 6.11 shows the stress-strain curves for all geometries. More is presented in Section 6.3 and 6.4 that quantify the repeatability in each geometry. All curves, from Figure 6.4 - 6.11, show the stress-strain response from the start of the test to the point right before failure occurred.

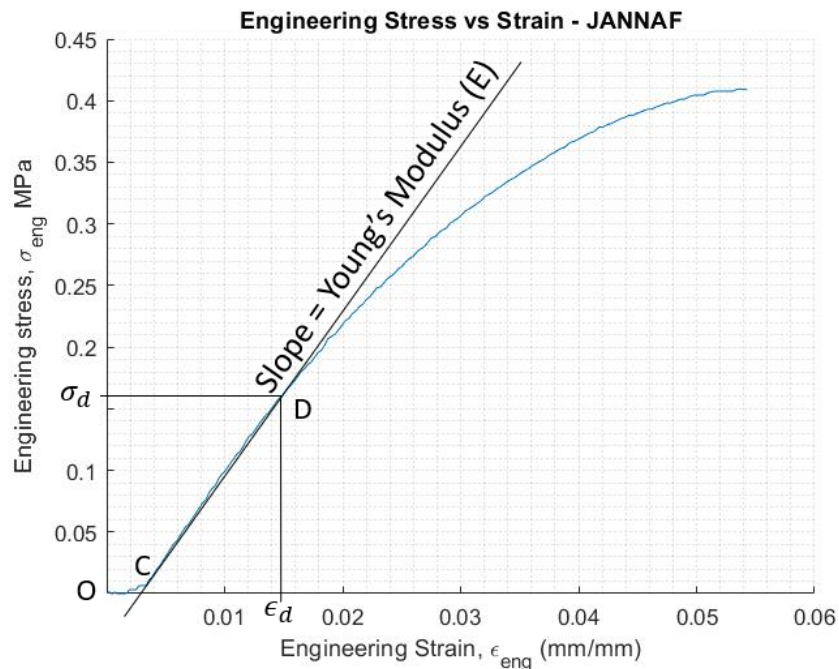


Figure 6.3: Engineering stress and strain of a JANNAF tensile sample showing the toe region originating from point O to C, and the linear part of the curve from C to D.

As per the ASTM D638-10, in the case when the material exhibited a curve OC, shown in Figure 6.3, a correction was allowed to account for this. This "toe" region within the stress-strain curves is present in some, not all, of the tensile tests as shown in Figures 6.4 - 6.11. The toe region does not represent a physical property. Rather, it is caused by misalignment in the grips or by slack within the system that was present due to improper positioning of tensile samples within their corresponding grips. Point O was manually selected and served as the initial point of the linear region. Point D was manually selected by visually inspecting where the linear portion of the curves ended. This point also served as the location where the final dewetting stresses and strain were determined for this work. The stress and strain values along the line CD were used to calculate E through linear

interpolation using MATLAB. If the toe region was not present, as shown in Figure 6.6, the initial point in the data served as the starting point for the linear region, and point D was chosen to be when the linear region ended.

Figure 6.5 shows the stress-strain relations for several JANNAF samples, which were tested at different strain rates. The strain rate was varied on the Mark-10 from 0.5 to 5 to 20 mm/s. The results show a curve when the strain rate was set to 20 mm/s. This sample experienced a large toe region, but it then began to follow the general slope observed in the other stress-strain curves. The goal of this work was not to study the strain rate dependence but rather to study the effects geometry has on material response; therefore, once it was determined that the slopes remained the same regardless of the strain rate, all samples were chosen to have a strain rate of 0.5 mm/s to focus the work on studying any variation in the material response caused by geometrical effects.

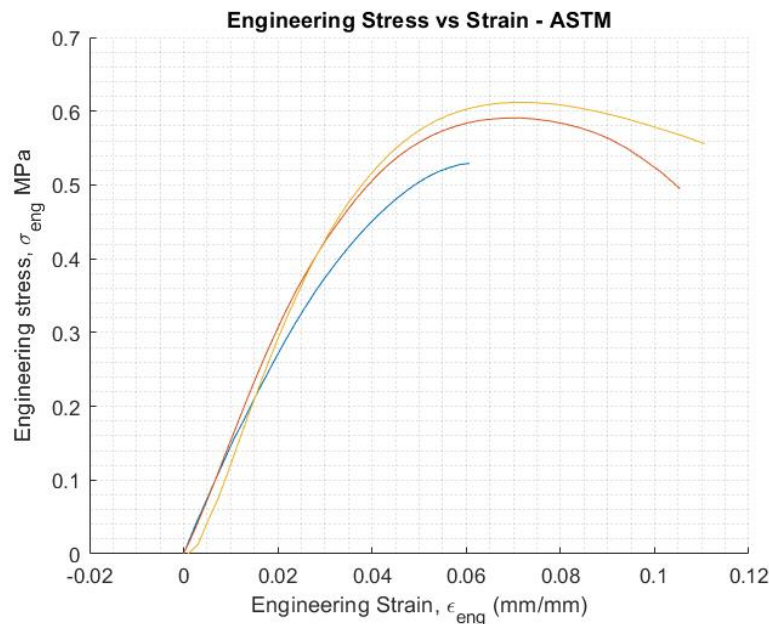


Figure 6.4: Engineering stress-strain curve of ASTM geometry with H-10 aluminum powder at 0.5 mm/s.

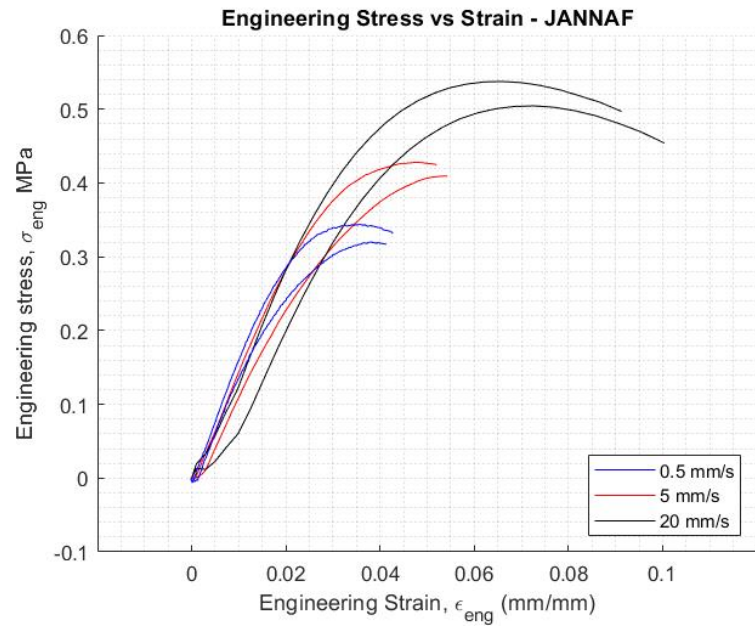


Figure 6.5: Engineering stress-strain curve of JANNAF geometry with H-10 aluminum powder at 0.5 mm/s, 5mm/s and 20 mm/s.

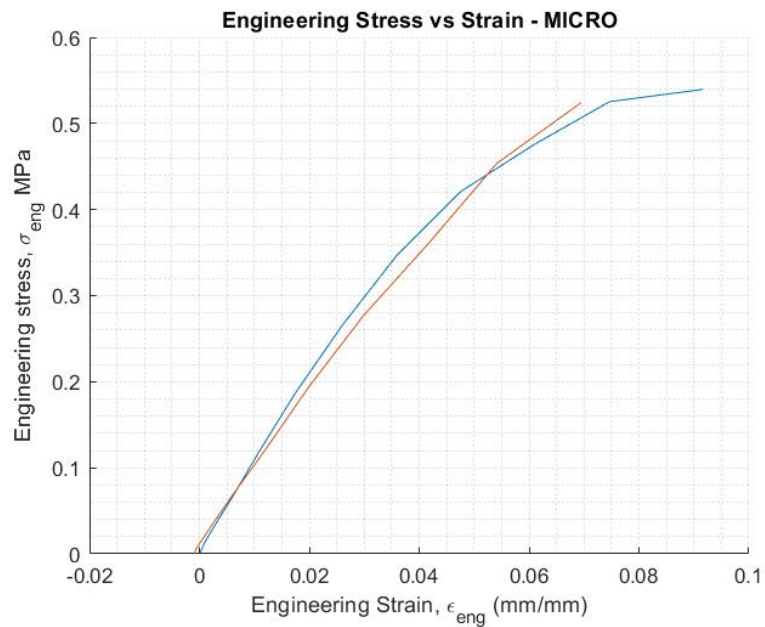


Figure 6.6: Stress-Strain curve of MICRO geometry with H-10 aluminum powder at 0.5 mm/s.n

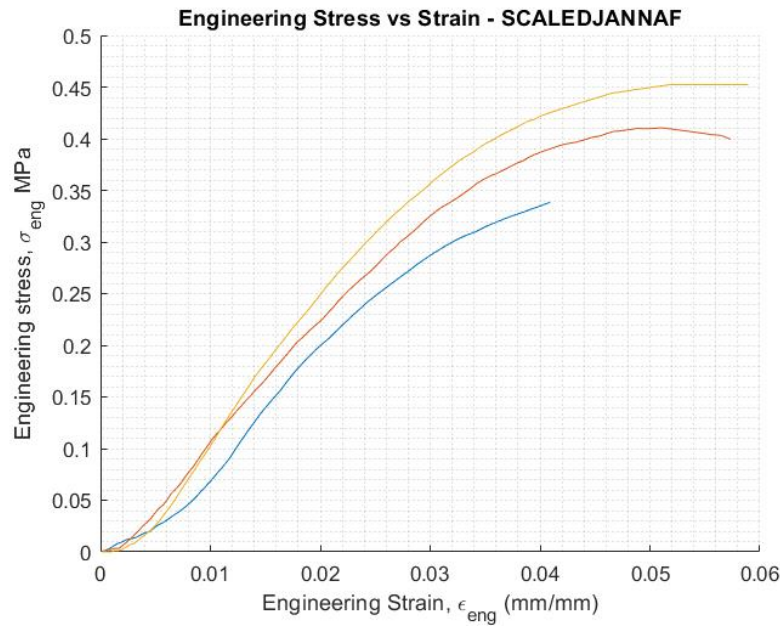


Figure 6.7: Engineering stress-Strain curve of SJF geometry with H-10 aluminum powder at 0.5 mm/s.

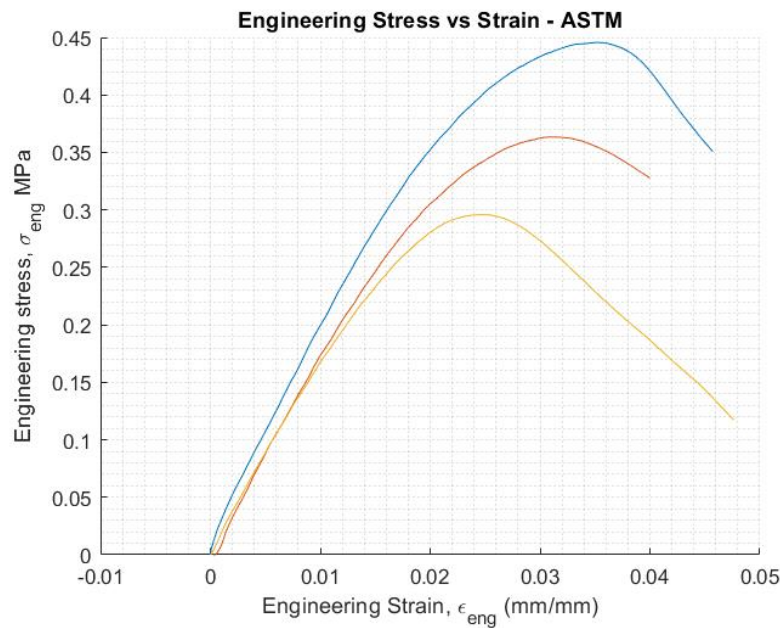


Figure 6.8: Engineering stress-strain curve of ASTM geometry with H-3 aluminum powder at 0.5 mm/s

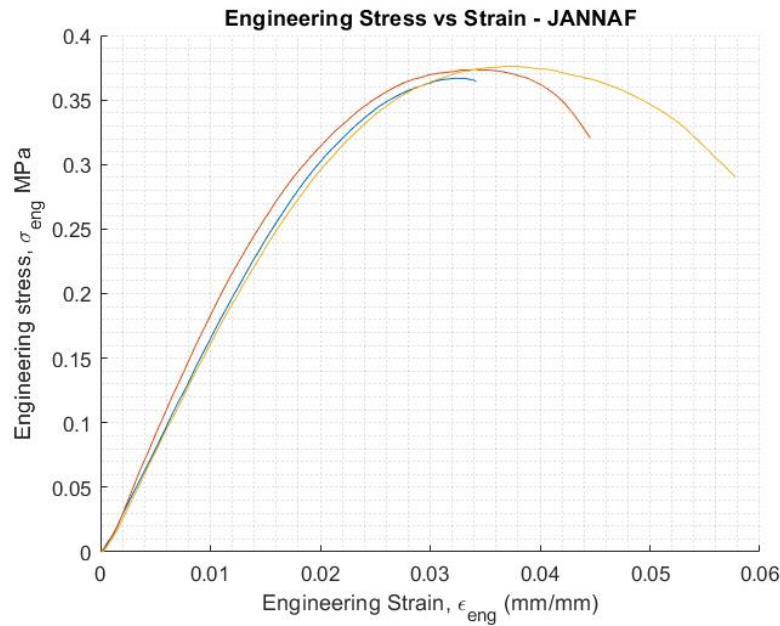


Figure 6.9: Engineering stress-strain curve of JANNAF geometry with H-3 aluminum powder at 0.5 mm/s

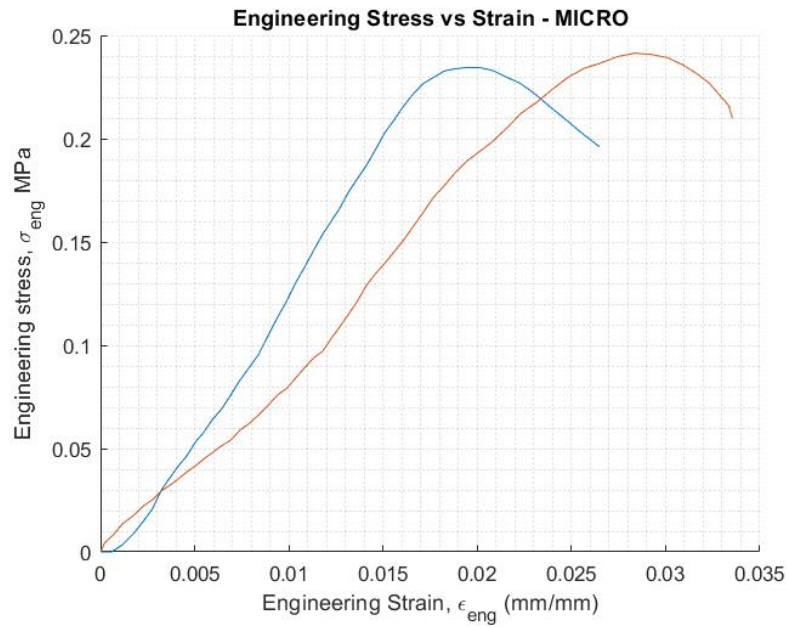


Figure 6.10: Engineering stress-strain curve of MICRO geometry with H-3 aluminum powder at 0.5 mm/s

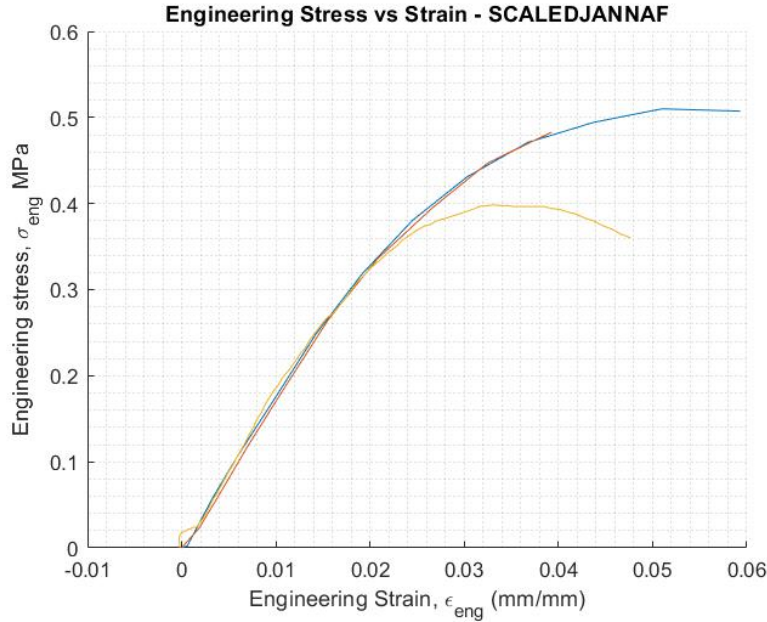


Figure 6.11: Engineering stress-strain curve of SJF geometry with H-3 aluminum powder at 0.5 mm/s

6.2 Uncertainty of DIC Measurements

The uncertainty in the strain measurements originates from the pixels/mm conversion determined from the stereo system's calibration. For this work, the pixel blur (δ_{blur}), which is given by equation 5.1, was used to determine the image resolution (δ_{res}) given by:

$$\delta_{res} = \frac{\delta_{blur}}{C_{px}} \quad (6.3)$$

The image scale (C_{px}) is the pixels/mm conversion determined from VIC-3D. This resolution error was then divided by the VSG length ($L_{o,VSG}$) of each tensile geometry, resulting in the longitudinal and lateral strain uncertainty given by:

$$\delta_{strain} = \frac{\delta_{res}}{L_{o,VSG}} \quad (6.4)$$

The standard deviation of σ_d , E , and v_{avg} was determined by using [46]:

$$\Delta = \sqrt{\frac{1}{N-1} \left[\sum_{i=1}^N (t_i - \bar{t})^2 \right]} \quad (6.5)$$

where t_i is the measured value and \bar{t} is the mean of all tests.

6.3 Material Analysis Results for H-10 Composition

The measured values E , v_{avg} , and σ_d for samples with H-10 aluminum powder are listed in Table 6.4. The stress-strain response for the H-10 aluminum powder composition with all geometry types is shown in Figure 6.12. The ASTM, JANNAF, and SJF tensile samples generally had slightly higher values of E and v_{avg} compared to the MICRO tensile sample. This is believed to be occurring due to the difference in the geometry size, which is more evident when observing Figure 6.13 and Figure 6.14.

A clear trend was observed for tensile samples having larger cross-sectional areas by exhibiting higher values of E and v_{avg} ; however, the MICRO and SJF samples gave values that were within 80% of the ASTM sample pointing towards the use of smaller geometries to minimize batch size and maximize the number of samples made per batch for rapid testing. For this work, most geometries had at least a total of 5 tests performed; however, due to failures occurring on behalf of improper application of the speckle pattern or voids within the propellant causing the samples to fail early, the analysis provided here is for samples that exhibited no signs of failure due to either of the aforementioned causes.

Table 6.4: Young's modulus (E), average Poisson's ratio (v_{avg}), and dewetting stress (σ_d) of all experimental tests for all tensile geometries of the H-10 composition.

		Test 1	Test 2	Test 3	Test 4	Test 5	Test 6
ASTM	E (± 1.4 MPa)	13.14	15.21	15.76	-	-	-
	v_{avg} (± 0.01)	0.50	0.51	0.49	-	-	-
	σ_d (± 0.02 MPa)	0.22	0.38	0.36	-	-	-
JANNAF	E (± 2.4 MPa)	12.11	15.06	12.00	8.83	12.50	15.22
	v_{avg} (± 0.04)	0.42	0.38	0.42	0.42	0.48	0.48
	σ_d (± 0.02 MPa)	0.25	0.27	0.24	0.21	0.21	0.27
MICRO	E (± 1.0 MPa)	10.44	9.07	-	-	-	-
	v_{avg} (± 0.01)	0.40	0.41	-	-	-	-
	σ_d (± 0.01 MPa)	0.26	0.37	-	-	-	-
SJF	E (± 2.5 MPa)	13.56	11.79	8.69	-	-	-
	v_{avg} (± 0.03)	0.43	0.49	0.45	-	-	-
	σ_d (± 0.05 MPa)	0.20	0.16	0.22	-	-	-

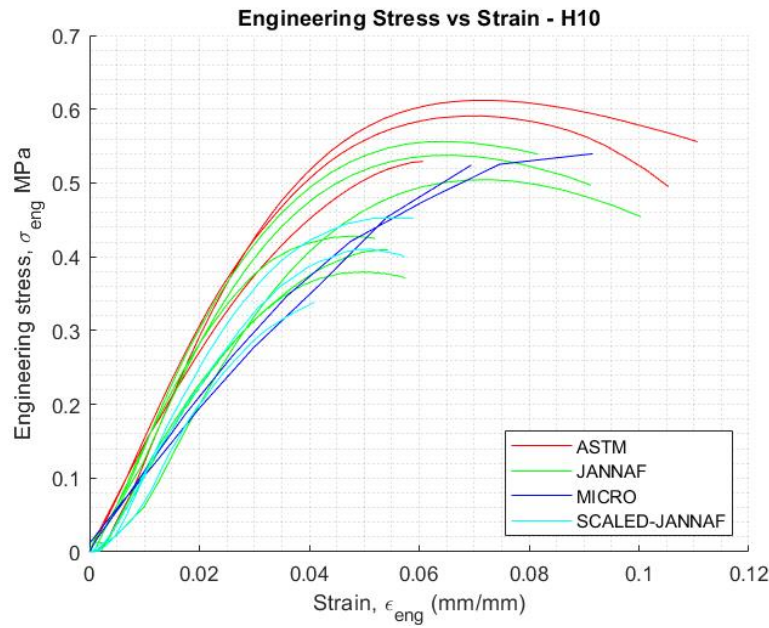


Figure 6.12: Engineering stress-strain response for all geometry types for H-10 composition.

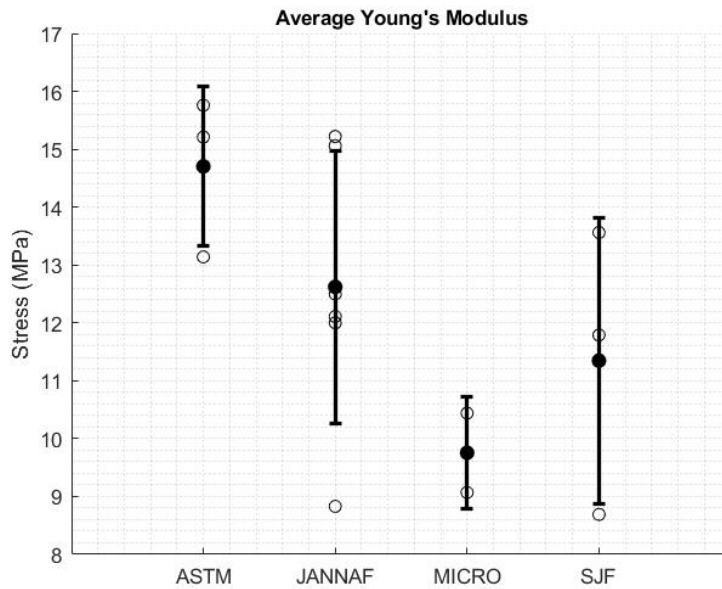


Figure 6.13: Calculated Young's modulus (E) with the averages and errors for all geometry types of H-10 composition.

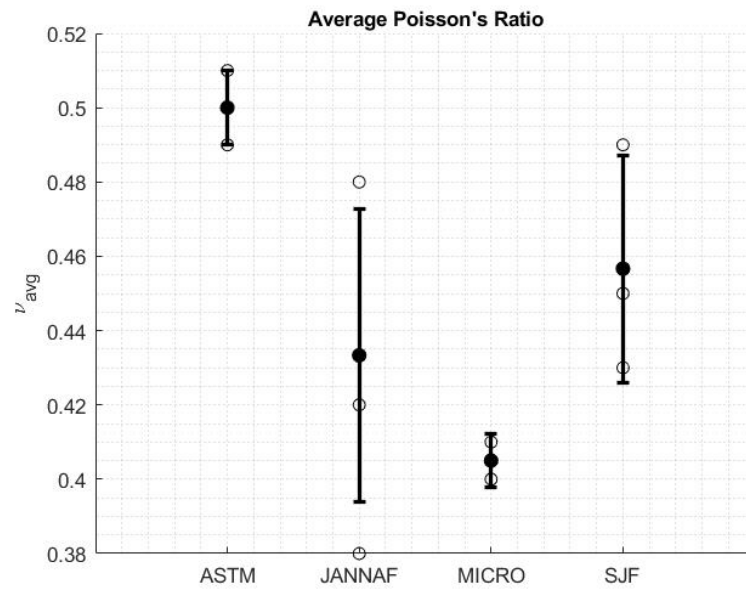


Figure 6.14: Calculated average Poisson's ratio (ν_{avg}) with the averages and errors for all geometry types of H-10 composition.

6.4 Material Analysis Results for H-3 Composition

The engineering stress-strain response curves for the H-3 composition are shown in Figure 6.15. Tables 6.5 lists the measured values of E , v_{avg} and σ_d with their calculated standard deviation. The H-3 series was shown to have slightly higher values of E and v_{avg} for all geometries. Figures 6.16 and Figure 6.17 show E and v_{avg} , where the same trend, as seen in the H-10 series, is observed for the measured E . The measured v_{avg} has large error bars for the MICRO, which is expected to have been caused by improper application of the speckle pattern and improper alignment in the tensile heads.

Table 6.5: Young's modulus (E), average Poisson's ratio (v_{avg}), and dewetting stress (σ_d) of all experimental tests for all tensile geometries of the H-3 composition.

		Test 1	Test 2	Test 3
ASTM	E (± 1.4 MPa)	18.57	16.40	16.00
	v_{avg} (± 0.05)	0.48	0.49	0.57
	σ_d (± 0.01 MPa)	0.16	0.16	0.17
JANNAF	E (± 1.5 MPa)	16.87	19.44	16.75
	v_{avg} (± 0.04)	0.46	0.52	0.54
	σ_d (± 0.02 MPa)	0.14	0.13	0.17
MICRO	E (± 3.7 MPa)	13.54	8.37	-
	v_{avg} (± 0.05)	0.51	0.44	-
	σ_d (± 0.01 MPa)	0.10	0.09	-
SJF	E (± 1.1 MPa)	16.85	18.84	16.88
	v_{avg} (± 0.02)	0.45	0.49	0.47
	σ_d (± 0.02 MPa)	0.19	0.19	0.20

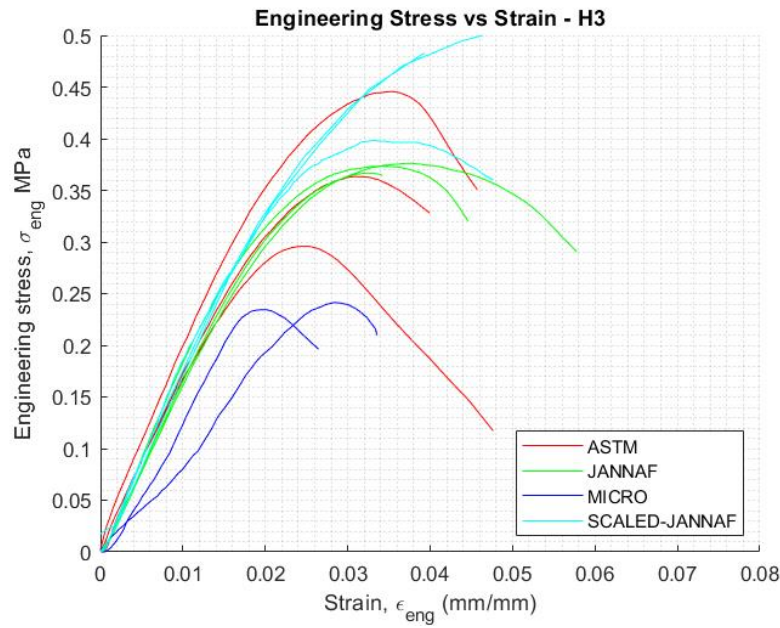


Figure 6.15: Engineering stress-strain response of ASTM, JANNAF Type-C, MICRO, and scaled-JANNAF tensile samples for H-3 composition.

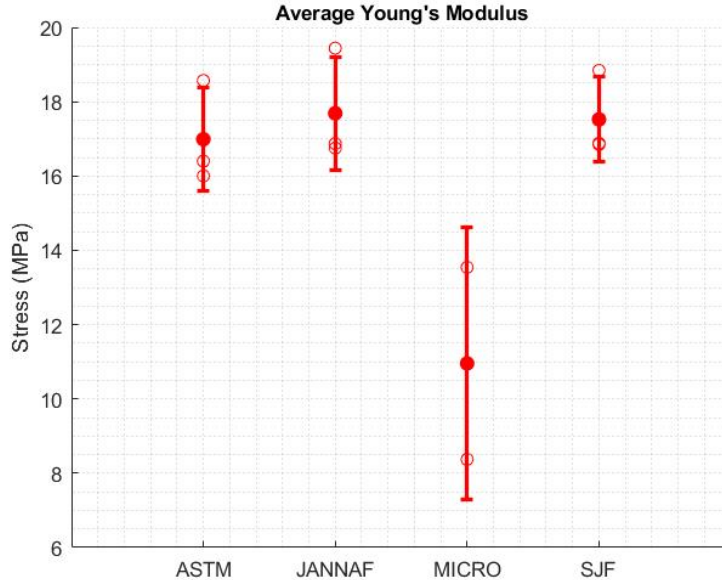


Figure 6.16: Calculated Young's modulus (E) with the averages and errors for all geometry types of H-3 composition.

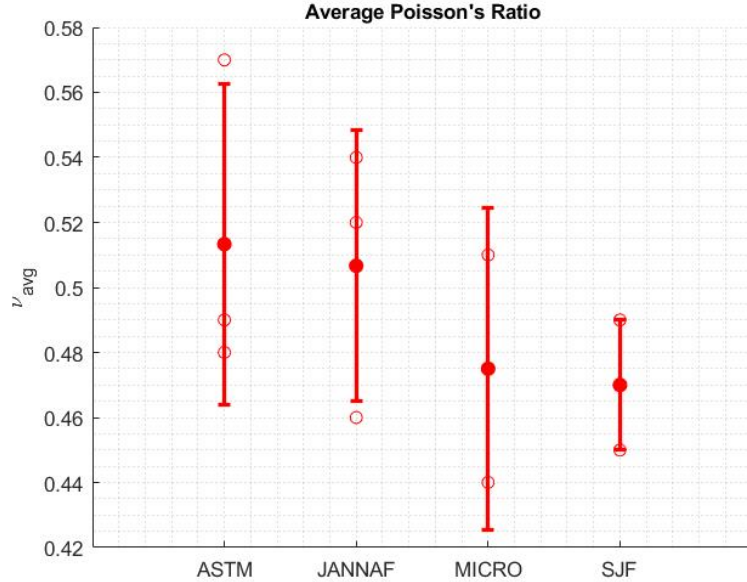


Figure 6.17: Calculated average Poisson's ratio (ν_{avg}) with the averages and errors for all geometry types of H-3 composition.

6.5 Discussion

The material properties of the two APCPs using H-10 and H-3 aluminum powders were found to vary slightly under uniaxial loading. The percent difference between the average Young's modulus of both compositions for the ASTM, JANNAF, SJF, and MICRO was 13%, 36%, 11%, and 35%, respectively. Altering the particle size of the aluminum does appear to have some measurable effect. Figure 6.18 shows all stress-strain curves of all geometry samples and both H-10 and H-3 compositions. The combined results for E and ν_{avg} are shown in Figures 6.19 and 6.20. Previous work has been performed that shows similar results of E and ν_{avg} [6, 30, 47]. Jaroki used a similar composition, using 17% Al with measured values of Young's modulus of 8.0 to 8.8 MPa for the JANNAF and MICRO tensile samples. His work exhibited a lower value for E , but had a 10% difference between the MICRO and JANNAF, where this work had a 20% difference. The decrease in material strength is due to a lower AP percentage than that used in this work. Work performed by Himanshu et al. [29] showed values between 0.45 and 0.48 for an APCP using nominally 15 - 20 μm Al and 200 - 300 μm AP particle sizes. The Al percentage for this propellant was also 17% with 67% AP and 15% HTPB.

The composition containing H-10 aluminum exhibited lower values of E compared to the H-3 composition, as shown in Figure 6.19, whereas the average Poisson ratio of the H-3 composition was nominally higher than that of the H-10 for all tensile samples as shown in Figure 6.20. An average dewetting stress $\sigma_{d,avg}$ for H-10 and H-3 is presented in Figure 6.21. The H-10 composition has larger values of $\sigma_{d,avg}$ while having lower values of E . This is a result of the H-10 composition having more elastic deformation, maintaining the interfacial bonding between solid particles and the binder matrix, allowing it

to reach large values of $\sigma_{d,avg}$. It is believed that the smaller aluminum particle size is changing the micro-structure arrangement between the polymer matrix, aluminum, and AP particles, causing these slight but measurable differences.

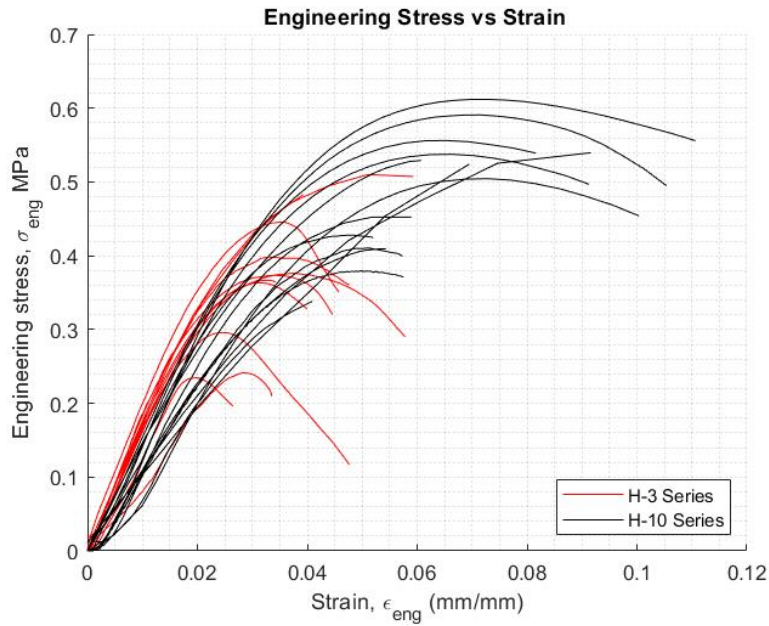


Figure 6.18: Engineering stress-strain response curves for H-10 (black) and H-3 (red) with all geometries plotted.

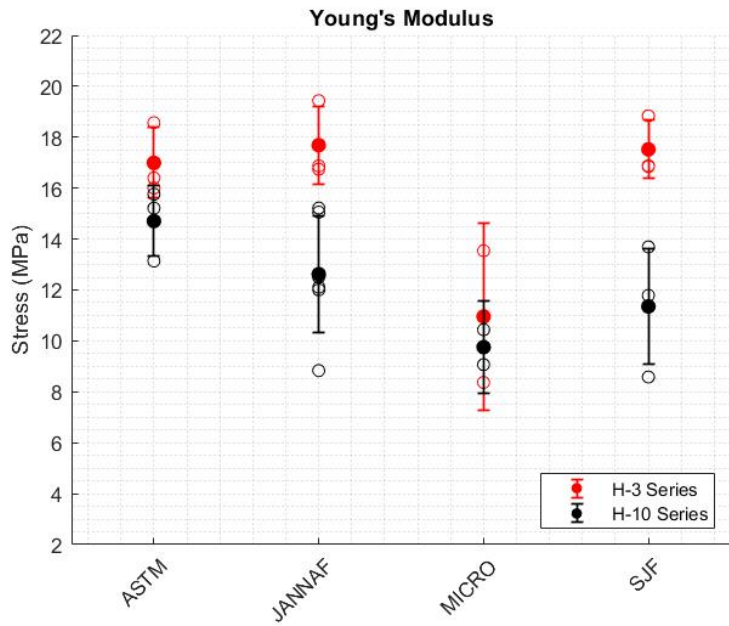


Figure 6.19: Average Young's modulus (E_{avg}) for H-10 and H-3 ammonium perchlorate compositions for ASTM, JANNAF, MICRO, and SJF tensile geometries with the standard deviation from the average value.

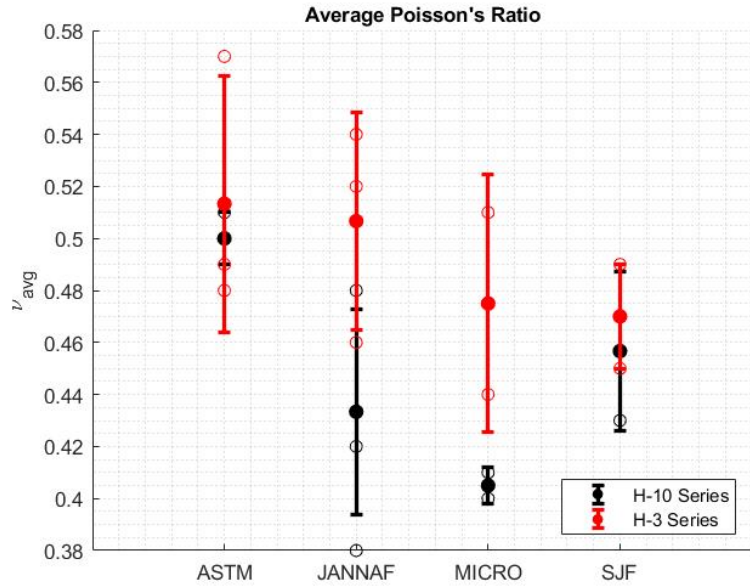


Figure 6.20: Average Poisson's ratio (ν_{avg}) for H-10 and H-3 ammonium perchlorate compositions for ASTM, JANNAF, MICRO, and SJF tensile geometries with the standard deviation from the average value.

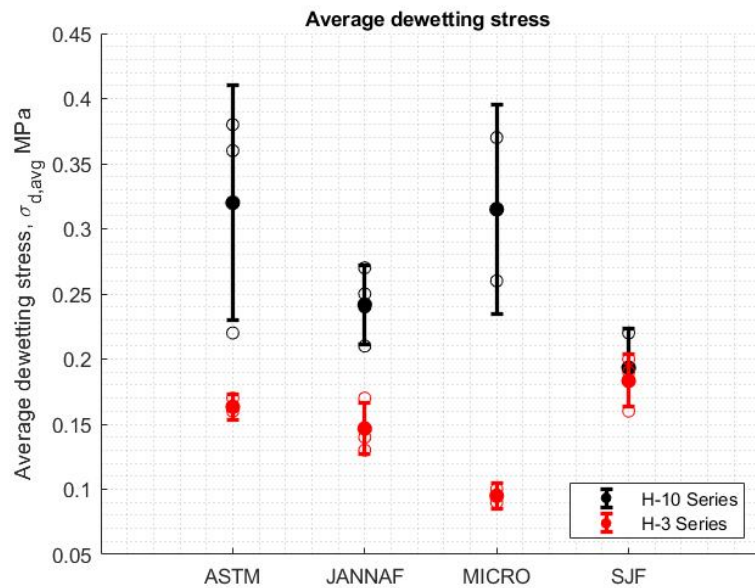


Figure 6.21: Average dewetting stress ($\sigma_{d,\text{avg}}$) for H-10 and H-3 composition with the standard deviation from the average value.

CHAPTER 7

CONCLUSIONS AND RECOMMENDATIONS FOR FUTURE RESEARCH

7.1 Conclusions

A final composition using NASA CEA was determined for the two APCP formulations. Lower aluminum content for the final formulation was chosen to mitigate the small-scale effect errors. This adjustment was crucial, as small-scale designs typically yield lower performance parameters, such as specific impulse, due to decreased combustion efficiency. The strand burner developed for this study successfully conducted strand burning experiments for the two APCPs at various pressure ranges. Findings confirmed that the H-3 composition exhibited higher burn rates than H-10, attributed to the smaller particle size of the aluminum powder.

The four-color pyrometer and spectrometer systems provided bulk temperature measurements within 9% to 38% of the predicted combustion temperature across a range of pressures (3.45 to 6.89 MPa). While heat loss to the surroundings and the closed-volume design of the strand burner likely contributed to these discrepancies, the correlation between bulk flame temperature measurements and anticipated combustion temperatures suggests opportunities for further research. Future work could focus on optimizing measurement techniques and refining the experimental setup to improve accuracy, thereby enhancing the understanding of combustion dynamics in small-scale rocket motors and correlating bulk flame temperature measurements to the predicted combustion temperature for rapid testing.

The 76 mm BATES grain design SRM developed for the evaluation of the burn rate coefficient a and n was used to perform several static tests similar to the pressure ranges performed on the strand burner. Of the two burn rate analysis methods used in this work, the mass balance method provided final results for the predicted pressure and thrust profiles, minimizing the percent difference between the average pressures for the predicted and experimental between the ranges of 4% to 15.8% for all tests performed. The ignition delay prompted by the ignition system caused non-nominal flame spread within the motor. No pressure rise was observed from the igniter, which suggests that a more sophisticated ignition system be designed for future experiments. The four-color pyrometer measured exit temperatures within 7.7% of the predicted. The spectrometer provided measurements that were not within the expected range but were assumed to have occurred due to improper alignment of the fiber optic cable. The average specific impulse measured from the three repeated tests at 6.89 MPa for the H-10 composition was 228 s, which was within 4% of experimental values from a similar aluminized APCP [12].

This study investigated the material properties of two APCP formulations containing H-10 and H-3 aluminum powders under uniaxial loading. The results revealed that the H-10 composition exhibited lower Young's modulus and Poisson's ratio values compared to the H-3 composition, indicating a more flexible and less stiff material. This observation aligns with the larger deformations and higher dewetting stress observed in the H-10 series, which is consistent with its lower modulus.

The significant variation in dewetting stress between the formulations suggests that the particle size and distribution of aluminum powders play a crucial role in determining the mechanical behavior of APCP under stress. The geometric effects observed, particularly in the MIRCO tensile samples, highlight the influence of sample geometry on measured material properties. The lower values of Young's modulus and Poisson's ratio in these samples may be attributed to the non-uniform strain distribution across the sample, as indicated by the high standard deviation in the data.

These findings have practical implications for the design and optimization of APCP formulations in rocket propellants. The study suggests that optimizing the particle size distribution and addressing geometric effects can enhance the rapid diagnostics system used to determine the material properties and performance of APCP. Future work should focus on refining the methods used to measure dewetting stress, perhaps through the development of an algorithm that iteratively determines the linear region of the stress-strain curve. Additionally, varying the longitudinal and lateral lengths of virtual strain gauges could help mitigate the effects of localized strain variations, leading to more accurate measurements.

Overall, this study provides valuable insights into the combustion and mechanical behavior of APCP formulations and highlights the importance of considering both material composition and geometric factors in the development of rapid testing diagnostic systems for advanced rocket propellants.

7.2 Recommendations for Future Research

Recommendations for future research include the development of non-intrusive diagnostic techniques for measuring the internal temperature of SRMs. Work has been done by Yanlong Wei et al. [48], with their highest recorded temperature being 2017 K. High-temperature alloys or ablative material could be explored to determine whether reliable data can be attained at higher temperatures. Although the methods used in this work proved research opportunities for correlating the bulk flame temperature measurements to the predicted combustion of strand samples and or temperatures at the nozzle exit, direct measurements from within a combustion chamber would be more significant for large-scale performance analysis. Lastly, studying the effects of the nominal particle size within propellant compositions to optimize the sample dimensions would allow for a further reduction in the total batch size required for rapid material characterization testing.

REFERENCES

- [1] Tyler Allen, Andrew Demko, Mitch Johnson, Thomas Sammet, Eric Petersen, David Reid, Robert Draper, and Sudipta Seal. Study of Laboratory-Scale Burning of Composite Solid Propellant for Novel Methods of Nanoparticle Synthesis. 2013.
- [2] George P. Sutton and Oscar Biblarz. *Rocket Propulsion Elements - 9 Edition*. John Wiley Sons, 2017.
- [3] R.S. Fry. Solid Propellant Subscale Burning Rate Analysis Methods for U.S. and Selected NATO Facilities. Technical report, CPTR 75, 2002.
- [4] David R. Greatrix. *Solid-Propellant Rocket Motors*. Springer London, 2012.
- [5] K. Ramamurthi. *Rocket Propulsion*. Macmillian Publishers India Limited, 2nd edition, 2010.
- [6] Christopher Jarocki, Steven Son, Jeffrey Rhoads, Li Qiao, Sally Bane, and Gregory Blaisdell. Characterization of solid composite propellants using two-dimensional digital image correlation at large and small scales. Master's thesis, Purdue University, 2022.
- [7] Kenneth K. Kuo. *Fundamentals of Solid-Propellant Combustion*. American Institute of Aeronautics and Astronautics, 1984.
- [8] R.S.Fry. *Solid propellant test motor scaling*. CPTR 73. Chemical Propulsion Information Agency, 2001.
- [9] L Galfetti, L T De Luca, F Severini, L Meda, G Marra, M Marchetti, M Regi, and S Bellucci. Nanoparticles for solid rocket propulsion. *Journal of Physics: Condensed Matter*, 18(33):S1991–S2005, 2006.
- [10] Angelica Maria Toscano, Marco Rocco Lato, Donato Fontanarosa, and Maria Grazia De Giorgi. Optical diagnostics for solid rocket plumes characterization: A review. *Energies*, 15(4):1470, 2022.
- [11] Peihao Song, Akash Trivedi, and Clive R Siviour. Tensile testing of polymers: Integration of digital image correlation, infrared thermography and finite element modeling. *Journal of the Mechanics and Physics of Solids*, 171:105161, 2023.
- [12] B.H. Newman and G.J. Spickernell. Plastic Propellants: Aluminized Compositions. In *Explosive Research and Development Establishment*, 1961.
- [13] Randall Sobczak. Ammonium perchlorate composite basics. *Journal of Pyrotechnics*, 1996.

- [14] A. Dokhan, E.W. Price, J.M. Seitzman, and R.K. Sigman. The effects of bimodal aluminum with ultrafine aluminum on the burning rates of solid propellants. *Proceedings of the Combustion Institute*, 29(2):2939–2946, 2002.
- [15] S. Varunkumar and H.S. Mukunda. Aluminized composite propellant combustion modeling with Heterogeneous Quasi-One dimensional (HeQu1-D) approach. *Combustion and Flame*, 192:59–70, 2018.
- [16] Kathryn N. G Hoffmeyer Marcia A. Cooper Howard L. Stauffacher Michael S. Oliver Ephraim B. Washburn Yi Chen, Daniel R. Guildenecher. Study of aluminum particle combustion in solid propellant plumes using digital in-line holography and imaging pyrometry. *Combustion and Flame*, 2017.
- [17] Wilhelm Eckl and Norbert Eisenreich. Determination of the temperature in a solid and propellant flame by analysis of emission spectra. *Propellants, Explosives, Pyrotechnics*, (17):202–206, 1992.
- [18] Connor Woodruff, Steven W. Dean, Colton Cagle, Charles Luke Croessmann, and Michelle L. Pantoya. Comparing pyrometry and thermography in ballistic impact experiments. *Measurement*, 189:110488, 2022.
- [19] M.V. Mekhrengin, I.K. Meshkovskii, V.A. Tashkinov, V.I. Guryev, A.V. Sukhinets, and D.S. Smirnov. Multispectral pyrometer for high temperature measurements inside combustion chamber of gas turbine engines. *Measurement*, 139:355–360, 2019.
- [20] Daryl Dagel, Grant Grossetete, Danny MacCallum, and Scott Korey. Four-color imaging pyrometer for mapping temperatures of laserbased metal processes. *The International Society for Optics and Photonics*, 2016.
- [21] Alexander LePage Rodolphe Carro Eric Petersen, Jason Arvanites and Andreiev Powell. Monitoring strand burner combustion products using emission spectroscopy. *American Institute of Aeronautics*, 2007.
- [22] Garry Hale Paul C. Smith and . Pietrobon Raoul A. Refinement of Propellant Strand Burning Method to Suit Aluminized Composite Rocket Propellant. Technical Report DTSO-TN-1396, Weapons and Combat Systems Division, 2014.
- [23] Gordon R. Morrow. Correlating the effects of AP particle size and concentration on AP/HTPB composite propellant burning rates. Master’s thesis, Texas AM University, 2017.
- [24] Ozen Atak. Ultra sonic measurements of solid propellant burning rates in closed bombs and subscale motors. Technical Report UNIVERSITY, Middle East Technical University, 2016.
- [25] Donald H. Harrett. Solid Rocket Motor Igniters. NASA sp-8051. Technical report, NASA, 3 1971.
- [26] S. Nandagopal P.P. Singh K.K. Radhakrishnan Sunil Jain, Mehilal and B.Bhattacharya. Size and Shape of Ammonium Perchlorate and thier Influnce on Properties of Composite Propellant. *Defence Science Journal*, 59(3):294–299, 2009.

- [27] Liang Zhang Shijun Zhi and Zhibin Shen. Research on tensile mechanical properties and damage mechanism of composite solid propellants. *Propellants, Explosives, Pyrotechnics*, 2018.
- [28] Giuseppe L. DiBenedetto, Marthinus C. J. vanRamshorst, Willem Duvalois, Peter A. Hooijmeijer, and Antoine E. D. M. vanderHeijden. In-situ tensile testing of propellants in sem: Influence of temperature. *Propellants, Explosives, Pyrotechnics*, 42(12):1396–1400, 2017.
- [29] Himanshu S. and Anil D. S. Assesment of Poisson's Ratio and for Hydroxyl-Terminated Polybutadine-based Solid Rocket Propellant. *Defense Science Journal*, 60(5):497–501, 2010.
- [30] Miller Timothy. Poissons ratio extrapolation from digital image correlation experiments. AFRL-RQ-ED-TP-2013-154. Technical report, Air Force Research Laboratory (AFMC), 2013.
- [31] A. E. Oberth. Principle of strength reinforcement in filled rubbers. *Rubber Chemistry and Technology*, 40(5):1337–1363, November 1967.
- [32] Ma Quanjin, M.R.M. Rejab, Qayyum Halim, M.N.M. Merzuki, and M.A.H. Darus. Experimental investigation of the tensile test using digital image correlation (DIC) method. *Materials Today: Proceedings*, 27:757–763, 2020.
- [33] I. Yamaguchi. Speckle displacement and decorrelation in the diffraction and image fields for small object deformation. *Optica Acta: International Journal of Optics*, 28(10):1359–1376, 1981.
- [34] I. Yamguchi. A laser-speckle strain gage. *J. Phy. Eng. Sci. Instrum*, 14:1270–1273, 1981.
- [35] Junrui Li, Guobiao Yang, Thorsten Siebert, Ming F. Shi, and Lianxiang Yang. A method of the direct measurement of the true stress–strain curve over a large strain range using multi-camera digital image correlation. *Optics and Lasers in Engineering*, 107:194–201, 2018.
- [36] Sanford Gordon and Bonnie J. McBride. Computer Program for Calculations of Complex Chemical Equilibrium Compositions and Applications. i. Analysis. Technical report, NASA, 1994.
- [37] Kishore K. and Sridhara K. *Book-Solid Propellant Chemistry-HTPB*. Defence Scientific Information Documentation Centre (DESIDOC), Defense RD Organisation, 1999.
- [38] Patrick T Summers, Yanyun Chen, Christian M Rippe, Ben Allen, Adrian P Mouritz, Scott W Case, and Brian Y Lattimer. Overview of aluminum alloy mechanical properties during and after fires. *Fire Science Reviews*, 4(1), 2015.
- [39] Parker Hannifin Corporation. *Parker O-Ring Handbook ORD 5700*. Parker Hannifin Corporation, 1991.
- [40] Connor Woodruff, Steven W. Dean, and Michelle L. Pantoya. Comparison of pyrometry and thermography for thermal analysis of thermite reactions. *Applied Optics*, 60(16):4976, June 2021.

- [41] Chen Wang, He Chen, Yinчao Zhang, Siying Chen, Pan Guo, and Lifu Wang. Optical design of a crossed czerny–turner spectrometer with a linear array photomultiplier tube. *Applied Optics*, 58(28):7789, September 2019.
- [42] Stewart H. Youngblood. Design and testing of a liquid nitrous oxide and ethanol fueled rocket engine. Master’s thesis, New Mexico Institute of Mining and Technology, 2015.
- [43] Himanshu Shekhar. Studies of final modulus of solid rocket propellants in uni-axial tensile testing curves. *Science and Technology of Energetic Materials*, 70(4), 2010.
- [44] Junyan Gan, Xue Zhang, Wei Zhang, Rui Hang, Wuxi Xie, Yunfei Liu, Wen Luo, and Yu Chen. Research progress of bonding agents and their performance evaluation methods. *Molecules*, 27(2):340, 2022.
- [45] Mark A. Iadicola et al. Elizabeth M.C. A good practices guide for digital image correlation. In International Digital Image Correlation Society, editor, *Standards, Good Practices, and Uncertainty Quantification Committee*, 2018.
- [46] John R. Taylor. *An introduction to error analysis*. University Science Books, 2nd edition, 1997.
- [47] Shiang-Woei Chyuan. Studies of poisson’s ratio variation for solid propellant grains under ignition pressure loading. *International Journal of Pressure Vessels and Piping*, 80(12):871–877, 2003.
- [48] Yanlong Wei, Haijian Liang, Gao Wang, Wang Xingqi, Lu Yang, Hanchang Zhou, Luxia Yang, Xiaofang Mu, and Guimei Yin. Ultrasonic thermometric measurement system for solid rocket combustion chambers. *Ultrasonics*, 113:106361, 2021.

APPENDIX A

BATES GRAIN SURFACE REGRESSION MODELING

A.1 Ballistic Test and Evaluation System (BATES)

Ballistic test and evaluation systems (BATES) grains are standardized systems that were designed by the United States Air Force Research Laboratory (AFRL) in the 1960s with the US and NATO countries for ballistic evaluation systems. Conventionally, these systems are designed to produce neutral pressure and thrust profiles for accurate assessment of the burn rate exponent and coefficient of solid propellant compositions. Regression is assumed to occur normal to the burning surface; however, K. Klager and G. A. Zimmerman, and several others, showed that several factors such as aging, mechanical stresses, and migration of propellant ingredients affect the 1-D steady-state combustion wave causing it to deviate from the ideal case. In addition, the high strain between the propellant and bond line of large, above 0.5 m diameter, end burners have been shown to deviate from a normal regression of the combustion wave with respect to the burning surface into a conical contour, [2]. Since the current work involves much smaller grain sizes, the assumption of a 1-D combustion wave persists. The reader must be aware that if larger grains are to be modeled using this regression model, the deviation of the combustion wave from the ideal case must be considered.

A schematic of BATES grain geometry is shown in Figure A.1. The inner diameter D_i and the inner and outer lengths L_i and L_o have linear regression rates denoted by s_1 and s_2 respectively. The surface regression rate is defined as the burn rate r into dt plus the previous state of the surface regression with respect to time. The equation describing the previous statement is shown in equation A.1. This equation is then used to derive a geometrical model for the evolution of the surface regression in time.

Figure A.2 provides a general schematic of a conical frustum that is created due to the taper angle (θ_t) designed into the ends of BATES grains. The regression of the frustum has the slant height L_s which decreases in length as time progresses; however, the limiting factor of the model occurs when s_1 equals the web-thickness, $r_o - r_i$. The surface area of a conical frustum (A_f), excluding the top and bottom bases, and of the lateral surface area of the center perforation (A_c) are given by equations A.2 and A.3 where the total surface area of the initial burning surface area is given by $s_b = A_c + 2A_f$. The slant height L_s can be found by using θ and the inner and outer radius dimensions, refer to Figure A.1,. The resulting equation is shown in A.4. With these sets of equations, the surface regression with respect to time can be modeled and is shown in equation A.5. It must be noted that once the change in the r_i and L_i is accounted for, the change in L_s is naturally accounted for.

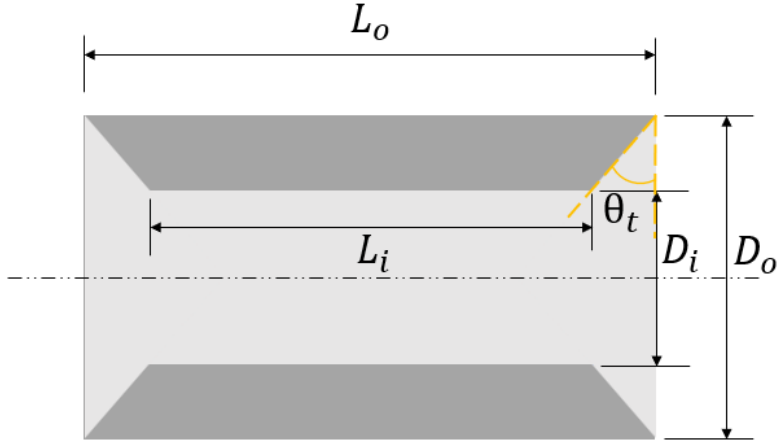


Figure A.1: Grain geometry of BATES grains with grain length L_o , inner length L_i , taper angle θ_t , and both inner and outer diameters D_i and D_o .

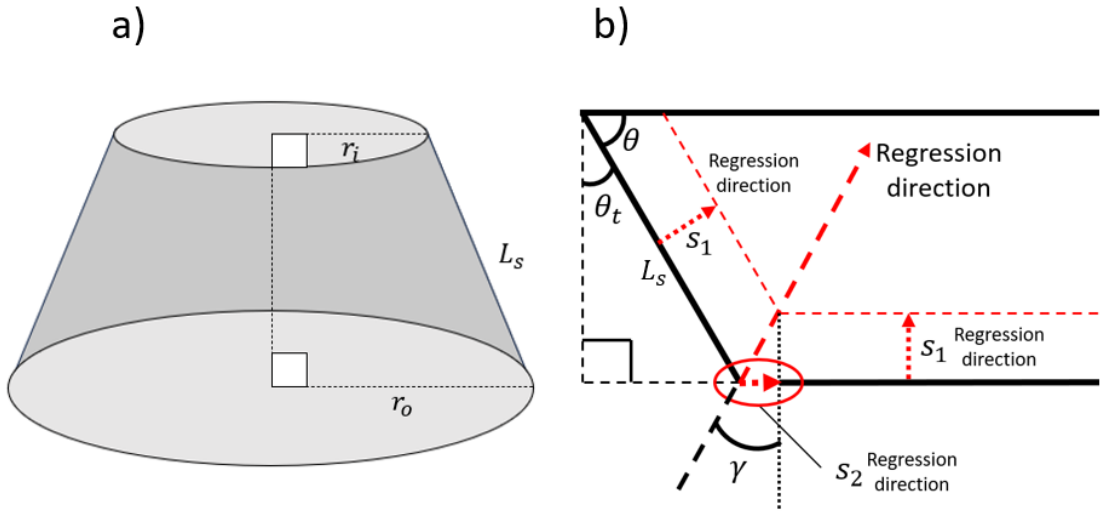


Figure A.2: a) Schematic of a conical frustum showing the inner and outer radius r_i and r_o respectively and the slant height L_s . b) A sectional view of a BATES grain highlighting the surface regression directions, s_1 and s_2 , in addition to the taper angle θ_t , the angle between the outer surface and grain ends θ , and the angle, γ , that the regression direction s_2 makes at a given time step dt .

$$s(i+1) = r(i)dt + s(i); \quad (\text{A.1})$$

$$A_f = \pi(D_0 + D_i)L_s \quad (\text{A.2})$$

$$A_c = \pi D_i L_i \quad (\text{A.3})$$

$$L_s = \frac{r_o - r_i}{\sin(\theta)} \quad (\text{A.4})$$

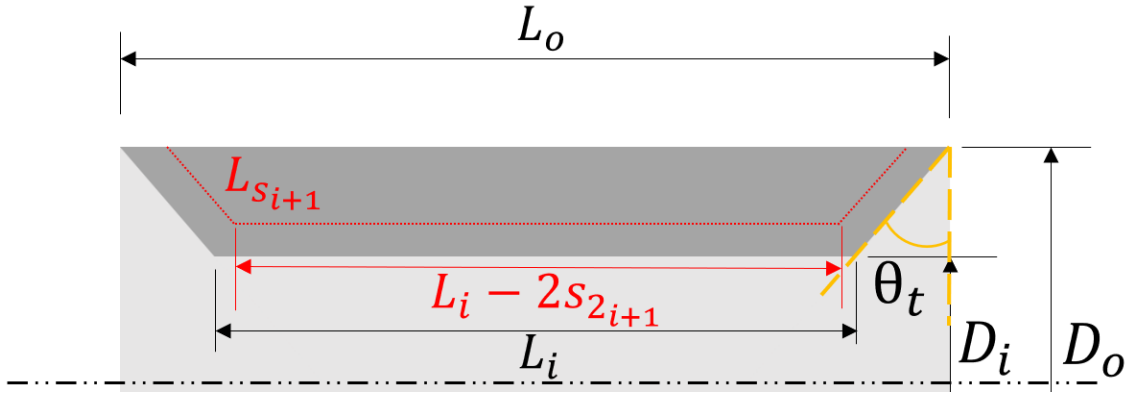


Figure A.3: A 2D contour of the burning surface is shown in red at t_{i+1} shows the inner length L_i is reduced to $L_i - 2s_{2_{i+1}}$. The new slant height, $L_{s_{i+1}}$ is shown to reduce in length which can be described by the change in the inner radius, r_i .

$$s_b(i+1) = \pi \left[(D_i + 2s_{1_{i+1}})(L_i - 2s_{2_{i+1}}) + (D_o + (D_i + 2s_{1_{i+1}})) \frac{r_o - (r_i + s_{1_{i+1}})}{\sin(\theta)} \right] \quad (\text{A.5})$$

APPENDIX B

MATLAB CODE

B.0.1 BATES Grain Ballistic Modeling

```
% This code is written to model theoretical pressure and thrust profiles
% of BATES grain geometry solid rocket motors.
% As of now, the code only simulates uninhibited surfaces.
% This code includes tapers on the ends of the grains
% Written by David Avalos
% 20240110
format long
clear all
% close all
% clc
%% Grain Parameters
N = 1; % Number of BATES grains
Inhib = 0; % Number of inhibited ends (0-2)

if Inhib == 0
    I = 2;
elseif Inhib == 1
    I = 1;
else
    I = 0;
end

% BATES grain geometry
Do = 2.4925; % Outer diameter [in]
Di = 1.2188; % Inner diameter [in]
ro = Do/2; % Outer radius
ri = Di/2; % Inner radius
Lo = 4.375; % Length [in]

theta_t = 4; % Taper angle
theta = 90 - theta_t; % Angle required for burning surface area
theta_d = (180 - theta)/2;
gamma = 90 - theta_d;

Ls = (ro - ri) / sind(theta);
Lh = Ls * cosd(theta);
Li = Lo - 2*Lh;
% Grain density and mass
rho_p = 0.0609900944; % Density of propellant from CEA [lbm/ cu in]
volume = pi/4*(Do^2 - Di^2)*Lo; % Volume of BATES grain [cu in]
mass = rho_p * volume; % Mass of a single BATES grain [lbm]
motor_mass = N * mass; % Total propellant mass of motor
web_thickness = (Do - Di)/2; % Thickness of propellant grain [in]
%% Propellant Parameters
a = 0.007708968; % Burn rate coefficient determined experimentally .0012
n = 0.4587; % Burn rate exponent determined experimentally 0.45
c_star = 1556.6*3.28084; % Determined either by CEA or experimentally [ft/s]
```

```

%% Nozzle Flow Parameters
Dt = 0.293; % Diameter of nozzle throat [in]
At = Dt^2 * (pi/4); % Area of the throat [in sq]
eps = 10.137;
Ae = At*eps;
De = sqrt(4*Ae/pi);
fprintf('Nozzle exit diameter = %4.4f in\n', De)
width = 3;
fonts = 14;
%% Slag build up correction factor
tol = 0.0005;
rt = Dt/2;
slagThickness = 0.019 - tol;
rtprime = rt - slagThickness;
Atprime = pi*(rtprime)^2;
k = ((rt - slagThickness)/rt)^2;
At = k*At;
%% Initial Surface Regression
gc = 32.2; % Correction factor [lbm-ft/lbf- sq s]
s1 = 0; % Initial surface regression rate
s2 = 0;
t = 0; % Time set to zero to find initial burning surface
Ab = pi * (Di^2*Li + (Do+Di)*Ls);
Peq = ((rho_p/gc * a * c_star * Ab)/At)^(1/(1-n)); % Equilibrium pressure assuming density of gas is negligible [psi]
r = a*Peq^n; % Burn rate using Veille's Law [in/s]
Kn = Ab/At; % Ratio of initial burning area to nozzle throat area [dimless]
%% Pressure Profile
dt = 0.0001; % Time step to ensure surface regression is not more than web_thickness
i = 1; % Matrix indexing
% The following while loop determines the equilibrium pressure of the motor
% It must be noted that the density of the gas is assumed to be negligible
% when compared to the density of the propellant ( $\rho_p - \rho_g$ ) =  $\rho_p$ 
% and nozzle erosion and grain erosion is neglected at this point
while s1(i) <= web_thickness
    if s1(i) == web_thickness % if statement breaks while loop when propellant is consumed
        break
    end
    t(i+1) = t(i) + dt; % Burn time
    s1(i+1) = r(i)*dt + s1(i); % Surface regression wrt time
    s2(i+1) = tand(gamma) * s1(i+1);
    Ab(i+1) = N*pi*((Di + 2*s1(i+1))*(Li - 2*s2(i+1)) + (Do + (Di + 2*s1(i+1))) * ((ro - (ri +
    s1(i+1)))/sin(theta))); % Burning surface history
    Peq(i+1) = ((rho_p/gc * a * c_star * Ab(i+1))/At)^(1/(1-n)); % Equilibrium pressure history [psi]
    r(i+1) = a*Peq(i+1)^n; % Burn rate using Veille's Law [in/s]
    Kn(i+1) = Ab(i+1)/At; % Ratio of burning area to nozzle throat area [dimless]
    i = i+1;
end

```

```

%% Print out motor characteristics and plot the pressure history
% Motor parameters
fprintf('Initial Kn = %3.1f \n', Kn(1))
fprintf('Max Kn = %3.1f \n', max(Kn))
fprintf('Final Kn = %3.1f \n', Kn(length(t)))
fprintf('Max pressure = %4.2f psi \n', max(Peq))
fprintf('Burn time = %3.2f sec \n', t(length(t)))
% Plot figure for pressure
figure()
yyaxis left
plot(t,Peq*0.00689476,'LineWidth',width)
% hold on
% plot(t,Kn)
grid on
ylabel('Pressure (MPa)','FontSize',fonts)
xlabel(' Time (s)',FontSize,fonts)
ylim([0 (max(Peq)*0.00689476+1)])
xlim([-0.1 (t(length(t)) + 0.1)])
%% Theoretical Motor Characteristics
k = 1.2256; % Specific heat ratio from CEA at 1000 psi
Ru = 1545; % Universal Gas constant [ft-lbf/lbm-mol-°R]
MW = 24.279; % Molecular weight from CEA
R = Ru/MW; % Gas Constant
T1_CEA = 3022; % Stagnation chamber temp from CEA [K]
T1 = T1_CEA * 1.8; % Stagnation temperature [°R]
vt = sqrt(k*R*T1); % Velocity at throat [ft/s]
m_dot1 = At.*Peq.*k.* (sqrt((2/(k-1))^((k+1)/(k-1))))/ vt;
m_dot2 = Ab.*rho_p.*r;
Pt = Peq./((1 + ((k-1)/2))^((k/(k-1))));

syms m
e1 = 1/m;
e2 = (k+1)/2;
e3 = 1 + (((k-1)/2) * m.^2);
e4 = (k+1)/(2 - 2^k);
eqn = (e1 * (e2/e3)^e4) == eps;
S = vpasolve(eqn,eps);
M = double(S(1));
Pe = Peq.* (1/ ((1+ ((k-1)/2)*M^2))^((k/(k-1))));
P3 = 12.5;
F = At.*Peq.*sqrt((2*k^2)/(k - 1) * (2/(k+1))^((k+1)/(k-1)) *...
(1 - (Pe./Peq).^(k-1/k))) + (Pe - P3).*Ae;
yyaxis right
plot(t, F*4.44822,'LineWidth',width)
ylabel('Force (N)','FontSize',fonts)

ylim([0 max(F)*4.44822 + 250])
%% Save

```

```
time = t;
Pressure = Ped;
Force = F;
save("1000PSI_TOT.mat", "time", "Pressure", "Force")
```

B.0.2 Strand Burner Burn Rate Analysis

```

ylim([0 max(cellpressure(:,2))*0.00689476+2.5])
ylabel('Pressure (MPa)')
hold on
yyaxis right
plot(cellwire(:,1), cellwire(:,2), cellwire(:,1), cellwire(:,3),...
      cellwire(:,1), cellwire(:,4), cellwire(:,1), cellwire(:,5), ...
      cellwire(:,1), cellwire(:,6), cellwire(:,1), cellwire(:,7))
ylabel('mV')
xlabel('Time (s)')
% title('select points (from left-to-right) when trigger wires drop to "0 mV" and press "Enter"')

grid minor
tol = 0.01;
[a] = ginput;
A = find(abs(cellwire(:,1) - a(1,1)) < tol);
B = find(abs(cellwire(:,1) - a(2,1)) < tol);
C = find(abs(cellwire(:,1) - a(3,1)) < tol);
D = find(abs(cellwire(:,1) - a(4,1)) < tol);
E = find(abs(cellwire(:,1) - a(5,1)) < tol);
F = find(abs(cellwire(:,1) - a(6,1)) < tol);

d = 0.5;
burntime = [cellwire(A(1),1) cellwire(B(1),1), cellwire(C(1),1),...
            cellwire(D(1),1), cellwire(E(1),1), cellwire(F(1),1)];
burntime = burntime - burntime(1);
r_i = [d/(burntime(2)-burntime(1)) d/(burntime(3)-burntime(2))...
        d/(burntime(4)-burntime(3)) d/(burntime(5)-burntime(4))...
        d/(burntime(6)-burntime(5))];
log_r{i,f} = log10(r_i*25.4);
r{i,f} = r_i;
p{i,f} = [mean(cellpressure(A(1):B(1), 2)),...
           mean(cellpressure(B(1):C(1), 2)), ...
           mean(cellpressure(C(1):D(1), 2)),...
           mean(cellpressure(D(1):E(1), 2)),...
           mean(cellpressure(E(1):F(1), 2))];
log_p{i,f} = log10(p{i,f}*0.00689476);
ptime{i,f} = cellpressure(A(1):F(1), 1);
close all
end
end
%% Plot r vs P and determine a and n
r_si = [];
P = [];
for i = 1: numel(p)
    r_si = [r_si, r{i}*25.4];
    P = [P, p{i}*0.00689476];
end

```

```

x = log(P);
y = log(r_si);
coeffs = polyfit(x, y, 1);
n = coeffs(1);
log_a = coeffs(2);
a = exp(log_a);

fprintf('Burn rate coefficient (a): %.6f \n', a)
fprintf('Exponent (n): %.4f\n', n)
figure()
loglog(P, r_si, 'k.', 'MarkerFaceColor', 'k');
hold on
h = loglog(P, a * P.^n, 'r-');
grid on
xlabel('Pressure (MPa)')
ylabel('Burn Rate (in/s)')
xlim([10^0 10^1])
ylim([10^0 10^1])
title('Burn Rate vs Pressure on Log-Log Scale')
legendText = sprintf('r = %.2f P^{%.4f}', a, n);
legend(h(1), {legendText})
hold off
% % Save Data
save("H10SB.mat", "a", "n", "r", "p")

```

B.0.3 SRM Burn Rate Analysis

```
% This code was developed to extract excel files from the rocket test stand
% from REF and perform burn rate analysis using the average mass balance
% method r_MB and the thickness/time r_tot for determining the burn rate
% coefficient and exponent of an APCP with H-10 aluminum powder
% Written on 07/09/2024 by David Avalos
format long
close all
clear all
clc
i = 1;
%% Load data from file path for pressure and force data for 500 - 1000 psi
filePath500 = 'C:\Users\dflav\Desktop\StaticFire\davidSStatic_PressForce\H10\500\test1';
filePath750 = 'C:\Users\dflav\Desktop\StaticFire\davidSStatic_PressForce\H10\750\test1';
filePath1000T1 = 'C:\Users\dflav\Desktop\StaticFire\davidSStatic_PressForce\H10\1000\test1';
filePath1000T2 = 'C:\Users\dflav\Desktop\StaticFire\davidSStatic_PressForce\H10\1000\test2';
filePath1000T3 = 'C:\Users\dflav\Desktop\StaticFire\davidSStatic_PressForce\H10\1000\test3';
%% Load and plot 500 psi test and find burn rate
fixp = 0.000001;
Data = dir(filePath500);
DataStruct = {Data.name};
DataStruct = DataStruct(~ismember(DataStruct , {'.'})); % Remove the current directory entry
path(path,filePath500)
Pressure = xlsread(DataStruct{2});
Pressure(:,1) = datenum(Pressure(:,1));
Pressure(:,1) = (Pressure(:,1) - Pressure(1)) * 24 * 3600;
% Trim data for force and pressure curves
tol = 0.001;
figure()
plot(Pressure(:,1),Pressure(:,2))
grid minor
[a_tot,b] = ginput;
e = find(abs(Pressure(:,1) - a_tot(1)) < tol);
start_idx = e(1);
f = find(abs(Pressure(:,1) - a_tot(2)) < tol);
end_idx = f(1);
tp = Pressure(start_idx:end_idx,1) - Pressure(start_idx);
P = Pressure(start_idx:end_idx,2);
close(figure(1))
figure()
plot(tp, P*0.00689476)
grid minor
title('Experimental Pressure')
xlabel('Time (s)')
ylabel('Pressure (MPa)')
ylim([min(P)*0.00689476 - 1, max(P)*0.00689476 + 1])
clearvars a b e f
% Mass Balance Method
Do = 2.4925; % Outer diameter [in]
```

```

Di = 1.2335; % Inner diameter [in]
W_avg = (Do - Di)/2; % Thickness of propellant grain [in]
figure(1)
title('Select time points for A, D, and E and press "Enter"')
[a_tot] = ginput;
A = find(abs(tp - a_tot(1,1)) < tol);
A = A(1);
D = find(abs(tp - a_tot(2,1)) < tol);
D = D(1);
E = find(abs(tp - a_tot(3,1)) < tol);
E = E(1);
avgPressure(i) = mean(P(D:E)*0.00689476);
b = avgPressure(i)*fixp;
tol = 0.1;
[y_tot] = find(abs(P - b) < tol);
B = y_tot(1);
G = y_tot(end);
t_b = tp(E) - tp(B);
BE_Pressure = P(B:E);
AG_Pressure = P(A:G);
Time_BE = tp(B:E);
Time_AG = tp(A:G);
integral_AG = trapz(Time_AG,AG_Pressure);
integral_BE = trapz(Time_BE,BE_Pressure);
r_mb = (W_avg/t_b) * (integral_AG/integral_BE);
% Thickness/time
figure(1)
title('Select point of first pressure rise and press "Enter"')
x_zoom = [0,1];
y_zoom = [-0.35, avgPressure(i)];
xlim(x_zoom)
ylim(y_zoom)
o = ginput;
O = find(abs(tp - o(1)) < 0.001);
O = O(1);

figure(1)
title('Select point H and press "Enter"')
x_zoom = [t_b,tp(end)];
y_zoom = [-0.35, avgPressure(i)];
xlim(x_zoom)
ylim(y_zoom)
h = ginput;
H = find(abs(tp - h(1)) < 0.001);
H = H(1);
OH_Pressure = P(O:H);
DE_Pressure = P(D:E);
Time_OH = tp(O:H);

```

```

Time_DE = tp(D:E);
integral_OH = trapz(Time_OH,OH_Pressure);
integral_DE = trapz(Time_DE,DE_Pressure);
t_bTOT = (tp(E) - tp(B))*(integral_OH/integral_DE);
r_tot = W_avg/t_bTOT;

R_MB(i) = r_mb;
R_TOT(i) = r_tot;
fprintf('r_mb = %2.4f in/s \n',r_mb)
fprintf('r_tot = %2.4f in/s \n',r_tot)
% clearvars A B D E G H O r_mb r_tot Data DataStruct Pressure Di
close all
i = i+1;
%% Load and plot 750 psi test and find burn rate
Data = dir(filePath750);
DataStruct = {Data.name};
DataStruct = DataStruct(~ismember(DataStruct , {'.'})); % remove current directory
path(path filePath750)
Pressure = xlsread(DataStruct{2});
Pressure(:,1) = datenum(Pressure(:,1));
Pressure(:,1) = (Pressure(:,1) - Pressure(1)) * 24 * 3600;
% Trim data for force and pressure curves
tol = 0.001;
figure()
plot(Pressure(:,1),Pressure(:,2))
grid minor
[a_tot,b] =гинput;
e = find(abs(Pressure(:,1) - a_tot(1)) < tol);
start_idx = e(1);
f = find(abs(Pressure(:,1) - a_tot(2)) < tol);
end_idx = f(1);
tp = Pressure(start_idx:end_idx,1) - Pressure(start_idx);
P = Pressure(start_idx:end_idx,2);
close(figure(1))
figure()
plot(tp, P*0.00689476)
grid minor
title('Experimental Pressure')
xlabel('Time (s)')
ylabel('Pressure (MPa)')
ylim([min(P)*0.00689476 - 1, max(P)*0.00689476 + 1])
clearvars a b e f
% Mass Balance Method
Do = 2.4925; % Outer diameter [in]
Di = 1.2265; % Inner diameter [in]
W_avg = (Do - Di)/2; % Thickness of propellant grain [in]
figure(1)
title('Select time points for A, D, and E and press "Enter"')

```

```

[a_tot] = ginput;
A = find(abs(tp - a_tot(1,1)) < tol);
A = A(1);
D = find(abs(tp - a_tot(2,1)) < tol);
D = D(1);
E = find(abs(tp - a_tot(3,1)) < tol);
E = E(1);
avgPressure(i) = mean(P(D:E)*0.00689476);
b = avgPressure(i)*fixp;
tol = 0.1;
[y_tot] = find(abs(P - b) < tol);
B = y_tot(1);
G = y_tot(end);
t_b = tp(E) - tp(B);
BE_Pressure = P(B:E);
AG_Pressure = P(A:G);
Time_BE = tp(B:E);
Time_AG = tp(A:G);
integral_AG = trapz(Time_AG,AG_Pressure);
integral_BE = trapz(Time_BE,BE_Pressure);
r_mb = (W_avg/t_b) * (integral_AG/integral_BE);
% Thickness/time
figure(1)
title('Select point of first pressure rise and press "Enter"')
x_zoom = [0,1];
y_zoom = [-0.35, avgPressure(i)];
xlim(x_zoom)
ylim(y_zoom)
o = ginput;
O = find(abs(tp - o(1)) < 0.001);
O = O(1);

figure(1)
title('Select point H and press "Enter"')
x_zoom = [t_b,tp(end)];
y_zoom = [-0.35, avgPressure(i)];
xlim(x_zoom)
ylim(y_zoom)
h = ginput;
H = find(abs(tp - h(1)) < 0.001);
H = H(1);
OH_Pressure = P(O:H);
DE_Pressure = P(D:E);
Time_OH = tp(O:H);
Time_DE = tp(D:E);
integral_OH = trapz(Time_OH,OH_Pressure);
integral_DE = trapz(Time_DE,DE_Pressure);
t_bTOT = (tp(E) - tp(B))*(integral_OH/integral_DE);

```

```

r_tot = W_avg/t_bTOT;

R_MB(i) = r_mb;
R_TOT(i) = r_tot;
fprintf('r_mb = %2.4f in/s \n',r_mb)
fprintf('r_tot = %2.4f in/s \n',r_tot)
clearvars A B D E G H O r_mb r_tot Data DataStruct Pressure Di
close all
i = i+1;
%% Load and plot 1000 psi test 1 and find burn rate
Data = dir(filePath1000T1);
DataStruct = {Data.name};
DataStruct = DataStruct(~ismember(DataStruct ,{'.','.'}));
path(path filePath1000T1)
Pressure = xlsread(DataStruct{2});
Pressure(:,1) = datenum(Pressure(:,1));
Pressure(:,1) = (Pressure(:,1) - Pressure(1)) * 24 * 3600;
% Trim data for force and pressure curves
tol = 0.001;
figure()
plot(Pressure(:,1),Pressure(:,2))
grid minor
[a_tot,b] = ginput;
e = find(abs(Pressure(:,1) - a_tot(1)) < tol);
start_idx = e(1);
f = find(abs(Pressure(:,1) - a_tot(2)) < tol);
end_idx = f(1);
tp = Pressure(start_idx:end_idx,1) - Pressure(start_idx);
P = Pressure(start_idx:end_idx,2);
close(figure(1))
figure()
plot(tp, P*0.00689476)
grid minor
title('Experimental Pressure')
xlabel('Time (s)')
ylabel('Pressure (MPa)')
ylim([min(P)*0.00689476 - 1, max(P)*0.00689476 + 1])
clearvars a b e f
% Mass Balance Method
Do = 2.4925; % Outer diameter [in]
Di = 1.2320; % Inner diameter [in]
W_avg = (Do - Di)/2; % Thickness of propellant grain [in]
figure(1)
title('Select time points for A, D, and E and press "Enter"')
[a_tot] = ginput;
A = find(abs(tp - a_tot(1,1)) < tol);
A = A(1);
D = find(abs(tp - a_tot(2,1)) < tol);

```

```

D = D(1);
E = find(abs(tp - a_tot(3,1)) < tol);
E = E(1);
avgPressure(i) = mean(P(D:E)*0.00689476);
b = avgPressure(i)*fixp;
tol = 0.1;
[y_tot] = find(abs(P - b) < tol);
B = y_tot(1);
G = y_tot(end);
t_b = tp(E) - tp(B);
BE_Pressure = P(B:E);
AG_Pressure = P(A:G);
Time_BE = tp(B:E);
Time_AG = tp(A:G);
integral_AG = trapz(Time_AG,AG_Pressure);
integral_BE = trapz(Time_BE,BE_Pressure);
r_mb = (W_avg/t_b) * (integral_AG/integral_BE);
% Thickness/time
figure(1)
title('Select point of first pressure rise and press "Enter"')
x_zoom = [0,1];
y_zoom = [-0.35, avgPressure(i)];
xlim(x_zoom)
ylim(y_zoom)
o = ginput;
O = find(abs(tp - o(1)) < 0.001);
O = O(1);

figure(1)
title('Select point H and press "Enter"')
x_zoom = [t_b,tp(end)];
y_zoom = [-0.35, avgPressure(i)];
xlim(x_zoom)
ylim(y_zoom)
h = ginput;
H = find(abs(tp - h(1)) < 0.001);
H = H(1);
OH_Pressure = P(O:H);
DE_Pressure = P(D:E);
Time_OH = tp(O:H);
Time_DE = tp(D:E);
integral_OH = trapz(Time_OH,OH_Pressure);
integral_DE = trapz(Time_DE,DE_Pressure);
t_bTOT = (tp(E) - tp(B))*(integral_OH/integral_DE);
r_tot = W_avg/t_bTOT;

R_MB(i) = r_mb;
R_TOT(i) = r_tot;

```

B.0.4 Bulk Flame Temperature Analysis

```
% This code was written for extracting excel data from the 4-color
% pyrometer to perform bulk flame temperature measurements of the exhaust
% plume of a SRM using an APCP with H-10 aluminum powder and can be adjusted
% pyrometry measurements
format long
close all
clear all
clc
%% Calibration using 2700K lamp
% wavelength1000ThorLabs = 0.981918272720474;
% wavelength700ThorLabs = 0.557659957281691;
% wavelength600ThorLabs = 0.3275505249915;
% wavelength550ThorLabs = 0.218427248311306;
%
% wavelength1000BB = 0.291224232037272;
% wavelength700BB = 0.648995649798499;
% wavelength600BB = 0.411364132920225;
% wavelength550BB = 0.291224232037272;
%% Calibration using 1900K lamp
wavelength1000 = 0.936991523340057;
wavelength700 = 0.226995353472629;
wavelength600 = 0.0798951994581979;
wavelength550 = 0.0383814333222495;

wavelength1000BB = 0.603113127295186;
wavelength700BB = 0.139330128436196;
wavelength600BB = 0.0495538329656811;
wavelength550BB = 0.0242831144976211;
%% Load in all excel data
windowsize = 100;
vscale1 = 5e-2;
vscale2 = 5e-2;
vscale3 = 5e-2;
vscale4 = 2e-2;
% defining the wavelengths and emissivity of the channels 1,2,3,4 respectively
lambda1 = 1000e-9;
lambda2 = 700e-9;
lambda3 = 600e-9;
lambda4 = 550e-9;
% Black Body
eps1000 = 1;
eps700 = 1;
eps600 = 1;
eps550 = 1;

filePath = 'C:\Users\dflav\Desktop\StaticFire\davidStatic_Pyrometer\H3\1000\test1';
Data = dir(filePath);
FolderName = {Data.name};
```

```

FolderName = FolderName(~ismember(FolderName , {'..'}));
path(path,filePath)
range = 'A13:E100012';
ambient = readmatrix(FolderName{1}, 'Range', range);
ambient(isnan(ambient)) = 0;
ambient(:,1) = ambient(:,1) + abs(ambient(1));
burn = readmatrix(FolderName{2}, 'Range', range);
burn(isnan(burn)) = 0;
burn(:,1) = burn(:,1) + abs(burn(1));
cal = readmatrix(FolderName{3}, 'Range', range);
cal(isnan(cal)) = 0;
cal(:,1) = cal(:,1) + abs(cal(1));
Time = burn(:,1);

%% Fix zero on vertical axis for ambient, cal, and burn data
avgPoints = 1000;
windowsize = 75;
lambda1 = 1000e-9;
lambda2 = 700e-9;
lambda3 = 600e-9;
lambda4 = 550e-9;
eps1000 = 1;
eps700 = 1;
eps600 = 1;
eps550 = 1;

ambient(:,2) = ((ambient(:,2) - mean(ambient(end - avgPoints:end, 2))).*eps1000);
ambient(:,3) = ((ambient(:,3) - mean(ambient(end - avgPoints:end, 3))).*eps700);
ambient(:,4) = ((ambient(:,4) - mean(ambient(end - avgPoints:end, 4))).*eps600);
ambient(:,5) = ((ambient(:,5) - mean(ambient(end - avgPoints:end, 5))).*eps550);

cal(:,2) = ((cal(:,2) - mean(cal(end - avgPoints:end, 2))).*eps1000);
cal(:,3) = ((cal(:,3) - mean(cal(end - avgPoints:end, 3))).*eps700);
cal(:,4) = ((cal(:,4) - mean(cal(end - avgPoints:end, 4))).*eps600);
cal(:,5) = ((cal(:,5) - mean(cal(end - avgPoints:end, 5))).*eps550);

tol = 0.05;
figure()
plot(cal(:,1), cal(:,2))
[a] = ginput;
start_idx = find(abs(cal(:,1) - a(1,1)) < tol);
Cal(:,1) = cal(start_idx:end,1);
Cal(:,2) = norm(cal(start_idx:end,2));
Cal(:,3) = norm(cal(start_idx:end,3));
Cal(:,4) = norm(cal(start_idx:end,4));
Cal(:,5) = norm(cal(start_idx:end,5));

burn(:,2) = ((burn(:,2) - mean(burn(end - avgPoints:end, 2))).*eps1000);

```

```

burn(:,3) = ((burn(:,3) - mean(burn(end - avgPoints:end, 3))).*eps700);
burn(:,4) = ((burn(:,4) - mean(burn(end - avgPoints:end, 4))).*eps600);
burn(:,5) = ((burn(:,5) - mean(burn(end - avgPoints:end, 5))).*eps550);

calchannel1 = movmean(Cal(:,2), windowsize);
calchannel2 = movmean(Cal(:,3), windowsize);
calchannel3 = movmean(Cal(:,4), windowsize);
calchannel4 = movmean(Cal(:,5), windowsize);

ambientchannel1 = movmean(ambient(:,2), windowsize);
ambientchannel2 = movmean(ambient(:,3), windowsize);
ambientchannel3 = movmean(ambient(:,4), windowsize);
ambientchannel4 = movmean(ambient(:,5), windowsize);

burnChannel1 = movmean(burn(:,2), windowsize);
burnChannel2 = movmean(burn(:,3), windowsize);
burnChannel3 = movmean(burn(:,4), windowsize);
burnChannel4 = movmean(burn(:,5), windowsize);

correctionFacotorCh1 = mean(calchannel1./wavelength1000);
correctionFacotorCh2 = mean(calchannel2./wavelength700);
correctionFacotorCh3 = mean(calchannel3./wavelength600);
correctionFacotorCh4 = mean(calchannel4./wavelength550);

correctedChannel1 = abs((burnChannel1 - mean(ambientchannel1))./correctionFacotorCh1);
correctedChannel2 = abs((burnChannel2 - mean(ambientchannel2))./correctionFacotorCh2);
correctedChannel3 = abs((burnChannel3 - mean(ambientchannel3))./correctionFacotorCh3);
correctedChannel4 = abs((burnChannel4 - mean(ambientchannel4))./correctionFacotorCh4);

% correctedChannel1 = (burnChannel1 - mean(ambientchannel1));
% correctedChannel2 = (burnChannel2 - mean(ambientchannel2));
% correctedChannel3 = (burnChannel3 - mean(ambientchannel3));
% correctedChannel4 = (burnChannel4 - mean(ambientchannel4));
% % Use ginput() to select bounds on the event
figure(), plot(Time, correctedChannel1, Time, correctedChannel2, Time, ...
    correctedChannel3, Time, correctedChannel4)

legend('ch1', 'ch2', 'ch3', 'ch4')
grid minor
title('Select the start and end of the event and press "Enter"')
tol = 0.01;
[a] = ginput;
A = find(abs(Time - a(1,1)) < tol);
A = A(1);
D = find(abs(Time - a(2,1)) < tol);
D = D(1);

```

```

channel1 = correctedChannel1(A:D);
channel2 = correctedChannel2(A:D);
channel3 = correctedChannel3(A:D);
channel4 = correctedChannel4(A:D);
Timebg = Time;
Time = Time(A:D);
Time = Time - Time(1);

h = 6.62607015e-34; % Plank's constant [sq m / kg s]
c = 299792458; % Speed of light in vaccum [m/s]
k = 1.380649e-23; % Boltzmann's constant [sq m kg /sq s K]
C1 = 2*h*(c^2); % W/ sq m
C2 = (h*c) / k; % m K

% Emmissivity of 1
ch1_ybg = C2/lambda1;
ch1_xbg = log(C1) - log((lambda1.^5).*correctedChannel1);
ch1_xbg = real(ch1_xbg);
ch2_ybg = C2/lambda2;
ch2_xbg = log(C1) - log((lambda2.^5).*correctedChannel2);
ch2_xbg = real(ch2_xbg);
ch3_ybg = C2/lambda3;
ch3_xbg = log(C1) - log((lambda3.^5).*correctedChannel3);
ch3_xbg = real(ch3_xbg);
ch4_ybg = C2/lambda4;
ch4_xbg = log(C1) - log((lambda4.^5).*correctedChannel4);
ch4_xbg = real(ch4_xbg);

y = [ch1_ybg ch2_ybg ch3_ybg ch4_ybg];
for i = 1:numel(ch1_xbg)
    x = [ch1_xbg(i) ch2_xbg(i) ch3_xbg(i) ch4_xbg(i)];
    p = polyfit(x,y,1);
    T_bg(i) = p(1);
end

ch1_y = C2/lambda1;
ch1_x = log(C1) - log((lambda1.^5).*channel1);
ch1_x = real(ch1_x);
ch2_y = C2/lambda2;
ch2_x = log(C1) - log((lambda2.^5).*channel2);
ch2_x = real(ch2_x);
ch3_y = C2/lambda3;
ch3_x = log(C1) - log((lambda3.^5).*channel3);
ch3_x = real(ch3_x);
ch4_y = C2/lambda4;
ch4_x = log(C1) - log((lambda4.^5).*channel4);
ch4_x = real(ch4_x);

```

```

y = [ch1_y ch2_y ch3_y ch4_y];
for i = 1:numel(ch1_x)
    x = [ch1_x(i) ch2_x(i) ch3_x(i) ch4_x(i)];
    p = polyfit(x,y,1);
    T(i) = p(1);
end

avg_temp = mean(T);
std_Temp = std(T,0,'all');
figure()
ax = gca();
% ax.FontSize = 12;
figure()

yyaxis right
h(1) = plot(Time,T,'-k');
hold on
h(2) = plot(Time, avg_temp*ones(size(Time)), 'c', 'LineWidth', 2);
h(3) = plot(Time, (avg_temp + std_Temp)*ones(size(Time)), 'm--', 'LineWidth', 2);
plot(Time, (avg_temp - std_Temp)*ones(size(Time)), 'm--', 'LineWidth', 2);
ylabel('Temperature (K)','FontSize', 20)
% ylabel('Temperature (K)')
% ylabel('Temperature (K)')
xlabel('Time (s)')

ylim([min(T_bg)/2 max(T_bg)/2])
title_text = sprintf('Average bulk flame temperature: %.2f K', avg_temp);
latex_part = '$\epsilon$ = const.$';
title([title_text, latex_part], 'Interpreter', 'latex');
yyaxis left
h(4) = plot(Time, channel1,'Color',[0.6350 0.0780 0.1840]);
h(5) = plot(Time, channel2,'Color','r');
h(6) = plot(Time, channel3,'Color',[0.8500 0.3250 0.0980]);
h(7) = plot(Time, channel4,'Color',[0.4660 0.6740 0.1880]);
ylabel('Arbitrary units','FontSize', 20)
% plot(Timebg, correctedChannel1, Timebg, correctedChannel2, Timebg, ...
% correctedChannel3, Timebg, correctedChannel4)
uncertainty_BB = std_Temp/sqrt(numel(T));
grid minor
% legend('Selected experimental data', 'Data history','Pyrometer data')
legend([h(1), h(2), h(3), h(4), h(5), h(6),h(7)],...
    'Experimental data', 'T_{avg}',...
    'Error bars', '\lambda_{1000}', '\lambda_{700}', '\lambda_{650}',...
    '\lambda_{550}', 'FontSize', 18)
hold off

figure()

```

```

plot(Time,T,'-k')
hold on
plot(Time, avg_temp*ones(size(Time)), 'b', 'LineWidth', 2);
plot(Time, (avg_temp + std_Temp)*ones(size(Time)), 'r-', 'LineWidth', 2);
plot(Time, (avg_temp - std_Temp)*ones(size(Time)), 'r--', 'LineWidth', 2);

grid minor
xlabel('Time (s)')
ylabel('Temperature (K)')
ylim([0.5*avg_temp-std_Temp 1.5*avg_temp+std_Temp])
title_text = sprintf('Average bulk flame temperature: %.2f K (+/- %.2f K)', avg_temp, std_Temp);
latex_part = '$\epsilon_{\text{approx}}$';
title({title_text, latex_part}, 'Interpreter', 'latex');
legend('Selected experimental data', 'Average bulk temperature','Error bars')
hold off

figure;
histogram(T, 100);
grid on
title_text = sprintf('Histogram of Temperature: %.2f K', avg_temp);
latex_part = '$\epsilon_{\text{approx}}$';
title({title_text, latex_part}, 'Interpreter', 'latex');
xlabel('Temperature (K)');
ylabel('Frequency')
clearvars negmask T
hold off
%%%%%%%%%%%%%
%%%%%%%%%%%%%
% Emmissivity of 1/lambda^-
ch1_y = C2/lambda1;
ch1_x = log(C1) - log(((lambda1.^5).*channel1)/lambda1^-1);
ch1_x = real(ch1_x);
ch2_y = C2/lambda2;
ch2_x = log(C1) - log(((lambda2.^5).*channel2)/lambda2^-1);
ch2_x = real(ch2_x);
ch3_y = C2/lambda3;
ch3_x = log(C1) - log(((lambda3.^5).*channel3)/lambda3^-1);
ch3_x = real(ch3_x);
ch4_y = C2/lambda4;
ch4_x = log(C1) - log(((lambda4.^5).*channel4)/lambda4^-1);
ch4_x = real(ch4_x);

y = [ch1_y ch2_y ch3_y ch4_y];
for i = 1:numel(ch1_x)
    x = [ch1_x(i) ch2_x(i) ch3_x(i) ch4_x(i)];
    p = polyfit(x,y,1);
    T(i) = p(1);
end

```

```

avg_temp = mean(T);
std_Temp = std(T,0,'all');
figure()
plot(Time,T,'k')
hold on
plot(Time, avg_temp*ones(size(Time)), 'b', 'LineWidth', 2);
plot(Time, (avg_temp + std_Temp)*ones(size(Time)), 'r-', 'LineWidth', 2);
plot(Time, (avg_temp - std_Temp)*ones(size(Time)), 'r--', 'LineWidth', 2);
grid minor
xlabel('Time (s)')
ylabel('Temperature (K)')
ylim([0.5*avg_temp-std_Temp 1.5*avg_temp+std_Temp])
title_text = sprintf('Average bulk flame temperature: %.2f K (+/- %.2f K)', avg_temp, std_Temp);
latex_part = '$\epsilon = 1/\{\lambda^{-1}\}$';
title({title_text, latex_part}, 'Interpreter', 'latex');
legend('Experimental data', 'Average bulk temperature', 'Upper and Lower error bars')
hold off
uncertainty_lam2 = std_Temp/sqrt(numel(T));

figure;
histogram(T, 100);
grid on
title_text = sprintf('Histogram of Temperature: %.2f K', avg_temp);
latex_part = '$\epsilon = 1/\{\lambda^{-1}\}$';
title({title_text, latex_part}, 'Interpreter', 'latex');
xlabel('Temperature (K)');
ylabel('Frequency');
%%%%%%%%%%%%%%%
%%%%%%%%%%%%%%%
% Emissivity of 1/lambda^-2
ch1_y = C2/lambda1;
ch1_x = log(C1) - log(((lambda1.^5).*channel1)/lambda1^-2);
ch1_x = real(ch1_x);
ch2_y = C2/lambda2;
ch2_x = log(C1) - log(((lambda2.^5).*channel2)/lambda2^-2);
ch2_x = real(ch2_x);
ch3_y = C2/lambda3;
ch3_x = log(C1) - log(((lambda3.^5).*channel3)/lambda3^-2);
ch3_x = real(ch3_x);
ch4_y = C2/lambda4;
ch4_x = log(C1) - log(((lambda4.^5).*channel4)/lambda4^-2);
ch4_x = real(ch4_x);

y = [ch1_y ch2_y ch3_y ch4_y];
for i = 1:numel(ch1_x)
    x = [ch1_x(i) ch2_x(i) ch3_x(i) ch4_x(i)];
    p = polyfit(x,y,1);

```

```

T(i) = p(1);
end

avg_temp = mean(T);
std_Temp = std(T,0,'all');
figure()
plot(Time,T,'k')
hold on
plot(Time, avg_temp*ones(size(Time)), 'b', 'LineWidth', 2);
plot(Time, (avg_temp + std_Temp)*ones(size(Time)), 'r--', 'LineWidth', 2);
plot(Time, (avg_temp - std_Temp)*ones(size(Time)), 'r--', 'LineWidth', 2);
grid minor
xlabel('Time (s)')
ylabel('Temperature (K)')
ylim([0.5*avg_temp-std_Temp 1.5*avg_temp+std_Temp])
title_text = sprintf('Average bulk flame temperature: %.2f K (+/- %.2f K)', avg_temp, std_Temp);
latex_part = '$\epsilon = 1/\{\lambda^{-2}\}$';
title({title_text, latex_part}, 'Interpreter', 'latex');
legend('Experimental data', 'Average bulk temperature', 'Upper and Lower error bars')
hold off
uncertainty_lam2 = std_Temp/sqrt(numel(T));

figure;
histogram(T, 100);
grid on
title_text = sprintf('Histogram of Temperature: %.2f K', avg_temp);
latex_part = '$\epsilon = 1/\{\lambda^{-2}\}$';
title({title_text, latex_part}, 'Interpreter', 'latex');
xlabel('Temperature (K)');
ylabel('Frequency');

```

B.0.5 DIC Analysis

```
close all
clear all
clc
format long
%%%%%%%%%%%%%%%
%%%%%%%%%%%%%%%
% This code is written to read in .txt files from MESUR gauge in addition
% to reading in .cvc files from VIC3D to determine the engineering/true
% stress-strain response of tensile samples and determines
$ Young's modulus and Poisson's ratio
% 06/19/2024
% H10
% Read in .txt file and plot Force vs Time of all tests
folderOutputDir = 'E:\David\Mark10Data\SCALEDJANNAF\Mark10';
folderList = dir(fullfile(folderOutputDir));
folderNames = {folderList([folderList.isdir]).name};
folderNames = folderNames(~ismember(folderNames , {'..','.'}));
err1 = 0;
err2 = 0;
for f = 1:numel(folderNames)
    mark10Dir = fullfile(folderOutputDir, folderNames{f});
    fileList = dir(fullfile(mark10Dir, '*.log'));
    for i = 1:numel(fileList)
        filePath = fullfile(mark10Dir, fileList(i).name);
        fid = fopen(filePath, 'r');
        if fid == -1
            error('Failed to open the file.');
        end
        data = struct();
        section = "";
        lines = {};
        Data = {};
        mf = 1;
        while ~feof(fid)
            line = fgetl(fid);
            lines = [lines; line];
            flag = vertcat(regexp(line,'\\d+\\.\\d*','match'));
            if length(flag)<=3
                Data = [Data; flag];
            end
        end
        MK10File{i} = lines;
        saveData{i} = Data;
        err1 = 0;
    end
    AllMK10Files{f} = MK10File;
    Mk10DATA{f} = Data;
    t_mk10{f} = str2double(Mk10DATA{1,f}(:,3));
```

```

force_mk10{f} = str2double(Mk10DATA{1,f}{(:,2)});
err2 = 0;
figure(1), plot(t_mk10{f},force_mk10{f})
hold on

end
xlabel('Time (s)'), ylabel('Force [N]')
title('Force vs Time ')
grid minor
xlim([0 32])
hold off
%% Determine the engineering stress and strain
strain_rate = [0.5, 0.5, 0.5];
Lo = 26;
Wg = [5.21, 5.16, 5.19];
Tg = [6.67, 6.70, 6.56];
area = (Wg.*Tg)/(1000^2);
for i = 1:length(strain_rate)
    strain{i} = (strain_rate(i)*str2double(Mk10DATA{1,i}{(:,3)}))/ Lo;
    stress{i} = ((str2double(Mk10DATA{1,i}{(:,2)}))/(area(i)))*10^-6;
    figure(2), plot(strain{1,i}, stress{1,i})
    true_stress{i} = stress{1,i}.*((strain{1,i}) + 1);
    true_strain{i} = log(1 + strain{i});
    hold on
end
figure(2)
title('Stress vs Strain - JANNAF')
xlabel('Strain, {epsilon}_{eng} (mm/mm)')
ylabel('Engineering stress, {\sigma}_{eng} (MPa)')
grid minor
xlim([0 0.16])
hold off
%% Load in .csv file from VIC3D
map_vic = ('E:\David\Dic Testing\H10\SCALEDJANNAF');
folderList = dir((map_vic));
folderNames = {folderList([folderList.isdir]).name};
folderNames = folderNames(~ismember(folderNames , {'..','Mark10Data'}));
test_matrix = {'Test1', 'Test2', 'Test3'};
for f = 1:numel(folderNames)
    for j = 1:numel(test_matrix)
        vicData = fullfile(map_vic, folderNames{f},test_matrix{j}, 'vic3d', 'strain','extensometer');
        csvFile = dir(fullfile(vicData, '*.csv'));
        path(path, csvFile.folder)
        opts{j} = detectImportOptions(csvFile.name,'NumHeaderLines',1);
        opts{j}.VariableNamingRule = 'preserve';
        excel_data{j} = readtable(csvFile.name, opts{j});
    end
    AllExcelData{f} = excel_data;
end

```

```

OPTS{f} = opts;

end
%%
bolo = {'L1_mm_','Y_mm_'};
eyylong = [];
endFrame = [460,386,331];
fps = 22; % 22 frames per second
t_deltaDIC = 1/fps; % time between frames
t = 1;
for i = 1:numel(AllExcelData)
    for k = 1:numel(AllExcelData{1,i})
        eyylong{1,i}{1,k} = [];
        for n = 1:numel(OPTS{1,i}{1,k}.VariableNames)
            does = contains(OPTS{1,i}{1,k}.VariableNames{n}, bolo);
            if does == true
                if n <= 3
                    y_mm{1,i}{1,k}{:,t} = table2array(AllExcelData{1,i}{1,k}{:,n});
                else
                    if isempty(eyylong{1,i}{1,k}) == 1
                        eyylong{1,i}{1,k}{:,t} = (table2array(AllExcelData{1,i}{1,k}{:,n})/...
                            table2array(AllExcelData{1,i}{1,k}{:,n+1})) - 1;
                    else
                        eyylat{1,i}{1,k}{:,t} = (table2array(AllExcelData{1,i}{1,k}{:,n})/...
                            table2array(AllExcelData{1,i}{1,k}{:,n+1})) - 1;
                    end
                end
            end
        end
    end
end

x = 1:size(eyylong{1,i}{1,k});
figure(), plot(eyylong{1,i}{1,k}{:,1}), hold on, ...
    plot(eyylat{1,i}{1,k}{:,1})
legend('Longitudinal Strain','Lateral Strain','Location','southeast')
grid on
title('Select t = 0 and press "Enter"')
ylabel('Strain (mm/mm)')
xlabel('Frame Index')
xlim([0 ,size(eyylong{1,i}{1,k},1) + 75])
yminlimit = min(eyylat{1,i}{1,k});
ymaxlimit = max(eyylong{1,i}{1,k});
ylim([min(min(yminlimit)) - 0.035, max(max(ymaxlimit))])
t = 1;
hold off
[a,b] = ginput;
eyyLong{1,i}{1,k} = eyylong{1,i}{1,k}(floor(a):endFrame(i,k));
eyyLat{1,i}{1,k} = eyylat{1,i}{1,k}(floor(a):endFrame(i,k));
poiss{1,i}{1,k} = -1*(eyyLat{1,i}{1,k})./eyyLong{1,i}{1,k};

```

```

    zeroed_time{1,i}{1,k} = [0: t_deltaDIC : (length(eyyLong{1,i}{1,k})-1)/fps];
end
eyy_DIC{i} = eyyLong{1,i};
eyy_LAT_DIC{i} = eyyLat{1,i};
poissonsRatio{i} = poiss{1,i};
eyylong{1,i}{1,k+1} = [];
clear eyyLat
y_mm = {};

end
%% Sync Mark-10 to DIC
tol = 0.03;
t_new = 0;
r = 1;
for i = 1:numel(zeroed_time)
    for f = 1:numel(zeroed_time{1,i})
        for j = 1:numel(zeroed_time{1,i}{1,f})
            x = zeroed_time{1,i}{1,f}(1,j);
            findme = find(abs(t_mk10{1,r}) - x) < tol;
            if findme >= length(t_mk10{1,r})
                zeroed_time{1,i}{1,f} = zeroed_time{1,i}{1,f}(1:j-1);
                zeroed_eyy{1,i}{1,f} = zeroed_eyy{1,i}{1,f}(1:j-1);
                break
            end
            t_find{1,i}{f,1} = findme(1);
            if t_find{1,i}{f,1} == 1
                sync_force{1,i}{1,f}(j,1) = 0;
            else
                x1 = t_mk10{1,r}(t_find{1,i}{f,1} - 1,1);
                x2 = t_mk10{1,r}(t_find{1,i}{f,1} + 1,1);
                y1 = force_mk10{1,r}(t_find{1,i}{f,1} - 1,1);
                y2 = force_mk10{1,r}(t_find{1,i}{f,1} + 1,1);
                sync_force{1,i}{1,f}(j,1) = y1 + ((x - x1)/(x2 - x1))*(y2 - y1);
            end
        end
        r = r + 1;
    end
end
%% Plot Engineering stress-strain of DIC system
tol = 0.005;
figure()
hold on
for i = 1:numel(sync_force)
    for j = 1:numel(sync_force{1,i})
        sync_stress{1,i}{1,j} = (sync_force{1,i}{1,j}./area(i,j))*10^-6;
        plot(eyy_DIC{1,i}{1,j}, sync_stress{1,i}{1,j})
    end
    [c, d] = ginput;

```

```

e = find(abs(eyy_DIC{1,i}{1,j} - c(1)) < tol);
start_idx = e(1);
f = find(abs(eyy_DIC{1,i}{1,j} - c(2)) < tol);
end_idx = f(1);
linear_Long_strain{1,i}{1,j} = eyy_DIC{1,i}{1,j}(start_idx:end_idx);
linear_Lat_strain{1,i}{1,j} = eyy_LAT_DIC{1,i}{1,j}(start_idx:end_idx);
linear_stress{1,i}{1,j} = sync_stress{1,i}{1,j}(start_idx:end_idx);
coeffs = polyfit(linear_Long_strain{1,i}{1,j}, linear_stress{1,i}{1,j}, 1);
YoungsM(i,j) = coeffs(1);
PoissonsRatio{i,j} = -1*(linear_Lat_strain{1,i}{1,j}./linear_Long_strain{1,i}{1,j});
end
end
grid minor
xlim([0 0.11])
title('Engineering Stress vs Strain - SCALED JANNAF')
xlabel('Engineering Strain, {\epsilon}_{eng} (mm/mm)')
ylabel('Engineering stress, {\sigma}_{eng} (MPa)')
hold off
%%
SCALEDJANNAF_eng_stress = sync_stress;
SCALEDJANNAF_eng_strain = eyy_DIC;
SCALEDJANNAF_poissons = PoissonsRatio;
SCALEDJANNAF_youngs = YoungsM;
SCALEDJANNAF_linear_Long_strain = linear_Long_strain;
SCALEDJANNAF_linear_Lat_strain = linear_Lat_strain;
save("H10_SCALED_FINAL.mat", "SCALEDJANNAF_eng_stress", "SCALEDJANNAF_eng_strain',...
    "SCALEDJANNAF_poissons", "SCALEDJANNAF_youngs","SCALEDJANNAF_linear_Long_strain',...
    "SCALEDJANNAF_linear_Lat_strain")
%% Plot True stress-strain of DIC system
% true_stress = cell(1, numel(eyy_DIC));
% true_strain = cell(1, numel(eyy_DIC));
% figure()
% hold on
% for i = 1:numel(sync_force)
%     for j = 1:numel(sync_force{1,i})
%         true_stress{1,i}{1,j}{:,1} = sync_stress{1,i}{1,j}.* (1 + eyy_DIC{1,i}{1,j});
%         true_strain{1,i}{1,j} = log(1 + eyy_DIC{1,i}{1,j});
%         plot(true_strain{1,i}{1,j}, true_stress{1,i}{1,j})
%     end
% end
% end
% grid minor
% xlim([0 0.11])
% title('True Stress vs Strain - JANNAF')
% xlabel('Strain, {\epsilon}_{true} (mm/mm)')
% ylabel('True stress, {\sigma}_{true} MPa')
% hold off
% % JANNAF_true_stress = sync_stress;

```

```

% % JANNAF_true_strain = eyy_DIC;
% % save("Treu_JANNAF.mat", "JANNAF_true_stress", "JANNAF_True_strain")
figure()

grid minor
hold on
k = 1;
l = 1;
for i = 1:numel(SCALEDJANNAF_eng_stress)
    for j = 1:numel(SCALEDJANNAF_eng_strain{1,i})
        h(k) = plot(smooth(SCALEDJANNAF_eng_strain{1,i}{1,j}),...
                    smooth(SCALEDJANNAF_eng_stress{1,i}{1,j}));
    end
end

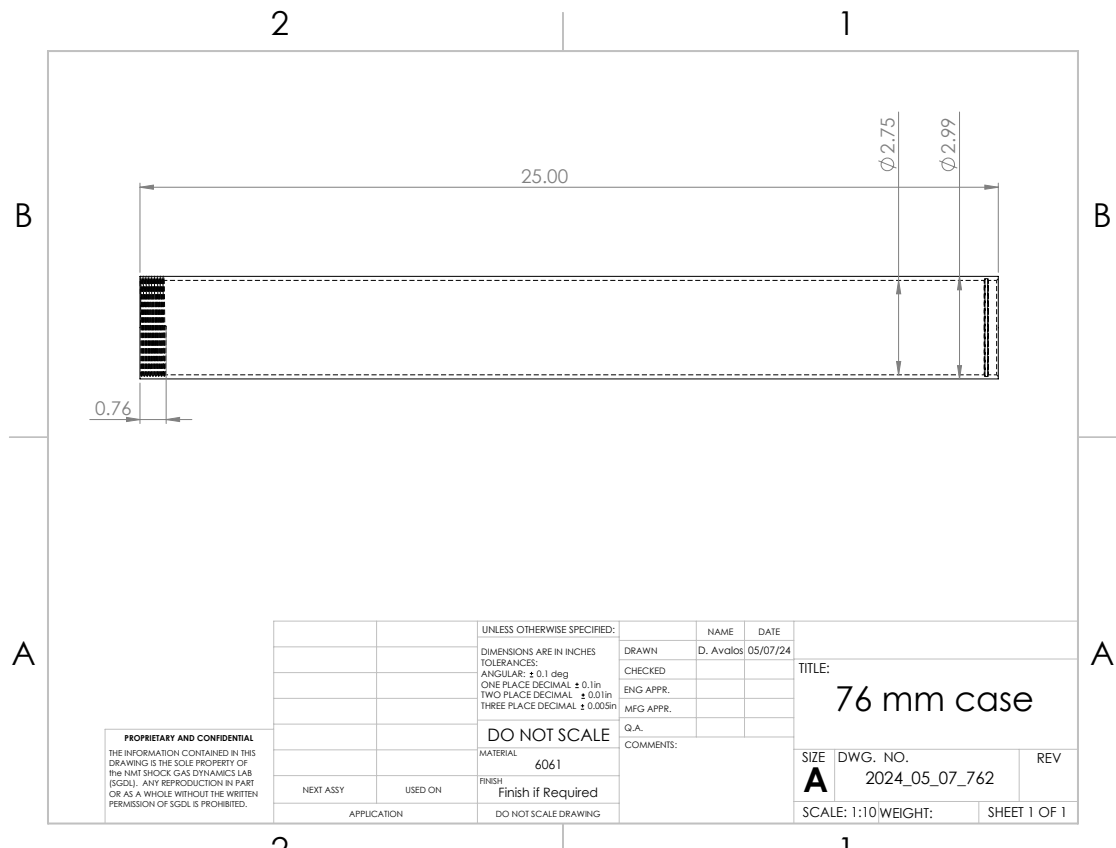
title('Engineering Stress vs Strain - SCALEDJANNAF')
xlabel('Engineering Strain, {\epsilon}_{eng} (mm/mm)')
ylabel('Engineering stress, {\sigma}_{eng} MPa')

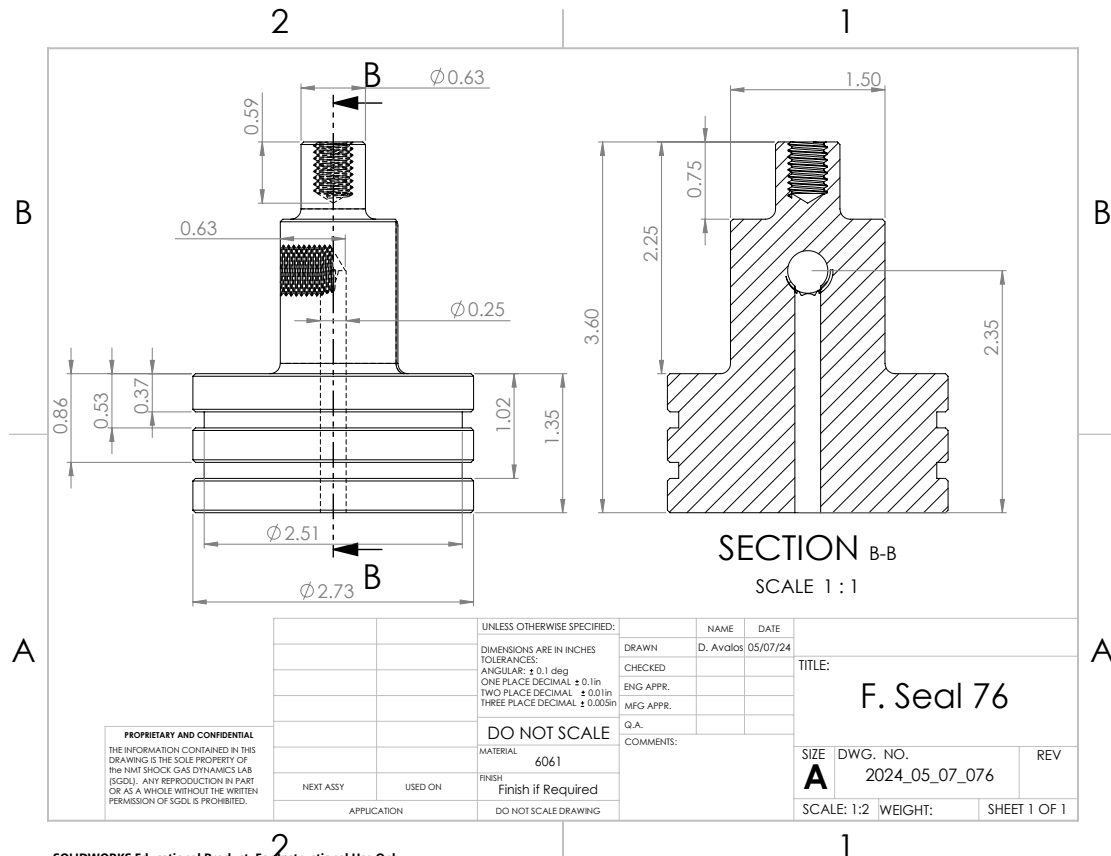
```

APPENDIX C

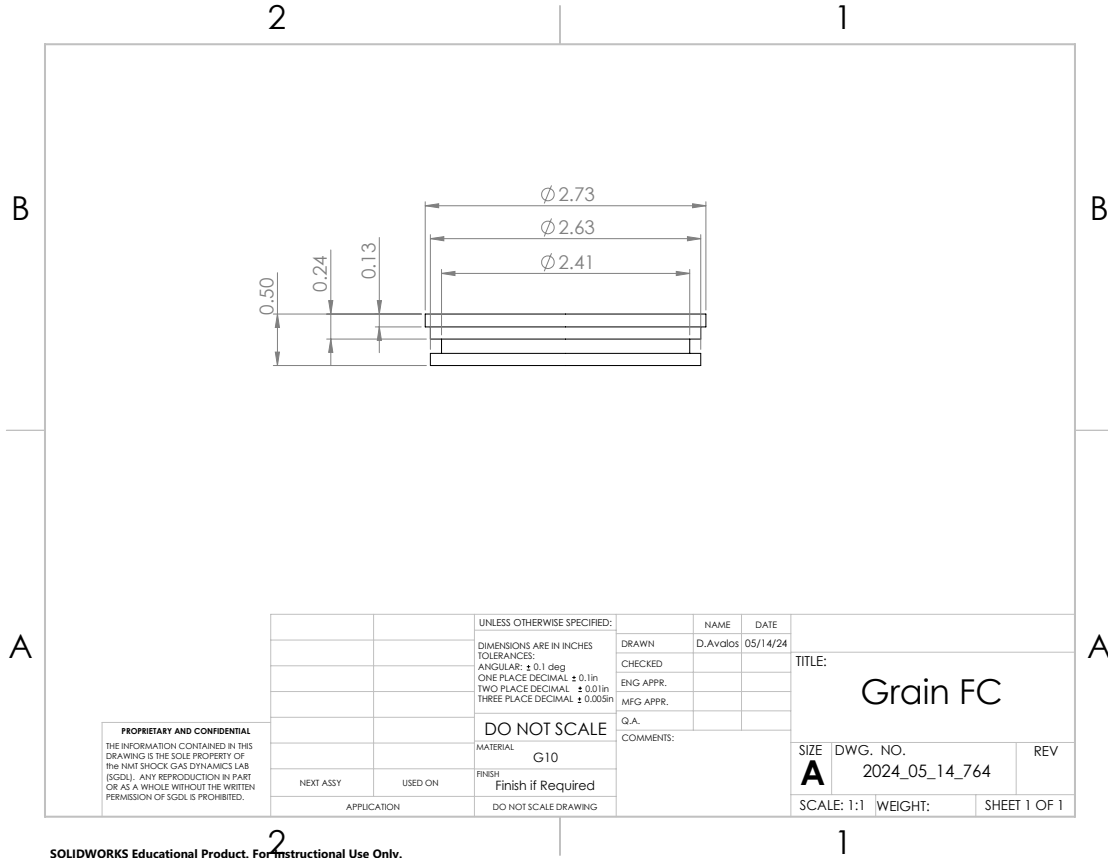
ENGINEERING DRAWINGS

C.0.1 76 mm Motor Engineering Drawings

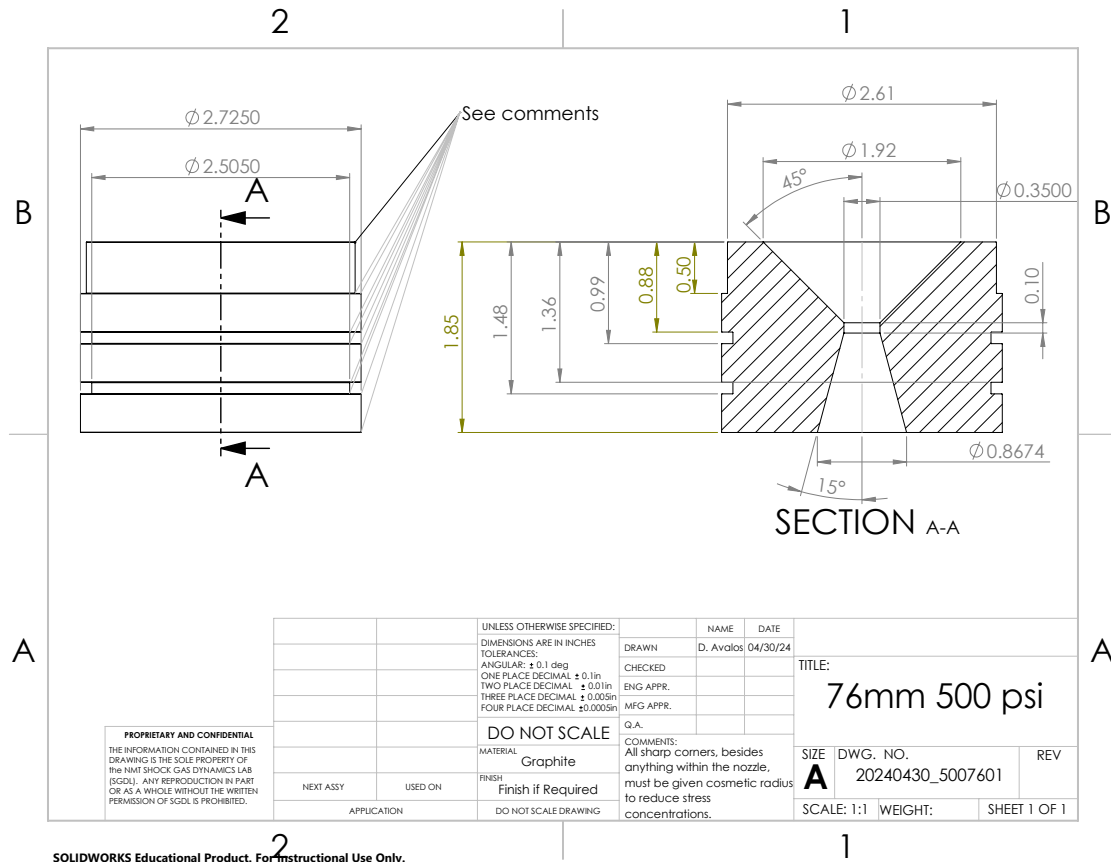




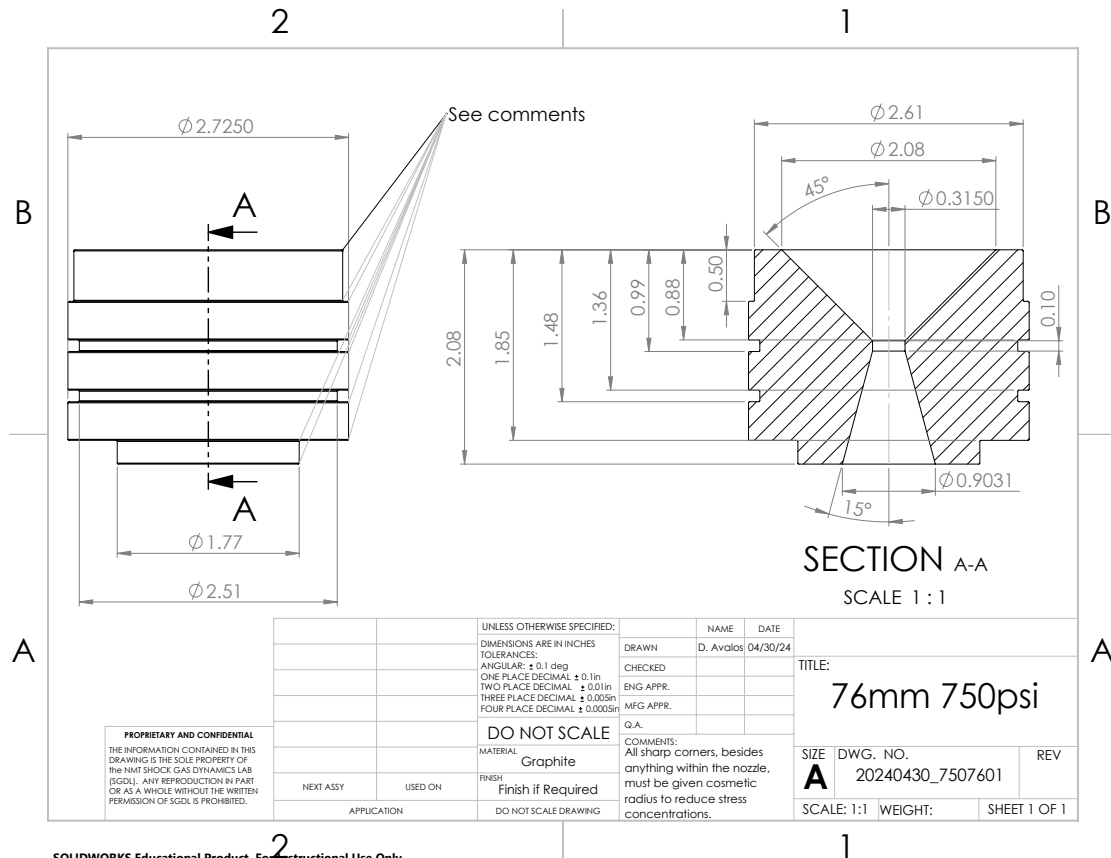
SOLIDWORKS Educational Product. For Instructional Use Only.



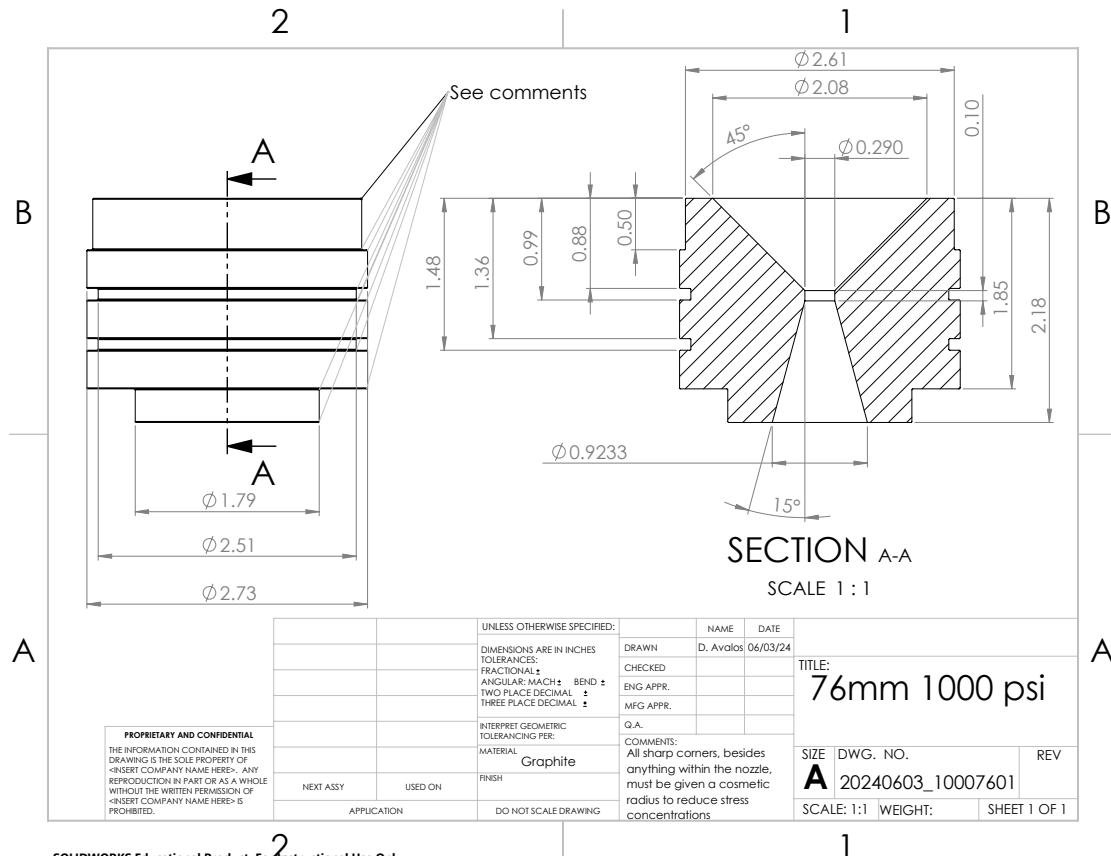
SOLIDWORKS Educational Product. For Instructional Use Only.



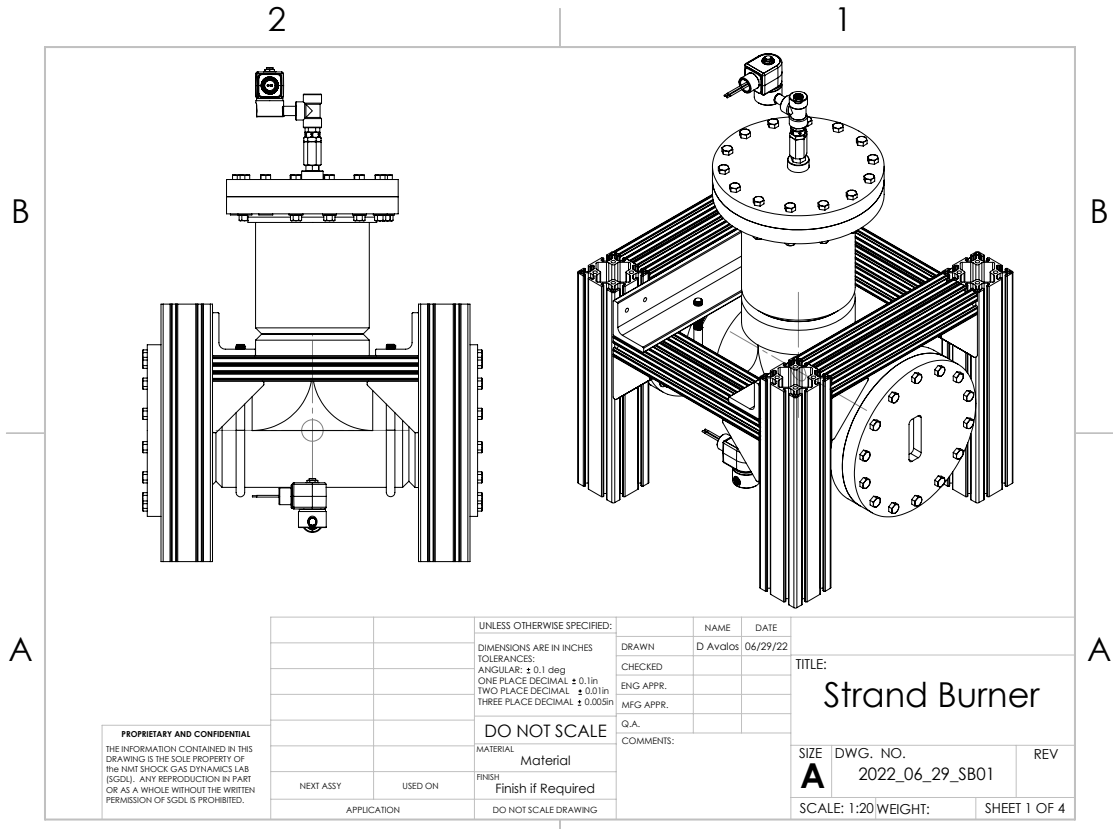
SOLIDWORKS Educational Product. For Instructional Use Only.



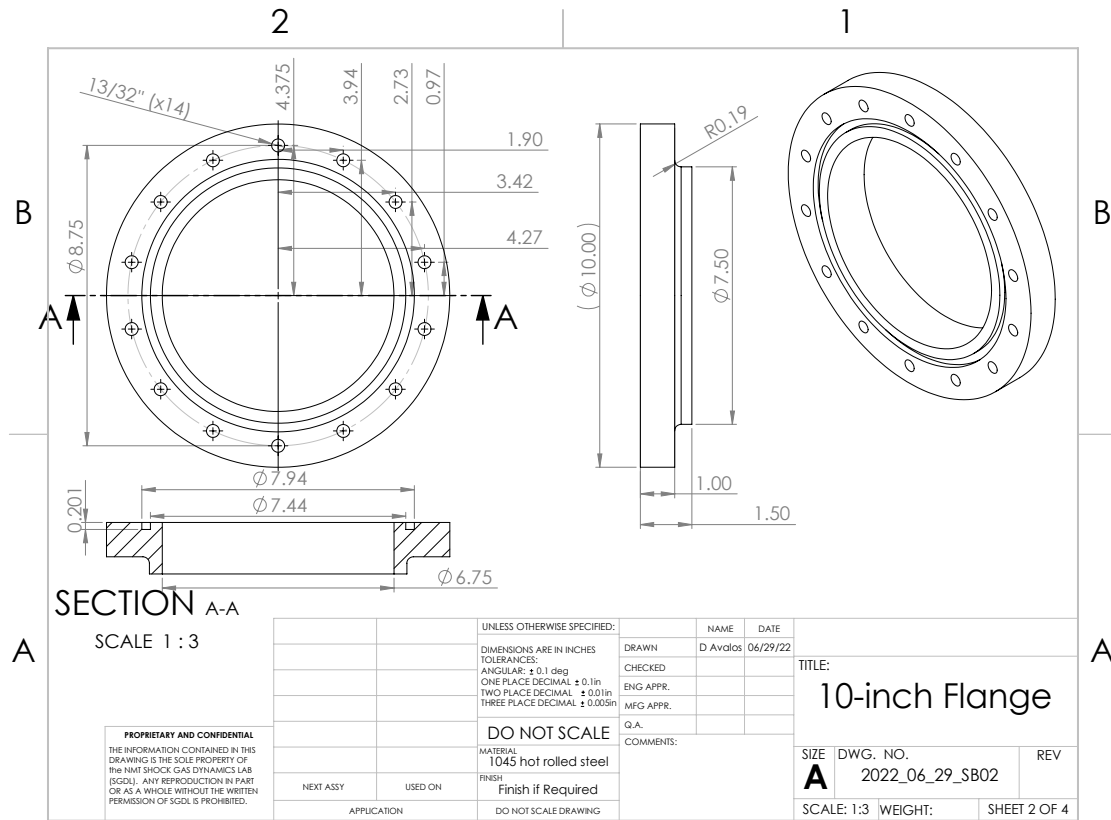
SOLIDWORKS Educational Product. For Instructional Use Only.

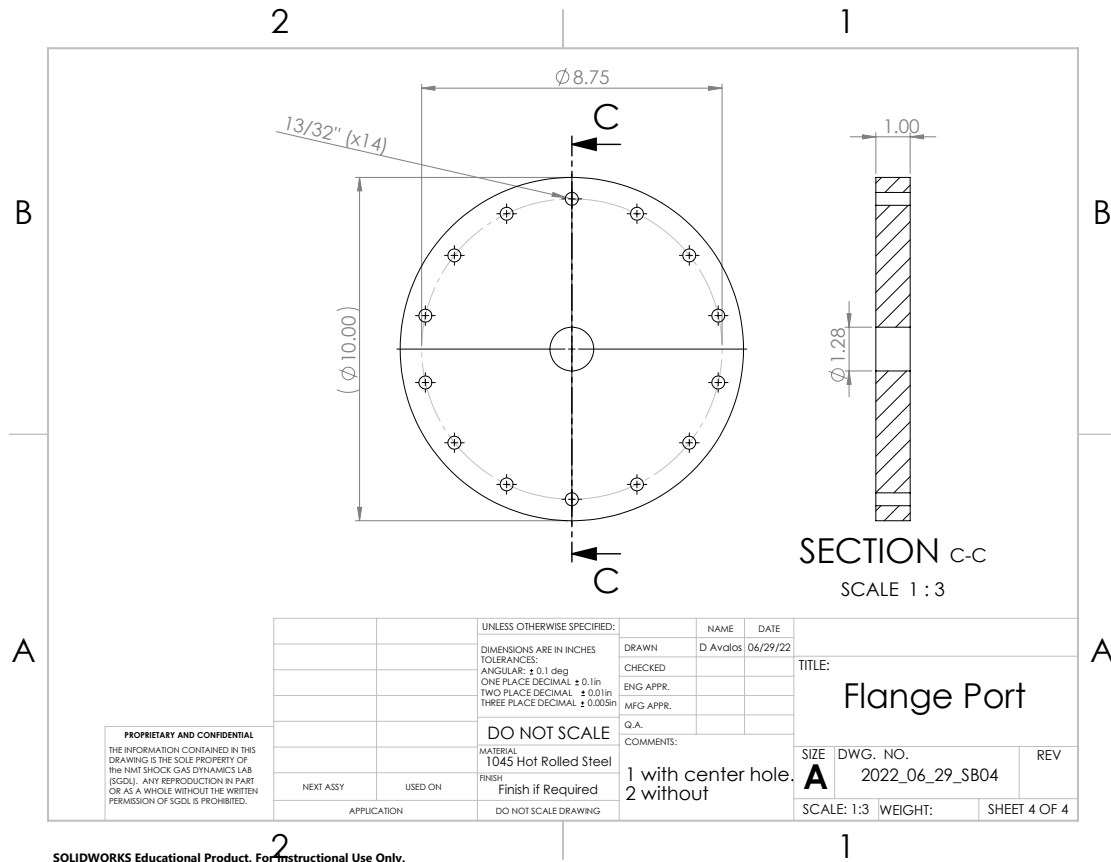


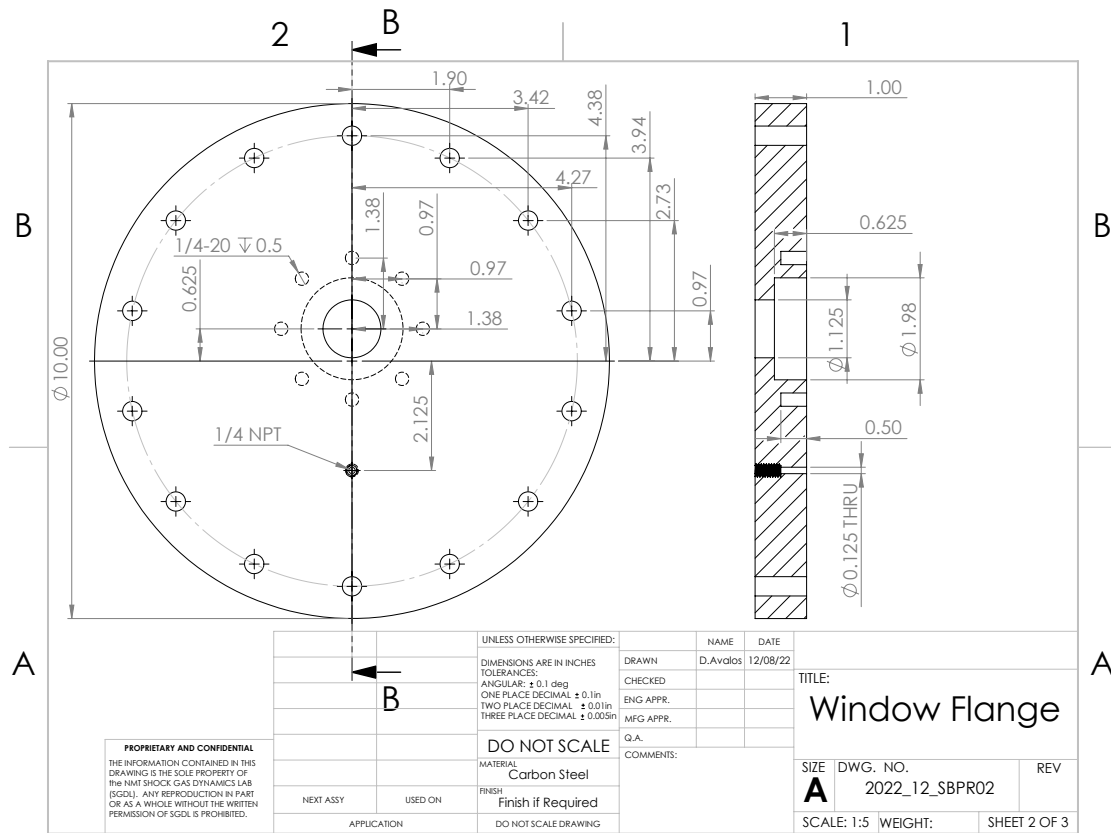
C.0.2 Strand Burner



SOLIDWORKS Educational Product. For Instructional Use Only.

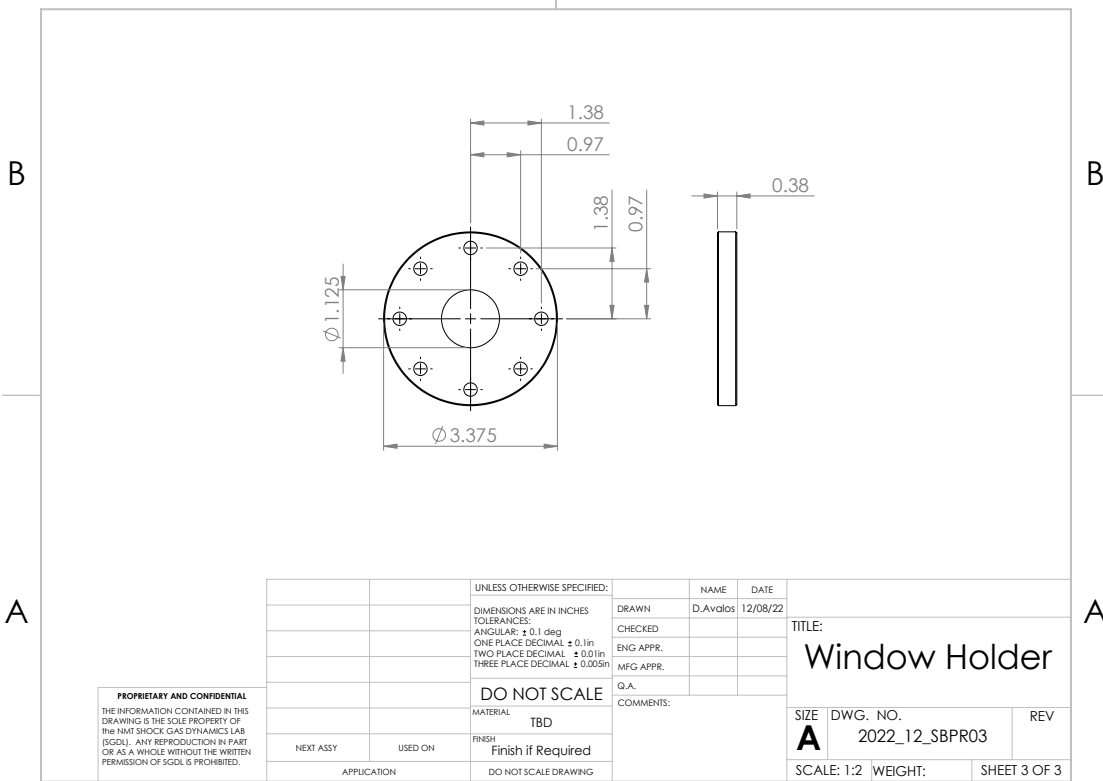


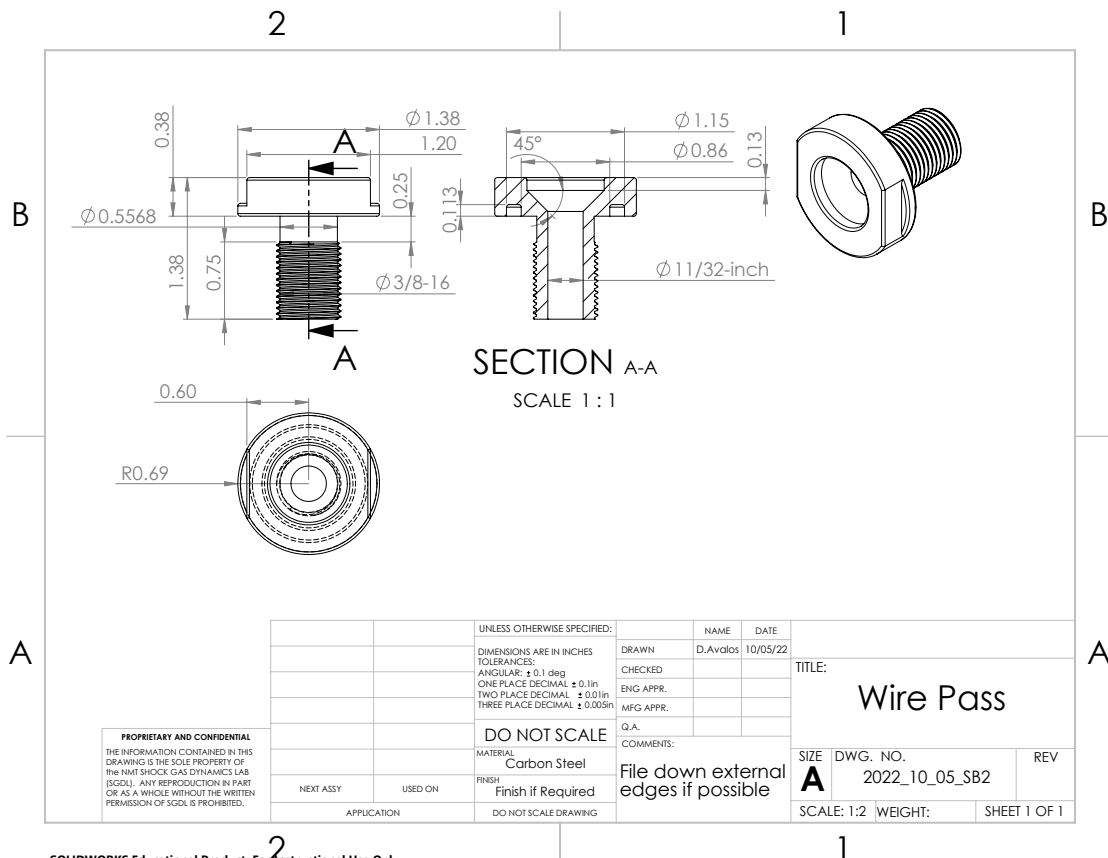




2

1





APPENDIX D

TEST PLANS

D.0.1 Propellant Mixing and Casting Test Plan

1. Purpose:

The purpose of this document is to provide a procedure for propellant mixing in Torres East Lab. Mixing and casting will be conducted on Ammonium Perchlorate composite propellants. The procedure includes an overview/summary, formulation, mixing, and casting. You must read this document in its entirety prior to beginning this procedure.

2. Overview/Summary

- 2.1.1.Prior to beginning the casting operations, all areas where measuring, mixing, and casting are to be conducted must be free of any physical hazards. All tools must be cleaned using isopropyl alcohol. Mixing tools must be checked for their operational status. Any components that show signs of degradation must be replaced.
- 2.1.2.All constituents of both the polymer matrix and solids loadings must be measured out individually and placed in an appropriate container.
- 2.1.3.Never measure both fuel and oxidizers at the same time or use the same tools/containers to measure them. It is recommended that the aluminum powder be measured first following a cleaning of the surface of the scale to ensure no powder has accumulated on the scale. A more thorough procedure for the mixing and casting process is given in *Attachment 4*.
- 2.1.4.All molds must be cleaned and prepped using isopropyl alcohol and compound 111 respectively prior to the addition of curative into the propellant mixture.
- 2.1.5.Propellant samples will be cured inside an oven at 60°C for 4-5 days. An inspection will be done to monitor the hardness of the propellant every 24 hours. No site closure must be done when measuring the hardness of the propellant.
- 2.1.6.Once casting operations have been concluded, a thorough cleaning must be done. All equipment must be stowed away. Nitrile gloves must be removed and properly disposed of before leaving the lab.

3. Location of Test

- 3.1.1.All energetic large-scale mixing will be conducted at Torres East lab.

4. Sequence of Steps

- 4.1. See attachment 4 for checklist

5. Test Matrix

Test #	Type of Test	Data Requirements	Energetics
1	APCP Castings Ops	Hardness (Shore A)	No less than 3 lbm No more than 14 lbm (84% solids)

6. Construction

- 7.1 All setup and construction of the APCP molds will be performed by members of SGDL.

7. Energetic Materials

8.1 APCP

Mix 1	
Ingredient	wt %
400 µ AP	36.5
90 µ AP	36.5
Aluminum	10
Carbon Black	0.5
CAO-5	0.05
HTPB	9.6
DDI	2.3
IDP	4.0
TPB	0.05
10-cst Si oil	0.5

8. Instrumentation

Provided by Dr. Hargather's group

9. Specific Tools and Equipment

1. Wooden popsicle sticks
2. 500 mL, 10 mL, 5 mL polypropylene beakers
3. 50 mL glass beaker
4. Weighing boats
5. Nitrile gloves
6. Laboratory wooden spatulas with silicone tip
7. High precision scale (0.01 g accuracy)
8. Analytical scale (0.0001 g accuracy)
9. Polypropylene syringes (5 mL and 10 mL)
10. 7 mL disposable graduated pipette
11. Single channel micro pipette w/micro pipette tips
12. Vacuum pump and vacuum cast pot
13. Shaker table
14. Air compressor
15. Baking oven
16. Static wrist straps

10. Documentation

1. Video monitoring
2. Measurements of all chemical ingredients and chemical containers
3. Temperature during curing
4. Shore A hardness every 24 hrs

11. References

- 11.1. DoD 4145.26-M, DoD Contractors Safety Manual for AA&E
- 11.2. SOP 101, Health and Safety

- 11.3. SOP 102, Field Laboratory Safety
- 11.4. SOP 103, Industrial Safety
- 11.5. SOP 108, HAZCOM Program
- 11.6. SOP 201, Grounding Procedures
- 11.7. SOP 202, Initiation of Energetic Materials
- 11.8. SOP 203, Arms, Ammunition and Explosives Procedures
- 11.9. SOP 402, Emergency Action Plan
- 11.10. SOP 403, Risk Management
- 11.11. SOP 500, Operating with COVID Restrictions

12. Attachments

- 1. Job Hazard Analysis
- 2. Safety and General Requirements
- 3. Site Closure Map
- 4. Checklist
- 5. Tailgate Briefing Form
- 6. Safety Data Sheets
- 7. Record Weights
- 8. In Process Hazard Analysis

Attachment 2 – Safety and General Requirements

Hazardous Waste:

- The use, recovery, collection, transport, and storage of military munitions for Research, Development, Testing and Evaluation (RDT&E) (e.g. safety, developmental testing, surveillance function testing, static fire, or quality control or assurance testing) is considered use for intended purpose and not subject to regulation under Resource Conservation and Recovery Act (RCRA). (Military Munitions Rule (MMR) paragraph 3.B.2.b.)
- As long as all excess energetic material is destroyed on site, and not removed from the facility, it is not considered waste and does not fall under RCRA. (MMR paragraph 10.C.3.)
- Any spilled loose material will be completely gathered up and determined if the material is still usable.
- If the material is still usable, it is not considered waste and should be used or stored as applicable.
- Spilled material deemed unusable will be properly containerized, labeled, and stored for later disposal in accordance with local policies and procedures.

Emergency Procedures:

- Lightning: (reference procedures in SOP 104)
- Fire:
 - If there is a fire on or near the test site, all personnel will evacuate to a previously identified location immediately (or further depending on the severity of the fire) and the safety office will be notified.

WARNING

Personnel WILL NOT fight a fire that could have any remote possibility of involving propellant.

- All personnel will immediately assemble at a previously identified location and all personnel accounted for;
- All personnel will be checked for possible injuries, first aid applied as needed, and the area inspected for remaining hazards by ordnance personnel;
- Emergency Medical Services will be called for assistance, if needed;
- The safety office will then be notified immediately.

Personnel and AA&E Limits:

- Limit exposure to a minimum number of personnel, for a minimum amount of time, to the minimum amount of the hazardous material consistent with safe and efficient operations.
- Personnel Limits – All non-essential personnel will be located on the concrete pad outside of Torres East Lab, or in the control bunker, during all operations involving the handling of energetic material unless prior approval has been granted from the Safety Office.
- Propellant Limits – With the current formulation, a minimum of 3 lbm and a maximum of 14 lbm is allowed in the Hobart mixer.

Indicators for Identifying Abnormal Process Conditions:

WARNING

Immediately stop operations and notify the test engineer if any of the listed potential anomalous events occur during casting operations. Every effort has been made to capture all anomalies; however, any incident not covered in the normal casting procedure shall trigger a temporary work stoppage with notifications to ensure a safe path forward

- Parts or equipment are damaged
- Foreign objects located in mix
- Propellant residue left on surfaces
- Proper tools not available or damaged
- Power outage during mixing or casting
- Sudden onset of illness
- Accidental mixing of dry oxidizer and fuel

Attachment 4

Checklist

4. Mixing

All mixing and casting operations are to be performed during regular business hours, 8-5. All operations must be scheduled and approved by the faculty member and EMRTC. A minimum of two personnel are required during all operations. One individual will perform all mixing/casting operations while the other serves as a safety/assistant. Internal training must be provided to individuals assuming the role of mixing and casting. Untrained personnel must attend 3 full days of mixing and casting operations prior to assuming this role. Safety/assistant personnel are not required to meet this requirement.

Ensure necessary tools/equipment are cleaned prior to beginning operations. Tools include beakers, wooden popsicle sticks, pipettes, syringes, and scales. Individuals that are mixing must remain at the fume hood until the procedure is complete, or unless an emergency occurs.

Required PPE

- Lab coat/button-up fitted coat (on at all times)
- Full-length pants (on at all times)
- Close-toe shoes (on at all times)
- Protective eyewear (on at all times)
- Long hair tied back (on at all times)
- Nitrile gloves (on at all times)
- Static wrist straps (used with AP and AL additions and when casting into molds)
- Flame retardant gloves (used when placing or removing propellant samples from the oven)

4.1.1 Mold Assembly

Mold release, MOLYKOTE 111 Compound, must be applied to all surfaces on molds that may come into contact with propellant. Regardless of whether or not the surface in question is not a part of the final product, mold release should be applied to prevent propellant from adhering to other parts of the mold. Only a thin layer is required. Ensure there are no threads or areas of metal-to-metal contact that the propellant could find it's way into.

- Clean molds using isopropyl alcohol
- For multi-component molds, apply a thin layer of 111 compound before assembling, then proceed to assemble the molds once all required surfaces have mold release
- For single-component molds, apply a thin layer of 111 compound to all required surfaces
- Set molds aside for later use

4.1.2 Measuring Binder System:

Ensure all personnel have all required PPE. If gloves become contaminated, change gloves before handling a separate chemical. All constituent weights are listed in section 7.

o Water bath

- Set up a large (~1 gallon) polypropylene container and fill it with water. This will be used to neutralize anything that comes in contact with DDI.
 - o Do not use this to neutralize any area of skin. Running water must be used in the instance DDI comes into contact with your skin.

- **HTPB**
- Label a 500 mL beaker “Main”. Weigh the beaker on scale and annotate tare weight
- Measure out the required HTPB and pour it into the beaker
 - Use a wooden popsicle stick to add or remove HTPB from the main vessel. Do this until you reach the desired amount. Annotate the final measurement. Keep this popsicle stick as it will be the main mixing tool for the casting operation
- **IDP & Silicone Oil**
- Use high shear blender container for measuring IDP and Sili
- Zero the scale and measure out required IDP into the blender
- Use a disposable syringe to measure the IDP. Discard the syringe when done into the non-hazardous chemical trash
- Use another syringe to measure our required silicone in the same blender. Dispose of syringe in the non-hazardous chemical trash
- Place cap on the blender and turn on the blender for 30 seconds
- Set aside for later use
 - **TPB**
- Measure TPB on a weight boat. Label a 50mL glass beaker “Pre-Batch DDI”. Weigh the beaker on scale and annotate the measurement
- Carefully pour the TPB into a pre-batch vessel
- Any spilled TPB must be immediately cleaned up using a damp paper towel, with isopropyl alcohol, and tossed into a non-hazardous chemical trash
 - **DDI**
 - **DDI is toxic. Be cautious when handling.**
- Measured DDI using a syringe
- Pour DDI into the Pre-Batch vessel that contains TPB
- Properly dispose of stings in water bath
- Mix thoroughly for about 5 minutes. Any spilt DDI must be immediately cleaned up and tossed into a water bath
- Store in oven at 50-60 °C for 30 minutes
 - Set a timer so you do not forget!!!
- Ensure the DDI bottle is closed and stored in the proper cabinet
- Dispose of gloves using the proper glove removal technique directly into the water bath

Store away any bulk other items at this point. Clean the working area of any spilled chemicals. Keep in mind, if it's spilled DDI, all paper towels/tools go into the water bath. All other contaminated paper towels used to clean HTPB, TPB, IDP, and Sili can go in the non-hazardous chemical trash. Use isopropyl to clean all surfaces contaminated. Change gloves and ensure the appropriate tools for measuring out solids are in the fume hood.

4.1.3 Measuring Solids

A separate, clean vessel is required per constituent for all the following steps. Be careful when measuring fine powders. Ensure the measuring vessel remains within the fume hood at all times. Properly secure

static wrist straps. Static wrist straps must be connected when handling either AP, Al, propellant slurry, or cured propellant.

- Ensure gloves are changed out between handling dry AL and AP.
 - Place the small vessel on the analytical scale and zero the scale
 - Measure out the required CAO-5 and place the vessel to the side for later use
 - Place a small vessel on the digital scale and zero scale
 - Measure out the required carbon black and place the vessel to the side for later use
 - Place a vessel on the digital scale and measure out the required Al and place vessel to the side for later use
 - o Ensure to place the aluminum vessel as far from the scale for measuring oxidizer
 - o Replace gloves prior to handling AP
 - o Clean the scale of any spilt aluminum using a towel and isopropyl alcohol
 - Don't forget about your DDI!! Ensure the 30-minute mark has not been met, if so, remove DDI & TPB pre-batch vessel from the oven and ensure the TPB has fully dissolved into the DDI. If not, place in for another 5-10 minutes.
 - Do not allow the pre-batch vessels to sit in the oven for more than an hour since this may activate the curative and reduce the pot-life of the propellant
 - Place a vessel on the digital scale and zero scale
 - Measure out the required AP, for both particle sizes, and place vessel to the side for later use
 - o Each particle size gets measured in its own vessel

Store away any bulk items in the appropriate storage locations. Clean off any surface with isopropyl alcohol and throw towels away in the non-hazardous chemical trash. If needed, change out gloves.

4.1.4 Mixing

Wrist straps must be secured once the addition of AP is introduced into the mixture.

- Add Al, CAO-5, and carbon black into the Hobart mixer
 - o When adding fine powders, carefully pour into the mixing bowl to prevent excessive dry powder dispersion
 - o Add each powder individually
 - Order does not matter
- Add the required amount of IDP & Silicone into the Hobart mixer
- Add the required amount of HTPB into the Hobart mixer
- Secure the bowl into the Hobart mixer and relocate to the control bunker
- Turn on the blue beacon inside the control room
- Ensure the control monitor for pressure and temperature measurements is working properly
 - o If the software is not working, troubleshoot until the problem is solved
 - If the problem cannot be solved, the SGDL supervisor and EMRTC safety officer must be notified before a decision is made as to how to continue
- Rapidly turn on and off the control switch to the Hobart mixer
 - Do this 3-4 times
- Leave the control switch in the ON position of the Hobart for 5-minutes
- Turn off mixer turn off the blue beacon and proceed to the mixing bunker
- Lower the bowl of the Hobart mixer and visually inspect the mixture for any dry aluminum power

- If any dry aluminum powder is used, use a large mixing utensil to wet out the dry powder
 - If an excess amount of agglomerates are found, repeat the steps above and begin mixing remotely for another 5 minutes
- Add $\frac{1}{2}$ of the total amount of both coarse and fine AP into the Hobart mixer
- Secure the bowl into the Hobart mixer and relocate to the control bunker
- Turn on the blue beacon inside the control room
- Ensure the control monitor for pressure and temperature measurements is working properly.
- Troubleshoot according to the previous similar step
- Rapidly turn on and off the control switch to the Hobart mixer
 - Do this 3-4 times
- Leave the control switch in the ON position of the Hobart for 5-minutes
- With the Hobart mixer on, turn the actuator valve to pull the vacuum in the Hobart mixer for 5 minutes. Visually inspect your pressure gage to ensure the pressure drops to the anticipated pressure
 - If any anomalies occur at this time, immediately turn off the vacuum pump first followed by the Hobart mixer
 - Troubleshoot the VI module if you are familiar with it
 - Contact SGDL supervisor and EMRTC safety officer to discuss troubleshooting options
 - Always monitor the power output of the Hobart and ensure it is in the normal range of 2-5 Volts. Any more than this could mean the propellant is curing inside the Hobart mixer and immediate action must be taken to prevent the propellant from curing inside the mixing bowl
- Turn off the vacuum pump
- Turn off the mixer and visually confirm that the pressure gauge returned to ambient conditions
- Turn off the blue beacon and proceed to the mixing bunker
- Lower mixing bowl
- Add $\frac{1}{2}$ of the remaining fine and course AP into the Hobart mixer
 - Safe a couple grams of the course AP for later use
- Secure the bowl into the Hobart mixer and relocate to the control bunker
- Turn on the blue beacon inside the control room
- Ensure the control monitor for pressure and temperature measurements is working properly.
- Troubleshoot according to the previous similar step
- Rapidly turn on and off the control switch to the Hobart mixer
 - Do this 3-4 times
- Leave the control switch in the ON position of the Hobart for 5-minutes
- With the Hobart mixer on, turn the actuator valve to pull the vacuum in the Hobart mixer for 5 minutes. Visually inspect your pressure gage to ensure the pressure drops to the anticipated pressure. If needed, troubleshoot as mentioned in the previous similar step
- Turn off the vacuum pump
- Turn off the mixer and visually confirm that the pressure gauge returned to ambient conditions
- Turn off the blue beacon and proceed to the mixing bunker
- Observe for any dry powder
- Add the remaining fine and course AP into the Hobart mixer
- Secure the bowl into the Hobart mixer and relocate to the control bunker
- Turn on the blue beacon inside the control room
- Ensure the control monitor for pressure and temperature measurements is working properly.
- Troubleshoot according to the previous similar step

- Rapidly turn on and off the control switch to the Hobart mixer
 - Do this 3-4 times
- Leave the control switch in the ON position of the Hobart for 5-minutes
- With the Hobart mixer on, turn the actuator valve to pull the vacuum in the Hobart mixer for 5 minutes. Visually inspect your pressure gage to ensure the pressure drops to the anticipated pressure. If needed, troubleshoot as mentioned in the previous similar step
- Turn off the vacuum pump
- Turn off the mixer and visually confirm that the pressure gauge returned to ambient conditions
- Turn off the blue beacon and proceed to the mixing bunker
- Observe for any dry powder
- Add DDI & TPB into the Hobart mixer. Make a little pocket on the side of the bowl to pour the curative into. DO not just pour the curative mixer not the Hobart mixer since this might cause excess losses due to the rapidly moving blade in the mixer upon start up
 - Take note of the time when the curative prebatch was added to the main batch
- Use the 2 grams of AP and pour it into the pre-batch vessel to attempt to pull out as much DDI from the pre-batch vessel as possible
- Add this AP covered in curative into the Hobart mixer
- Secure the bowl into the Hobart mixer and relocate to the control bunker
- Turn on the blue beacon inside the control room
- Ensure the control monitor for pressure and temperature measurements is working properly. Troubleshoot according to the previous similar step
- Rapidly turn on and off the control switch to the Hobart mixer
 - Do this 3-4 times
- Leave the control switch in the ON position of the Hobart for 5-minutes
- With the Hobart mixer on, turn the actuator valve to pull the vacuum in the Hobart mixer for 5 minutes. Visually inspect your pressure gage to ensure the pressure drops to the anticipated pressure. If needed, troubleshoot as mentioned in the previous similar step
- Turn off the vacuum pump
- Turn off the mixer and visually confirm that the pressure gauge returned to ambient conditions
- Turn off the blue beacon and proceed to the mixing bunker
- Final scrape down. Using a silicone or wooden mixing utensil, carefully scrap down all walls inside the mixing bowl
- Secure the bowl into the Hobart mixer and relocate to the control bunker
- Turn on the blue beacon inside the control room
- Ensure the control monitor for pressure and temperature measurements is working properly. Troubleshoot according to the previous similar step
- Rapidly turn on and off the control switch to the Hobart mixer
 - Do this 3-4 times
- Leave the control switch in the ON position of the Hobart for 5-minutes
- With the Hobart mixer on, turn the actuator valve to pull the vacuum in the Hobart mixer for 5 minutes. Visually inspect your pressure gage to ensure the pressure drops to the anticipated pressure. If needed, troubleshoot as mentioned in the previous similar step
- Turn off the vacuum pump
- Turn off the mixer and visually confirm that the pressure gauge returned to ambient conditions
- Turn off the blue beacon and proceed to the mixing bunker

4.1.5 Casting:

Clear the working area of any unnecessary tools that were used in the mixing process.)

Grains

- Set the shaking table up and connect it to an air compressor
- Place the vacuum pot (vac cast pot) on top of the shaker table
- Place the guiding funnel, SDGDL provides this, onto the top of the mold for the grain
- Set grain mold into the vac cast pot
- Set the stainless steel funnel on top of the table in the casting bunker and place the silicone plunger in the center hole of the funnel
- With assistance, carefully pour the propellant slurry from the Hobart mixing bowl into the large stainless steel funnel ensuring to hold the plunger in place to keep the propellant from falling into the vac cast pot
- Set the Hobart mixing bowl aside
- Secure the stainless steel funnel onto the vac cast pot and replace all the required lines from the vacuum pump onto the vac cast pot
- Close outlet and open inlet valves to begin pulling vacuum
- Turn on shaker table
- Once the pressure inside the vac cast pot has reached about 25 in h, allow a small portion of propellant to enter through the slit by carefully raising the plunger
 - o Fill the grain up by ¼ of the way every time and intermittently break the vacuum, or open the outlet valve to allow ambient pressure to enter the vac cast pot
 - o Only pour propellant when the pressure dial reads +/- 2 in hg from the required pressure as stated above
- Once the grain is completely filled, allow the propellant to degas about 2-5 minutes under vacuum
- Turn off shaker table and turn off vacuum pump
- Carefully remove the grain from the vac cast pot and place it onto the working bench
- Remove the funnel from the mold and place the follower onto the top of the mold
- Secure the follower onto the mold using electrical tape or plastic wrap
- Carefully clean off any excess propellant
- Place the molds into oven at 60°C with the follower at the top
 - o Take note the time the grain were placed into the oven
- Repeat these steps for all grains

Molds

- Set the shaking table up and connect it to an air compressor
- Place the vacuum pot on top of the shaker table
- Carefully place propellant into tensile molds using a wooden popsicle stick ensuring you minimize the amount of air re-introduced into the uncured propellant
- Place mold assembly into vacuum pot and close the vac cast pot
- Turn on the shaker table for 5-minutes
- Pull vacuum and wait until the dial reads 25 in hg
- Leave vacuum on for another 3-5 minutes
- Turn off vacuum pump
- Turn off shaker table

- Remove molds from pot
- Place the molds into oven at 60°C
 - o Take note the time the samples were placed into the oven
- Repeat the above steps for all tensile sample molds

Clean all equipment using isopropyl alcohol. Ensure to clean the inside of the vacuum pot and any surfaces that have any spilt propellant. Place all contaminated towels into a separate electrostatic bag and secure bag in the proper HAZAMT locker.

4.1.6 Cleaning

After all chemicals have been stored away, all tools that came into contact with propellant must be cleaned using isopropyl alcohol. All contaminated paper towels must be placed in the hazardous trash for later disposal through HAZMAT. All beakers and tools must be thoroughly cleaned of any propellant.

- Clean main mixing vessel of any propellant using isopropyl alcohol
- Any wooden sticks with propellant get thrown away in hazardous trash bag
- Use Q-Tips to clean any areas that are difficult to clean by hand
 - o Dispose in hazardous trash bag
- Once all equipment/tools have been cleaned and all surfaces are clean of propellant, dispose of gloves in hazardous trash bag
- Wash hands under the sink using soap and water
 - o AT NOT TIME CAN YOU USE ANY METAL TOOL TO CLEAN ANY SURFACE THA HAS PROPELLANT ON IT

4.1.7 HAZMAT Disposal

- Allow propellant to cure for 4-5 days
- Contact the HAZMAT officer in charge of disposal to inform them the hazardous items
- Disposal of hazardous items must be done in a timely fashion

4.1.8 Monitor Propellant & Removing Grains from Molds

For the following few days, monitor the propellant. Put on all required PPE listed in the beginning of attachment 4. Remove the shore sample from the oven and allow it to cool to room temperature prior to measuring the hardness. It takes about an hour to cool down. The first harness measurement should be taken using a toothpick. Very gently, touch the tip of the toothpick to the top of the shore sample. Do not exceed more than 1 mm into the surface of the propellant. If any propellant sticks to the tip of the toothpick, place the shore sample in and attempt this again in 24 hours. If no propellant sticks, use the hardness tester to measure the hardness daily. See the comments below for more information on what to look for.

- The oven must be reset every 24 hours to the appropriate settings
- o Harness values are typically seen to rise after 24 hours and range from 20 to 30 shore A
- o A steady value, usually 50-60 shore A, is seen around 4-5 days. If the propellant has not reached a hardness value between the ranges given within this time frame, assume the batch is unsuitable
- o Once the harness of the propellant has reached an acceptable value and has remained relatively steady of +/- 3 shore A for three consecutive days, proceed to the next steps
- Place on all required PPE as stated in the very beginning of attachment 4 including wrist straps and flame retardant gloves
- Turn off oven

- Remove the molds from the oven and allow them to cool
- When cooled, remove the propellant from mold
- Visually inspect propellant and properly store away until later use
 - o Store individual grains in their own individual electrostatic bag
 - o A day box will be assigned to you by the lab supervisor
- Using a scale to measure the exact weight of each propellant grain/tensile sample and assign a date, a batch number, and the # of the grain/tensile sample

D.0.2 Strand Burner Test Plan

1. Purpose:

Burn rate, temperature, and spectral emission measurements will be conducted on combusting ammonium perchlorate composite propellant (APCP) samples at pressures ranging from 500 conditions to 1250 psi. The combusting test is conducted within a pressure vessel, named hereafter as a strand burner, see Figure 1. Testing will be conducted in room 101 located within the HP building.

2. Test Overview/Summary:

- 2.1. Inspection of specific components will be conducted before conducting testing, listed in attachment 4, to ensure the components perform nominally.
- 2.2. A bifurcated cable, which is fixed to a mount outside of the strand burner, connects to a spectrometer and a pyrometer that gathers emitted light through a sapphire window for spectral and temperature measurements.
- 2.3. Prepared propellant samples will be secured onto a platform that is connected to a wire harness that leads to an external circuit for data acquisition using cDAQ 9188 NI and LabVIEW VI for recording burn rate measurements.
- 2.4. Pressurization of the strand burner, located in the testing room, will be controlled via inlet and outlet solenoid control room valves from a control room adjacent to the test room.
- 2.5. Ignition of samples will be performed with a 26 AWG nichrome wire and will be triggered using an initiation control system. Once the sample has been fully consumed, the outlet valve will be opened, and the strand burner will be vented for 30 seconds.

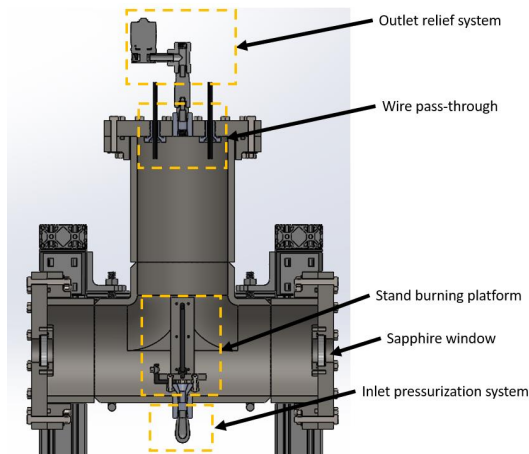


Figure 1: Strand burner configuration

3. Location of Test:

- 3.1. All testing will be conducted within room 101 of the HP building located on the northwest side of Jones Hall.

4. Sequence of Steps: (See Attachment 4 for checklist)

5. Test Matrix:

5.1.

Test #	Type of Test	Data Requirements	Energetics
1	APCP combustion characterization	Burn rate, pressure history, temperature, and spectral emission analysis	7 g (0.007 kg composite propellant samples)

Table 1 – Test Matrix

6. Construction: (non-standard items only)

- 6.1. All setup and construction of the strand burner will be performed by the test engineer.

7. Firing Detail Schematic:



Figure 2: Initiation Schematic.

8. Energetic Materials:

- 8.1. APCP: Approximately 7 g (0.007 kg)

8.2. Igniter

- 8.2.1.1. Bare 26 AWG nichrome wire (hot-wire initiation)

9. Instrumentation:

Provided by SGDL.

10. Specific Tools and Equipment: (Includes specialty tools, heavy equipment, initiation control system, etc.)

- 10.1. Initiation control system

- 10.2. Solenoid control set
- 10.3. NI cDAQ 9188 – NI 9263, NI 9205, and NI 9203 cDAQ cards – Electric circuit box for embedded wires
- 10.4. Camera control 5
- 10.5. Camera for direct imaging and surveillance
- 10.6. Compact CCD Spectrometer (Thorlabs)
- 10.7. SGDL 4-color pyrometer
- 10.8. TD1000 pressure transducer

11. Documentation: (Includes videos, reports, etc.)

- 11.1. Video from monitoring cameras throughout HP

12. Instructions for Spill Cleanup and Disposal of any Scrap and Waste A&E: (if different than those listed in Attachment 2)

13. Specific Hazards: (Include hazards in Safety Data Sheets (SDS))

14. PPE Required: (As determined by JHA; include setup, test, and post-test operations)

- 14.1. Safety glasses for strand burner operations
- 14.2. Nitrile gloves for the handling of propellant
- 14.3. Anti-static wrist straps for handling propellant
- 14.4. Lab attire
 - 14.4.1. Long sleeve shirt or lab coat, jeans, close-toed shoes (preferably steel toes for the test engineer)

15. Emergency Procedures: (if different than those listed in Attachment 2)

16. References: (Include all references pertinent to the project/test)

- DoD 4145.26-M, DoD Contractors Safety Manual for AA&E
- SOP 101, Health and Safety
- SOP 102, Field Laboratory Safety
- SOP 103, Industrial Safety
- SOP 108, HAZCOM Program
- SOP 201, Grounding Procedures
- SOP 202, Initiation of Energetic Materials

Attachment 2 – Safety and General Requirements

Igniter:

- Before installing the igniter, the external igniter leads must be checked they are not connected to the initiation control system and they must be spliced to prevent accidental ignition.
- A bare nichrome wire (26 AWG) will be placed on the top exposed surface of the propellant samples. This is to be conducted while the samples are secured on the sample platform while ensuring the internal wire harness is not connected to the platform.

Hazardous Waste:

- The use, recovery, collection, transport, and storage of military munitions for Research Development Testing and Evaluation (RDT&E) (e.g., safety, developmental testing, surveillance function testing, static fire, or quality control or assurance testing) is considered used for the intended purpose and not subject to regulation under Resource Conservation and Recovery Act (RCRA). (Military Munitions Rule (MMR) paragraph 3.B.2.b.)
- As long as all excess energetic material is destroyed on-site, and not removed from the test range, it is not considered waste and does not fall under RCRA. (MMR paragraph 10.C.3.)
- Any spilled loose material will be completely gathered up and determined if the material is still usable.
- If the material is still usable, it is not considered waste and should be used or stored as applicable.
- Spilled material deemed unusable will be properly containerized, labeled, and stored for later disposal in accordance with local policies and procedures.

Misfire Procedures:

- Firstly, if there is no visible ignition event noted in the surveillance footage, a continuity check must be performed. If the surveillance footage is down the LabVIEW NI monitoring system may be used to tell whether or not the ignitor was initiated. All connections will be checked to ensure continuity. After instrumentation has been reset, another attempt to fire may be made. The SGDL supervisor must be informed of the misfire. A maximum of 2 attempts per sample are allowed.
- If there is still no indication that the ignitor initiated, begin the applicable wait time as stated below:
 - Depressurize the strand burner and proceed to wait for 5 minutes before resetting the sample and igniter.
- During the wait time, the engineer/test manager will contact the SGDL Supervisor, or their designated representatives, to inform them of the misfire.
- If the sample does not initiate but a continuity check shows the ignitor has been consumed, an additional 5-minute wait time before being permitted to approach the test article will begin. During this time, the engineer/test will contact the SGDL Supervisor, or their designated representatives, to inform them of the misfire.
 - Before approaching the strand burner, it must be depressurized.

Emergency Procedures:

- Fire:
 - If there is a fire on or near the test site, all personnel will evacuate outside of the HP (or further depending on the severity of the fire) and the safety office will be notified.
 - On the day of the test, if the back door is locked, an attempt to contact the personnel must be made. If contact is not made, the test must be postponed.

WARNING

Personnel WILL NOT fight a fire that could have any remote possibility of involving explosives.

- Unexpected Explosion or Rapid Disassembly of Strand Burner:

- Test engineer will ensure the inlet solenoid control valve is OFF and the outlet is ON.
- All personnel will immediately evacuate HP to Jones Hall (or another previously identified location) and all personnel accounted for.
- All personnel will be checked for possible injuries, first aid applied as needed, and the area inspected for remaining hazards.
- Emergency Medical Services will be called for assistance if needed.
- The SGDL supervisor will then be notified immediately to discuss further steps.

WARNING

If an explosion involves the Test Engineer (or any other personnel) within the test room, personnel in the personnel shelter must make a determination whether or not it is safe to attempt to treat or assist the individual on the test site.

Personnel and AA&E Limits:

- Limit exposure to a minimum number of personnel, for a minimum amount of time, to the minimum amount of hazardous material consistent with safe and efficient operations.
- Personnel Limits – All non-essential personnel will be located in the control room during all operations involving the handling of energetic material unless prior approval has been granted from the SGDL supervisor. A maximum number of 4 personnel are allowed to be present during testing.

Indicators for Identifying Abnormal Process Conditions:

- Unburned propellant is found on work surfaces within the strand burner.
- Abnormal pressure readings during testing are shown in the LabVIEW NI module.
- Burn rate is substantially different from the expected burn rate.

START OF DAY PRETEST SHEET

1.1. Testing Conditions and Safety:

- 1.1.1. Test Engineer: _____
- 1.1.2. Operator Safety: _____
- 1.1.3. Personnel present: _____

- Total persons present (max 4): _____
- 1.1.4. Note date/time: _____
- 1.1.5. Place the testing sign on the entry door to HP 101, place caution tape across the door, and lock the door.
- 1.1.6. Barometric pressure (inHg): _____
- 1.1.7. HP inside temperature: _____
- 1.1.8. Number of planned tests: _____

1.2. Safety Briefing:

- 1.2.1. Review hazards present on-site during testing and required personnel protective equipment (PPE) as specified by the PPE survey and JHA.
- 1.2.2. Distribute PPE to all personnel to be present during testing that will be working with/around the samples.

1.3. Signatures of Responsible Parties:

- 1.3.1. Test Engineer: _____
- 1.3.2. Operator Safety: _____

2. STRAND BURNER DATA ANALYSIS

All figures referenced within this attachment are listed in attachment 8

2.1. Safety Inspections

- 2.1.1. Ensure the external igniter wires located at the control station are spliced together
- 2.1.2. Ensure the N2 tank is not connected to the inlet pipeline of the strand burner
- 2.1.3. Ensure the power supply and the initiation control system (ICS) are both not connected and that the shunt is inserted in the ICS
- 2.1.4. Ensure the ICS key is connected to the other end of the shunt
- 2.1.5. Ensure the strand burner is grounded

2.2. Hardware Inspections

- 2.2.1. Inspect the strand burner for any cracks or pitting on all surfaces
 - 2.2.1.1. If any crack or pitting are found, inform the SGDL supervisor or their designated representatives
- 2.2.2. Inspect metal pot scrubbers stored in the central vertical column of the strand burner for excess residue (replace if needed)
- 2.2.3. Inspect o-rings and mating surfaces for signs of degradation
- 2.2.4. Clean any exposed mating surfaces using isopropyl alcohol and a paper towel. Dispose of the paper towel in the general trash can
- 2.2.5. Visually inspect all pipe fittings, valves, windows, sample holder platform, internal wire harness, and external components for signs of degradation
 - 2.2.5.1. If anything is found to be abnormal, notify the SGDL supervisor or their designated representatives to discuss troubleshooting options before proceeding
- 2.2.6. Visually inspect the N2 tank, pressure regulator, and pressure transducer for any damage

2.3. Hardware Setup and Strand Sample Platform Setup

- 2.3.1. Secure static wrist straps
- 2.3.2. Secure a strand sample onto the strand platform
 - 2.3.2.1. A 3D printed base is used to secure the sample onto the base of the platform
- 2.3.3. Connect the male connector clips to their respective location of the sample holder platform. Refer to figure 1
- 2.3.4. Install nichrome wire as shown in figure 1 onto the strand platform
- 2.3.5. Secure the strand sample platform into its respective position as shown in figure 2
- 2.3.6. Connect the two internal wire harnesses to the platform
 - 2.3.6.1. The harness with red tape is connected to the left connector while the green is connected to the right connector. Refer to figure 2

2.4. Continuity Check

- 2.4.1. Perform a continuity check on the igniter wires. Un-splice wires at the control station and use a multimeter to check continuity. Splice wires again once continuity is confirmed
 - 2.4.1.1. If continuity is not confirmed, check the nichrome wire is properly connected to the platform. If no continuity persists, check the contact between the nichrome wires and the male connector clips. Check if there is a break somewhere in the lines of the external igniter wires that run along the side of the room. Cease test at this point if no continuity can be confirmed and inform the SGDL supervisor or their designated representatives
- 2.4.2. Perform a continuity check on the embedded wires by using LabVIEW SB_DAA_FINALVERSION VI located in the Strand burner folder on the desktop of camera control 5. Run the VI and check that the embedded wire graph is as shown in figure 3
 - 2.4.2.1. If errors persist with the VI, open NI Max > Network Devices > NI CDAQ-9188 and run a self-test on the NI 9263, and NI 9205
 - 2.4.2.2. Refer to Attachment 9 for embedded wire circuitry to run diagnostics if needed
- 2.4.3. Ensure the SB_DAA_FINALVERSION VI is not running before moving on

2.5. Setting Voltage on 24 V Power Supply

- 2.5.1. Ensure the igniter leads are not connected to the ICS
- 2.5.2. Connect the ICS to the power supply with the shunt in place

- 2.5.3. Turn on the power supply
- 2.5.4. Set the voltage and current to zero
- 2.5.5. Connect a nichrome wire (26 AWG) of similar length as the actual igniter to the alligator clips of the ICS
 - 2.5.5.1. Ensure the nichrome wire is not touching any surface or conductive material. It will become very hot and burn during this test so it must be positioned carefully away from any combustible materials.
- 2.5.6. Arm ICS
 - 2.5.6.1. Flip the red switch and hold the key. The green, yellow, and red LEDs must all be lit
- 2.5.7. Turn the current knob clockwise until you no longer can
- 2.5.8. Slowly turn the voltage to 12 V or until the nichrome wire is observed to glow red
 - 2.5.8.1. This is the initiation voltage that will be used in the test. Do not adjust the voltage further.
- 2.5.9. Disarm the ICS by removing the key and flipping the red switch guard in the DOWN position
- 2.5.10. Insert the shunt into the ICS
- 2.5.11. Turn off the power supply
- 2.5.12. Allow the nichrome wire to cool and then proceed to remove the wire

2.6. Solenoid Valve Checks

- 2.6.1. Ensure the valve control box is connected to power and both switches are off. Refer to figure 4
- 2.6.2. Ensure the air compressor is set to output 120 psi. Connect the air compressor to the female plug at the bottom of the strand burner
- 2.6.3. Flip both switches to the on position
- 2.6.4. Walk over to the strand burner and ensure the indicators on the solenoid valves
 - 2.6.4.1. If the solenoids valve indicators are not as shown, proceed to check the following:
 - 2.6.4.1.1. Ensure the air compressor is set to output 120 psi
 - 2.6.4.1.2. Ensure the air compressor is properly connected to the strand burner
 - 2.6.4.1.3. Check if the solenoid valves are receiving 24 V DC
 - 2.6.4.1.3.1. If errors persist, contact the SGDL supervisor or their designated representative for troubleshooting options

2.7. Securing Flanges on Mating Surfaces

- 2.7.1. Open the outlet valve and close the inlet valve
- 2.7.2. Secure the remaining flanges on the strand burner using the provided bolts using the template provided in figure 6.

2.8. Securing Pressure Transducer to Flange

- 2.8.1. Apply an appropriate amount of Teflon tape to the NPT threads of the transducer and tighten the transducer to the thread NPT hole in the flange

2.9. Pulling Vacuum on Strand Burner

- 2.9.1. Secure the ball valve to the other flange using Teflon tape on the threads
- 2.9.2. Connect the vacuum pump to the other end of the valve
- 2.9.3. Run SB_DAA_FINALVERSION VI
- 2.9.4. Turn on the vacuum pump
- 2.9.5. Check the LabVIEW VI and ensure the pressure is dropping
- 2.9.6. Once a steady state is reached, close the ball valve and turn off the vacuum pump

- 2.9.7. Check the LabVIEW VI to ensure there is a vacuum seal on the chamber
- 2.9.7.1. If the chamber is not holding vacuum and is returning to ambient conditions rapidly, check all bolts and flanges to ensure they are secured properly

2.10. N2 Tank-to-Strand Burner Connection

- 2.10.1. Non-essential personnel relocate to the control room while the test engineer follows the next several steps
- 2.10.2. Connect the pressure tank to the pressure regulator
- 2.10.3. Connect the regulator to the inlet pipe
- 2.10.4. Ensure the regulator control valve is open fully in the counterclockwise direction shown as “Decrease ->” on the regulator.
- 2.10.5. Fully open the N2 control valve
- 2.10.6. Set the outlet on the regulator to 50 psi

2.11. Pressure/Leak Checks

- 2.11.1. Relocate to the control room and ensure the cation tape is on display
- 2.11.2. Begin running SB_DAA_FINALVERSION VI
- 2.11.3. Close the outlet valve
- 2.11.4. Open the inlet valve
 - 2.11.4.1. Check LabVIEW VI and ensure the live pressure reading reads 50 psi and then proceed to close the inlet
 - 2.11.4.1.1. Wait about 30-seconds and close the inlet valve
 - 2.11.4.2. Listen for any leaks. If leaks are heard, the test engineer may approach the strand burner and attempt to find the leak. Dawn soap, water, and a brush may be used to find the leak by brushing soap water on suspected locations
 - 2.11.4.3. If a leak is found on the physical strand burner, i.e., welds, the test must be stopped and the SGDL supervisor or their designated representatives must be notified
 - 2.11.4.4. If a leak is found on any of the pipe connections or wire pass-through components, attempt to tighten to resolve the leak. If this does not resolve the leak, depressurize the strand burner and proceed to remove the component for inspection. If one cannot fix the hardware, the SGDL supervisor or their designated representatives must be notified to discuss the next steps before proceeding
- 2.11.5. If no leaks are heard, proceed to the next step
- 2.11.6. The test engineer may then approach the strand burner and visually inspect that the sample is still standing upright through the window to make sure that is clear of any obstructions by using a mirror. If applicable, the surveillance footage may be used for visual inspection

2.12. Strand Burner Pressurization/Firing

- 2.12.1. Ensure the caution tape at the entrance of the testing room is on display. Refer to attachment 3 for placement
- 2.12.2. Set the regulator valve to the required pressure
- 2.12.2.1. Refer to the test matrix for approved pressures
- 2.12.3. Relocate to the control room
- 2.12.4. Open the inlet valve and wait for pressure to reach the desired range by running the LabVIEW VI and monitoring the live pressure reading
- 2.12.4.1. Close the inlet valve once desired pressure is reached
- 2.12.5. If no leaks are heard proceed to step 2.12.7
- 2.12.5.1. If leaks are heard, depressurize the strand burner and reset the pressure regulator to 50 psi, and repeat steps 2.11.4.1 – 2.11.4.4
- 2.12.6. Ensure the shunt is inserted into ICS

- 2.12.7. Turn on the power supply
- 2.12.8. Run SB_DAA_FINALVERSION VI
- 2.12.9. Un-splice the igniter leads and connect them to ICS
- 2.12.10. Turn on the power supply
- 2.12.11. Remove shunt
- 2.12.12. Arm ICS by positioning the red switch up and flipping the switch to the ON position
- 2.12.13. Test engineer announces intent to initiate
 - 2.12.13.1. Insert key
- 2.12.14. Count down – fire
 - 2.12.14.1. Hold the key in the on position for 5-10 seconds or until you have confirmed the sample is ignited
- 2.12.15. Monitor the LabVIEW VI embedded wire graph to verify that wire 6 triggers before terminating the test
 - 2.12.15.1. If a misfire occurs, or if a leak is heard during combustion that is not coming from the safety relief valve, refer to step 4 (4.1.16 for leaks)
 - 2.12.15.2. Relief valve is set to 1675 psi. If a leak is heard at or above this pressure, assume it's the safety relief valve. Wait for the pressure to drop 5% of the live pressure reading and if the leak persists, refer to step 4.1.16
- 2.12.16. After a successful test, disarm the ICS by removing the key and flipping the red switch down.
- 2.12.17. Insert the shunt
- 2.12.18. Disconnect the igniter leads them and splice together
- 2.12.19. Turn off the power supply
- 2.12.20. Stop and save all data

3. Clearing Strand Burner

- 3.1.1. Open the outlet valve and wait 30-seconds
- 3.1.2. Adjust the pressure regulator to 50 psi
- 3.1.3. Open the inlet valve for 30-second to flush the strand burner
- 3.1.4. Close the inlet valve
- 3.1.5. Close the main control valve on the N2 tank
- 3.1.6. Open the inlet valve and allow all lines to purge
- 3.1.7. Remove caution tape at the entrance to the testing room
- 3.1.8. Unbolt the flange
- 3.1.9. Place the flange aside and allow 2-minutes for the strand burner to vent
 - 3.1.9.1. Test engineer must clear the strand burner before any non-essential personnel are allowed to leave the controlled location
- 3.1.10. At this point, repeat appropriate steps if another sample is scheduled to be tested

4. Misfire/ Pressure Leak Procedures

- 4.1.1. If there is no pressure rise observed in the LabView module after firing, or if wires 1-6 in the embedded wire graph are not triggered after 30-seconds after firing, disarm ICS and wait 1-minute and call the SGDL supervisor or their designated representative and inform them of the misfire
 - 4.1.1.1. If applicable, step 4.1.1 may be replaced with a visual inspection using the camera for electrical misfire confirmation
- 4.1.2. If an electrical misfire is confirmed, perform a continuity check on the power supply and the ICS
 - 4.1.2.1. If continuity is confirmed, proceed to step 4.1.3

- 4.1.2.2. If no continuity is confirmed, continue to steps 4.1.5 – 4.1.14
- 4.1.3. Attempt to fire
 - 4.1.3.1. Each strand is allowed two attempts
- 4.1.4. If an electrical misfire is confirmed on the second attempt, proceed to do the following steps:
 - 4.1.5. Disarm ICS and power off the power supply
 - 4.1.6. Splice igniter leads together
 - 4.1.7. Stop running the LabVIEW VI
 - 4.1.8. Ensure the inlet valve is closed
 - 4.1.9. Open the outlet valve and visually/audibly confirm open
 - 4.1.10. Disconnect igniter leads
 - 4.1.11. Power off power supply and disconnect ICS
 - 4.1.12. Wait 5-minutes and call the SGDL supervisor or their designated representative and inform them of the second electrical misfire
 - 4.1.13. Close the main valve on the pressurized tank and then ensure the inlet and outlet valves are open to depressurize all lines
 - 4.1.14. Remove cation tape and remove the flange closest to the camera and reset the sample and igniter by following the appropriate steps
 - 4.1.15. For non-electrical misfires, a continuity check must confirm that the igniter has been consumed. If this is the case, a 5-minute wait period must be conducted. During this time, contact the SGDL supervisor or their designated representative and inform them of the misfire. Proceed to depressurize the strand burner as stated in steps 4.1.5 – 4.1.11 and 4.1.13 and 4.1.14. Follow the appropriate steps to reset the sample and igniter
 - 4.1.16. If a leak is heard, ensure inlet is closed, open the outlet, and reset the pressure regulator to 50 psi and repeat step 2.11 and proceed to 2.12
 - 4.1.17. In case of a rapid disassembly of the strand burner the test engineer must attempt to open the outlet valve. All personnel are to immediately exit Jones Hall Close the door to room 101
 - 4.1.18. All personnel will be checked for possible injuries, first aid applied as needed, and the area inspected for remaining hazards.
 - 4.1.19. Emergency Medical Services will be called for assistance if needed.
 - 4.1.20. The SGDL supervisor or their designated representative will then be notified immediately.

5. Post testing

5.1. Terminating Test

- 5.1.1. Once the strand burner has been cleared by the test engineer of energetic, proceed to the following steps:
 - 5.1.1.1.** Disconnect the pressure regulator
 - 5.1.1.2.** Disconnect N2 tank from the main inlet line
 - 5.1.1.3.** Secure the inlet cover on the N2 tank
 - 5.1.1.4.** Disconnect the ICS from the power supply
 - 5.1.1.5.** Disconnect the power supply from the wall outlet
 - 5.1.1.6.** Ensure all data has been saved to an external drive
 - 5.1.1.7.** Turn off data acquisition system
 - 5.1.1.8.** Tear down all equipment pertaining to the spectrometer and pyrometer
 - 5.1.1.9.** Ensure all energetics have been stored away in the energetics locker
 - 5.1.1.10.** Disconnect the strand platform from the internal wire harness

- 5.1.1.11.** Remove the strand platform from the strand burner
- 5.1.1.12.** Using nitrile gloves, clean the platform and the inside of the strand burner using isopropyl alcohol and a paper towel
- 5.1.1.13.** Inspect the strand burner for severe signs of degradation
 - 5.1.1.13.1.** If any are found, notify the SGDL supervisor or their appointed representative
- 5.1.1.14.** Disconnect the MINI DIN transducer cable from the pressure transducer
 - 5.1.1.14.1.** Inspect pressure transducer for any signs of degradation, notify the SGDL supervisor or their appointed representative if damage is found
- 5.1.1.15.** Store flanges and all bolts away in an appropriate location
- 5.1.1.16.** Store all other equipment/tools used throughout the test in their respective locations
- 5.1.1.17.** Remove both sets of caution tape and the test sign secured to the front door

D.0.3 Static Fire Test Plan

Solid Rocket Motor Thrust Testing

TP-23-D-46

1. Purpose:

Static fire testing will be conducted on ammonium perchlorate composite propellant (APCP) solid rocket motors (SRMs). The tests will be used to collect thrust and pressure measurements to evaluate the burn rate performance of the 76 mm and 98 mm APCP SRMs in small and full-scale formats.

2. Test Overview/Summary:

- 2.1. Initial checks will be conducted on all diagnostic systems before testing. This will include the pressure and force transducers, spectrometer, and pyrometer.
- 2.2. The APCP SRMs will be cartridge-loaded as small grains into either the 76 mm or 98 mm diameter motor cases that have been backfilled with an inert material to reduce the total volume of the system. The backfill process and cartridge loading will be conducted by hand. The cartridge loading process will be performed at Torres West Lab.

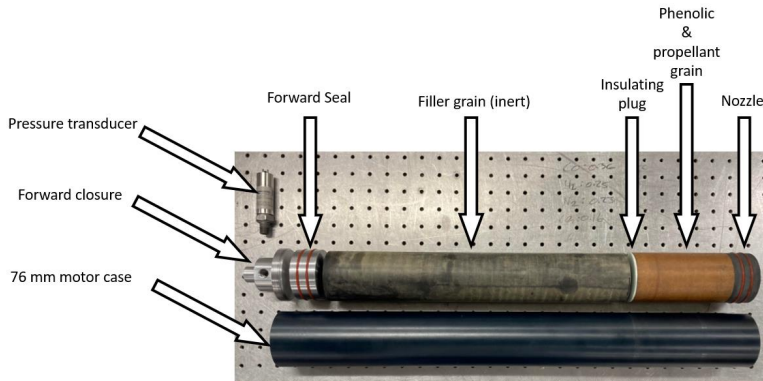


Figure 1: Components of a 76 mm motor case with placeholder tubes for grains.

- 2.3. The testing of the motor grains will be conducted at Torres West Lab. The loaded motor case will be mounted into the thrust stand currently in place. The case will be supported along the length at one point and anchored to the stand itself at the front of the case. The motor mount includes bottom supports and a top cross-bar to keep the motor case rigid and horizontal.



Figure 2: Thrust test stand with motor case inserted. Nozzle and force transducer assembly not pictured.

- 2.4. The test will be initiated using the selected igniter from within the Control Bunker.
- 2.5. The motor performance will be evaluated by thrust measurements taken by a force transducer centered and normal to the central anchoring face of the motor case. Data will be collected with a National Instruments DAQ system in place in Torres West Lab. The transducer and DAQ will be provided and operated by Dr. Hargather's laboratory group.
- 2.6. Cameras positioned around Torres West Lab will take footage of the burn tests and will also function as safety checks from the control room. These cameras are already installed in the facility.
- 2.7. Additional cameras will be set up to record high-speed or low-speed images of the motor firing from various positions as supplemental data.

3. Location of Test:

- 3.1. The motor preparation: The motor will be cartridge loaded at Torres West Lab
- 3.2. The motor will be tested at the Torres West Lab.

4. Sequence of Steps: (See Attachment 4 for checklist)

5. Test Matrix:

5.1.

Test #	Type of Test	Data Requirements	Energetics
1	Motor ignited in thrust stand and burned until consumed.	Full burn time of motor: Data acquisition from pressure and force transducer.	.453 kg APCP motor grain, 1 igniter.
2	Motor ignited in thrust stand and burned until consumed.	Full burn time of motor: Data acquisition from pressure and force transducer	1 kg APCP motor grain, 2 igniters.
3	Motor ignited in thrust stand and burned until consumed	Full burn time of motor: Data acquisition from pressure and force transducer.	4.5 kg APCP motor 2 igniters.

Table 1 – Test Matrix

6. Construction: (non-standard items only)

- 6.1. All setup and construction of the rocket test stand will be performed by the SGDL.

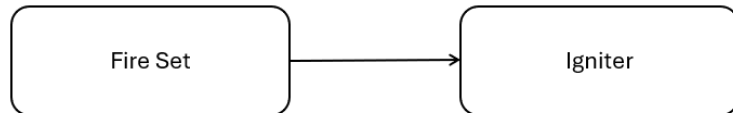


Figure 2: Firing Schematic.

8. Energetic Materials:

8.1. APCP: Approximately 0.453 kg to 1 kg

8.2. Igniter (mg range).

8.2.1. Commercial pyrogen pyrotechnic for hobby rocket motors. Purchased from:
https://www.apogeerockets.com/Rocket_Motors/Motor_Starters/Fat_Boy_Starters

9. Instrumentation:

Provided by SGDL.

10. Specific Tools and Equipment: (Includes specialty tools, heavy equipment, Fire Sets, etc.)

- 10.1. O-ring pliers
- 10.2. Fire set
- 10.3. Nikon camera with lens
- 10.4. Pyrometer
- 10.5. Spectrometer
- 10.6. TD1000 pressure transducer
- 10.7. WMC-2000 force transducer
- 10.8. Viton o-rings for nozzle and dash number 229 o-rings for retaining support

11. Documentation: (Includes videos, reports, etc.)

- 11.1. Video from monitoring cameras throughout Torres West Lab.
- 11.2. Data from Force Transducer.

12. Instructions for Spill Cleanup and Disposal of any Scrap and Waste A&E: (if different than those listed in Attachment 2)

13. Specific Hazards: (Include hazards in Safety Data Sheets (SDS))

14. PPE Required: (As determined by JHA; include setup, test and post-test operations)

- 14.1. Safety glasses for loading, motor case mounting.
- 14.2. Nitrile gloves for loading
- 14.3. Thermal gloves for post-firing cleanup.
- 14.4. Ear protection for anyone in the Test Bunker.
- 14.5. Ordnance must wear cotton for anti-static.
- 14.6. Wrist stats for grounding in the Test Bunker while handling the motor/igniter.

15. Emergency Procedures: (if different than those listed in Attachment 2)

16. References: (Include all references pertinent to the project/test)

- DoD 4145.26-M, DoD Contractors Safety Manual for AA&E
- SOP 101, Health and Safety
- SOP 102, Field Laboratory Safety
- SOP 103, Industrial Safety
- SOP 108, HAZCOM Program
- SOP 201, Grounding Procedures

- SOP 202, Initiation of Energetic Materials
- SOP 203, Arms, Ammunition and Explosives Procedures
- SOP 402, Emergency Action Plan
- SOP 403, Risk Management
- SOP 500, Operating with COVID Restrictions

17. Attachments:

1. Job Hazard Analysis
2. Safety and General Requirements
3. Site Closure Map
4. Test Checklist
5. Tailgate Briefing Form
6. Safety Data Sheets

Attachment 2 – Safety and General Requirements

Igniter:

- The igniter shall not be inserted into the motor grain until all other processes of setup have been completed and all personnel save for Ordnance have relocated to the control room.
- Ignition circuit shall not be connected until all personnel are within the control room.

Hazardous Waste:

- The use, recovery, collection, transport, and storage of military munitions for Research, Development, Testing and Evaluation (RDT&E) (e.g. safety, developmental testing, surveillance function testing, static fire, or quality control or assurance testing) is considered use for intended purpose and not subject to regulation under Resource Conservation and Recovery Act (RCRA). (Military Munitions Rule (MMR) paragraph 3.B.2.b.)
- As long as all excess energetic material is destroyed on site, and not removed from the test range, it is not considered waste and does not fall under RCRA. (MMR paragraph 10.C.3.)
- Any spilled loose material will be completely gathered up and determined if the material is still usable.
- If the material is still usable, it is not considered waste and should be used or stored as applicable.
- Spilled material deemed unusable will be properly containerized, labeled and stored for later disposal in accordance with local policies and procedures.

Misfire Procedures:

- If there are no indications through the video feed that the ignitor initiated, all connections will be checked (in the bunker or personnel shelter only) to ensure they are connected correctly. If instrumentation does not need to be reset, then another attempt to fire may be made. The engineer/test manager will be consulted prior to attempting to fire again.
- If there is still no indication that the ignitor initiated, begin the applicable wait time as stated below:
 - All electric misfires will include a 15-minute wait time before personnel are permitted to approach the test article, unless determined to be otherwise.
 - All non-electric misfires will include a 30-minute wait time before personnel are permitted to approach the test article, unless determined to be otherwise.
- During the wait time, the engineer/test manager and the ordnance technician will contact the Ordnance Supervisor and Safety Officer, or their designated representatives, to inform them of the misfire and to discuss troubleshooting options.
- If the motor does not initiate but a continuity check and video feed shows the ignitor has been consumed, an additional 30-minute wait time before personnel are permitted to approach the test article will begin. During this time, the ordnance technician will contact the Ordnance Supervisor and Safety Officer or their designated representatives to inform them of the misfires and to discuss troubleshooting options.

- If the motor initiates but video and transducer data indicate highly abnormal performance, a 30-minute wait time before personnel are permitted to approach the test article will be implemented, and shall be reported to the ordnance supervisor and safety officer.

Emergency Procedures:

- Lightning: (reference procedures in SOP 104)
- Fire:
 - If there is a fire on or near the test site, all personnel will evacuate to the personnel shelter immediately (or further depending on the severity of the fire) and the safety office will be notified. If the grain is ejected, personnel shall seek shelter while remaining clear of the grain.

WARNING

Personnel WILL NOT fight a fire that could have any remote possibility of involving explosives.

WARNING

Personnel WILL NOT fight a fire that is located off the test pad. There is a strong possibility of unexploded ordnance being present off the test pad.

- Unexpected Explosion:

- All personnel will immediately assemble at the personnel shelter (or other previously identified location) and all personnel accounted for;
- All personnel will be checked for possible injuries, first aid applied as needed, and the area inspected for remaining hazards by ordnance personnel;
- Emergency Medical Services will be called for assistance, if needed;
- The safety office will then be notified immediately.

WARNING

If an explosion involves the Ordnance Technician (or any other personnel) on the test pad, personnel in the personnel shelter must make a determination whether or not it is safe to attempt to treat or assist the individual on the test pad.

Personnel and AA&E Limits:

- Limit exposure to a minimum number of personnel, for a minimum amount of time, to the minimum amount of the hazardous material consistent with safe and efficient operations.
- Personnel Limits – All non-essential personnel will be located in the personnel shelter during all operation involving the handling of energetic material unless prior approval has been granted from the Safety Office.
- Explosive Limits – Only explosives needed for a single test will be allowed on the test pad at any one time.

Indicators for Identifying Abnormal Process Conditions:

- Igniter fails to ignite propellant mixture
- Not all propellant is expended during burning
- Propellant is found on work/ground surfaces after a burn

Solid Rocket Motor Thrust Testing
START OF DAY PRETEST SHEET

TP-23-D-46

1.1. Testing Conditions and Safety:

- 1.1.1. Test Engineer: _____
- 1.1.2. Ordnance: _____
- 1.1.3. Operator Safety: _____
- 1.1.4. Personnel present: _____

- Total persons present (max 5): _____
- 1.1.5. Note date/time: _____
- 1.1.6. Check that a Z-sign is on entry road to Torres facility and a Z-sign is in place approaching Torres West Lab.
- 1.1.7. Check that the two gates at the Butler building are closed.
- 1.1.8. Check the Torres Main Building. If non-test related personnel are to be present in the Torres Main Building, inform them of testing to be performed in the Torres West Lab and that they are to remain inside the Torres building unless prior clearance is obtained from the test engineer.
- 1.1.9. Ensure Torres facilities Northwest and East of Torres West Lab are clear of personnel.
- 1.1.10. Review current wildfire conditions. If "extreme" conditions exist, priority of testing should be reviewed with the safety office.
- 1.1.11. Review wind conditions. If winds greater than 15mph are present, testing shall not commence.
- 1.1.12. Barometric pressure (inHg): _____
- 1.1.13. Torres West Lab inside temperature: _____
- 1.1.14. Number of planned tests: _____

1.2. Safety Briefing:

- 1.2.1. Review hazards present on site during testing and required personnel protective equipment (PPE) as specified by the PPE survey and JHA.
- 1.2.2. Distribute PPE to all personnel to be present during testing that will be working with/around the motor sample.

Page 20 of

1.3. Signatures of Responsible Parties:

1.3.1. Test Engineer: _____

1.3.2. Ordnance: _____

1.3.3. Operator Safety: _____

2. IGNITER INITIATION TESTS**2.1. Setup**

- 2.1.1. Ensure Start of Day Pretest Sheet has been properly filled out.
- 2.1.2. Perform a walk-through of the procedure with all personnel.
- 2.1.3. Ensure all personnel have been properly briefed on testing hazards and have received proper safety briefing and PPE.
- 2.1.4. Run igniter lines from control room to Test location.
- 2.1.5. Turn on safety camera system to monitor test location.
- 2.1.6. Propellant specimen (< 0.25 kg) prepared from printed material shall be placed into a steel cup on the concrete pad outside the building. The igniter firing lines shall be run into the control bunker.

2.2. Igniter Placement

- 2.2.1. All following steps in 2.2 shall be performed by Ordnance.
- 2.2.2. Igniter shall be placed facing the propellant specimen and secured as necessary with tape if the flat surface causes it to roll.
- 2.2.3. Igniter leads shall be connected to the firing lines.
- 2.2.4. Ordnance personnel will return to the Control Bunker after verifying the igniter is secured and that the leads are wired to the firing lines.

2.3. Igniter Trigger Check

- 2.3.1. All personnel shall be verified to be in the Control Bunker.
- 2.3.2. The test engineer will announce that they are firing the igniter and flip the ignition switch when ready.
- 2.3.3. After a delay, flip the switch back to the off position.
- 2.3.4. External cameras shall be initially used to verify if ignition occurs. If misfires occur, misfire procedures shall be implemented.
- 2.3.5. Ordnance will confirm all material consumed at the end of the test. Ordnance will approach the material with safety glasses and gloves.

3. MOTOR TEST: PRETEST PROCEDURES**3.1. Start of Day**

- 3.1.1. Ensure Start of Day Pretest Sheet has been properly filled out.
- 3.1.2. Perform a walk-through of the procedure with all personnel.
- 3.1.3. Ensure all personnel have been properly briefed on testing hazards and have received proper safety briefing and PPE.
- 3.1.4. Ensure all safety videos are operating and recording.
- 3.1.5. Ensure NI DAQ system power cycles correctly.
- 3.1.6. Check all exposed wiring in the Test Bunker for damage.
- 3.1.7. Ensure doors to Test Bunker are secured in the open position.
- 3.1.8. Run igniter lines from control room to Test Bunker.

3.2. System Hardware Checkouts (Cameras, NI DAQ, Igniter)

- 3.2.1. Verify that all cameras are functional and streaming video.
- 3.2.2. Verify that the NI DAQ is set to record data to a new file. Ensure LABVIEW is capable of detecting the NI DAQ system.
- 3.2.3. Perform an initial no-voltage igniter firing line check with a voltmeter. The igniter lines should be spliced at this point in time.
- 3.2.4. Ensure test stand components are all grounded.
- 3.2.5. All personnel save for the Ordnance technician and test engineer should evacuate to the control room at this point.

4. ASSEMBLY PROCEDURES

- 4.1. In the event of anything unusable or unexpected during the cartridge loading, the engineer/test manager and the ordnance technician will contact the Ordnance Supervisor and Safety Officer, or their designated representatives, to inform them of the event and to discuss troubleshooting options.

4.2. Setup

- 4.2.1. Ensure propellant grain has no visible cracks on exposed surfaces.
- 4.2.2. Insert the snap-ring/rear retaining ring into the motor case.
- 4.2.3. With nitrile gloves, apply a layer of high-temperature grease to the viton o-rings and place the o-rings onto the nozzle.
- 4.2.4. Apply a layer of high-temperature grease onto the section of the nozzle supporting the o-rings.
- 4.2.5. Insert the graphite nozzle from the forward end of the motor case and push the nozzle up the the snap-ring/retaining ring.
- 4.2.6. Apply a layer of high-temperature grease to the inside of the phenolic tube.
- 4.2.7. Apply a layer of high-temperature to the o-ring for the insulator plug and apply a layer of the grease to all surfaces of the insulator plug.
- 4.2.8. Insert the insulator plug by placing the phenolic tube vertically onto the test stand and push down onto the phenolic until the insulator seats all the way in.
- 4.2.9. Insert the propellant grain into the phenolic tube.
- 4.2.10. Insert the assembled grain into the forward end of the motor case with the exposed propellant face first.
- 4.2.11. Apply a thick layer of high-temperature grease onto all surfaces of the inert grain.
- 4.2.12. Insert the inert grain into the motor case.
- 4.2.13. Apply a layer of high-temperature grease onto the forward plug o-ring and secure the o-ring onto the forward plug.
- 4.2.14. Apply a thick layer onto the back of the forward closure and secure the forward closure onto the motor case.
 - Tighten the forward closure until it sits flush to the motor case.

5. MOTOR TEST: PROCEDURE

(May only begin if Start of Day Pretest Sheet and all system checkouts have been performed.)

5.1. Inserting Igniter

- 5.1.1. Confirm all personnel are accounted for and are in the control bunker. Confirm the surrounding area is clear.
- 5.1.2. All following steps in 5.1 should be performed by Ordnance.
- 5.1.3. Ensure personnel handling the igniters are grounded to the main thrust stand table and are wearing safety glasses.
- 5.1.4. Insert the igniter into the motor case. The igniter compound should be inserted past the nozzle structure.
- 5.1.5. Ensure the igniter will remain within the motor but that it is loose and able to be ejected.
- 5.1.6. Connect firing lines to the igniter leads. The igniter firing system shall be locked and the test engineer will have the key.
- 5.1.7. Return to the control room and close the external door.

5.2. Motor Firing

- 5.2.1. Verify with the Test Engineer that all personnel are accounted for and are in the control room. Obtain final clearance from the engineer that the test is ready to proceed.
- 5.2.2. Ensure NI DAQ is active.
- 5.2.3. The test engineer shall perform the firing procedure.
- 5.2.4. Arm the fire set.
- 5.2.5. Announce intent to fire loudly and fire when ready.
- 5.2.6. Wait for 5 seconds and return the igniter switch to its original position.
- If misfire occurs, refer to attachment 2 for appropriate steps.
- 5.2.7. Turn off NI DAQ.
- 5.2.8. When the Ordnance technician determines the area is safe from video feeds and at least 5 minutes have passed, the Ordnance technician shall leave the Control Bunker to inspect the motor case. The Ordnance technician shall be wearing thermal gloves and safety glasses. The Ordnance technician will disassemble the assembly to inspect the grain location to verify that it has been consumed, refer to step 6 for motor removal. Once the Ordnance technician has given permission, other personnel may exit the control room. All personnel should be cautioned to avoid touching the motor case as it may be hot.
- 5.2.9. Ordnance will remove the spent motor cartridge from the motor case.
- 5.2.10. Ordnance and Dr. Hargather's lab personnel will inspect the motor case before additional testing is to be performed.

6. Motor Test: End-of-test procedure

(If another test is to be performed, allow for additional cooling if necessary, and proceed to section 4.2 for loading a new grain)

6.1. Motor Removal

- 6.1.1. All personnel entering the Test Bunker should be equipped with safety glasses.
- 6.1.2. If the motor case is still hot, allow nozzle and case to cool before proceeding to following steps.
- 6.1.3. Remove the retaining bars on the "cradles".
- 6.1.4. Unscrew the motor case from the test stand.
- 6.1.5. Remove the forward closure and slide out the forward seal, and filler grain.
- 6.1.6. Visually inspect the filler grains within the case for damage and

- record, if applicable.
- 6.1.7. Remove the grain assembly
 - 6.1.8. Inspect paper liner to ensure all propellant was consumed.
 - In the instance there is still propellant, the engineer/test manager and the ordnance technician will contact the Ordnance Supervisor and Safety Officer, or their designated representatives, to inform them and troubleshoot.
 - 6.1.9. Remove the nozzle and allow to cool.
 - 6.1.10. Reset the test stand “cradles” and carriage system.

7. End-of-day procedures

7.1. Equipment and Facility Shutdown

- 7.1.1. Verify igniter voltage source is disconnected from all wiring. Firing line shall be retrieved and stored.
- 7.1.2. Verify NI DAQ has powered down.
- 7.1.3. Turn off video feeds in control room.
- 7.1.4. Turn off power supplies to all control equipment.
- 7.1.5. Collect all motor case components from the test facility.
- 7.1.6. Secure the doors to the control room and Test Bunker.

D.0.4 Tensile Testing Test Plan

1. Purpose:

Uniaxial tensile testing will be performed in Jones 16 with a Mark-10 test stand and a digital image correlation (DIC) system to measure the strain response of ammonium perchlorate composite propellant (APCP) samples loaded in tension. Tensile tests will include JANNAF Type-C, Scaled JANNAF Type-C, micro dog bone, and ASTM D638 Type III geometries to assess the effect of geometry on the calculated material properties.

2. Test Overview/Summary:

- 2.1. Inspection of components will be performed before conducting testing, listed in attachment 4, to ensure the components perform nominally.
- 2.2. Inert propellant samples are used for the initial setup of field-of-view (FOV) and exposure times of the DIC system.
- 2.3. Calibration targets are used by rotating horizontally, vertically, and in-plane taking about 30 images for calibrating the DIC system.
- 2.4. A Mark-10 tensile machine will be used to measure the force vs time being applied to a tensile sample along with recording high-speed digital images for DIC of the full-field stress-strain response.
- 2.5. Four different specimen geometries will be studied: JANNAF Type C, Scaled JANNAF Type-C, micro dog bone, and ASTM D 638 Type III.

3. Location of Test:

- 3.1. All testing will be conducted in Jones 16.
- 3.2. Preparation of samples will be conducted in Jones 16 and the HP building

4. Sequence of Steps: (See Attachment 4 for checklist)

5. Test Matrix:

5.1.

Sample ID	Geometry	Type of Test	Data Requirements	Energetics in each sample
JFSC	JANNAF	Tensile Test	Force vs Time FLIR Blackfly Images	45.2 g APCP
JQSD	Scaled JANNAF	Tensile Test	Force vs Time FLIR Blackfly Images	6.7 g APCP
MIC	Micro	Tensile Test	Force vs Time FLIR Blackfly Images	3.2 g APCP
TMD638T3	ASTM Type III	Tensile Test	Force vs Time FLIR Blackfly Images	72.6 g APCP

Table 1 – Test Matrix

6. Construction: (non-standard items only)

- 6.1. All setup and construction of the DIC system and Mark-10 will be performed by the test engineer.

This electrical diagram is for the data acquisition system. No energetics are being initiated here.

7. Energetic Materials:

- 7.1. JANNAF geometry – 45.2 g each sample
- 7.2. Scaled JANNAF geometry – 6.7 g each sample
- 7.3. Micro geometry – 3.2 g each sample
- 7.4. ASTM D 638 Type III geometry – 72.6 g each sample

8. Instrumentation:

Provided by SGDL.

9. Specific Tools and Equipment: (Includes specialty tools, heavy equipment, initiation control system, etc.)

- 9.1. Camera control 5
- 9.2. DIC system
 - 9.2.1. 2 FLIR Blackfly GigE cameras, tripod mount, LED lights, and camera mounts
 - 9.3. Oscilloscope
 - 9.4. BNC and ethernet cables
 - 9.5. Power over Ethernet switch

10. Documentation: (Includes videos, reports, etc.)

- 10.1. Tailgate Briefing Form
- 10.2. Video from monitoring cameras throughout Jones 16

11. Instructions for Spill Cleanup and Disposal of any Scrap and Waste A&E: (if different than those listed in Attachment 2)

12. Specific Hazards: (Include hazards in Safety Data Sheets (SDS))

13. PPE Required: (As determined by JHA; include setup, test, and post-test operations)

- 13.1. Safety glasses
- 13.2. Nitrile gloves
- 13.3. Anti-static wrist straps for handling propellant
- 13.4. Lab attire
 - 13.4.1. Long sleeve shirt or lab coat, jeans, close-toed shoes (preferably steel toes for the test engineer)

14. Emergency Procedures: (if different than those listed in Attachment 2)

15. References: (Include all references pertinent to the project/test)

- DoD 4145.26-M, DoD Contractors Safety Manual for AA&E
- SOP 101, Health and Safety
- SOP 102, Field Laboratory Safety
- SOP 103, Industrial Safety
- SOP 108, HAZCOM Program
- SOP 201, Grounding Procedures
- SOP 202, Initiation of Energetic Materials
- SOP 203, Arms, Ammunition and Explosives Procedures
- SOP 402, Emergency Action Plan
- SOP 403, Risk Management

16. Attachments:

1. Job Hazard Analysis
2. Safety and General Requirements
3. Site Closure Map
4. Test Checklist
5. Tailgate Briefing Form
6. Safety Data Sheets

Attachment 2 – Safety and General Requirements

Mark-10 Operation:

- Ensure that the machine is grounded while performing propellant testing.
- Note the force gauge's capacity before use and ensure that the capacity is not exceeded. Producing a force greater than 200% of the gauge's capacity can damage the internal load cell. An overload can occur whether the gauge is powered on or off.
- Never operate the gauge if there is any visible damage to the AC adapter or the gauge itself.
- Ensure that the gauge is kept away from water or any other electrically conductive liquids at all times.
- The gauge should be serviced by a trained technician only. AC power must be disconnected, and the gauge must be powered off before the housing is opened.
- Always consider the characteristics of the sample being tested before initiating a test.
- Wear eye and face protection when testing, especially when testing brittle samples that have the potential to shatter under force. Be aware of the dangers posed by potential energy that can accumulate in the sample during testing. Extra bodily protection should be worn if a destructive failure of a test sample is possible.
- In certain applications, such as the testing of brittle samples that can shatter, or other applications that could lead to a hazardous situation, it is strongly recommended that a machine guarding system be employed to protect the operator and others in the vicinity from shards or debris.
- When the gauge is not in use, ensure that the power is turned off.

Hazardous Waste:

- The use, recovery, collection, transport, and storage of military munitions for Research Development Testing and Evaluation (RDT&E) (e.g., safety, developmental testing, surveillance function testing, static fire, or quality control or assurance testing) is considered used for the intended purpose and not subject to regulation under Resource Conservation and Recovery Act (RCRA). (Military Munitions Rule (MMR) paragraph 3.B.2.b.)
- Any spilled loose material will be completely gathered up and determined if the material is still usable.
- If the material is still usable, it is not considered waste and should be used or stored as applicable.
- Spilled material deemed unusable will be properly containerized, labeled, and stored for later disposal in accordance with local policies and procedures.

Emergency Procedures:

- Fire:
 - If there is a fire on or near the test site, all personnel will evacuate to the south side parking lot of Jones (or further depending on the severity of the fire) and the safety office will be notified.

WARNING

Personnel WILL NOT fight a fire that could have any remote possibility of involving explosives.

- Unexpected ignition of sample:
 - Test engineer will attempt to move DIC system away from the test stand
 - All personnel will immediately evacuate to the south side parking lot of Jones (or another previously identified location) and all personnel accounted for.
 - All personnel will be checked for possible injuries, first aid applied as needed, and the area inspected for remaining hazards.
 - Emergency Medical Services will be called for assistance if needed.
 - The SGDL supervisor will then be notified immediately to discuss further steps.

Personnel and AA&E Limits:

- Limit exposure to a minimum number of personnel, for a minimum amount of time, to the minimum amount of hazardous material consistent with safe and efficient operations.
- Personnel Limits – All non-essential personnel will be asked to keep a standoff distance of 5 ft from the test stand during all operations involving the handling of energetic material unless prior approval has been granted from the SGDL supervisor. A maximum number of 4 personnel are allowed to be present during testing.

START OF DAY PRETEST SHEET

1. Testing Conditions and Safety:

1.1. Test Engineer: _____

1.2. Operator Safety: _____

1.3. Personnel present: _____

Total persons present (max 3): _____

1.4. Note date/time: _____

1.5. Place the testing sign on the entry door to Jones 16, place caution tape across the door, and close the door.

1.6. Barometric pressure (inHg): _____

1.7. Temperature: _____

1.8. Number of planned tests: _____

2. Safety Briefing:

2.1. Review hazards present on-site during testing and required personnel protective equipment (PPE) as specified by the PPE survey and JHA.

2.2. Distribute PPE to all personnel to be present during testing that will be working with/around the samples.

3. Signatures of Responsible Parties:

3.1. Test Engineer: _____

3.2. Operator Safety: _____

4. Mark-10 Setup

- 4.1. Ensure that the Mark-10 machine is in good working condition
- 4.2. Confirm all necessary accessories, such as grips and fixtures, are available
- 4.3. Connect the Mark-10 to a power source
- 4.4. Turn on the Mark-10 and wait for the machine to initialize
- 4.5. Ensure the correct load cell is installed
 - 4.5.1. If the incorrect load cell is installed, remove the hex head bolt using a 3/8 allen key that is located at the top of the load cell mounting fixture and install the correct load cell

4.6. Zero the load cell

- 4.7. Position the upper and lower solid state switches to prevent overtravel or as a test stand condition

4.8. Install the appropriate grips and fixtures

5. DIC System Setup and Calibration

- 5.1. Ensure the DIC system is in good working condition

- 5.2. Position the system perpendicular to where the speckle pattern face of the specimen sample is to be positioned

- 5.2.1. Adjust the height and level of the cameras using the spirit levels fixed to the camera mounts

5.3. Open up the VIC-Snap software and connect camera/cameras

5.4. Save the project name, i.e. 20240101Test 1

- 5.5. Set the required FOV for the camera and ensure the sample is clearly in focus. Use an inert sample with the appropriate specimen geometry to conduct the initial setup

5.6. Open the aperture on the camera

5.7. Using the focus tool, reduce the exposure using the slider below the image

- 5.8. On the camera lens, adjust the focus until you move past the lowest predicted noise value seen in VIC-snap

- 5.9. Return back so that the sample is set to the minimum value and relock the focus collar

5.10. Uncheck the focus tool

- 5.10.1. Conduct steps 5.5-5.10 for both cameras if using two cameras

5.11. Make sure VIC-snap is in the calibration image mode

- 5.11.1. Remove the inert sample to calibrate

5.12. Select the proper calibration target size

- 5.12.1. Choose a calibration target that remains within the field of view (FOV) while being able to tilt it at various angles. Ideally, the target should cover 75-80% of the FOV of both cameras. More importantly, VIC-snap should be able to identify which calibration target is being used

- 5.12.1.1. Three reference markers should register in VIC-Snap for positive ID

- 5.13. Using the space bar or the capture button, take about 10 images while rotating the target on the vertical axis, another 10 images while rotating the target on the horizontal axis, and another 10 images rotating the target in-plane

- 5.13.1. Any score < 0.1 is acceptable (the lower the better)

- 5.13.2. Any score > 0.1 is unacceptable and the calibration process should be redone

5.14. Exit calibration mode

6. Applying Speckle Pattern

- 6.1. Set up a large cardboard sheet (at least 24" x 24") on top of the gravel near the stones on the south side of HP

- 6.2. Lay an untreated propellant sample at the center of the board

- 6.2.1. A maximum of 220 g of propellant samples will be spray painted at once.
 All other samples will remain in storage in HP building.
- 6.3.** Using matte white spray paint, apply several thin layers until the propellant is completely white and no visible propellant is observed
- 6.3.1. Hold the paint can 10" to 12" away
- 6.3.2. Be careful not to apply a thick coat in a single pass since the paint will run when you pick up the sample
- 6.4.** Using matte black spray paint, hold the can 30" – 40" above the propellant sample holding the can completely parallel to the ground
- 6.5.** Tilt the can to be at 15° from vertical ensuring the tip of the nozzle stays at the distance stated above
- 6.6.** Move the can back towards you about 6"
- 6.7.** Press and hold the nozzle to eject paint for 1-2 seconds
- 6.7.1. During each spray, ensure you translate the can up and down +/- 4-to-10 inches depending on the size of the sample
- 6.7.2. Observe the speckle pattern form. You will have to apply several coats (about 4-6 coats).
- 6.8.** Steps 6.4 – 6.7 are shown in Figure 1
- 6.9.** Carefully pick up the sample ensuring not to touch the speckle pattern applied to the top face and move to Jones 16
- 6.9.1. A maximum of 220 g of propellant samples will be moved into Jones at once.
- 6.10.** Spray paint and area outside of HP building will be cleaned after samples are placed in Jones.
- 6.10.1. Spray paint will be stored appropriately in HP building
- 6.10.2. The cardboard may be thrown away in the general trash

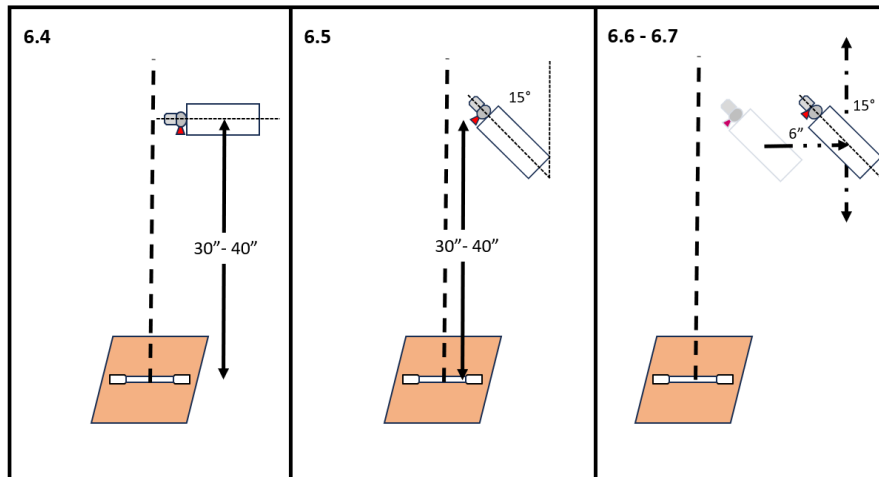


Figure 1: Sequence shown for steps 6.4-6.7.

7. Tensile testing

- 7.1.** Ensure the Mark-10 is properly grounded
- 7.2.** Secure static wrist straps and ensure they are grounded
- 7.3.** Secure the specimen onto the fixture
- 7.4.** Ensure all data acquisition systems (DAS) are armed
- 7.5.** Using the digital control system for the Mark-10, begin the test
 - 7.5.1.** If Mark-10 fails to begin testing, reset DAS and reattempt step 7.3
 - 7.5.2.** If Mark-10 fails to trigger the DAS and the specimen sample has experienced any applied load, return to steps 6 and 7.1-7.3
 - 7.5.2.1.** These post-testing samples must be placed in an electrostatic bag and marked as Year_Month_Day_FAIL_SAMPLE_ID_Test#. For example, A full-scale JANNAF would be labeled as 20240101FAILJFSCTest1
 - 7.5.2.1.1.** Sample IDs are in the Test Matrix in section 5 of page 3
- 7.6.** If a successful test has been completed, save all data from DAS
- 7.7.** Post-test sample must be placed into an electrostatic bag marked as Year_Month_Day_PASS_SAMPLE_ID_Test#
- 7.8.** Clean grips and any fixtures using isopropyl alcohol (IPA) and a paper towel
 - 7.8.1.** If any extraneous ammonium perchlorate (AP) is not present, throw the paper towel away in the general trash
 - 7.8.2.** If extraneous AP is present, place the paper towel in a zip-lock bag with an appropriate label.
 - 7.8.2.1.** At the end of the test, this zip-lock bag must be handled as hazardous waste and the HAZMAT safety officer (HMSO) in charge must be notified for pickup within 5 days of concluding testing
 - 7.8.2.1.1.** Once the test has concluded, pour water into the zip-lock bag until all the paper towels are submerged. The following day, place the zip-lock bag in a hazardous waste container, contact the HMSO if one is required, and hand off the container to the HMSO
 - 7.8.2.1.2.** The SGDL supervisor must be notified once step 7.7.2.1.1 has been completed
- 7.9.** Repeat steps 6, and 7.1-7.8 if more samples are to be tested
 - 7.9.1.** Note that the maximum of 220 g of samples will be in Jones at once
 - 7.9.2.** If testing more than 220 g, the initial 220 g of samples will be tested, then all moved to storage in HP building and a new test sequence will begin from steps 6, and 7.1-7.8
- 7.10.** Remove static wrist straps

8. Post-test tear down

- 8.1.** Save all data onto an external flash drive
- 8.2.** Power off all equipment
- 8.3.** Remove any fixtures and thoroughly clean them with IPA
 - 8.3.1.** See steps 7.8.1 and 7.8.2 if applicable
- 8.4.** Disconnect any cables between the DAS, Mark-10, and oscilloscope
- 8.5.** Remove camera lenses and attached front and rear dust covers and place them in their appropriate storage unit
- 8.6.** Pack up all items listed in section 10, Specific Tools and Equipment, and relocate them to L4 in the EMRTC building
 - 8.6.1.** The cardboard may be thrown away in the general trash

8.6.1.1. Find a dumpster near Jones, or it can be thrown away in the dumpsters on EMRTC property

8.7. All test specimens must be placed back into their corresponding package and stored in secure storage in HP building.

COMBUSTION PERFORMANCE AND
MATERIAL CHARACTERISTICS OF AN
AMMONIUM PERCHLORATE COMPOSITE PROPELLANT (APCP) WITH
VARYING ALUMINUM PARTICLE SIZE

by

David A. Avalos Violante

Permission to make digital or hard copies of all or part of this work for personal or classroom use is granted without fee provided that copies are not made or distributed for profit or commercial advantage and that copies bear this notice and the full citation on the last page. To copy otherwise, to republish, to post on servers or to redistribute to lists, requires prior specific permission and may require a fee.

